Analysis of localized solutions in coupled Gross-Pitaevskii equations

Muhammad Irfan Qadir

Thesis submitted to The University of Nottingham
for the degree of Doctor of Philosophy

October 2013

Dedicated to my beloved parents

who did many dua's for me!

Abstract

Bose-Einstein condensates (BECs) have been one of the most active areas of research since their experimental birth in 1995. The complicated nature of the experiments on BECs suggests to observe them in reduced dimensions. The dependence of the collective excitations of the systems on the spatial degrees of freedom allows the study in lower dimensions. In this thesis, we first study two effectively one-dimensional parallel linearly coupled BECs in the presence of external potentials. The system is modelled by linearly coupled Gross-Pitaevskii (GP) equations. In particular, we discuss the dark solitary waves and the grey-soliton-like solutions representing analogues of superconducting Josephson fluxons which we refer to as the fluxon analogue (FA) solutions. We analyze the existence, stability and time dynamics of FA solutions and coupled dark solitons in the presence of a harmonic trap. We observe that the presence of the harmonic trap destabilizes the FA solutions. However, stabilization is possible by controlling the effective linear coupling between the condensates. We also derive theoretical approximations based on variational formulations to study the dynamics of the solutions semi-analytically.

We then study multiple FA solutions and coupled dark solitons in the same settings. We examine the effects of trapping strength on the existence and stability of the localized solutions. We also consider the interactions of multiple FA solutions as well as coupled dark solitons. In addition, we determine the oscillation frequencies of the prototypical structures of two and three FA solutions using a variational approach.

Finally, we consider two effectively two-dimensional parallel coupled BECs enclosed in a double well potential. The system is modelled by two GP equations coupled by linear and nonlinear cross-phase-modulations. We study a large set of radially symmetric nonlinear solutions of the system in the focusing and defocusing cases. The relevant three principal branches, i.e. the ground state and the first two excited states, are continued as a function of either linear or nonlinear couplings. We investigate the linear stability and time evolution of these solutions in the absence and presence of a topological charge. We notice that only the chargeless or charged ground states can be

stabilized by adjusting the linear or nonlinear coupling between the condensates.

Publications

Most of the work of this thesis has been published or going to appear for publication.

1. Parts of Chapter 3 in this thesis have been published in:

   M. I. Qadir, H. Susanto and P. C. Matthews, Fluxon analogues and dark solitons in linearly coupled Bose-Einstein condensates, J. Phys. B: At. Mol. Opt. Phys. 45, 035004 (2012).

2. Parts of Chapter 4 in this thesis have appeared as a chapter in:

   M. I. Qadir, H. Susanto and P. C. Matthews, Multiple fluxon analogues and dark solitons in linearly coupled Bose-Einstein condensates. In B. A. Malomed (Ed), Spontaneous Symmetry Breaking, Self-Trapping, and Josephson Oscillations in Nonlinear Systems (Springer, Berlin, 2013), $485 - 508$.

Acknowledgements

First of all, I praise and say bundle of thanks to Almighty Allah, the Most Gracious and the Most Merciful. Certainly, it is just due to His mercy, favours and bounties that I have completed this thesis.

I was fortunate to have Dr. Hadi Susanto and Dr. Paul Matthews as my supervisors who provided me invaluable guidance throughout my PhD studies. Their knowledge and way of thinking and doing work always inspired me. I feel honoured while getting benefits from their knowledge and mathematical experience. So, I would like to offer my sincerest gratitude and thanks to both of them who have supported me throughout my PhD studies with their patience and knowledge. I am grateful for their suggestions during my studies, including their comments and corrections on the manuscripts of the thesis.

Next, I would like to express my heartiest gratitude to my father Ghulam Qadir and my mother Bushra Bibi for their moral support and encouragement during my studies. Their continuous prayers brought me to this stage. My sincere thanks go to my brothers Muhammad Imran Qadir, Rizwan Qadir, Adnan Qadir, my sisters-in-law, my nephew Hamza Imran and my nieces for their encouragement and prayers.

Special thanks goes to Dr. Muhammad Ozair Ahmad Chairman of the Department of Mathematics, University of Engineering and Technology, Lahore, who helped me a lot in getting funded every year during my stay in England.

It is a pleasure to single out Dr. Mahdhivan Syafwan, Dr. Mainul Haq and Dr. Hafiz Saeed Ahmad for their support, help and warm brotherhood. There are many other people who supported and encouraged me during my PhD studies. To list all of them is, of course, not possible here but I acknowledge all of them. Finally, I am thankful to the University of Engineering and Technology, Lahore, Pakistan for providing me financial support.

List of Abbreviations

KdV	Korteweg-de Vries (Equation)
IST	Inverse Scattering Transform
NLS	Nonlinear Schrödinger (Equation)
GL	Ginzburg-Landau (Equation)
BEC	Bose-Einstein Condensate
JILA	Joint Institute for Laboratory Astrophysics
MIT	Massachusetts Institute of Technology
GP	Gross-Pitaevskii (Equation)
BJJ	Bose-Josephson Junction
FA	Fluxon Analogues
JV	Josephson Vortices

Contents

List of Figures

CHAPTER 1

Introduction

A soliton is a self-guided non-linear wave which does not change its profile or speed during propagation. The first description of the occurrence of a soliton was made by a young Scottish engineer John Scott Russell (1808-1882) who observed a solitary wave on the Union Canal at Hermiston Edinburgh in 1834 and named it the *wave of translation* [1]. The name *soliton* was given by Norman Zabusky and Martin Kruskal while studying solitary waves in the Korteweg-de Vries (KdV) equation [2]. In general, solitary waves and solitons can be distinguished from each other through some particular interaction and collision properties. For example when two solitons collide with each other, they do not give radiation. Also, the number of solitons remains conserved [3]. This is not the case with solitary waves. However solitary waves like solitons still show particle-like properties. So in general all solitary waves are loosely called solitons.

A revolutionary development after the second world war which improved our understanding of Russell's *wave of translation* was the use of the modern digital computer. The usage of computers along with the fact that several processes in physics, engineering and biology can be illustrated by the mathematical and physical theory of the soliton gave birth to multi-disciplinary activities. Solitons are ideal for fibre optics communications networks where billions of solitons per second carry information down fibre circuits for telephone, computers and cable TV [4, 5]. The reason for this perfection is the fact that the soliton does not spread or dissociate during propagation. The Nobel Prize in chemistry 2000 was awarded to A.J. Heeger, A.G. MacDiarmid and H. Shirakawa for the discovery and development of electrically conductive polymer, which is closely related to solitons due to the solitonic charge carriers in conducting polymers. The importance of solitons is evident from the fact that they appear as the solution of a large set of non-linear partial differential equations [4].

Solitons have been the object of intensive theoretical and experimental studies dur-

ing the last fifty years. They have been recognized in optics, condensed matter, plasmas and fluids [6]. However the research on solitons in the field of nonlinear optics remained prominent in the last three decades. In nonlinear optics, the solitons are evolved due to the intensity dependency of the refractive index of a substance (the ratio between the velocity of light of a given wavelength in empty space and its velocity in the substance). When the combined effects of the intensity dependency of the refractive-index nonlinearity are balanced by the dispersion or diffraction, the pulse or beam travels without distortion. In such a case, the equation which describes the dynamics of the solitons is the celebrated nonlinear Schrödinger (NLS) equation [7]

$$i\psi_z + \frac{1}{2}\psi_{tt} \pm |\psi|^2\psi = 0, \tag{1.0.1}$$

where z represents the propagation distance along the optical waveguide or fibre, t is the time coordinate while ψ denotes the amplitude envelope of the electric field. Eq. (1.0.1) with positive sign is known as the focusing version or NLS(+) and with the negative sign it corresponds to the defocusing version or NLS(−). Several kinds of nonlinearity in various contexts which emerge from reality have been studied through the NLS equation. One of the major issues that arises in this respect is that of integrability. Most of the non-linear forms make the NLS equation non-integrable. Many studies to address this issue have been carried out globally. There was a time when inverse scattering transform (IST) [8] was the only dominant method that allowed to carry out the integration of only a few of the non-linear evolution equations. Today there are several methods available to integrate these kinds of equations. Some of these methods are sine-cosine method, tanh-coth method, Darboux transformation method, F-expansion method, Hirota bilinear method, Bäcklund transformation method, Painleve expansion method and many others.

The NLS equation arises in the description of various physical phenomena such as non-linear optics [9, 10], non-linear water waves [11–13], plasma waves [14] and Bose-Einstein condensates [15, 16]. The physics of Bose-Einstein condensates which motivated the studies presented in this thesis will be discussed further later.

The relevance of the NLS equation is not only confined to the study of solitons but it is directly connected to the famous Ginzburg-Landau (GL) equation [17]. The GL equation has been studied extensively in the context of pattern formation [18]. Although the NLS equation has many solutions, the most studied ones are bright solitons, dark solitons and plane wave solution.

Bright solitons are the fundamental envelope excitations identified by a localized intensity peak. In nonlinear optics, bright solitons are induced as trains of localized pulses due to the instability of the continuous wave solution of the focusing NLS Eq. (1.0.1).

The possibility of the propagation of bright solitons in optical fibres was predicted in [3, 19] while their propagation has been verified experimentally by Mollenauer et al. [20, 21]. The optical bright solitons can have very important applications in optical communications [22] and optical switching.

In the realm of Bose-Einstein condensate, when the interatomic interaction is attractive, a bright soliton evolves as the solution of a time-dependent nonlinear Schrödinger equation [23]. Experimentally, these solitons have been formed in the condensate of lithium [24, 25].

A dark soliton is an envelope soliton which comprises a rapid dip in the intensity with a phase jump across its intensity minimum. This localized nonlinear wave exists on top of a stable continuous wave background. Dark solitons are the prototypical nonlinear excitations of the defocusing NLS equation and as such have been studied in several branches of physics. The existence of optical dark soliton was anticipated primarily in [26] while their experimental observation was carried out later in [27, 28]. There are several papers available on theoretical and experimental studies of optical dark solitons describing their properties [29–33]. It was suggested in [32] that several kinds of optical switching devices may be based on the propagation and interaction of dark solitons.

Bose-Einstein condensate has been identified as one of the recent developments in atomic and quantum physics in the last few years. To understand the properties of this fascinating state of matter, dark solitons were one of the nonlinear states that were observed experimentally in the condensate of rubidium [34]. Dark solitons also exist in several other phenomena, such as optical fibres (from which the name *dark* was conceived) [35], thin magnetic films [36], movement of static kink in a parametrically driven shallow liquid [37, 38], standing waves in mechanical systems [39], and many more.

In addition to a single governing equation describing the physical systems, there are many problems in the fields of mathematical physics, condensed matter physics, nonlinear optics and fluid flows that lead to systems of partial differential equations which consist of two coupled NLS equations. Coupled systems of NLS equations have natural realizations in two-component Bose-Einstein condensates and in nonlinear optics. In the case of Bose-Einstein condensates, the wave functions represent the densities of the condensates while in the case of nonlinear optics, they describe the amplitudes of two propagating signals. Coupled systems are also used in the modelling of physical systems involving water wave interactions and fibre communication systems [40].

1.1 Bose-Einstein condensate (BEC) and subatomic particles

In our daily life, we deal with three states of matter which are solid, liquid and gas. A fourth high energy state of matter is plasma which appears in high energy processes such as fire, the charged air produced by lightning and the core of a star such as the sun. The existence of a fifth low energy state of matter known as Bose-Einstein condensate (BEC) was a theoretical concept before the last decade of the twentieth century but became reality in 1995 [41, 42]. In the following we will discuss the physics of BEC. To understand the concept of BEC, we begin by giving some basic information about different types of subatomic particles.

Subatomic particles can be categorized as elementary particles and composite particles. An elementary particle is one of the building blocks of the universe from which all particles are made. Such particles cannot divide into further smaller units, i.e. they do not have substructures. A quark is an example of an elementary particle which is a fundamental constituent of matter. Other examples of elementary particles are photons, bosons, fermions, etc. Composite particles are the combinations of elementary particles. Examples of composite particles are proton (which consists of two up quarks and one down quark), neutron (which have one up quark and two down quarks), meson (which is a combination of bosons), etc.

All known matter is ultimately composed of elementary particles called fermions. In particle physics, fermions are subatomic particles which obey Fermi-Dirac statistics. According to Pauli Exclusion Principle [43], two or more fermions cannot occupy the same quantum state at the same time. This means that if one fermion is in a minimum energy state, the other fermion must be in a higher energy state. Examples of fermions are the electron and positron. On the other hand, bosons are subatomic particles which obey Bose-Einstein statistics. Examples of bosons are the photon and gluon. Pauli Exclusion Principle however is not applicable for bosons. So, all bosons can occupy the same quantum state at the same time and they do not have to be distinguishable from each other. When this happens, a Bose-Einstein condensate is formed.

Particles are either so-called real particles, also known as fermions, or they are force particles also known as bosons. Quarks which are fermions are bound together by gluons which are bosons. Quarks and gluons form nucleons, and nucleons bound together by gluons form the nuclei of atoms.

The electron, which is a fermion, is bound to the nucleus by photons, which are bosons. The whole structure together forms atoms. Atoms form molecules and molecules form objects. Everything that we see, from most distant object in the sky to a tiny particle of

sand on earth are made up from a mere 3 fermions and 9 bosons. The 3 fermions are up quark, down quark and the electron. The 9 bosons are 8 gluons and the photon.

1.2 Bose-Einstein condensation

Bose-Einstein condensation is a phenomenon of a quantum-phase transition in which a finite fraction of particles of a boson gas condenses into the same quantum state when cooled below a critical transition temperature. In this state, matter ceases to behave as independent particles and degenerates into a single quantum state that can be described by a single wave function. This phenomenon was originally predicted by Bose and Einstein in 1924. The first realization of BEC in dilute gases for rubidium [41] and sodium [42] dates back to 1995, when JILA and MIT performed their milestone experiments for producing BECs. The JILA group published their results of rubidium atoms on July 14, 1995. Few months after that, the MIT group reported condensation of sodium atoms on November 24, 1995. Since then, the research in this field has been an active and growing part both theoretically as well as experimentally and has had impressive impact in many branches of physics such as atomic physics, nuclear physics, optical physics, etc. Currently, there are more than one hundred and fifty experimental BEC groups around the world.

The world's first BEC [41], reported by Eric Cornell, Carl Wieman and their collaborators was formed inside a carrot-sized glass cell, and made visible by a video camera. The result was a BEC of about 2000 rubidium atoms and its life was 15 to 20 seconds. Shortly after this, W. Ketterle also achieved a BEC in the laboratory with sodium vapours at MIT. E.A. Cornell, W. Ketterle and C.E. Wieman were awarded the Nobel Prize in Physics 2001 for this achievement.

Very active research has been carried out into the systems that are closer to the Bose-Einstein's condensation theory since 1970. Many groups started searching globally for BECs with a combination of laser and magnetic cooling apparatus. Latest powerful methods developed in the last quarter of the 20th century for cooling alkali metal atoms by using lasers were used for the first realization of BECs. All experiments with gaseous condensates start with the laser cooling except atomic hydrogen. The technique of laser cooling [44] was developed by Cohen-Tannoudji, S. Chu and W.D. Philipps for which they were awarded the Nobel Prize in Physics 1997.

Today, scientists can produce condensates with much larger number of atoms that can survive for several minutes. BEC has been found experimentally in many atomic species such as atomic hydrogen, metastable helium, lithium, sodium, potassium, ru-

bidium, caesium, ytterbium and Li_2 molecules [45].

1.3 Phases of matter

The phases of matter are distinguishable in several ways. On the most elementary level, gases have no definite shape and volume. Liquids have definite volume but no definite shape while solids have fixed volume and definite shape. Gases have weak intermolecular forces than their corresponding liquids, which in turn have weak intermolecular forces than solids. Solids have the lowest energy levels whereas liquids and gases have increasingly higher energy levels. Plasma which is an ionized state of matter is very energetic and emits energy in the form of photons and heat and hence can be put at the top end of this scale.

BECs are less energetic than solids. They are more coherent than solids as their confinement occur on the atomic level rather than molecular level. The systems of BECs provide exclusive opportunities for investigating quantum phenomena on the macroscopic scale. They differ from ordinary gases, liquids and solids in several ways [46]. For example, the density of particles at the centre of the atomic cloud of BEC is typically $10^{13} - 10^{15}\text{cm}^{-3}$. On the contrary, the density of particles in air at room temperature and pressure is about 10^{19}cm^{-3}. In liquids and solids, the atomic density is of order 10^{22}cm^{-3} whereas the density of nucleons in atomic nuclei is approximately 10^{38}cm^{-3}. For the observation of quantum phenomena in such low-density systems, the temperature should be of order 10^{-5}k or less. This is in contrast with the temperature at which quantum effects occur in solids and liquids. The temperature required for observing quantum phenomena in liquid helium is of order 1k.

1.4 Formation of BEC by Laser cooling technique

In this technique the atoms of the gas at room temperature are first slowed down and captured in a trap created by laser light. This cools the atoms to approximately 10^{-7} of a degree above absolute zero but still it is very far away from the temperature required to produce BECs and needs to reduce the temperature further. To do this, D. Kleppner developed a technique for hydrogen called evaporative cooling. In evaporative cooling, once the atoms of the gas are trapped, the lasers are switched off and the atoms are held in place by the magnetic field. The atoms are further cooled in the magnetic trap by selecting the hottest atoms and ejecting them out of the trap. Now the next task is to trap a sufficient high density of atoms at temperatures that are cold enough

to produce a BEC. It is important to mention that under these conditions, the equilibrium configuration of the system would be the solid phase. So, to observe BEC, the system has to be maintained in a metastable gas phase for a sufficiently long time. One tries to keep the collision rate constant at the centre of the trap during the evaporation process. The final step of the process is the visualization of the atomic cloud, which is usually performed by illuminating the remaining atomic cloud with a flash of resonant light, and imaging the shadow of the atomic cloud onto a CCD camera which gives the spatial distribution of the atoms. Alternatively, if one releases the atoms from the trap and waits before transmitting the flash, one obtains the velocity distribution. However both methods are inherently destructive because in the former case absorbed photons heat the atoms whereas atoms are released from the trap in the latter case. So, to avoid this, the non-destructive formal imaging, relying on dispersion rather than absorption, was designed after the first BEC was reported [45].

1.5 Characteristics and future applications of BECs

Most of the research on BECs deals with knowing about the world in general rather than its implementation on a particular technology. However, BECs have bizarre properties with several potential applications in future technologies. A most intriguing application is in etching or lithography. When BECs are designed into a beam, they are like a laser in their coherence, called atom laser. A conventional laser light releases a beam of coherent photons which are all in phase and can be focused to a very small bright spot. Similarly, an atom laser induces a coherent beam of atoms which can be focused at high intensity. The massive particles of atom laser are more energetic than the massless photons of laser light even at low kinetic energy state. So, an atom laser has higher energy than a light laser. Atom lasers could produce precisely trimmed objects down to a very small scale possibly a nano scale. Potential applications include enhanced techniques to make electronic chips.

One of the possible applications of BECs is in precision measurement. Some of the most sensitive detectors ever made come from atom interferometry using the wavelike characteristics of atoms. The interferometers based on atom lasers could provide new methods of making measurements accurately.

BECs are related to two remarkably low temperature phenomena, i.e. superfluidity and superconductivity. Due to their property of superfluidity, BECs flow without any internal resistance. Even the best lubricants available have some frictional losses due to interaction of molecules with each other, but since BECs are effectively superatoms,

they do not have energy losses. The amazing property of superfluidity can help in preventing the loss of electric power during transmission.

Another promising property of BECs is that they can slow down light. In 1998, Lene Hau of Harvard university with her colleagues showed [47] that speed of light travelling (with speed $3 \times 10^8 m/s$) through BEC reduces to mere $17 m/s$. Any other substance so far has been unable to slow down the light to that speed. Later, Hau and others have completely stopped and stored a light pulse within a BEC [48]. These achievements can possibly be used for novel types of light based telecommunications and optical data storage. There is also a good deal of interest in looking for ways to use BECs system for quantum information processing to build a quantum computer.

The connection of BEC with matter is analogous to the connection of laser with light. Lasers were invented in 1960, but their technological applications were started after approximately twenty years of their invention and now they are everywhere. BECs hold a promise of many inquisitive future developments and a challenging research is still on the way.

1.6 The external potential

The external potential denoted by V is used to trap and manipulate the atoms of the BEC. In the earlier experiments of BECs, the condensates were trapped using magnetic fields [49] which are typically harmonic and can be approximated with the quadratic form

$$V = \frac{1}{2} m(\Omega_x^2 x^2 + \Omega_y^2 y^2 + \Omega_z^2 z^2), \tag{1.6.1}$$

where m is the mass of the condensate and Ω_x, Ω_y, Ω_z are the trap frequencies along the coordinate axis respectively. These frequencies in general are different from each other. The shape of the condensate can be controlled by using suitable values of these confining frequencies. The symmetry of the problem is determined by the shape of the trap. If $\Omega_x = \Omega_y = \Omega \approx \Omega_z$, the trap is isotropic (i.e. same in all directions) and the BEC is almost spherical. When the confinement is tight in two directions and relatively weak in the third direction i.e. $\Omega_x = \Omega_y = \Omega > \Omega_z$, this leads to the cigar-shaped condensate while the case $\Omega_z > \Omega = \Omega_x = \Omega_y$ gives rise to disk-shaped condensates. The strongly anisotropic cases with $\Omega_z \ll \Omega$ and $\Omega_z \gg \Omega$ are of special interest because they are related to effectively quasi-one-dimensional and quasi-two-dimensional BECs respectively. Such lower dimensional BECs have been studied theoretically in [50–52] and experimentally in [53–55].

The use of magnetic field in certain cases enforces limitations on the study of BEC as

it may cause heating and trap loss. Also, when different hyperfine states (i.e. states of the electron clouds in the atoms) are trapped simultaneously, the trap loss can increase significantly which restricts the study of BECs condensates [56]. Moreover, the spin flips in the atoms lead to untrapped states. To overcome these limitations, the atoms of BECs were confined using optical dipole traps. These optical traps are based on the optical dipole force which confines atoms in all hyperfine states [56, 57]. The shape of these traps is highly flexible and controllable. An important example of these traps is the periodic optical traps known as optical lattices. An optical lattice is made by the interference of counter-propagating laser beams which produces a periodic potential. A typical form of optical lattices in one dimension is

$$V(x) = v_0 \cos^2\left(\frac{2\pi}{\lambda_x}x\right). \tag{1.6.2}$$

Similarly, in two dimensions, an egg-carton potential

$$V(x) = v_0\left[\cos^2\left(\frac{2\pi}{\lambda_x}x\right) + \cos^2\left(\frac{2\pi}{\lambda_y}y\right)\right], \tag{1.6.3}$$

is related to disc-shaped condensate. Here v_0 is the height of the lattice and λ_x, λ_y are the wave lengths of the laser beams in the two dimensions.

The combination of a harmonic and a periodic optical potential gives rise to a double-well potential [58]. Several traps with different other combinations have been formed and applied experimentally [59, 60]. Trapping of atoms on microchips called atom chips [61, 62] is also possible. The diversity of shapes and types of external potentials opens up new possibilities of many fascinating applications.

CHAPTER 2

Mathematical Background

In the previous chapter we provided the basic information about solitons and the physics of BECs along with their potential applications. In this chapter we will use a variational approach to derive the Gross-Pitaevskii equation that describes the dynamics of BECs. We will present the ground state properties of BECs. The basic nonlinear solutions such as bright and dark solitons that exist in one dimensional Gross-Pitavskii equation will be considered and their stability analysis will be presented.

2.1 The variational approximations

One of the most commonly used mathematical techniques in the study of BECs and nonlinear optics is the variational approximation. This technique has been employed to approximate solutions in various cases, particularly in the cases where solutions do not exist in an analytical form. This method reduces a system having infinitely many degrees of freedom to a finite-dimensional one. The objective of this method is to reduce a system with complex dynamics characterized by partial differential equations to a relatively simple system of a few ordinary differential equations. It is a semi-analytic method which is well known and has long been used to approximate solutions of nonlinear evolution equations. It is called semi-analytic because in practice this method involves equations which may be too complicated to solve analytically and hence need some numerical techniques for their solutions.

The method of the variational approximation can be systematically described in the following steps [63]:

1. Find the Lagrangian or the Hamiltonian of the governing equations.

2. Select a suitable and mathematically tractable trial function (ansatz) that contains

a finite number of parameters called variational parameters. Typically, these parameters are the amplitude, width, phase, etc. of the wavefunction. These parameters are allowed to be functions of spatial and temporal variables.

3. Substitute the chosen ansatz into the Lagrangian and find the resulting sums (for discrete systems) or integrations (for continuous systems).

4. Derive the Euler-Lagrange equations which lead to ordinary differential equations for the variational parameters. These equations can be solved either analytically or numerically to understand the dynamics of the system. It is important to mention that there is no direct formal relationship between the governing equations and the system of Euler Lagrange equations [64].

There are several factors involved for the successful implementation of the variational method. Mainly, this method depends on the ansatz representing the shape of the wavefunction but the ansatz should be such that the resulting sums or integration can be expressed in a closed form. Moreover, the number of variational parameters representing the nature of the system also affects the accuracy of the method. A more accurate approximation can be achieved at the cost of introducing more parameters in the ansatz. However, the complexity of the calculations, of course, increases by adding more parameters.

The applicability of a particular variational ansatz can be tested by comparison of the results with direct numerical simulations of the given evolution equations. The comparison of the direct numerical simulation is really essential for the study of the stability of the solution because this method sometimes shows a false instability of the solution which is actually stable [64]. However, for the validity of the results, it is sufficient to do the comparison at a few distinct values of the variational parameters. The approximations are considered to be reliable in wide parametric domains if at several benchmark points they are sufficiently close to the results obtained through numerical simulations.

In the following, we employ the variational approach to derive the famous Gross-Pitaevskii equation that describes the dynamics of BECs.

2.2 The Gross-Pitaevskii equation

We discuss a simple approach to describe a pure BEC taking into account the atom-atom interactions in a mean-field approach (i.e. considering a many-body problem as an effective one-body problem). Although the nature of the gases is very dilute in a

real condensate, atom-atom interactions cannot be neglected. In fact, the BEC in the harmonic trap significantly increases the effects of the atom-atom interaction.

Let us consider a system of N number of spinless bosons described by spatial coordinates $\mathbf{r}_n$. The starting point is the N-body Hamiltonian

$$\mathbf{H} = \sum_{n=1}^{N} \left(\frac{\mathbf{p}_n^2}{2m} + V(\mathbf{r}_n) \right) + \frac{1}{2} \sum_{n=1}^{N} \sum_{i \neq n}^{N} W(\mathbf{r}_n - \mathbf{r}_i). \tag{2.2.1}$$

The first term herein represents the kinetic energy in which $\mathbf{p}$ is the momentum, V corresponds to the external trapping potential and W is the two-body interaction potential. We use the Hartree approximation for seeking the ground state of the many-body system. The physical idea of this approximation is that each boson feels the same mean-field potential due to all the other bosons and the many-body wave function can be approximated as a product of identical single-boson wave functions. For the N-body system, we take the ansatz

$$u_N(\mathbf{r}_1, \mathbf{r}_2, ..., \mathbf{r}_N, t) = \phi(\mathbf{r}_1, t)\phi(\mathbf{r}_2, t)...\phi(\mathbf{r}_N, t), \tag{2.2.2}$$

where ϕ denotes the wave function of the single-particle normalized to unity, that is to be determined. This approximation assumes that all atoms occupy the same macroscopic state which is correct only for simple BECs. A more rigorous approach with a time-dependent macroscopic number of particles in the condensate has been considered in [65]. Much more complicated cases, with more than one state with a macroscopic number of particles, called fragmented BECs, are also possible.

The collisional properties of particles in a dilute ultracold gas at low energies are described by the s-wave scattering length and expressed in terms of one parameter − the scattering length denoted by a [66]. The value of atomic scattering length can be either positive or negative depending on the BEC species. The positive and negative values correspond to repulsive and attractive interactions respectively between the atoms of BEC. For example, the BEC formed by atomic vapors of sodium is repulsive and for lithium is attractive. Once the atomic scattering length has been calculated or determined experimentally, one can use the fact that the two potentials having the same scattering length exhibit the same properties in a system of dilute cold gas. Hence, the interatomic interaction potential can replaced by an effective delta-function interaction potential, i.e. $W(\mathbf{r}_j - \mathbf{r}_i) = g\delta(\mathbf{r}_j - \mathbf{r}_i)$, where $g = 4\pi\hbar^2 a/m$, in which a represents the scattering length and m is the mass of the particle.

Since $\mathbf{p}_n = -i\hbar\nabla_n$, the Hamiltonian for N interacting particles in the presence of trapping potential V can be written as

$$\mathbf{H} = \sum_{n=1}^{N} \left(\frac{-\hbar^2}{2m} \nabla_n^2 + V(\mathbf{r}_n) \right) + \frac{g}{2} \sum_{n=1}^{N} \sum_{i \neq n}^{N} \delta(\mathbf{r}_n - \mathbf{r}_i), \tag{2.2.3}$$

where ∇_n is the gradient relative to $\mathbf{r}_n$. The total Lagrangian associated with the Hamiltonian can then be written as

$$\mathbf{L} = \int_{-\infty}^{\infty} \prod_{k=1}^{N} d\mathbf{r}_k \left[\frac{i\hbar}{2}(u_N^* \frac{\partial u_N}{\partial t} - u_N \frac{\partial u_N^*}{\partial t}) - \sum_{n=1}^{N} \left(\frac{\hbar^2}{2m} |\nabla_n u_N|^2 + V(\mathbf{r}_n)|u_N|^2 + \frac{g}{2} \sum_{i \neq n}^{N} \delta(\mathbf{r}_n - \mathbf{r}_i)|u_N|^2 \right) \right], \quad (2.2.4)$$

where the asterisk denotes the complex conjugation. Substituting the Hartree ansatz (2.2.2) in the above expression of Lagrangian, we obtain several terms. Using the notation $\phi(\mathbf{r}_n, t) = \phi_n$, the first term is

$$\begin{aligned} \int_{-\infty}^{\infty} \prod_{k=1}^{N} d\mathbf{r}_k \frac{i\hbar}{2} u_N^* \frac{\partial u_N}{\partial t} &= \frac{i\hbar}{2} \int_{-\infty}^{\infty} \prod_{k=1}^{N} d\mathbf{r}_k \left(\prod_{i=1}^{N} \phi_i^* \right) \left(\sum_{l=1}^{N} \frac{\partial \phi_l}{\partial t} \prod_{k \neq l}^{N} \phi_k \right) \\ &= \frac{i\hbar}{2} \sum_{l=1}^{N} \left(\int_{-\infty}^{\infty} d\mathbf{r}_l \phi_l^* \frac{\partial \phi_l}{\partial t} \right) \left[\prod_{k \neq l}^{N} \int_{-\infty}^{\infty} d\mathbf{r}_k \phi_k^* \phi_k \right] \\ &= \frac{i\hbar}{2} N \int_{-\infty}^{\infty} d\mathbf{r} \phi^*(\mathbf{r}, t) \frac{\partial \phi(\mathbf{r}, t)}{\partial t}. \end{aligned} \quad (2.2.5)$$

Here, the expression within square brackets above is equal to unity since ϕ has been normalized.

The second term is the complex conjugate of the first term. i.e.

$$\int_{-\infty}^{\infty} \prod_{k=1}^{N} d\mathbf{r}_k \frac{i\hbar}{2} u_N \frac{\partial u_N^*}{\partial t} = \frac{i\hbar}{2} N \int_{-\infty}^{\infty} d\mathbf{r} \phi(\mathbf{r}, t) \frac{\partial \phi^*(\mathbf{r}, t)}{\partial t}. \quad (2.2.6)$$

The third term is

$$\begin{aligned} \frac{\hbar^2}{2m} \int_{-\infty}^{\infty} \prod_{k=1}^{N} d\mathbf{r}_k \sum_{n=1}^{N} |\nabla_n u_N|^2 &= \frac{\hbar^2}{2m} \sum_{n=1}^{N} \left(\int_{-\infty}^{\infty} d\mathbf{r}_n |\nabla_n \phi(\mathbf{r}_i, t)|^2 \right) \left(\prod_{k \neq n}^{N} \int_{-\infty}^{\infty} d\mathbf{r}_k \phi_k^* \phi_k \right) \\ &= \frac{\hbar^2}{2m} N \int_{-\infty}^{\infty} d\mathbf{r} |\nabla \phi(\mathbf{r}, t)|^2. \end{aligned} \quad (2.2.7)$$

The fourth term leads to

$$\int_{-\infty}^{\infty} \prod_{k=1}^{N} d\mathbf{r}_k \sum_{n=1}^{N} V(\mathbf{r}_n)|u_N|^2 = N \int_{-\infty}^{\infty} d\mathbf{r} V(\mathbf{r})|\phi(\mathbf{r}, t)|^2. \quad (2.2.8)$$

Finally, the interaction term is

$$\int_{-\infty}^{\infty} \prod_{k=1}^{N} d\mathbf{r}_k \sum_{n=1}^{N} \sum_{i \neq n}^{N} \delta(\mathbf{r}_n - \mathbf{r}_i)|u_N|^2 = N(N-1) \int_{-\infty}^{\infty} d\mathbf{r} |\phi(\mathbf{r}, t)|^4. \quad (2.2.9)$$

Substituting all these values in Eq. (2.2.4), we obtain

$$\mathbf{L} = N\int_{-\infty}^{\infty} d\mathbf{r}\left[\frac{i\hbar}{2}(\phi^*\frac{\partial\phi}{\partial t} - \phi\frac{\partial\phi^*}{\partial t}) - \frac{\hbar^2}{2m}|\nabla\phi|^2 - V(\mathbf{r})|\phi(\mathbf{r},t)|^2 - \frac{g}{2}(N-1)|\phi(\mathbf{r},t)|^4\right]. \tag{2.2.10}$$

The stationarity condition with respect to ϕ^* is

$$\frac{\delta\mathbf{L}}{\delta\phi^*} = 0, \tag{2.2.11}$$

i.e.

$$N\left[i\hbar\frac{\partial\phi}{\partial t} + \frac{\hbar^2}{2m}\nabla^2\phi(\mathbf{r},t) - V(\mathbf{r})\phi(\mathbf{r},t) - g(N-1)|\phi(\mathbf{r},t)|^2\phi(\mathbf{r},t)\right] = 0. \tag{2.2.12}$$

Hence, we obtain

$$i\hbar\frac{\partial\phi(\mathbf{r},t)}{\partial t} = \left[-\frac{\hbar^2}{2m}\nabla^2 + V(\mathbf{r}) + g(N-1)|\phi(\mathbf{r},t)|^2\right]\phi(\mathbf{r},t). \tag{2.2.13}$$

The factor $(N-1)$ in the last term on the right hand side ensures that the interaction term will vanish when $N = 1$. Nonetheless, in actual BECs the number of atom N is at least 10^5. So we can replace the factor $(N-1)$ by N. The equation describing the dynamics evolution of the BECs can then be written as

$$i\hbar\frac{\partial\phi(\mathbf{r},t)}{\partial t} = \left[-\frac{\hbar^2}{2m}\nabla^2 + V(\mathbf{r}) + gN|\phi(\mathbf{r},t)|^2\right]\phi(\mathbf{r},t). \tag{2.2.14}$$

We use scaling $\psi(\mathbf{r},t) = \sqrt{N}\phi(\mathbf{r},t)$ to write the equation in its conventional form which is

$$i\hbar\frac{\partial\psi(\mathbf{r},t)}{\partial t} = \left[-\frac{\hbar^2}{2m}\nabla^2 + V(\mathbf{r}) + g|\psi(\mathbf{r},t)|^2\right]\psi(\mathbf{r},t). \tag{2.2.15}$$

This nonlinear equation was derived by Gross and Pitaevskii independently in 1961. The Eq. (2.2.15) is called the time-dependent Gross-Pitaevskii (GP) equation also known as the time-dependent nonlinear Schrödinger equation and is used to describe the ground state as well as the excitations of the BEC. The predictions that arise from this equation are in excellent agreement with experiments dealing with a quasi-pure condensate. The complex function $\psi(r,t)$ in GP Eq. (2.2.15) is generally called the macroscopic wave function that characterizes the static and dynamic behavior of the condensate. This function can be expressed in terms of density $\rho(r,t) = |\psi(r,t)|^2$ and phase $\theta(r,t)$ of the condensate as $\psi(r,t) = \sqrt{\rho}e^{i\theta t}$. The GP model owns two integrals of motion which represent respectively the total number of atoms N and the energy of the system E and are given as

$$N = \int_{-\infty}^{\infty}|\psi(r,t)|^2 dr, \tag{2.2.16}$$

$$E = \int_{-\infty}^{\infty} \left[\frac{\hbar^2}{2m} |\nabla \psi|^2 + V|\psi|^2 + \frac{1}{2} g|\psi|^4 \right] dr, \tag{2.2.17}$$

where the first term represents the kinetic energy while the second and third terms correspond to the potential energy and the interaction potential, respectively.

2.3 Ground state and Thomas-Fermi approximation

The ground state of Eq. (2.2.15) can be easily obtained by expressing the condensate wave function $\psi(r,t) = \psi_0(r)e^{-i\rho_0 t/\hbar}$, where ψ_0 is a function normalized to the number of atoms $N = \int |\psi_0|^2 dr$ and $\rho_0 = \frac{\partial E}{\partial N}$ is the chemical potential. Substitution of the above expression into Eq. (2.2.15) gives the following time-independent form

$$\left[-\frac{\hbar^2}{2m}\nabla^2 + V(r) + g|\psi_0(r)|^2 - \rho_0 \right] \psi_0(r) = 0. \tag{2.3.1}$$

When there is no interaction between the atoms of the condensates, i.e. $g = 0$, the above equation reduces to the usual Schrödinger equation with the potential V. The ground state (or the minimum energy state) in the presence of a harmonic trap can be obtained by assuming that all bosons are in the lowest single body state. In this state, the ground state solution ψ_0 is the Gaussian function and is given as

$$\psi_0 = \sqrt{N} \left(\frac{m\Omega_{gm}}{\pi\hbar} \right)^{3/4} \exp\left[\frac{-m}{2\hbar} (\Omega_x x^2 + \Omega_y y^2 + \Omega_z z^2) \right], \tag{2.3.2}$$

where Ω_{gm} is the geometric mean of the confining frequencies, i.e. $\Omega_{gm} = (\Omega_x \Omega_y \Omega_z)^{1/3}$.

For the attractive interatomic interaction, i.e. $g < 0$, the density of the atoms at the centre of the trap increases while the kinetic energy tends to stabilize this increase. Nevertheless, if the number of atoms N goes beyond a critical number N_{cr}, i.e. $N > N_{cr}$, the central density and hence the rate of collisions grows to some such extent that the kinetic energy could not balance this increase. Due to these strong collisions, atoms are ejected out from the condensate in an energetic explosion resulting in the collapse of the system. Experimental observations of collapse in the cases of attractive lithium and rubidium were carried out in [67] and [68], respectively.

When the interaction between the atoms of the condensate is repulsive, i.e. $g > 0$, and the number of atoms is reasonably large satisfying the condition $Na/a_{ho} \gg 1$, where $a_{ho} = \sqrt{\frac{\hbar}{m\Omega_{gm}}}$, the atoms are pushed towards the boundaries of the condensate. Consequently, the density at the centre tends to become flat with slow spatial variation and the radius of condensate increases and is shown is Fig. 2.1 which has been taken from [69]. Then the kinetic energy becomes very small as compared with the interaction and

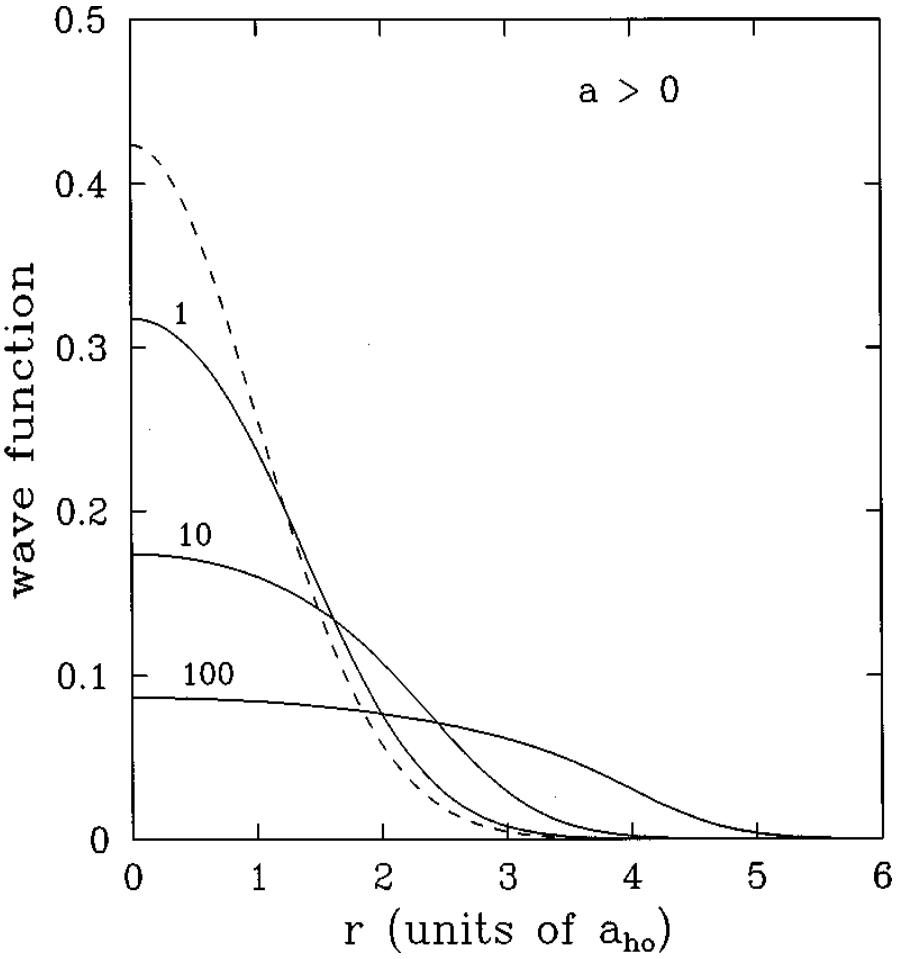

Figure 2.1: Numerically obtained solutions (solid) of the stationary GP Eq. (2.3.1) in a spherical trap with repulsive interatomic interaction corresponding to $\frac{Na}{a_{ho}} = 1, 10, 100$. The dashed curve represents the prediction for the ideal gas. Figure has taken from [69].

potential energies and is significant only near the boundaries. If we neglect completely the kinetic energy term in Eq. (2.3.1), the expression for the ground state density profile of the system is

$$\rho(r) = |\psi_0(r)|^2 = \frac{\rho_0 - V(r)}{g}, \tag{2.3.3}$$

in the region where $\rho_0 > V(r)$ and $\rho = 0$ otherwise. This is known as the Thomas-Fermi approximation [69] and is shown in Fig. 2.2.

2.4 Dimensionality reduction in GP models

The three dimensional GP Eq. (2.2.15) can be reduced to an effectively one dimensional equation [70] by assuming the transverse confinement of the condensate tight enough,

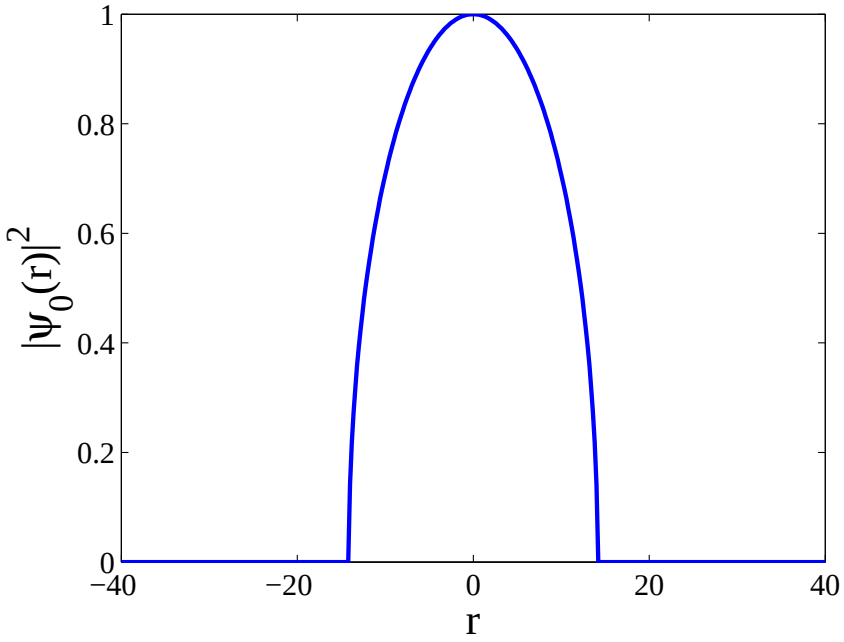

Figure 2.2: The plot of the Thomas-Fermi approximation (2.3.3) with the harmonic potential $V = \frac{1}{2}\Omega^2 x^2$. Here, $\Omega = 0.1$, $\rho_0 = 1$ and $g = 1$.

i.e. $\Omega_y = \Omega_z = \Omega \gg \Omega_x$, to give a cigar shaped BEC. In such a case, we assume that it is possible to factorize the solution ψ into longitudinal (along the x-axis) and transverse (on the (y,z) plane) components, i.e.

$$\psi(x,y,z,t) = \Psi(x,t)\Theta(y,z,t), \tag{2.4.1}$$

where $\Theta(y,z,t)$ is further decomposed as $\Theta(y,z,t) = \Phi(y,z)e^{-i\rho_0 t}$ with ρ_0 representing the chemical potential. The transverse wave function $\Phi(y,z)$ is chosen such that it should satisfy the equation

$$\frac{\hbar^2}{2m}\left[\left(\frac{\partial^2}{\partial y^2}+\frac{\partial^2}{\partial z^2}\right)-\frac{1}{2}m\Omega^2(y^2+z^2)+\hbar\rho_0\right]\Phi(y,z)=0. \tag{2.4.2}$$

Substituting (2.4.1) into (2.2.15), we obtain

$$\begin{aligned} i\hbar\frac{\partial}{\partial t}[\Psi\Phi e^{-i\rho_0 t}] &= \left[\frac{-\hbar^2}{2m}\left(\frac{\partial^2}{\partial x^2}+\frac{\partial^2}{\partial y^2}+\frac{\partial^2}{\partial z^2}\right)\right. \\ &+ \left.\frac{1}{2}m(\Omega_x^2x^2+\Omega^2y^2+\Omega^2z^2)+g|\Psi|^2|\Phi|^2\right]\Psi\Phi e^{-i\rho_0 t}. \\ i\hbar\Phi e^{-i\rho_0 t}\left[\frac{\partial\Psi}{\partial t}-i\rho_0\Psi\right] &= \left[\frac{-\hbar^2}{2m}\frac{\partial^2\Psi}{\partial x^2}+\frac{1}{2}m\Omega_x^2x^2\Psi+g|\Psi|^2|\Psi|^2|\Phi|^2\right]\Phi e^{-i\rho_0 t} \\ &+ \left[\frac{-\hbar^2}{2m}\left(\frac{\partial^2}{\partial y^2}+\frac{\partial^2}{\partial z^2}\right)\Phi+\frac{1}{2}m\Omega^2(y^2+z^2)\Phi\right]\Psi e^{-i\rho_0 t}. \end{aligned}$$

Cancelation of $e^{-i\rho_0 t}$ on both sides and rearranging the terms gives

$$\left[\frac{\hbar^2}{2m}\left(\frac{\partial^2}{\partial y^2}+\frac{\partial^2}{\partial z^2}\right)-\frac{1}{2}m\Omega^2(y^2+z^2)+\hbar\rho_0\right]\Phi\Psi+i\hbar\Phi\frac{\partial\Psi}{\partial t}=\left[\frac{-\hbar^2}{2m}\frac{\partial^2\Psi}{\partial x^2}+\frac{1}{2}m\Omega_x^2x^2\Psi+g|\Psi|^2\Psi|\Phi|^2\right]\Phi.$$

Using (2.4.2), the first term on the left hand side vanishes and we obtain

$$i\hbar\Phi\frac{\partial\Psi}{\partial t}=\left[\frac{-\hbar^2}{2m}\frac{\partial^2\Psi}{\partial x^2}+\frac{1}{2}m\Omega_x^2x^2\Psi+g|\Psi|^2\Psi|\Phi|^2\right]\Phi.$$

Multiplying both sides by Φ^* and taking the double integral with respect to y and z from $-\infty$ to ∞ by letting $\int_{-\infty}^{\infty}\int_{-\infty}^{\infty}|\Phi(y,z)|^2dydz=C_1$ and $\int_{-\infty}^{\infty}\int_{-\infty}^{\infty}|\Phi(y,z)|^4dydz=C_2$, we get

$$i\hbar C_1\frac{\partial\Psi}{\partial t}=\frac{-\hbar^2}{2m}C_1\frac{\partial^2\Psi}{\partial x^2}+\frac{1}{2}C_1m\Omega_x^2x^2\Psi+gC_2|\Psi|^2\Psi.$$

Finally, dividing throughout by C_1 and setting $\frac{gC_2}{C_1}=g_1$ yields

$$i\hbar\frac{\partial}{\partial t}\Psi(x,t)=\frac{-\hbar^2}{2m}\frac{\partial^2}{\partial x^2}\Psi(x,t)+V(x)\Psi(x,t)+g_1|\Psi(x,t)|^2\Psi(x,t),\tag{2.4.3}$$

with $V(x)=\frac{1}{2}m\Omega_x^2x^2$. Similarly, one can reduce (2.2.15) into a two dimensional GP equation by assuming that the condensate is disc shaped. In that case, Eq. (2.2.15) takes the following form

$$i\hbar\frac{\partial}{\partial t}\Psi(x,y,t)=\frac{-\hbar^2}{2m}\left(\frac{\partial^2}{\partial x^2}+\frac{\partial^2}{\partial y^2}\right)\Psi(x,y,t)+V(x,y)\Psi(x,y,t)+g_2|\Psi(x,y,t)|^2\Psi(x,y,t),\tag{2.4.4}$$

where $V(x,y)=\frac{1}{2}m\Omega^2(x^2+y^2)$.

2.5 Dimensionless form of GP equation

One can reduce Eq. (2.4.3) to dimensionless form. To do so, we substitute $\Psi=\alpha u$, $t=\beta\tilde{t}$, $x=\gamma\tilde{x}$, where α, β and γ are real constants, in Eq. (2.4.3) to obtain

$$i\frac{\hbar\alpha}{\beta}u_{\tilde{t}}=-\frac{\hbar^2\alpha}{2m\gamma^2}u_{\tilde{x}\tilde{x}}+\frac{1}{2}\alpha\gamma^2\Omega^2\tilde{x}^2u+g_1\alpha^3|u|^2u.$$

Multiplying throughout by $\beta/\hbar\alpha$, we obtain

$$iu_{\tilde{t}}=-\frac{\hbar\beta}{2m\gamma^2}u_{\tilde{x}\tilde{x}}+\frac{\beta\gamma^2\Omega^2}{2\hbar}\tilde{x}^2u+\frac{g_1\alpha^2\beta}{\hbar}|u|^2u.$$

When $g_1>0$, say $g_1=\tilde{g}$, we set

$$\frac{\hbar\beta}{m\gamma^2}=1,\qquad\frac{\beta\gamma^2}{\hbar}=1,\qquad\frac{\tilde{g}\alpha^2\beta}{\hbar}=1.$$

These equations yield

$$\beta = m^{1/2}, \qquad \gamma = \hbar^{1/2} m^{-1/4}, \qquad \alpha = \tilde{g}^{-1/2} \hbar^{1/2} m^{-1/4}.$$

For $g_1 < 0$, say $g_1 = -\tilde{g}$, we use the same settings as above. Finally, we omit tilde to obtain the following dimensionless form of the one-dimensional GP equation

$$iu_t = -\frac{1}{2} u_{xx} + Vu \pm |u|^2 u, \tag{2.5.1}$$

where subscripts denote the partial derivatives.

When the condensate is homogeneous, i.e. $V = 0$, Eq. (2.5.1) reduces to

$$iu_t = -\frac{1}{2} u_{xx} \pm |u|^2 u, \tag{2.5.2}$$

The homogeneous Eq. (2.5.2) is completely integrable [3, 71] and has an infinite number of integrals of motion. The most fundamental ones which have clear meanings are the number of particles N, the momentum P and the energy E, which are respectively given as

$$N = \int_{-\infty}^{\infty} |u|^2 dx, \tag{2.5.3}$$

$$P = \frac{i}{2} \int_{-\infty}^{\infty} (u u_x^* - u^* u_x) dx, \tag{2.5.4}$$

$$E = \frac{1}{2} \int_{-\infty}^{\infty} (|u_x|^2 + |u|^4) dx. \tag{2.5.5}$$

These quantities remain conserved as the systems described by Eq. (2.5.2) are conservative.

2.6 Solutions of one-dimensional GP equations and their stability

The homogeneous one-dimensional GP Eq. (2.5.2) possess an infinite number of solutions. The well-known solutions are the plane-wave solution, the dark solitons and the bright solitons. In the following, we will present the basic information and the stability analysis of these solutions.

2.6.1 The plane-wave solution

The simplest nontrivial solution of Eq. (2.5.2) is the plane-wave solution given by

$$u(x,t) = \sqrt{\rho_0} \exp[i(\kappa x - \omega t)], \tag{2.6.1}$$

where κ, ω and ρ_0, represent respectively the wave number, frequency and square of the amplitude of the plane-wave. A relationship between the wave number and frequency can be obtained by introducing this solution into Eq. (2.5.2), which yields

$$\omega = \frac{1}{2}\kappa^2 \pm \rho_0. \tag{2.6.2}$$

The above expression describing the plane-wave solution is known as the dispersion relation. Differentiating Eq. (2.6.2) partially with respect to κ gives the group velocity v of the plane wave solution, i.e. $v = \frac{\partial \omega}{\partial \kappa} = \kappa$. Since $|u|^2$ represents the density, when the density is small, the plane-wave solution satisfies the linear GP equation $iu_t + \frac{1}{2}u_{xx} = 0$, with the dispersion relation $\omega = \frac{1}{2}\kappa^2$. If the system is confined to a length L, the integrals of motion for the plane-wave solution have the following values,

$$N = \rho_0 L, \qquad P = \kappa\rho_0 L = \kappa N, \qquad E = \frac{1}{2}[\rho_0 L(\kappa^2 + \rho_0)] = \frac{1}{2}\left[\frac{P^2}{N} + \frac{N^2}{L}\right]. \tag{2.6.3}$$

These equations show that the plane-wave solution behaves as a classical particle with the effective mass M_{pws}, momentum P_{pws} and energy E_{pws} given by

$$M_{pws} = \rho_0 L, \qquad P_{pws} = M_{pws} v, \qquad E_{pws} = \frac{1}{2}M_{pws}v^2 + \frac{M_{pws}^2}{2L}.$$

One can differentiate energy E_{pws} and momentum P_{pws} partially with respect to velocity $v = \kappa$ to obtain a standard equation of classical mechanics

$$\frac{\partial E_{pws}}{\partial P_{pws}} = v,$$

which justifies the particle-like nature of the plane-wave solution.

Let us now discuss the stability of the plane wave solution given by Eq. (2.6.1) in the defocusing NLS equation

$$iu_t = -\frac{1}{2}u_{xx} + |u|^2 u, \tag{2.6.4}$$

We add a small perturbation to the plane wave solution, i.e.

$$u(x,t) = \sqrt{\rho_0}\exp[i(\kappa x - \omega t)] + \epsilon f(x,t), \tag{2.6.5}$$

where f is any complex valued function and $\epsilon \ll 1$ is a perturbation parameter. Differentiating Eq. (2.6.5) partially with respect to t and x, we obtain

$$u_t = -i\omega\sqrt{\rho_0}\exp[i(\kappa x - \omega t)] + \epsilon f_t,$$
$$u_{xx} = -\kappa^2\sqrt{\rho_0}\exp[i(\kappa x - \omega t)] + \epsilon f_{xx}.$$

Substituting these values into Eq. (2.6.4) and retaining the terms linear in ϵ gives

$$\left(\omega - \frac{\kappa^2}{2} - \rho_0\right)\sqrt{\rho_0}\exp[i(\kappa x - \omega t)] + \epsilon\left[if_t + \frac{1}{2}f_{xx} - 2\rho_0 f - \rho_0 f^* \exp\left(2i\kappa x - 2i\omega t\right)\right] = 0.$$

Using the dispersion relation, the first term above will vanish and we are left with

$$if_t + \frac{1}{2}f_{xx} - 2\rho_0 f - \rho_0 f^* \exp(2i\kappa x - 2i\omega t) = 0.$$

We substitute $f(x,t) = F(x,t)\exp[i(\kappa x - \omega t)]$ (where F is any complex valued function) in the above equation to obtain

$$iF_t + \frac{1}{2}F_{xx} + i\kappa F_x - \rho_0(F + F^*) = 0.$$

Next, suppose that $F(x,t) = \alpha(x)\exp(iqt) + i\beta^*(x)\exp(-iqt)$, where α and β are complex valued functions and q is a real number. Inserting this expression of F into the last equation and equating to zero the coefficients of $\exp(iqt)$ and $\exp(-iqt)$, we obtain

$$\frac{1}{2}\alpha_{xx} + i\kappa\alpha_x - (q + \rho_0)\alpha - \rho_0\beta = 0,$$
$$\frac{1}{2}\beta_{xx} - i\kappa\beta_x + (q - \rho_0)\beta - \rho_0\alpha = 0.$$

Since the above coupled equations are linear in α and β, one can substitute $\alpha = \alpha_0\exp(-ipx)$ and $\beta = \beta_0\exp(-ipx)$ to obtain the following linear algebraic equations

$$(q - \kappa p + \rho_0 + p^2/2)\alpha_0 + \rho_0\beta_0 = 0, \tag{2.6.6}$$
$$-\rho_0\alpha_0 + (q - \kappa p - \rho_0 - p^2/2)\beta_0 = 0. \tag{2.6.7}$$

The system of Eq. (2.6.6) and Eq. (2.6.7) is homogeneous and can be expressed in the matrix form $AX = b$ with the coefficient matrix A given as

$$A = \begin{bmatrix} q - \kappa p + \rho_0 + p^2/2 & \rho_0 \\ -\rho_0 & q - \kappa p - \rho_0 - p^2/2 \end{bmatrix}.$$

The system will have a non-trivial solution if $det(A) = 0$. This implies that

$$(q - \kappa p)^2 = p^2\left(\frac{p^2}{4} + \rho_0\right), \tag{2.6.8}$$

or

$$q = \kappa p \pm \sqrt{p^2\left(\frac{p^2}{4} + \rho_0\right)}. \tag{2.6.9}$$

Eq. (2.6.9) shows that the value of q will remain real for any given real value of p. Hence,

$$\begin{aligned} f(x,t) = F(x,t)\exp[i(\kappa x - \omega t)] &= [\alpha(x)\exp(iqt) + i\beta^*(x)\exp(-iqt)]\exp[i(\kappa x - \omega t)] \\ &= \alpha_0\exp[i(\kappa - p)x + i(q - \omega)t] \\ &+ \beta_0\exp[i(\kappa - p)x - i(q + \omega)t]. \end{aligned}$$

The above expression shows that f will not grow for any real values of p and q which in turn implies that the small excitations of the plane wave solution of the defocusing NLS equation will be stable. One can find the minimum group velocity of these small excitations for $\kappa = 0$. Differentiating Eq. (2.6.8) with respect to p gives the group velocity of the excitation which is denoted by v_g, i.e.

$$v_g = \frac{dq}{dp} = \frac{2\rho_0 + p^2}{\sqrt{4\rho_o + p^2}}. \tag{2.6.10}$$

Now, we differentiate v_g twice with respect to p and equate the first derivative of v_g to zero. The critical value we obtain is $p = 0$ and the second derivative of v_g is positive at this value of p, indicating that $p = 0$ is the point of minimum value. We plug $p = 0$ in Eq. (2.6.10) to get the minimum value of the group velocity which is $(v_g)_{min} = \sqrt{\rho_0}$.

Let us now consider the stability of the plane wave solution in the focusing NLS equation

$$iu_t = -\frac{1}{2}u_{xx} - |u|^2 u. \tag{2.6.11}$$

It is easy to see that if we follow a similar procedure as before, the following relation between p and q is obtained

$$q = \kappa p \pm \sqrt{p^2\left(\frac{p^2}{4} - \rho_0\right)}. \tag{2.6.12}$$

This shows that q will be complex for $p^2 < 4\rho_0$. Consequently, f will grow exponentially and hence the plane wave solution will become unstable.

2.6.2 Matter wave dark solitons

Let us now take into account the case of repulsive interatomic interaction in the condensate. In this case the sign of the nonlinear term in Eq. (2.5.2) should be positive and the resulting GP equation possesses a dark soliton solution. This solution can be considered as the nonlinear excitation of the plane-wave solution. The general form of the dark soliton solution is [71]

$$u(x,t) = \sqrt{\rho_0}[A \tanh \eta + iB] \exp[i(\kappa x - \omega t)], \tag{2.6.13}$$

where $\eta = \sqrt{\rho_0}A(x - \sqrt{\rho_0}x_0)$ and the parameters A, B, x_0 are in general functions of time t. The parameter A determines the depth $\sqrt{\rho_0}A$ of the dark soliton, while the parameter x_0 represents the soliton centre and is given by $x_0 = x_i + vt$. Here x_i is an arbitrary real number which denotes the initial location of the dark soliton. The frequency ω of the dark soliton is given by the dispersion relation (2.6.2) (with the positive

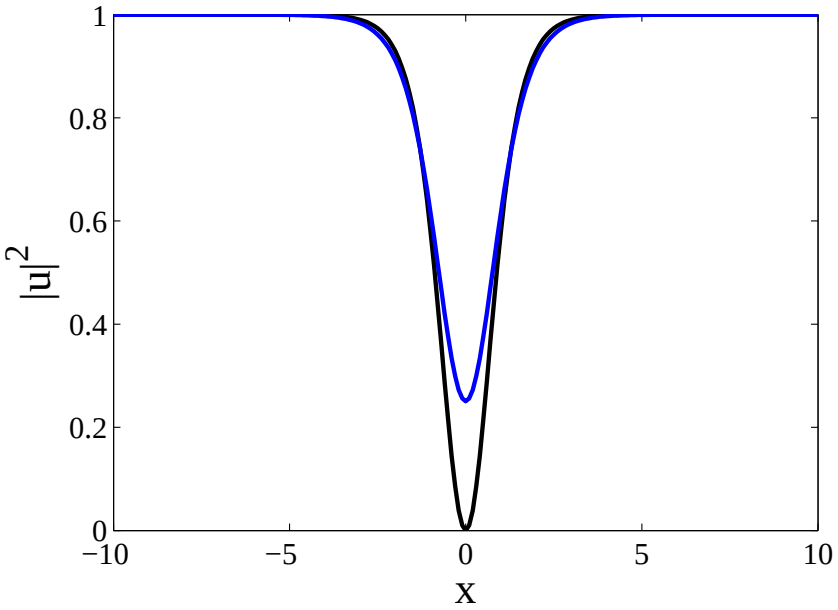

Figure 2.3: Plot of a black soliton (black) with parameter values $A = 1$, $B = v = 0$ and a grey soliton (blue) with $A = \frac{\sqrt{3}}{2}$, $B = v = 0.5$.

sign) of the background solution. To obtain the relationships between the parameters of the dark soliton, we differentiate the solution (2.6.13) partially with respect to t and x to yield

$$\begin{aligned} u_t &= \left(B\omega\sqrt{\rho_0} - \rho_0 v A^2 \text{sech}^2\eta - iA\omega\sqrt{\rho_0}\tanh\eta \right) \exp[i(\kappa x - \omega t)], \\ u_{xx} &= \left(-\kappa^2 A\sqrt{\rho_0}\tanh\eta + 2i\kappa A^2\rho_0 \text{sech}^2\eta - i\kappa^2 B\sqrt{\rho_0} \right) \exp[i(\kappa x - \omega t)]. \end{aligned}$$

Here, we have assumed that the initial location of the dark soliton is at the origin. Substituting the above expressions of u, u_t and u_{xx} in Eq. (2.5.2) (with positive sign) and equating to zero the real and imaginary parts, we find that the parameters A, B and v are related through the equations $A^2 + B^2 = 1$ and $\kappa + (B - v)\sqrt{\rho_0} = 0$. In the case of $B = v = 0$, the dark soliton becomes a stationary kink also called a black soliton and has unit depth. The dark soliton moving with some non-zero velocity is also called a grey soliton. In particular, for $B = v = \pm 1$, the depth of the solution vanishes and the dark soliton becomes the background solution. The profiles of the black and grey solitons are shown in Fig. 2.3.

When the background solution is at rest, i.e. $\kappa = 0$, we have $B = v$. Then the minimum value ρ_{min} of the dark soliton can be obtained by differentiating $|u|^2$ partially with respect to x and equating it to zero, i.e.

$$\frac{\partial |u|^2}{\partial x} = 0. \tag{2.6.14}$$

Here,

$$|u|^2 = \rho_0[A^2 \tanh^2 \eta + B^2]. \tag{2.6.15}$$

Using Eq. (2.6.14), the critical point we obtain is $x = \sqrt{\rho_0}x_0$. Substituting this value back in Eq. (2.6.15) yields

$$\rho_{min} = \rho_0 B^2 = \rho_0 v^2. \tag{2.6.16}$$

Sometimes, it is convenient to parameterize A and B as $A = \cos\phi$ and $B = \sin\phi$, where ϕ is called the soliton phase angle. In the limiting case when $x \to \pm\infty$, the dark soliton coincides with the plane-wave solution. However, the plane waves are shifted in phase at the different edges. The total phase jump $\Delta\phi$ across the dark soliton is given by

$$\Delta\phi = 2\left[\arctan\left(\frac{B}{A}\right) - \frac{\pi}{2}\right] = -2\arctan\left(\frac{A}{B}\right). \tag{2.6.17}$$

We now consider the integrals of motion for dark soliton. Since the integrals of motion (2.5.3-2.5.5) describe both the background and the dark soliton, they have been modified [7] to extract the corresponding contribution of the background. After such a modification, the integrals of motion for the dark soliton become finite. The renormalized integrals of motion for the dark soliton are

$$N_{ds} = \int_{-\infty}^{\infty} (\rho_0 - |u|^2) dx, \tag{2.6.18}$$

$$P_{ds} = \frac{i}{2}\int_{-\infty}^{\infty} (uu_x^* - u^* u_x)\left(1 - \frac{\rho_0}{|u|^2}\right) dx, \tag{2.6.19}$$

$$E_{ds} = \frac{1}{2}\int_{-\infty}^{\infty} \left[|u_x|^2 + (|u|^2 - \rho_0)^2\right] dx, \tag{2.6.20}$$

where N_{ds}, P_{ds} and E_{ds} represent respectively the number of atoms, momentum and energy of the dark soliton. We evaluate these integrals of motion in the simpler case when the background is static, i.e. $\kappa = 0$. Substituting the soliton solution (2.6.13) into the above integrals, we find

$$N_{ds} = 2A\sqrt{\rho_0}, \quad P_{ds} = -2v\rho_0\sqrt{1-v^2} + 2\rho_0 \arctan\left(\frac{\sqrt{1-v^2}}{v}\right), \quad E_{ds} = \frac{4}{3}{\rho_0}^{3/2}(1-v^2)^{3/2}. \tag{2.6.21}$$

Differentiating the momentum and energy of the dark soliton with respect to velocity, we obtain

$$\frac{dP_{ds}}{dv} = -4c_s^2\sqrt{1-v^2}, \tag{2.6.22}$$

$$\frac{dE_{ds}}{dv} = -4c_s^2 v\sqrt{1-v^2}. \tag{2.6.23}$$

Using chain rule, we find the following simple relation

$$\frac{dE_{ds}}{dP_{ds}} = v, \tag{2.6.24}$$

which clearly indicates that the dark soliton behaves as a classical particle. Since the left hand side of Eq. (2.6.22) represents the mass, an effective mass m_{ds} can be incorporated to the dark soliton as $m_{ds} = -4\rho_0 A$. This shows that the dark soliton is described by a negative effective mass.

2.6.2.1 The stability of dark solitons

Several methods have been used to study the dynamics of matter wave dark solitons in a quasi one dimensional GP equation. Physicists first thought that dark solitons are stable solutions. Kivshar and Krolikowski were the first who used a variational approach and determined a criterion for the stability of dark solitons [72]. However, the existence and stability of dark solitons in a generalized model of GP equation were recently studied rigorously in [73, 74]. The persistence and stability of dark solitons in the absence of external potential was considered in [73] while a more general model in the presence of the potential was investigated in [74]. Here, we will discuss the linear stability of dark solitons numerically in the absence and presence of a harmonic trap.

In order to discuss the linear stability of dark soliton, we set $u = U\exp(-it)$ into Eq. (2.5.1) with defocusing nonlinearity to obtain

$$iU_t = -\frac{1}{2}U_{xx} + VU - U + |U|^2U. \tag{2.6.25}$$

We first find the dark soliton solution numerically in the absence of the magnetic trap, i.e. $V = 0$, and Eq. (2.6.25) reduces to

$$iU_t = -\frac{1}{2}U_{xx} - U + |U|^2U. \tag{2.6.26}$$

Let us assume $U_t = 0$, so that we are considering the black soliton described in the previous section. Discretizing the resulting equation, we obtain

$$\frac{U_{n+1} - 2U_n + U_{n-1}}{2\Delta x^2} - |U_n|^2U_n + U_n = 0, \text{ for } n = 1, 2, ..., N. \tag{2.6.27}$$

Eq. (2.6.27) represents a system of nonlinear algebraic equations. We solve this system by using Newton's method with Neumann boundary conditions $U_0 = U_1$, $U_{N+1} = U_N$ through the MATLAB built-in function FSOLVE to obtain the dark soliton solution numerically which is shown in Fig. 2.4. Note that Eq. (2.6.26) is invariant under the transformation $U \to -U$. This means that the negative dark soliton exists and can be obtained similarly.

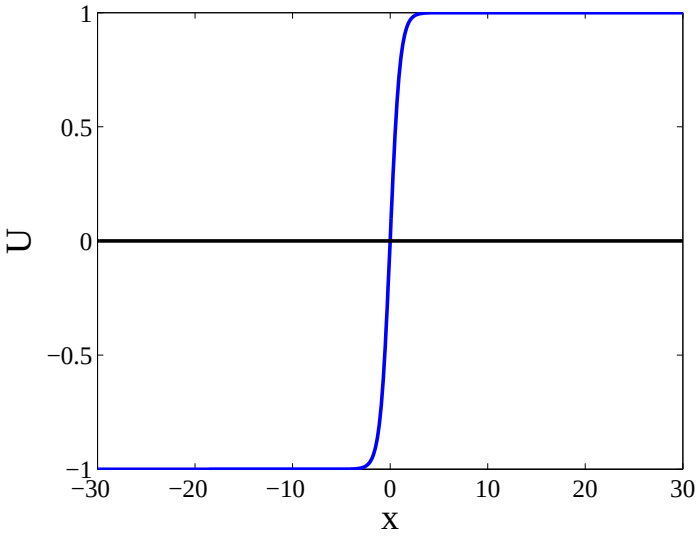

Figure 2.4: A numerically obtained dark soliton solution. The blue curve represents the real part while the black horizontal line represents the imaginary part of the solution.

Next, we assume that $U^{(0)}(x)$ is a static solution of Eq. (2.6.26). Now we add a small perturbation to the static solution $U^{(0)}$ and look for a perturbed solution of the form

$$U = U^{(0)}(x) + \epsilon[a(x)\, e^{i\lambda t} + b^*(x)\, e^{-i\lambda^* t}], \tag{2.6.28}$$

where λ represents the eigenvalue with the corresponding eigenfunctions a and b. The solution will be stable if the imaginary parts of all the eigenvalues are zero. Differentiating Eq. (2.6.28) with respect to t and x yields

$$\begin{aligned} U_t &= i\epsilon[\lambda a e^{i\lambda t} - \lambda^* b^* e^{-i\lambda^* t}], \\ U_{xx} &= U^{(0)}_{xx} + \epsilon[a_{xx} e^{i\lambda t} + b^*_{xx} e^{-i\lambda^* t}]. \end{aligned}$$

We substitute these values of U, U_t and U_{xx} in Eq. (2.6.26) and keep only the linear terms in ϵ since ϵ is small. Then equating the coefficients of $\epsilon e^{i\lambda t}$ and $\epsilon e^{-i\lambda^* t}$ on both sides of Eq. (2.6.26), we obtain

$$\begin{aligned} \frac{1}{2}a_{xx} + a - 2|U^{(0)}|^2 a - \left(U^{(0)}\right)^2 b &= \lambda a, \\ -\frac{1}{2}b^*_{xx} - b^* + 2|U^{(0)}|^2 b^* + \left(U^{(0)}\right)^2 a^* &= \lambda^* b^*. \end{aligned} \tag{2.6.29}$$

Taking the complex conjugate of the second equation yields

$$-\frac{1}{2}b_{xx} - b + 2|U^{(0)}|^2 b + \left(U^{(0)*}\right)^2 a = \lambda b. \tag{2.6.30}$$

The system of Eq. (2.6.29) and Eq. (2.6.30) represents a linear eigenvalue problem. Discretizing Eq. (2.6.29) and Eq. (2.6.30) gives

$$\frac{a_{n+1}-2a_n+a_{n-1}}{2\Delta x^2}+a_n-2|U_n^{(0)}|^2a_n-\left(U_n^{(0)}\right)^2b_n=\lambda a_n, \tag{2.6.31}$$

$$-\frac{b_{n+1}-2b_n+b_{n-1}}{2\Delta x^2}-b_n+2|U_n^{(0)}|^2b_n+\left(U_n^{(0)*}\right)^2a_n=\lambda b_n, \tag{2.6.32}$$

where $n=1,2,...,N$. Using the Neumann boundary conditions $a_0=a_1$, $a_N=a_{N+1}$, $b_0=b_1$, $b_N=b_{N+1}$, the above system of Eq. (2.6.31) and Eq. (2.6.32) can be written in a matrix form as

$$AX=\lambda X,$$

where

$$A=\begin{bmatrix} A_1 & D \\ -D^* & -A_1 \end{bmatrix},$$

with

$$A_1=\begin{bmatrix} a_{11} & \frac{1}{2\Delta x^2} & 0 & \dots & 0 \\ \frac{1}{2\Delta x^2} & a_{22} & \frac{1}{2\Delta x^2} & \dots & 0 \\ 0 & \frac{1}{2\Delta x^2} & a_{33} & \dots & 0 \\ \vdots & \vdots & \vdots & \ddots & \vdots \\ 0 & 0 & 0 & \dots & a_{NN} \end{bmatrix},$$

$$D=\begin{bmatrix} -\left(U_1^{(0)}\right)^2 & 0 & \dots & 0 \\ 0 & -\left(U_2^{(0)}\right)^2 & \dots & 0 \\ \vdots & \vdots & \ddots & \vdots \\ 0 & 0 & \dots & -\left(u_N^{(0)}\right)^2 \end{bmatrix}.$$

In the matrix A_1 the entries of the principal diagonal are given by $a_{ii}=1-2|U_i^{(0)}|^2-\frac{1}{2\Delta x^2}$ when $i=1,N$ and $a_{ii}=1-2|U_i^{(0)}|^2-\frac{1}{\Delta x^2}$ when $i=2,3,...,N-1$.

We find the eigenvalues of the stability matrix A, which are depicted in Fig. 2.5. This shows that all the eigenvalues are real except a pair of eigenvalues lying on the vertical axis. The magnitude of this pair of eigenvalues is very small. As $\Delta x\to 0$, this pair tends to zero so that all the eigenvalues become real, showing that the dark solution is a stable solution. We also solve the time-dependent Eq. (2.6.26) using a Runge-Kutta method of order four to confirm the stability of the solution as shown in Fig. 2.6.

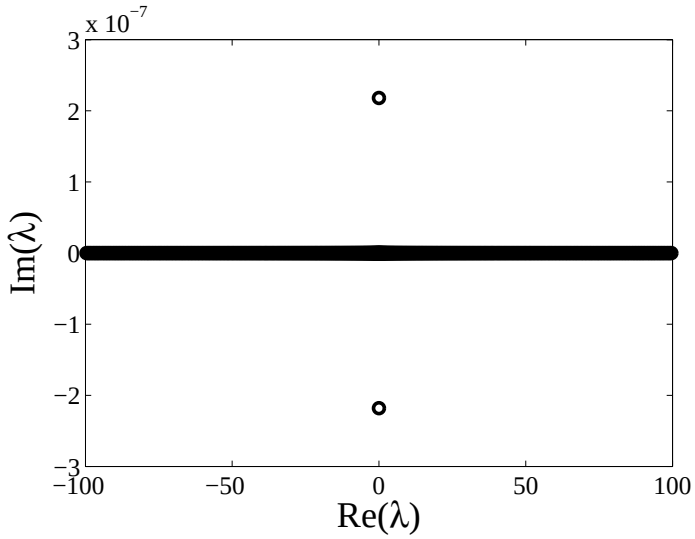

Figure 2.5: The structure of the eigenvalues in the complex plane for the solution shown in Fig. 2.4.

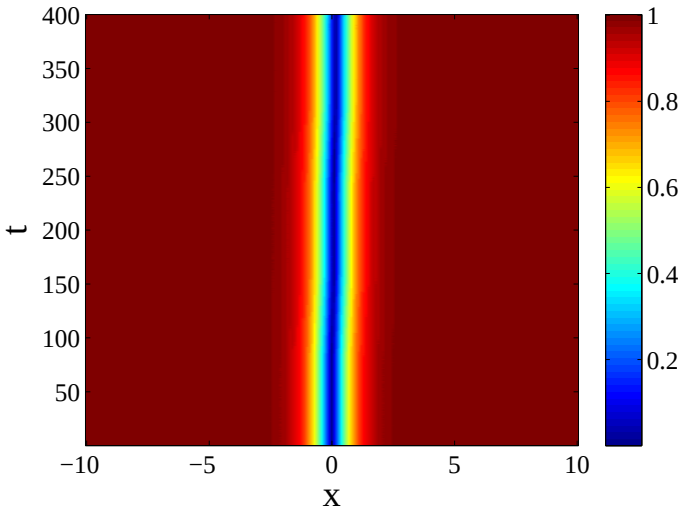

Figure 2.6: Contour plot obtained through the direct numerical integration of Eq. (2.6.26) depicting the time evolution of the dark soliton solution shown in Fig. 2.4.

2.6.2.2 The stability of dark solitons in the inhomogeneous case

Let us now consider the inhomogeneous case with $V = \frac{1}{2}\Omega^2 x^2$. We follow the same procedure as above and find numerically the dark soliton solution in the presence of the magnetic trap. The profiles of the dark soliton for different values of the trapping strength Ω are shown in Fig. 2.7. The profiles show that the width of the dark soliton decreases with the increasing strength of the trap. One can also see that the solution tends to zero due to the influence of the magnetic trap.

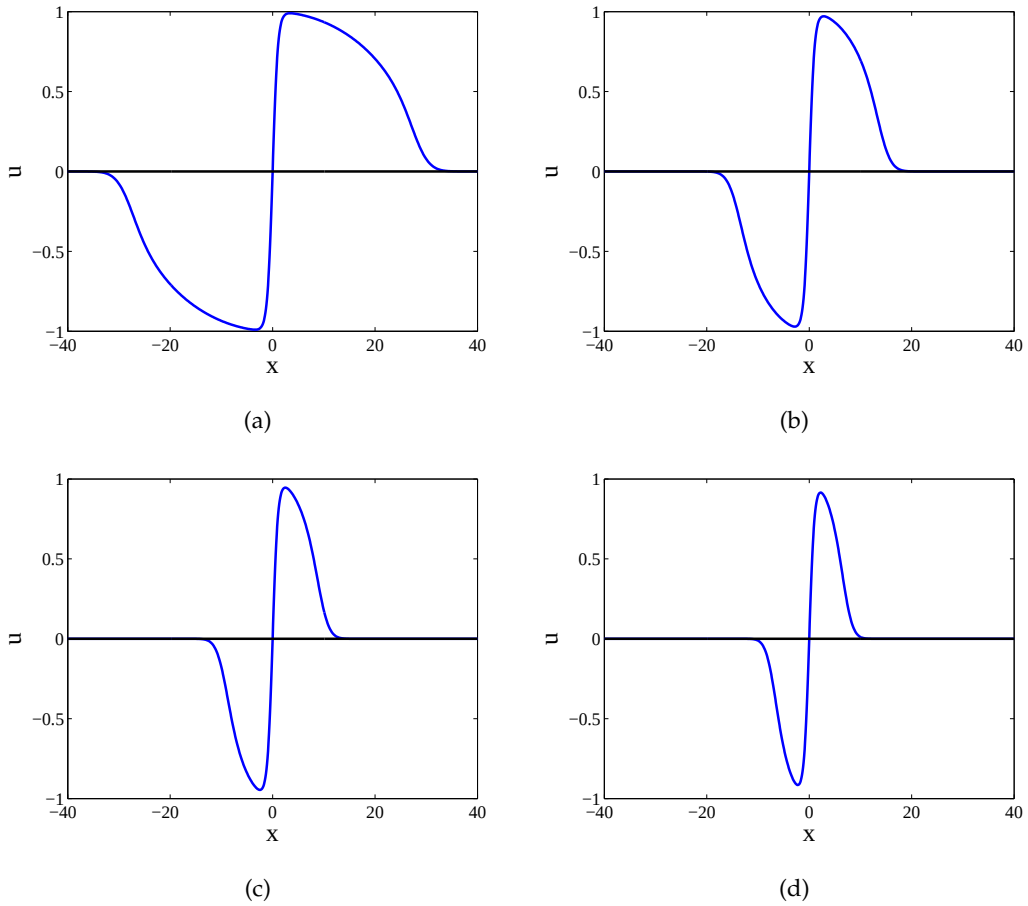

Figure 2.7: The profiles of a dark soliton in the presence of the magnetic trap with trapping strength $\Omega = 0.05, 0.1, 0.15, 0.2$ respectively. In each figure the blue curve represents the real part while the black horizontal line represents the imaginary part of the solution. The higher the value of Ω, the smaller the width of the dark soliton.

Starting from the static solution shown in Fig. 2.7 and adding a small perturbation to

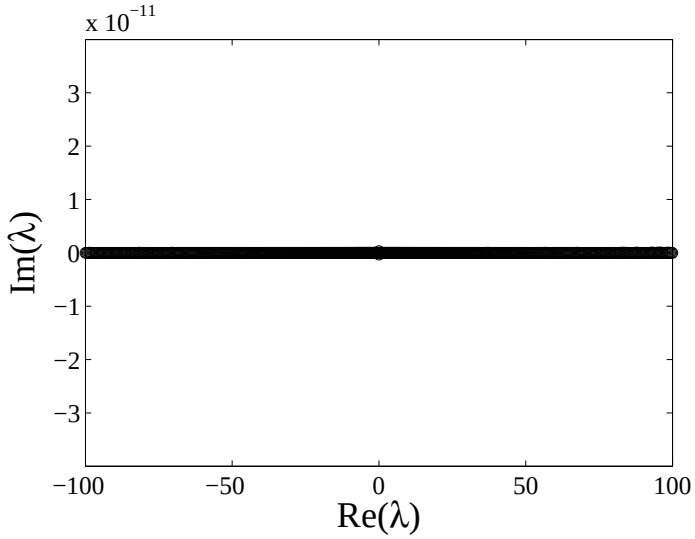

Figure 2.8: The structure of the eigenvalues in the complex plane for the dark soliton in the presence of the magnetic trap with $\Omega = 0.1$.

it, the following stability equations are obtained

$$\frac{1}{2}a_{xx} - Va + a - 2|U^{(0)}|^2 a - \left(U^{(0)}\right)^2 b = \lambda a, \tag{2.6.33}$$

$$-\frac{1}{2}b_{xx} + Vb - b + 2|U^{(0)}|^2 b + \left(U^{(0)*}\right)^2 a = \lambda b. \tag{2.6.34}$$

We discretize the above two equations and write the resulting system of equations in a matrix form. Then we find the eigenvalues of the stability matrix and are shown in Fig. 2.8. The figure shows that the dark soliton in the presence of the magnetic trap is stable. The time evolution of the solution is shown in Fig. 2.9.

2.6.2.3 Travelling dark solitons

Because solitons of Eq. (2.6.26) are translationally invariant, we can study the existence and stability of solitons in a moving coordinate frame. Therefore, we substitute $\xi = x - vt$ and $\tau = t$ (where v represents the velocity of the dark soliton) in Eq. (2.6.26), then

$$U_t = -vU_\xi + U_\tau, \quad U_{xx} = U_{\xi\xi},$$

and Eq. (2.6.26) takes the form

$$i(-vU_\xi + U_\tau) + \frac{1}{2}U_{\xi\xi} + U - |U|^2 U = 0. \tag{2.6.35}$$

The exact analytical solution independent of τ of Eq. (2.6.35) is given by

$$U(\xi) = A\tanh(A\xi) + iv, \qquad A^2 + v^2 = 1. \tag{2.6.36}$$

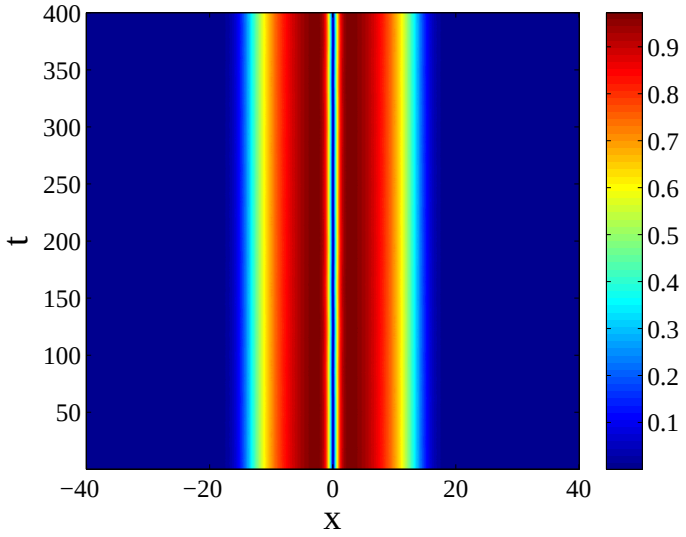

Figure 2.9: Contour plot obtained through the direct numerical integration of Eq. (2.6.25) depicting the time evolution of the dark soliton solution shown in Fig. 2.7.

To find this solution numerically we discretize Eq. (2.6.35) to obtain

$$-iv\left(\frac{U_{n+1}-U_{n-1}}{2\Delta x}\right)+\frac{U_{n+1}-2U_n+U_{n-1}}{2\Delta x^2}+U_n-|U_n|^2U_n=0,\ \text{for}\ n=1,2,...,N. \tag{2.6.37}$$

Solving this above system of equations using Newton's method with the Neumann boundary conditions, we obtain numerically the travelling dark soliton solution in one dimension having velocity v.

2.6.2.4 The stability of travelling dark soliton solution

Suppose that $U^{(0)}$ is a steady state solution of Eq. (2.6.35) and

$$U=U^{(0)}(\xi)+\epsilon[a(\xi)\,e^{i\lambda\tau}+b^*(\xi)\,e^{-i\lambda^*\tau}], \tag{2.6.38}$$

be the perturbed solution of Eq. (2.6.35), then we have

$$\frac{1}{2}a_{\xi\xi}-iva_\xi+a-2|U^{(0)}|^2a-\left(U^{(0)}\right)^2b=\lambda a, \tag{2.6.39}$$

$$-\frac{1}{2}b_{\xi\xi}-ivb_\xi-b+2|U^{(0)}|^2b+\left(U^{(0)*}\right)^2a=\lambda b. \tag{2.6.40}$$

The system of Eq. (2.6.39) and Eq. (2.6.40) represents a linear eigenvalue problem. Discretizing these equations gives

$$\frac{a_{n+1}-2a_n+a_{n-1}}{2\Delta x^2}-iv\frac{a_{n+1}-a_{n-1}}{2\Delta x}+a_n-2|U_n^{(0)}|^2a_n-\left(U_n^{(0)}\right)^2b_n=\lambda a_n, \tag{2.6.41}$$

$$-\frac{b_{n+1}-2b_n+b_{n-1}}{2\Delta x^2}-iv\frac{b_{n+1}-b_{n-1}}{2\Delta x}-b_n+2|U_n^{(0)}|^2b_n+\left(U_n^{(0)*}\right)^2a_n=\lambda b_n, \tag{2.6.42}$$

where $n = 1, 2, ..., N$. We use the Neumann boundary conditions and write the above system of equations (2.6.41) and (2.6.42) in a matrix form. After finding the eigenvalues of the stability matrix we conclude that the travelling dark soliton solution of one dimensional NLS equation is stable for all the values of velocity v where it exists.

2.6.3 Matter wave bright solitons and their stability

The negative sign in Eq. (2.5.2) corresponds to the attractive interaction between the atoms of BECs. In such a case, there exists a bright soliton solution of the following form [3]

$$u(x,t) = D\text{sech}\theta \exp[i(\kappa x - \omega t)], \qquad \theta(x,t) = D(x - vt), \tag{2.6.43}$$

and is shown in Fig. 2.11. Here, the parameter D denotes the amplitude of the bright soliton. Differentiating Eq. (2.6.43) partially with respect to t and x, we get

$$\begin{aligned} u_t &= D\text{sech}\theta[Dv\tanh\theta - i\omega]\exp[i(\kappa x - \omega t)], \\ u_{xx} &= D\text{sech}\theta(D^2 - \kappa^2 - 2D^2\text{sech}^2\theta - 2i\kappa D\tanh\theta)\exp[i(\kappa x - \omega t)]. \end{aligned}$$

Substituting u_t and u_{xx} in Eq. (2.6.11) and equating the real and imaginary parts to zero, the following relations are obtained

$$\omega = \frac{1}{2}(\kappa^2 - D^2), \qquad v = \kappa.$$

To find the integrals of motion for the bright soliton, we insert Eq. (2.6.43) into Eqs. (2.5.3-2.5.5), which yield

$$N = 2D, \qquad P = 2D\kappa = N\kappa, \qquad E = D\kappa^2 - \frac{1}{3}D^3 = \frac{1}{2}\left[2D\kappa^2 - \frac{1}{12}(2D)^3\right]. \tag{2.6.44}$$

It is easy to associate the concept of effective mass M_{bs}, momentum P_{bs} and energy E_{bs} to the bright soliton through these equations by expressing them into the following form

$$M_{bs} = 2D, \qquad P_{bs} = M_{bs}v, \qquad E_{bs} = \frac{1}{2}M_{bs}v^2 - \frac{1}{24}M_{bs}^3.$$

The right hand side in the energy equation is the sum of two terms, the kinetic energy and the binding energy respectively of the quasi-particle associated with the bright solion. Differentiating the above expressions for energy and momentum over the soliton velocity v, we obtain

$$\frac{\partial E_{bs}}{\partial P_{bs}} = v.$$

This equation shows that the bright soliton behaves as a classical particle like the dark soliton.

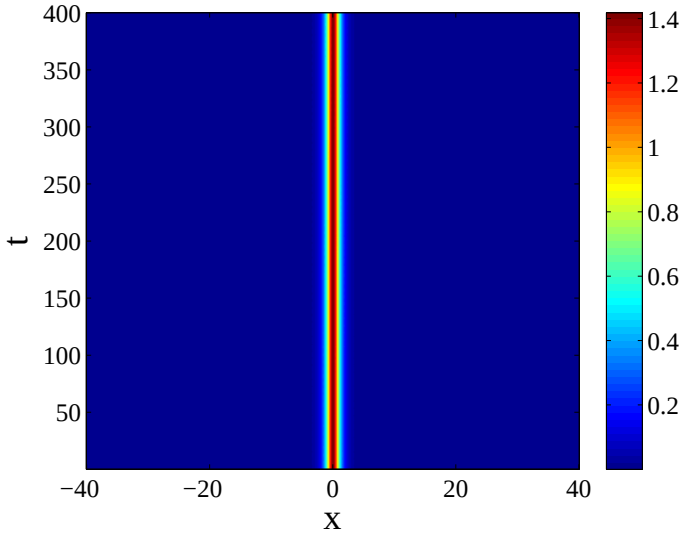

Figure 2.10: Contour plot obtained through the direct numerical integration of Eq. (2.6.11) depicting the time evolution of the bright soliton solution shown in Fig. 2.11.

Next, we follow the same procedure as for the dark soliton to investigate the stability of bright soliton. The eigenvalues of the stability matrix found in this case indicate that the bright soliton is a stable solution. The time evolution of the solution is shown in Fig. 2.10.

We also find the bright soliton solution in the presence of a magnetic trap. The presence of the trap does not affect the solution significantly as the width of the bright soliton is small as compared with the trapping strength Ω. The two bright soliton solutions, one in the absence and other in the presence of the trap are shown in Fig. 2.11. Both solutions are almost same. The solution in the presence of the trap is found to stable as well.

2.7 Multi-component BECs and coupled system of Gross-Pitaevskii equations

Gaseous BECs were first achieved in the clouds of atoms in a single spin state of the ground state of rubidium [41], sodium [42] and lithium [75]. The diversity in the trapping techniques for BECs made it possible to confine simultaneously the different hyperfine states of the condensate. The first such experiment was reported for mixtures of two magnetically trapped hyperfine states of rubidium [76], in which similarities and differences between the behaviours of the two spin states were studied. Simultaneous

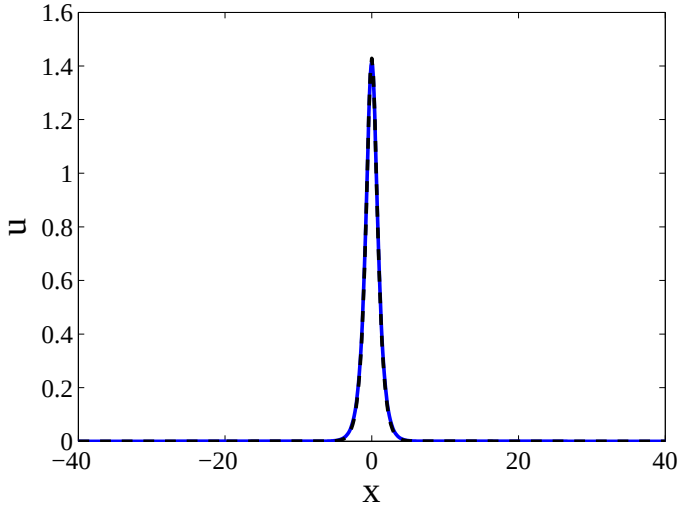

Figure 2.11: Comparison between the untrapped (blue) and the trapped (black dashed) bright solitons. For the trapped bright soliton, $\Omega = 0.2$. Both graphs are almost same showing that the magnetic trap does not affect the stability of the solution.

confinement of BECs of sodium atoms in several hyperfine states using optical trap was achieved in [56]. The optical trap allowed the confinement of atoms of sodium condensate independent of their spin orientations and provided the opportunity of studying the so called spinor condensates [77].

On the other hand, mixtures of two different species of condensates such as potassium-rubidium $(^{41}K -^{87} Rb)$ [78] and lithium-cesium $(^{7}Li -^{133} Cs)$ [79] have been created experimentally. The mean field model describing the dynamics of such multi-component condensates is a system of coupled GP equations. Typically, the two-mode representation of the GP system is derived below.

2.7.1 Two-mode representations of the GP equation

The dynamics of a dilute gas containing interacting bosons of the same species in the context of mean field under the influence of a magnetic trap can be illustrated by the GP equation which in the cartesian coordinate system can be given as

$$i\hbar\frac{\partial\psi}{\partial t} = \left[\frac{-\hbar^2}{2m}\left(\partial_x^2 + \partial_y^2 + \partial_z^2\right) + V(x,y,z)\right]\psi + g|\psi|^2\psi. \tag{2.7.1}$$

Here $V(x,y,z) = V_1(x) + V_2(y) + V_3(z)$ is the external magnetic trap.

To obtain an accurate formulation, the two-mode representation of ψ along with the

combination of symmetric and asymmetric functions has been used as [80]

$$\psi = f(z)[\psi_1(x,t)\Phi_1(y) + \psi_2(x,t)\Phi_2(y)], \tag{2.7.2}$$

where

$\Phi_{1,2}(y) = \frac{\Phi_+(y)\pm\Phi_-(y)}{\sqrt{2}}$, $\Phi_\pm(y) = \pm\Phi_\pm(-y)$, $\int_{-\infty}^{\infty} dy\Phi_p\Phi_q = \delta_{p,q}N$, $p,q = +,-$.

Here, Φ_+, Φ_- are assumed to be real functions. Substituting (2.7.2) into (2.7.1), we obtain

$$\begin{aligned} i\hbar f(z)\left(\Phi_j\frac{\partial\psi_j}{\partial t} + \Phi_{3-j}\frac{\partial\psi_{3-j}}{\partial t}\right) &= -\frac{\hbar^2}{2m}f(z)\Bigg[\left(\Phi_j\frac{\partial^2\psi_j}{\partial x^2} + \Phi_{3-j}\frac{\partial^2\psi_{3-j}}{\partial x^2}\right) \\ &+ \left(\psi_j\frac{\partial^2\Phi_j}{\partial y^2} + \psi_{3-j}\frac{\partial^2\Phi_{3-j}}{\partial y^2}\right) \\ &+ (\psi_j\Phi_j + \psi_{3-j}\Phi_{3-j})\frac{1}{f(z)}\frac{\partial^2 f(z)}{\partial z^2}\Bigg] \\ &+ f(z)\Bigg[(V_1+V_2+V_3)(\psi_j\Phi_j + \psi_{3-j}\Phi_{3-j}) \\ &+ g|f(z)|^2(\psi_j\Phi_j + \psi_{3-j}\Phi_{3-j})^2(\psi_j^*\Phi_j + \psi_{3-j}^*\Phi_{3-j})\Bigg],\ j = 1,2. \end{aligned}$$

We multiply both sides of the above equation by Φ_j, $(j = 1,2)$ and integrate the resulting equation w.r.t y from $-\infty$ to $+\infty$ to yield

$$\begin{aligned} i\hbar N f(z)\frac{\partial\psi_j}{\partial t} &= -\frac{\hbar^2}{2m}f(z)\Bigg[N\frac{\partial^2\psi_j}{\partial x^2} + \psi_j\int_{-\infty}^{\infty}\Phi_j\frac{\partial^2\Phi_j}{\partial y^2}dy + \psi_{3-j}\int_{-\infty}^{\infty}\Phi_j\frac{\partial^2\Phi_{3-j}}{\partial y^2}dy \\ &+ N\psi_j\frac{1}{f(z)}\frac{\partial^2 f(z)}{\partial z^2}\Bigg] + f(z)\psi_j\left[N(V_1+V_3) + \int_{-\infty}^{\infty}V_2\Phi_j^2 dy\right] \\ &+ f(z)\psi_{3-j}\int_{-\infty}^{\infty}V_2\Phi_j\Phi_{3-j}dy + g|f(z)|^2 f(z)\Bigg[|\psi_j|^2\psi_j\int_{-\infty}^{\infty}\Phi_j^4 dy \\ &+ (\psi_j^2\psi_{3-j}^* + 2|\psi_j|^2\psi_{3-j})\int_{-\infty}^{\infty}\Phi_j^3\Phi_{3-j}dy \\ &+ (\psi_{3-j}^2\psi_j^* + 2|\psi_{3-j}|^2\psi_j)\int_{-\infty}^{\infty}\Phi_j^2\Phi_{3-j}^2 dy + |\psi_{3-j}|^2\psi_{3-j}\int_{-\infty}^{\infty}\Phi_j\Phi_{3-j}^3 dy\Bigg]. \end{aligned}$$

Now, we multiply throughout by $f^*(z)$ and integrate w.r.t z from $-\infty$ to $+\infty$ by assuming that $\int_{-\infty}^{\infty}|f(z)|^2dz = C$ to obtain

$$\begin{aligned} i\hbar CN\frac{\partial\psi_j}{\partial t} &= -\frac{\hbar^2 C}{2m}\Bigg[N\frac{\partial^2\psi_j}{\partial x^2} + \psi_j\int_{-\infty}^{\infty}\Phi_j\frac{\partial^2\Phi_j}{\partial y^2}dy + \psi_{3-j}\int_{-\infty}^{\infty}\Phi_j\frac{\partial^2\Phi_{3-j}}{\partial y^2}dy \\ &+ \psi_j\frac{N}{C}\int_{-\infty}^{\infty}f^*(z)\frac{\partial^2 f(z)}{\partial z^2}dz\Bigg] + NCV_1\psi_j + \psi_j N\int_{-\infty}^{\infty}V_3|f(z)|^2 dz \\ &+ C\psi_j\int_{-\infty}^{\infty}V_2\Phi_j^2 dy + C\psi_{3-j}\int_{-\infty}^{\infty}V_2\Phi_j\Phi_{3-j}dy \\ &+ \frac{\int_{-\infty}^{\infty}|f(z)|^4dz}{4}\Big[\gamma_{++}P_{j+} + \gamma_{--}P_{j-} + \gamma_{+-}Q_j\Big], \end{aligned}$$

where

$$\begin{aligned} P_{j\pm} &= |\psi_j|^2\psi_j \pm (\psi_j^2\psi_{3-j}^* + 2|\psi_j|^2\psi_{3-j}) + (\psi_{3-j}^2\psi_j^* + 2|\psi_{3-j}|^2\psi_j) \pm |\psi_{3-j}|^2\psi_{3-j}, \\ Q_j &= 6|\psi_j|^2\psi_j - 4|\psi_{3-j}|^2\psi_j - 2\psi_{3-j}^2\psi_j^*, \\ \gamma_{pq} &= g\int_{-\infty}^{\infty}\Phi_p^2(y)\Phi_q^2(y)dy. \end{aligned}$$

The last equation is equivalent to the following equation

$$\begin{aligned} i\hbar\frac{\partial\psi_j}{\partial t} &= -\frac{\hbar^2}{2m}\left[\frac{\partial^2\psi_j}{\partial x^2} + \psi_{3-j}\frac{1}{N}\int_{-\infty}^{\infty}\Phi_j\frac{\partial^2\Phi_{3-j}}{\partial y^2}dy\right] + V_1\psi_j + \psi_{3-j}\frac{1}{N}\int_{-\infty}^{\infty}V_2\Phi_j\Phi_{3-j}dy \\ &+ \frac{\int_{-\infty}^{\infty}|f(z)|^4dz}{4NC}\left[\gamma_{++}P_{j+} + \gamma_{--}P_{j-} + \gamma_{+-}Q_j\right]. \end{aligned}$$

Finally, multiplying throughout by $\frac{m}{\hbar^2}$ and using scaling $\tilde{t} = \frac{\hbar}{m}t$, we obtain

$$\begin{aligned} i\frac{\partial\psi_j}{\partial\tilde{t}} &= -\frac{1}{2}\frac{\partial^2\psi_j}{\partial x^2} + R\left[\gamma_{++}P_{j+} + \gamma_{--}P_{j-} + \gamma_{+-}Q_j\right] \\ &- \left[\frac{1}{2N}\int_{-\infty}^{\infty}\Phi_j\left(\frac{\partial^2\Phi_{3-j}}{\partial y^2} - \frac{2m}{\hbar^2}V_2\Phi_{3-j}\right)dy\right]\psi_{3-j} + \frac{m}{\hbar^2}V_1\psi_j, \end{aligned}$$

where $\frac{m\int_{-\infty}^{\infty}|f(z)|^4dz}{4\hbar^2NC} = R$.

If we take only the first term of each of $P_{j\pm}$ and Q_j, i.e. $|\psi_j|^2\psi_j$, while ignoring the remaining terms as they are significantly smaller than $|\psi_j|^2\psi_j$ and setting

$$k = \frac{1}{2N}\int_{-\infty}^{\infty}\Phi_j\left(\frac{\partial^2\Phi_{3-j}}{\partial y^2} - \frac{2m}{\hbar^2}V_2\Phi_{3-j}\right)dy,$$

the last equation above will be the following coupled system of equations

$$i\frac{\partial\psi_j}{\partial\tilde{t}} = -\frac{1}{2}\frac{\partial^2\psi_j}{\partial x^2} + \mu|\psi_j|^2\psi_j - k\psi_{3-j} + V_1\psi_j. \tag{2.7.3}$$

2.8 Vortices in optics and BECs

Light can be twisted like a rotation of a corkscrew about its axis. When a twisted light is projected onto a flat surface, it induces a ring of light with a dark hole at the centre which is known as an optical vortex. The vortex can be represented by a number, called the topological charge. The value of the topological charge is equal to the number of twists that the light produces in one wavelength. This value is always an integer and can be positive or negative according to the direction of twist. The higher the topological charge, the faster the light spins about its axis. One of the applications of optical vortices is in optical tweezers. Optical tweezers are scientific instruments which are

capable of manipulating micrometer-sized objects by exerting extremely small forces via optical vortices. They have also been used to create micro-motors. Potential applications include quantum computing which could allow for faster data communication.

Vortices in a superfluid can be generated when it is subject to a rotational motion. Such a situation also occurs in dilute BECs with repulsive interatomic interactions where vortices represent the fundamental higher dimensional nonlinear excitations [46] and can be characterized by the GP equation. They have been studied considerably both theoretically [81–84] as well as experimentally [85–88] in the past few years. A large volume of studies on vortices is carried out not only due to their importance as prototypical nonlinear excitations, but also because they play a prominent role in the disruption of superflow of BECs [89, 90]. These nonlinear waves are described by their non-zero topological charge (vorticity) m with the property that the phase of the wave function has a phase jump of $2m\pi$.

There have been several ways to create vortices in BECs. The first realization of vortices in BECs was obtained in [85] between two hyperfine spin states of ^{87}Rb. Vortices can also be created by dragging an object through the condensate with certain critical speed [84, 89, 90]. Another possibility to generate vortices is to split the cloud of BECs into several fragments and then permitting them to collide [91, 92]. A common experimental technique to create vortices in BECs is based on stirring the condensate with a certain critical speed [93].

The study of vortex lattices in multicomponent condensates is an auspicious area of research. It was shown in [94] that in the case of two component BECs which are linearly coupled such that one of the component is loaded with a single atomic species containing a vortex lattice, it is possible to completely transfer the vortex lattice to the second component. This Rabi oscillation (the process of excitation and de-excitation of an atom) is a very useful tool for controlling the desired transfer of BECs atoms from one component to the other. It was also proposed that this mechanism can be extended to higher number of components.

2.9 Overview of the thesis

The study of trapped Bose-Einstein condensates has been a fascinating area of research in the last few years. The aim of the thesis is to study the dynamics of the excited states or localized solutions of the coupled Bose-Einstein condensates in the presence of an external potential in one and two dimensions. The system in such cases is modelled by coupled Gross-Pitaevskii equations.

We begin our work in Chapter 3 by considering two effectively one-dimensional parallel Bose-Einstein condensates in the presence of a harmonic trap. Closeness of the waveguides permits tunnelling of atoms between them. The system is assumed to be linearly coupled by a weak coupling k. The tunnelling and extended spatial dimension along the waveguide results in the formation of long Bose-Josephson junction and the system is described by Eq. (2.7.3). Analytical and numerical calculations are carried out to determine the existence and stability of stationary solitary solutions. In particular, we examine the dark soliton and fluxon analogue solutions in the defocusing system of coupled Gross-Pitaevskii equations. These solutions were studied earlier in [95, 96] in the absence of a magnetic trap. We investigate the existence and stability of these solutions numerically in the presence of the trap. Moreover, numerical integrations of Eq. (2.7.3) are performed to verify the stability results of our analysis.

Next, we solve the governing equation in moving coordinate frame and find the values of critical coupling k_{ce} at which FA solutions transform into coupled dark solitons for different values of velocity v. We also derive a relationship between k_{ce} and v analytically and its comparison with numerically obtained results is manifested. Lastly, we use a semi-analytical approach based on the variational approximation for the FA solutions in the two cases: (i) when k is close to a critical value k_{ce} and (ii) when k is close to zero, to comprehend the dynamical behaviours of FA solutions analytically.

In Chapter 4, we first consider the interactions of multiple dark solitons and determine a repulsive interaction potential in the uncoupled case of BECs which was briefly discussed in [97]. We then use this interaction potential to find the oscillation frequencies of multiple FA solutions in the coupled BECs when k is close to k_{ce} by employing the variational approach. Extending the work of [97], we study numerically the interactions of multiple coupled dark solitons as well as FA solutions in the absence of a magnetic trap. We also analyze the existence and stability of multiple FA solutions and coupled dark solitons in the presence of a trap to study the effects of the trapping strength on the existence and stability of the solutions. To confirm our stability findings, the numerical integrations are performed for both FA solutions and dark solitons.

The analysis of the existence, linear stability and time evolution of the nonlinear states in the spectrum of harmonically confined $(2+1)$-Dimensional uncoupled condensate was presented in [98]. In Chapter 5, we consider a two dimensional coupled system of Gross-Pitaevskii equations. Here, we assume that the condensates in each well have nearly pancake shapes and are coupled by the linear and nonlinear cross-phase modulation terms. We analyze the system in cases when the interatomic intreraction is either repulsive (defocusing) or attractive (focusing). We systematically study the ra-

dially symmetric nonlinear excitations and the interatomic interactions by converting our problem to polar coordinates. First, we consider the linear coupling to be zero and investigate the existence and linear stability of the ground and excited states in the absence and presence of an intrinsic topological charge. Secondly, we consider the nonlinear coupling zero and thirdly both linear and nonlinear coupling are nonzero and examine the dynamics of the nonlinear states of the coupled system. We also study the existence and stability of these states in the cases when two condensates have different values of the vorticity.

Finally, we summarise the work accomplished in this thesis in Chapter 6. We also suggest several intriguing and important problems for further study in the same chapter.

CHAPTER 3

Fluxon analogues and dark solitons in linearly coupled Bose-Einstein condensates

In Chapter 2, we have briefly discussed some characteristic of the solutions of the Gross-Pitaevskii (GP) equation such as bright and dark solitons. We also studied the stability of these solutions in the absence and presence of a harmonic trap. In this chapter we will study the defocusing coupled system of GP equations in the presence of the trap in the context of Bose-Einstein condensates (BECs).

3.1 Introduction

The concept of electron tunnelling between two superconductors separated by a thin insulating barrier predicted by Josephson [99] has been extended relatively recently to tunnelling of BECs across a potential barrier by Smerzi et al. [100–102]. Such tunnelling has been observed experimentally where a single [58, 103] and an array [104] of *short* Bose-Josephson junctions (BJJs) were realized. The dynamics of the phase difference between the wavefunctions of the condensates [80, 100–102, 105, 106] resembles that of point-like Josephson junctions [107].

Recently a proposal for the realization of a *long* BJJ has been presented by Kaurov and Kuklov [95, 96]. Similarly to superconducting long Josephson junctions, one may also look for an analogue of Josephson fluxons [108] in this case. It was shown in [95, 96] that fluxon analogues are given by coupled dark-soliton-like solutions, as the relative phase of the solutions has a kink shape with the topological phase difference equal to 2π. Moreover, it was emphasized that fluxon analogues (FA) can be spontaneously

formed from coupled dark solitons due to the presence of a critical coupling at which the two solitonic structures exchange their stability. The idea of FA solutions in tunnel-coupled BECs is then extended to rotational FA solutions in the ground state of rotating annular BECs confined in double-ring traps [109].

Experimentally a quasi one-dimensional BEC can be created in the so-called cigar-shaped magnetic trap, i.e. a three-dimensional parabolic trap confined in two directions and elongated in the other one. Two coupled cigar-shaped condensates can be made using a double-well potential along one of the confined directions. A sketch of the physical system is shown in Fig. 3.1. The parallel quasi one-dimensional BECs are linked effectively by a weak coupling k.

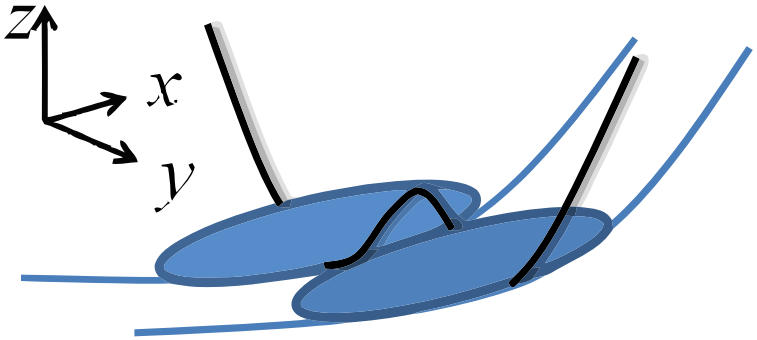

Figure 3.1: A sketch of the problem in the context of Bose-Einstein condensates, which are strongly confined in the $y-$ and $z-$direction and elongated along the $x-$direction.

Motivated by the possible experimental set-up, in this chapter we study the existence and the stability of the FA solutions in the presence of external potentials. The system can be modelled by the following normalized coupled Gross-Pitaevskii equations [95, 96] which are obtained by substituting $\psi_j = \Psi_j e^{-i\rho_0 \tilde{t}}$ into Eq. (2.7.3) and replacing $\tilde{t}$ by t and V' by V,

$$i\Psi_{j_t} = -\tfrac{1}{2}\Psi_{j_{xx}} + \mu|\Psi_j|^2\Psi_j - \rho_0\Psi_j - k\Psi_{3-j} + V\Psi_j, \tag{3.1.1}$$

where Ψ_j, $j = 1,2$, is the bosonic field, and t and x are time and axial coordinate, respectively. Here, we assume that the parallel quasi one-dimensional BECs are linked effectively by a weak coupling k. Note that herein we only consider $k > 0$. The case of $k < 0$ will only yield modulational instability of the background [110, 111]. V is the magnetic trap with strength Ω, i.e.

$$V(x) = \frac{1}{2}\Omega^2 x^2. \tag{3.1.2}$$

The total number of atoms in the two channels N is conserved, with

$$N = \int_{-\infty}^{+\infty} \sum_{j=1,2} |\Psi_j|^2 \, dx.$$

Different works have been done in similar settings as (3.1.1). Spontaneous symmetry breaking was analyzed in [112] when BECs are loaded in two parallel quasi-one-dimensional traps fitted with optical lattices. Before the experimental birth of BEC, the similar settings have been used in the study of stable defects in nonlinear patterns known as optical domain walls [113]. The investigation of the separation of two far separated domain walls along with their stability limits were considered in [114]. Recently, the studies were extended for the case when two components of BECs are coupled by both linear and nonlinear terms [115].

Extending the work [95, 96], which was without the magnetic trap, i.e. $\Omega \equiv 0$, in this chapter, we are particularly interested in the effects of $\Omega > 0$ to the localized excitations.

When the two condensates are uncoupled, i.e. $k = 0$, the dynamics of a dark soliton in BECs with magnetic trap has been considered before theoretically [116, 117] (see also [118] and references therein) and experimentally [34, 97, 119–121]. Interesting phenomena on the collective behavior of a quantum degenerate bosonic gas, such as soliton oscillations [97, 119, 120] and frequency shifts due to soliton collisions [121] were observed. A theoretical analysis based on variational formulation was developed in [35, 72] that is in good agreement with numerics as well as with experiments (see, e.g., [122, 123]). A similar variational method will be derived here to explain the dynamics of FA solutions.

3.2 Overview of the chapter

The present chapter is organized as follows. In the next section, we will give mathematical expressions for the FA and the coupled dark soliton solutions. In Section 3.4, we will solve the governing equations numerically and discuss the existence and stability of coupled dark soliton and FA solutions in the absence and presence of magnetic trap. In Section 3.5, we will find an analytical formula for the dependence of the critical coupling k_{ce} upon the velocity of the FA solution. Here, we will also solve the governing equations in moving coordinate frame and find numerically the values of k_{ce} corresponding to different values of velocity v of FA solution and hence will present a comparison between the numerical and the analytical results. In Section 3.6, we will derive a variational formulation for the FA solutions so that their dynamical behaviours can be studied analytically. Comparing the numerical and the analytical results, we show good agreement between them. We then briefly summarize the results of the chapter in the last section.

3.3 Fluxon analogues solution

A special solution in the study of long Josephson junction is the so-called Josephson vortex. The analogue of Josephson vortex in Eq. (3.1.1) when $V = 0$ is given by [95]

$$\Psi_1 = A\tanh(Bx) + iC\text{sech}(Bx) = \Psi_2^*, \tag{3.3.1}$$

where the parameters A, B and C are given as $A = \pm\sqrt{\frac{\rho_0+k}{\mu}}$, $B = 2\sqrt{k}$ and $C = \pm\sqrt{\frac{\rho_0-3k}{\mu}}$. In contrast to this solution, there exists a coupled dark soliton solution for which the value of parameter A is same as above while $B = \pm\sqrt{\rho_0+k}$.

Josephson vortices (JV) are vortices of supercurrent. Conventionally, JV are the soliton solutions of the non-linear sine-Gordon equation [124]. The investigation of non-linear wave theory can be done efficiently with the superconducting Josephson junction [107]. The Josephson vortex, also called fluxon, is of great significance in long Josephson junctions and has solitonic behavior. This robust and stable object can be controlled at high speed and used as a basic bit in information processing systems [95].

The soliton (3.3.1) can be regarded as an analogue of Josephson fluxons [95, 96] as the phase difference ϕ between the phases of Ψ_1 and Ψ_2 forms a spatial kink connecting $\phi = 0$ and $\phi = \pm 2\pi$ as shown in Fig. 3.2. In the following, solution (3.3.1) (and its continuations) will be referred to as FA solutions. From the expression, it is clear that an FA exists only for $0 < k < \rho_0/3$. For $k > \rho_0/3$, the solution in (3.3.1) transforms into dark soliton [95, 96] which exists for $k > -\rho_0$. Thus the FA and the dark soliton solutions coincide at $k = \rho_0/3$ and hence $k = \rho_0/3$ is the bifurcation point along the family of dark solitons. In the following, we denote this critical coupling as k_{ce}.

3.4 Numerical computations

In this section we will find the static coupled dark soliton and the FA solutions in the absence and presence of a magnetic trap and investigate their stability numerically.

3.4.1 Coupled one-dimensional GP equations with $k > 0$ and $V = 0$

We begin by considering the coupled system of GP equations with $V = 0$. In such a case our Eq. (3.1.1) reduces to

$$\begin{aligned} i\Psi_{1t} + \tfrac{1}{2}\Psi_{1xx} - \mu|\Psi_1|^2\Psi_1 + \rho_0\Psi_1 + k\Psi_2 = 0, \\ i\Psi_{2t} + \tfrac{1}{2}\Psi_{2xx} - \mu|\Psi_2|^2\Psi_2 + \rho_0\Psi_2 + k\Psi_1 = 0. \end{aligned} \tag{3.4.1}$$

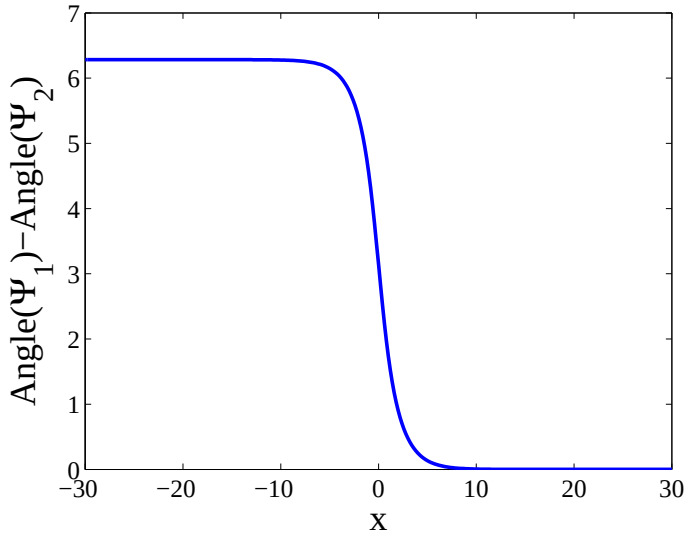

Figure 3.2: Spatial profile of the phase difference between Ψ_1 and Ψ_2 of FA solution for $k = 0.1$ forming a 2π-kink shape.

For the steady state solution, putting $\Psi_{1t} = 0 = \Psi_{2t}$ and then discretizing Ψ_{1xx} and Ψ_{2xx} in Eq. (3.4.1), we obtain a coupled system of nonlinear algebraic equations which can be solved using Newton's method with the Neumann boundary conditions $\Psi_{j,0} = \Psi_{j,1}$, $\Psi_{j,N+1} = \Psi_{j,N}$, $j = 1, 2$ to obtain numerically linearly coupled dark soliton solution shown in Fig. 3.3.

3.4.2 Stability of dark soliton in coupled one-dimensional GP equations

Assume first that $\Psi_1^{(0)}$ and $\Psi_2^{(0)}$ are the static solutions of Eq. (3.4.1). Then considering small perturbations of these solutions in the form

$$\Psi_1 = \Psi_1^{(0)}(x) + \epsilon[a_1(x)\, e^{i\lambda t} + b_1^*(x)\, e^{-i\lambda^* t}], \tag{3.4.2}$$

$$\Psi_2 = \Psi_2^{(0)}(x) + \epsilon[a_2(x)\, e^{i\lambda t} + b_2^*(x)\, e^{-i\lambda^* t}], \tag{3.4.3}$$

and substituting these values of Ψ_1 and Ψ_2 into Eq. (3.4.1), we obtain the following linearized equations

$$\frac{1}{2}a_{1xx} + \rho_0 a_1 - 2\mu|\Psi_1^{(0)}|^2 a_1 + k a_2 - \mu\left(\Psi_1^{(0)}\right)^2 b_1 = \lambda a_1, \tag{3.4.4}$$

$$\frac{1}{2}a_{2xx} + \rho_0 a_2 - 2\mu|\Psi_2^{(0)}|^2 a_2 + k a_1 - \mu\left(\Psi_2^{(0)}\right)^2 b_2 = \lambda a_2, \tag{3.4.5}$$

$$-\frac{1}{2}b_{1xx} - \rho_0 b_1 + 2\mu|\Psi_1^{(0)}|^2 b_1 - k b_2 + \mu\left(\Psi_1^{(0)*}\right)^2 a_1 = \lambda b_1, \tag{3.4.6}$$

$$-\frac{1}{2}b_{2xx} - \rho_0 b_2 + 2\mu|\Psi_2^{(0)}|^2 b_2 - k b_1 + \mu\left(\Psi_2^{(0)*}\right)^2 a_2 = \lambda b_2. \tag{3.4.7}$$

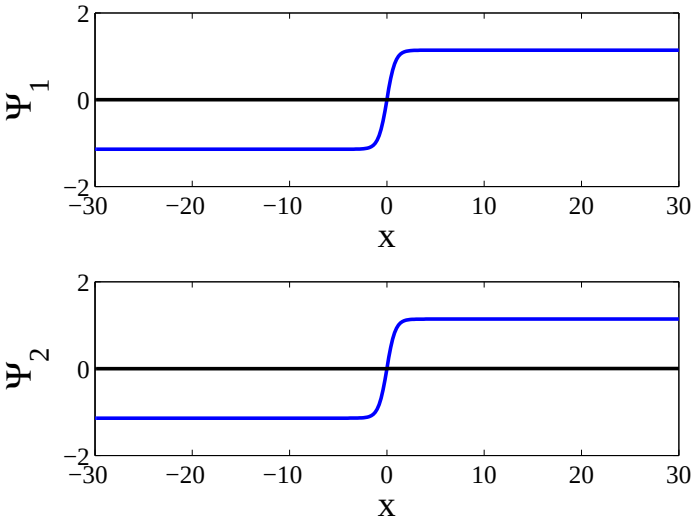

Figure 3.3: Numerical solution of two coupled one-dimensional GP equations for $\mu = 1$, $\rho_0 = 1$, $k = 0.3$, $\Delta x = 0.2$. The blue curves represent the real parts and the black horizontal lines represent the imaginary parts of the solution.

The above system of Eq. (3.4.4), Eq. (3.4.5), Eq. (3.4.6) and Eq. (3.4.7) describes a linear eigenvalue problem. Discretizing this system of equations and using the Neumann boundary conditions $a_{j,0} = a_{j,1}$, $a_{j,N+1} = a_{j,N}$, $b_{j,0} = b_{j,1}$, $b_{j,N+1} = b_{j,N}$, where j=1,2, the system can be written in matrix form.

We find the eigenvalues of the stability matrix in the complex plane for the solution depicted in Fig. 3.3 and is shown in Fig. 3.4. Here, we have set $\rho_0 = 1$. Because there is at least one pair of eigenvalues with nonzero imaginary parts, we conclude that the solitons are unstable. We have calculated the stability of dark solitons for different values of coupling constant k. The magnitude of the most unstable eigenvalues increases with k up to $k = 0.2$ and then decreases and ultimately becomes zero for $k \geq 1/3$. This shows that the coupled dark solitons solution is stable for $k \geq 1/3$ as shown in Fig. 3.5. We also investigate the stability of coupled dark soliton in its domain of existence for negative values of k. The dark soliton is found to be unstable for all negative values of k.

To verify the above results, we solve Eq. (3.4.1) using Runge-Kutta method of order 4. The time evolution of the coupled dark soliton in Fig. 3.3 for $k = 0.1$ is shown in Fig. 3.6. One can see that when $t \approx 40$, energy releases in the form of radiation due to the instability of solitons. Here, the energy splits into three parts. Some part of energy goes to the right, some towards left and the remaining goes straight. The time dynamics of the solution for different values of time is shown in Fig. 3.7.

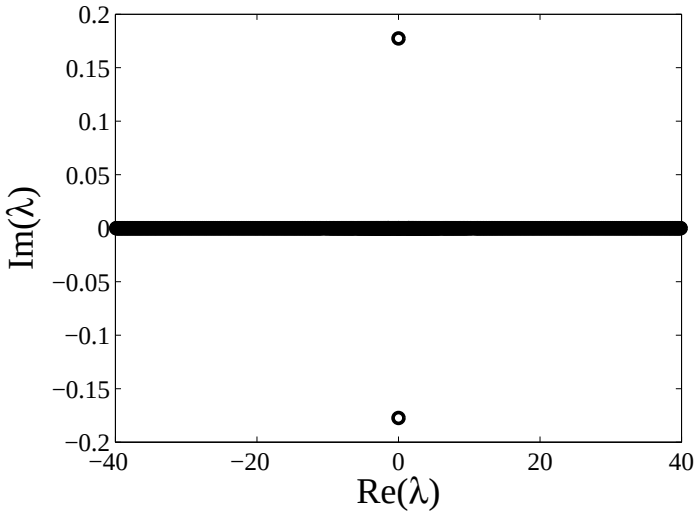

Figure 3.4: The eigenvalues λ of the solution in Fig. 3.3 in the complex plane showing the instability of the solution.

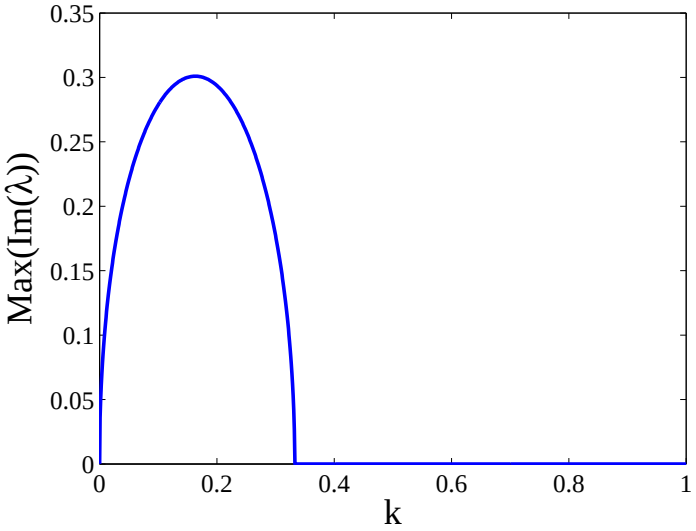

Figure 3.5: The critical eigenvalue of coupled dark solitons shown in Fig. 3.3 as a function of k.

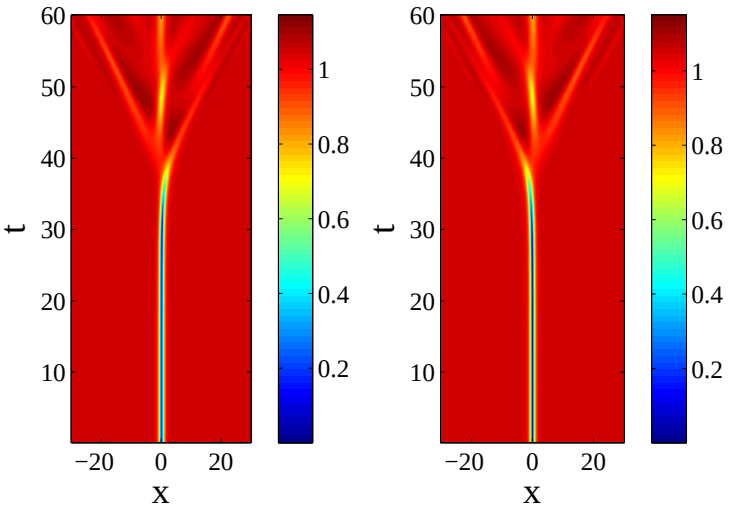

Figure 3.6: An evolution of the unstable coupled dark solitons shown in Fig. 3.3. The left panel corresponds to $|\Psi_1|$ and right panel to $|\Psi_2|$.

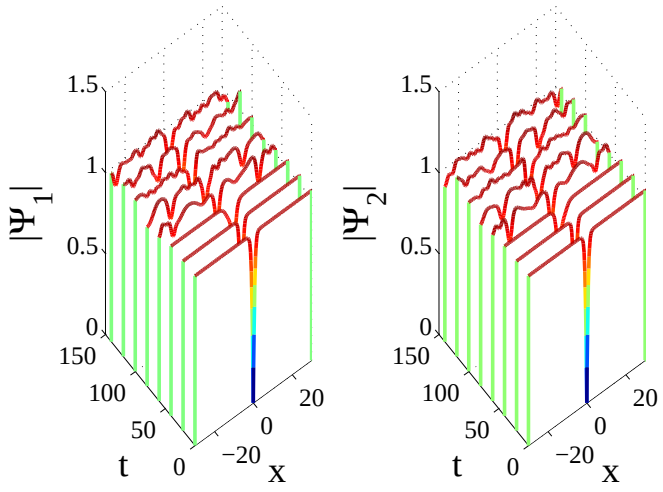

Figure 3.7: Time evolution of the unstable coupled dark solitons shown in Fig. 3.3 for few particular values of time.

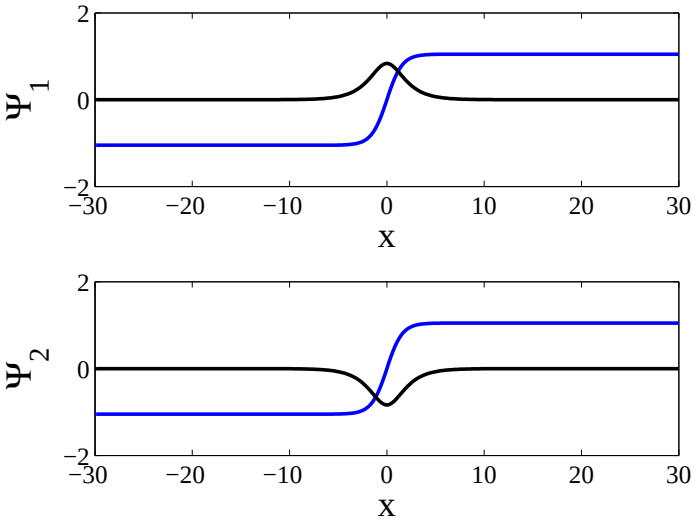

Figure 3.8: A numerically obtained FA for $\rho_0 = 1$, $\mu = 1$, and $k = 0.1$. The blue curves represent the real parts while the black curves are the imaginary parts of Ψ_1 and Ψ_2, respectively.

3.4.3 Existence of fluxon analogues solution

According to Kaurov and Kuklov [95], in the instability region of coupled dark soliton one can obtain an FA. The numerically obtained FA solution is shown in Fig. 3.8 which is the same solution given in Eq. (3.3.1). We observe that the amplitude of the real parts of the FA solution increases with k. However, the amplitude of the imaginary parts of FA solution decreases with k. As k approaches $1/3$, the amplitude of the humps in the imaginary parts tends to zero and the FA solution changes into a coupled dark solitons solution. This shows that the FA solution exists for $k < 1/3$ and at $k = k_{ce} = 1/3$, it transforms into a coupled dark solitons solution, where k_{ce} represents the critical value of existence of the solution. The transformation of FA into a coupled dark solitons can be comprehended as a pitchfork bifurcation as shown in Fig. 3.9.

3.4.4 Stability of fluxon analogues solution

Following the same procedure as the stability of coupled dark solitons, we investigate the stability of FA solution. The eigenvalues of the stability matrix for the FA solution are shown in Fig. 3.10. This shows that the FA solution is stable for $k = 0.1$. We observe that the FA solution indeed remains stable for those values of k where it exists. We also note that in Fig. 3.6, a grey-soliton-like structure in the centre at the end of the computation is an FA, as the profile of the phase difference between Ψ_1 and Ψ_2 forms

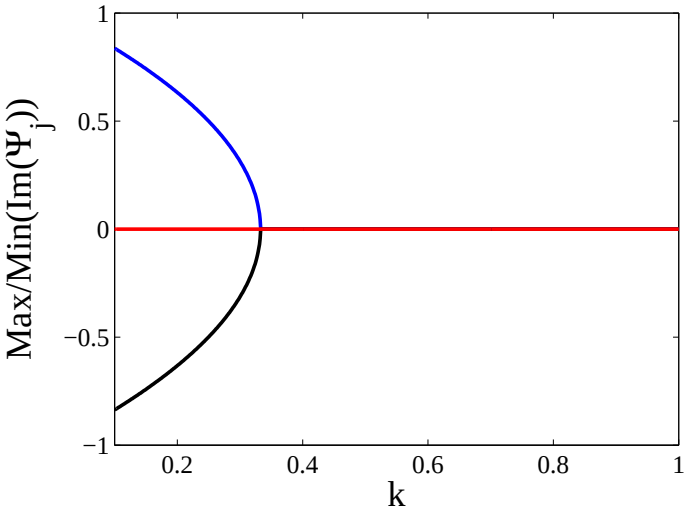

Figure 3.9: The hump amplitude of the imaginary parts of FA solution shown in Fig. 3.8 against k. The graph depicts the region of existence of FA solution. The blue and black curves correspond to the imaginary parts of Ψ_1 and Ψ_2 while the red line in the middle is for the coupled dark solitons.

a 2π-kink shape as depicted in Fig. 3.2. Nonetheless, it is important to note that it is not always the case. When the coupling constant is too small, instead of yielding FA solutions, the dark solitons repel and move away from each other as shown in Fig. 3.11. Hence, coupled dark solitons transform into FA solutions if the coupling is in an intermediate region.

3.4.5 Coupled BECs with a trap: $V \neq 0$

Next, we consider the existence and stability of FA solution in the presence of a harmonic trap, i.e. $\Omega \neq 0$. Two FA solutions for two different values of coupling constant k are shown in Fig. 3.12 and Fig. 3.13 with $\Omega = 0.1$. The value of Ω corresponds to the width of the trap. First we take $\Omega = 0.05$ which means that the width of the trap is large. Then we decrease the width of the trap by increasing the value of Ω. We consider $\Omega = 0.1, 0.15$ and 0.2 and find the FA solution for each mentioned value of Ω. It is found that the critical values k_{ce} where FA solution transforms into a dark soliton for $\Omega = 0.05, 0.1, 0.15, 0.2$ are $0.333, 0.334, 0.336, 0.337$ respectively. These values show that the critical coupling k_{ce} above which FA solutions do not exist is almost independent of the trapping parameter Ω, which is reasonable as the width of the non-zero imaginary part of the FA solution is small compared to the width of the trapping parameter Ω when $k \to k_{ce}$. The coupled dark soliton for a specific value of Ω is shown in Fig. 3.14.

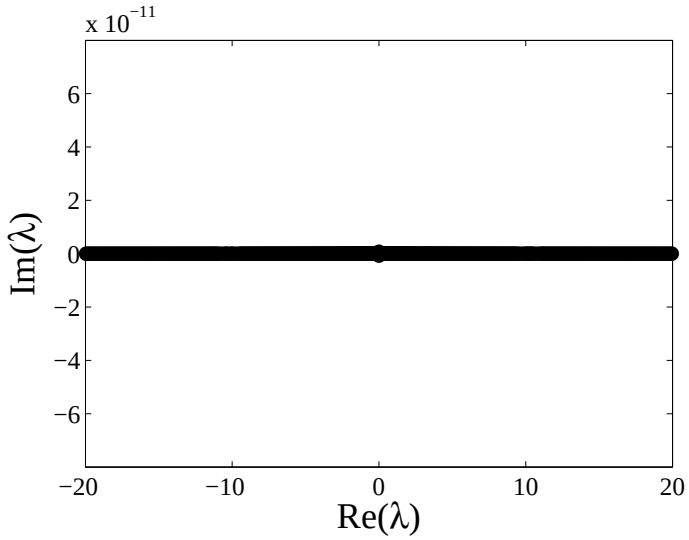

Figure 3.10: The eigenvalues distribution of the FA for $k = 0.1$ in the complex plane showing the stability of the solution.

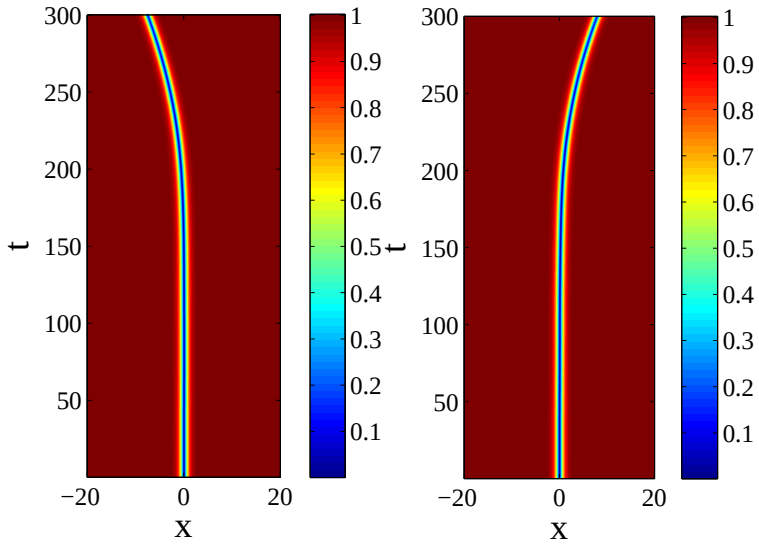

Figure 3.11: Time dynamics of the coupled dark solitons when the coupling between them is very small and the two coupled dark solitons repel each other. The left panel corresponds to $|\Psi_1|$ and right panel to $|\Psi_2|$. Here, $k = 0.001$.

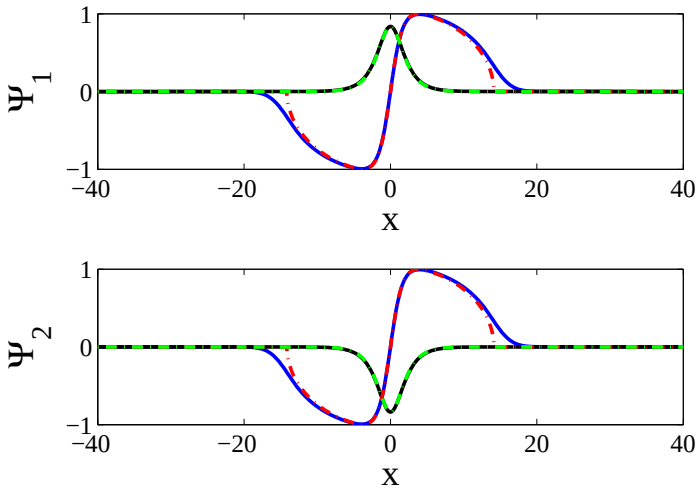

Figure 3.12: A numerically obtained FA solution for $\Omega = 0.1$, $\rho_0 = 1$, $\mu = 1$ and $k = 0.1$. The blue solid curves represent the real parts and the black solid curves are the imaginary parts of the FA solution. The dash-dotted curves are approximations (see Section 3.6, Eq. (3.6.1)).

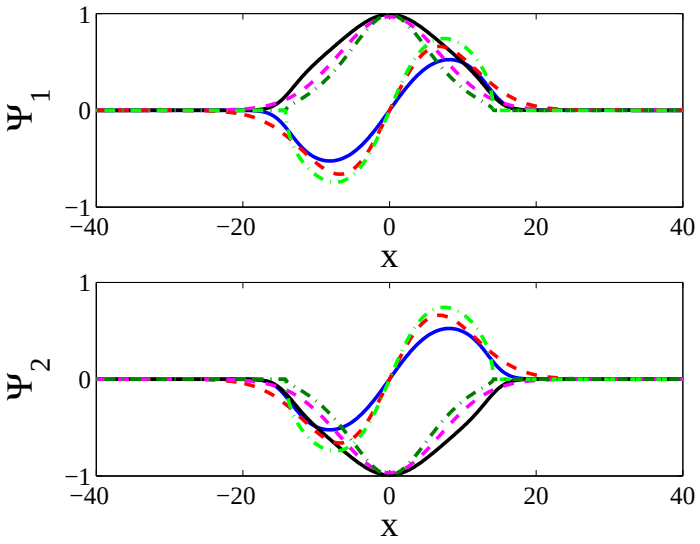

Figure 3.13: A numerically obtained FA solution for the same parameter values as in Fig. 3.12 but $k = 0.008$. The blue solid curves represent the real parts and the black solid curves are the imaginary parts of the FA solution. The dash-dotted curves and the dashed curves are two approximations obtained through different approaches (see Section 3.6, Eqs. (3.6.1) and (3.6.19) respectively).

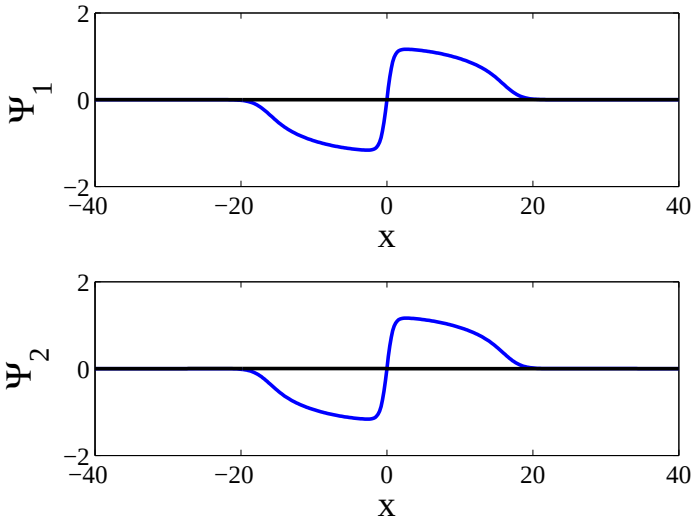

Figure 3.14: A numerically obtained coupled dark soliton for $\Omega = 0.1$, $\rho_0 = 1$, $\mu = 1$ and $k = 0.4$. The blue curves represent the real parts and the black horizontal lines are the imaginary parts of the solitons.

Now we investigate the stability of FA solution by finding the eigenvalues of the stability matrix. In Fig. 3.15, we present the eigenvalues of the FA solutions shown in Fig. 3.12 and Fig. 3.13. It can be easily seen in both panels that a pair of eigenvalues is not on the horizontal axis and hence the solitons are found to be unstable. The finding that the FA solutions above are unstable suggests to us to investigate whether FA solutions are always unstable for nonzero Ω. The result is summarized in Fig. 3.16. Shown in solid curves are the first few lowest squared eigenvalues as a function of k for $\Omega = 0.1$. As stability corresponds to $\lambda^2 > 0$, the figure shows that there is a critical value k_{cs} above which FA solutions are stable, which for the parameter value above is approximately 0.145. A spectrum of eigenvalues for $\Omega = 0.1$ and $k = 0.2$ is depicted in Fig. 3.17. The figure shows that the imaginary part of each eigenvalue is zero and all eigenvalues are lying on the horizontal axis. This underscores that the FA solution is stable for $\Omega = 0.1$ and $k = 0.2$. To find out the stability region of k for the FA solutions corresponding to different values of Ω, we plot k versus the maximum imaginary part of eigenvalues. The stability curves for different values of Ω are presented in Fig. 3.18. This shows that the critical value k_{cs} increases slightly with Ω. The reason for this little increase in k_{cs} is due to the tiny increase in the value of k_{ce} with Ω. We also note that k_{cs} decreases with Ω. As $\Omega \to 0$, $k_{cs} \to 0$ and the untrapped FA solution becomes stable for all values of the coupling constant where it exists.

We then perform the time dynamics of the unstable FA in Fig. 3.12. Shown in the upper

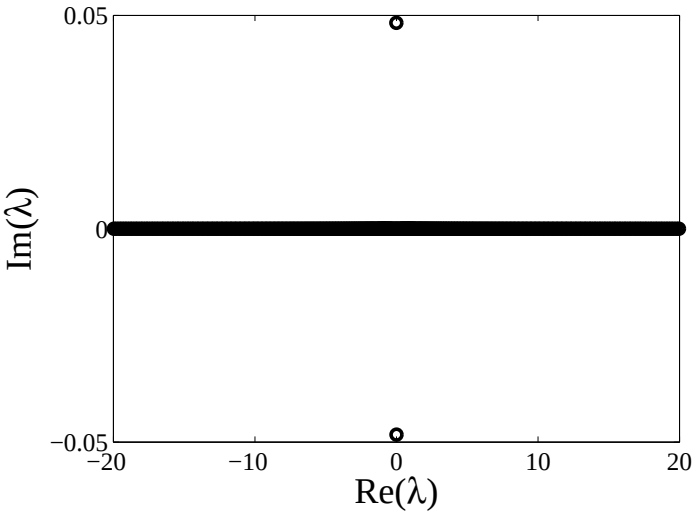

(a)

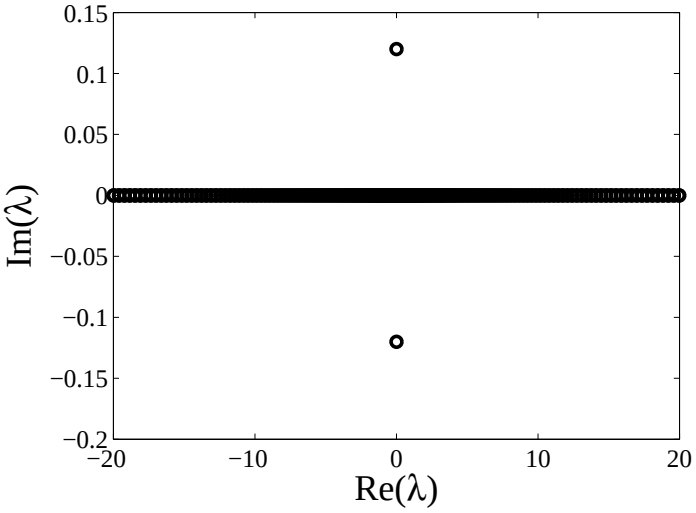

(b)

Figure 3.15: Eigenvalues structures for the FA solutions shown in Fig. 3.12 and Fig. 3.13 respectively. A pair of eigenvalues in both panels is lying on the vertical axis showing the instability of the solutions.

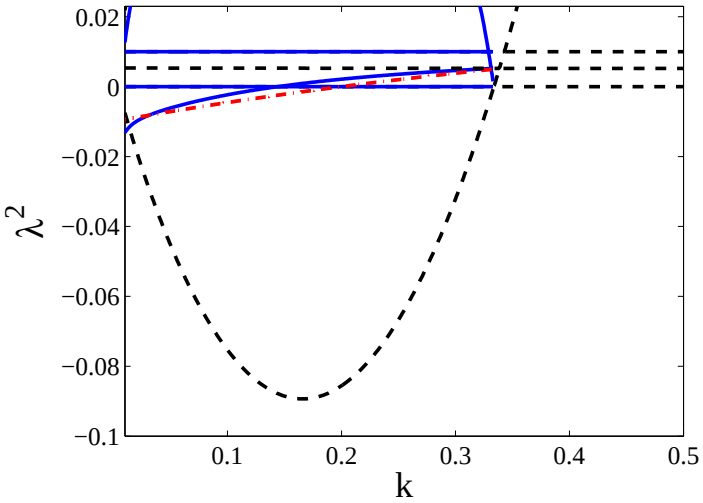

Figure 3.16: The first few lowest squared eigenvalues of FA (solid) and dark solitons (dashed) as a function of k for $\Omega = 0.1$. The dash-dotted curve represents the approximation (3.6.17).

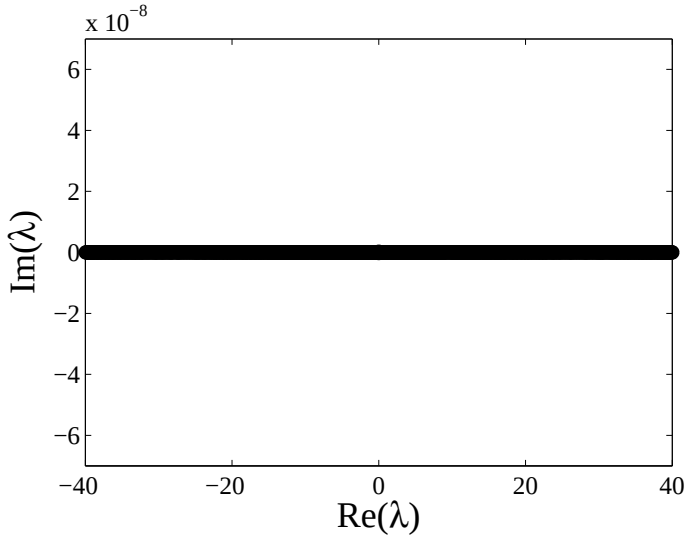

Figure 3.17: Eigenvalues structure showing the stability of the FA solution for $\Omega = 0.1$ and $k = 0.2$.

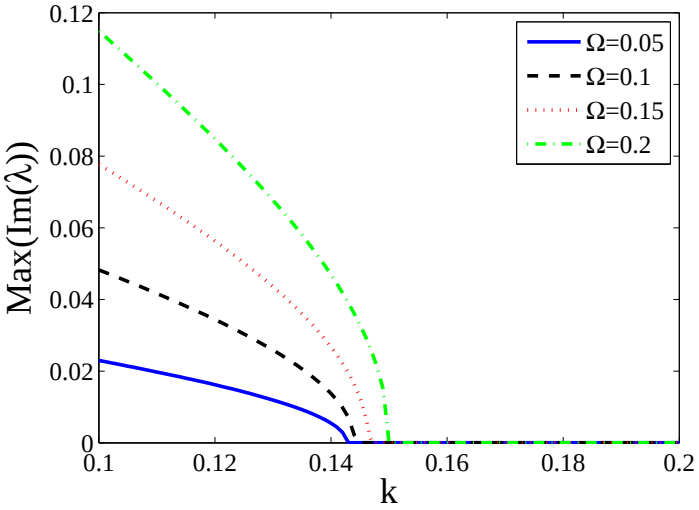

Figure 3.18: Stability curves for FA solutions corresponding to $\Omega = 0.05, 0.1, 0.15, 0.2$. For each value of Ω, there is a little change in the value of k_{cs}.

panel of Fig. 3.19 is the typical evolution of unstable FA, where one can see that the instability causes the solitons to oscillate about the minimum of the trap non-sinusoidally. Hence, despite the instability, the FA still persists. This result rather applies generally to other values of coupling constants where FA solutions are unstable. The numerical evolution of the phase difference for $k = 0.1$ is shown in the lower panel of Fig. 3.19. Clearly the phase difference varies from -2π to 0 which indicates the existence of FA.

We have also studied the existence and the stability of dark solitons. Shown as dashed lines in Fig. 3.16 are the first few lowest squared eigenvalues of coupled dark solitons, where similarly as before for k less than the critical coupling k_{ce} coupled dark solitons may transform into an FA as shown in Fig. 3.20.

3.5 Travelling FA solutions and the velocity dependence of the critical coupling k_{ce}

Because solitons of Eq. (3.1.1) without a trap are translationally invariant, they can move freely in space. This motivates us to study the existence and stability of moving solitons.

When FA solutions do not travel, it has been discussed above that $k_{ce} = 1/3$. When the solitons move with velocity v, it is natural to expect that the domain of existence of FA solutions will depend on v, i.e. $k_{ce} = k_{ce}(v)$. It is because dark solitons only exist for $v < 1$ [72], while at k_{ce} FA solutions become dark solitons. In the following, we

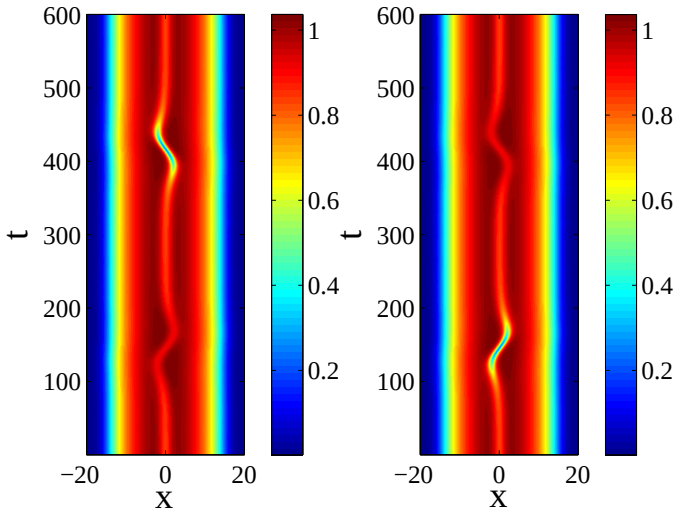

(a)

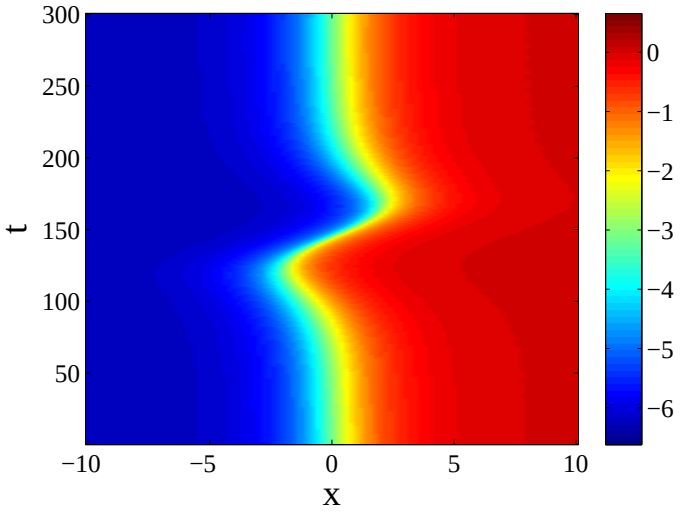

(b)

Figure 3.19: The upper panel shows a numerical evolution of the FA in Fig. 3.12 for $\Omega = 0.1$ and $k = 0.1$. The lower panel shows a numerical evolution of the phase difference for the same parameter values above. The phase changes from -2π to 0 and shows the presence of FA solution.

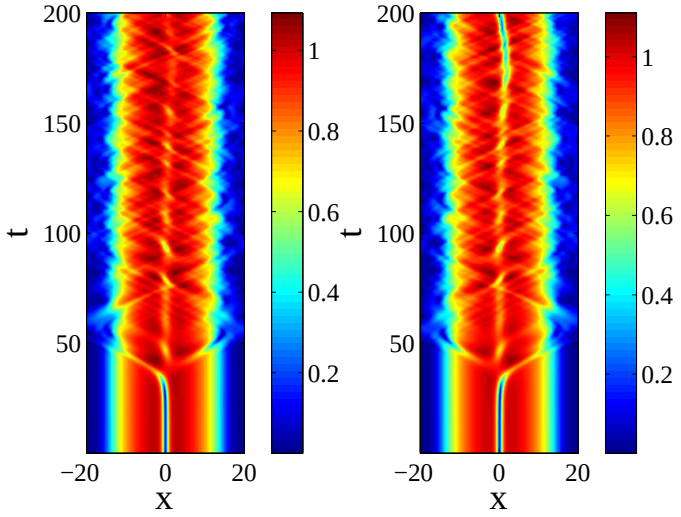

Figure 3.20: A numerical evolution of coupled dark solitons for $\Omega = 0.1$ and $k = 0.1$.

are interested in the expression of the critical coupling. We will determine the velocity dependence of k_{ce} analytically.

For simplicity, first we scale the governing Eq. (3.1.1) such that the nonlinearity coefficient and the chemical potential become $\mu = \rho_0 = 1$. We also scale the wavefunction Ψ_j, where j=1,2, by $\psi_j = \Psi_j/\sqrt{1+k}$, such that the Eq. (3.1.1) become

$$i\psi_{1\tilde{t}} + \frac{1}{2}\psi_{1\tilde{x}\tilde{x}} - |\psi_1|^2\psi_1 + \frac{\psi_1 + k\psi_2}{1+k} = \frac{V\psi_1}{1+k}, \tag{3.5.1}$$

$$i\psi_{2\tilde{t}} + \frac{1}{2}\psi_{2\tilde{x}\tilde{x}} - |\psi_2|^2\psi_2 + \frac{\psi_2 + k\psi_1}{1+k} = \frac{V\psi_2}{1+k}. \tag{3.5.2}$$

where $\tilde{t} = (1+k)t$ and $\tilde{x} = (\sqrt{1+k}x)$.

Defining $\xi = \tilde{x} - \tilde{v}\tilde{t}$, Eq. (3.5.1) and Eq. (3.5.2) with $V = 0$ in a moving coordinate frame can be written as

$$i\psi_{1\tilde{t}} - i\tilde{v}\psi_{1\xi} + \frac{1}{2}\psi_{1\xi\xi} - |\psi_1|^2\psi_1 + \frac{\psi_1 + k\psi_2}{1+k} = 0, \tag{3.5.3}$$

$$i\psi_{2\tilde{t}} - i\tilde{v}\psi_{2\xi} + \frac{1}{2}\psi_{2\xi\xi} - |\psi_2|^2\psi_2 + \frac{\psi_2 + k\psi_1}{1+k} = 0. \tag{3.5.4}$$

When $\psi_1 = \psi_2 = \psi$, the above system of equations has an explicit solution for the travelling dark soliton

$$\psi_{ds} = A\tanh(B\xi) + i\tilde{v}, \tag{3.5.5}$$

with $A = B$ and $A^2 + \tilde{v}^2 = 1$.

Let us perturb ψ_{ds} such that $\psi_1 = \psi_{ds} + \epsilon f(\xi)$ and $\psi_2 = \psi_{ds} - \epsilon f(\xi)$, where $\epsilon \ll 1$. Substituting these values of ψ_1 and ψ_2 into Eq. (3.5.3) and Eq. (3.5.4) and retaining

linear terms in ϵ only, we obtain

$$-\frac{1}{2}\frac{d^2 f(\tilde{\xi})}{d\tilde{\xi}^2}+\left[2(A^2\tanh^2(B\tilde{\xi})+\tilde{v}^2)+\frac{k-1}{k+1}\right]f(\tilde{\xi})$$
$$+\left[A^2\tanh^2(B\tilde{\xi})-\tilde{v}^2\right]f^*(\tilde{\xi})+i\tilde{v}\left[2A\tanh(B\tilde{\xi})f^*(\tilde{\xi})+\frac{df(\tilde{\xi})}{d\tilde{\xi}}\right]=0. \tag{3.5.6}$$

Choosing

$$f(\tilde{\xi})=p\,\mathrm{sech}(B\tilde{\xi})\tanh(B\tilde{\xi})+i\,q\,\mathrm{sech}(B\tilde{\xi}), \tag{3.5.7}$$

where p and q are real, and substitute it in the last equation above, we obtain the following two equations containing p and q,

$$\left[5A^2+2\tilde{v}^2+2\frac{k-1}{k+1}\right]p+6A\tilde{v}q=0 \tag{3.5.8}$$

$$2A\tilde{v}p+\left[A^2+6\tilde{v}^2+2\frac{k-1}{k+1}\right]q=0. \tag{3.5.9}$$

The matrix of coefficients of p and q of the above system of equations is

$$A=\begin{bmatrix}5A^2+2\tilde{v}^2+2\frac{k-1}{k+1} & 6A\tilde{v}\\ 2A\tilde{v} & A^2+6\tilde{v}^2+2\frac{k-1}{k+1}\end{bmatrix}.$$

The system will have a non-trivial solution if $det(A)=0$ that yields the following relation between k and v:

$$k=-\frac{1}{3}v^2-\frac{1}{21}+\frac{4}{21}\sqrt{7v^4-7v^2+4}, \tag{3.5.10}$$

where we have substituted $v=\sqrt{1+k}\tilde{v}$. Here, v is the velocity measured in the 'original' time t, while $\tilde{v}$ is in the scaled time $\tilde{t}$. The coupling constant k here is the critical coupling k_{ce}, which is clearly a function of v. Note from the above expression that $k_{ce}\to\frac{1}{3}$ as $v\to 0$ and $k_{ce}\to 0$ as $v\to 1$.

Next, we calculate the existence and stability of moving FA solutions and moving dark solitons numerically. We present in Fig. 3.21 an FA travelling with $v=0.2$ for $k=0.1$. One can see the deformation in the shape of the soliton due to the nonzero value of v. The shape of the deformation suggests the correction ansatz (3.5.7). For a fixed v, if the coupling constant is increased further, the FA changes into coupled dark solitons at a critical value $k_{ce}<1/3$. We recorded the critical values k_{ce} for different values of velocity v. The plot of k_{ce} as a function of v is shown in Fig. 3.22 as filled circles. The solid curve in the same figure is the graph of Eq. (3.5.10), where we obtain perfect agreement.

After examining the existence of the solitons, next we study their stability. We have calculated the stability of FA solutions for several values of k and found that the FA

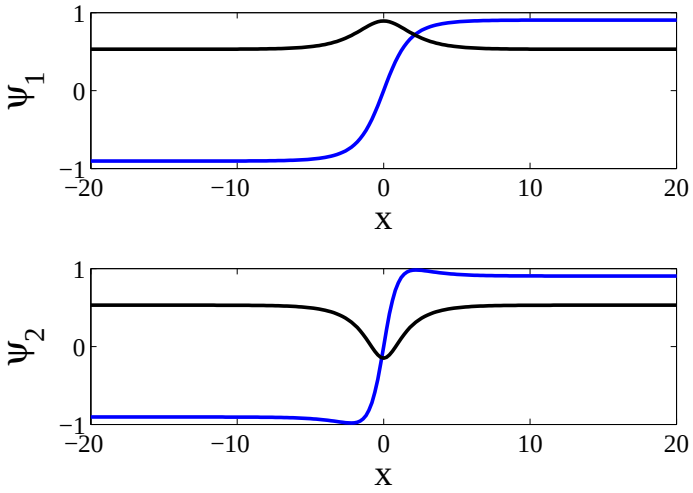

Figure 3.21: A numerically obtained FA for $v = 0.2$ and $k = 0.1$.

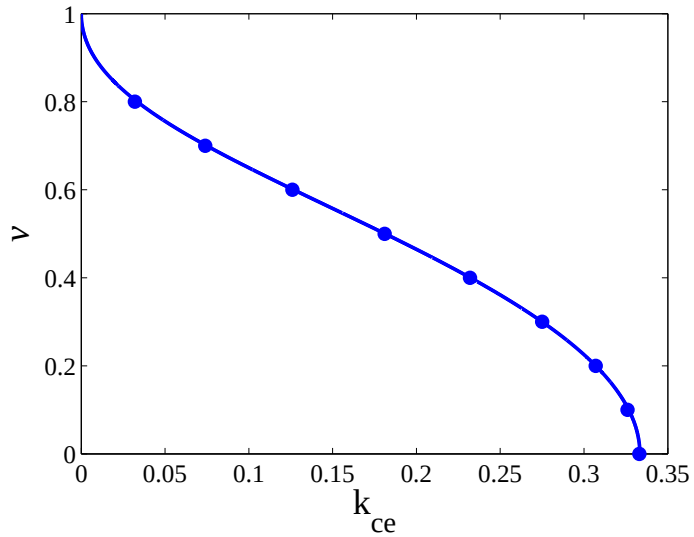

Figure 3.22: The critical coupling constant k_{ce} as a function of the velocity v for the existence of travelling FA. Filled circles are numerical data and the solid line is the function in Eq. (3.5.10). FA only exists on the left of the solid curve.

solutions are always stable in their existence domain. Extending the calculation to coupled dark solitons, we found that they are unstable for the values of the coupling constant $k < k_{ce}$ corresponding to each value of the velocity v. For the values of $k \geq k_{ce}$, the dark soliton becomes stable. The Runge-Kutta method of order 4 has been used to verify the time dynamics of the FA solutions as well as dark solitons. The typical time evolution of the coupled dark soliton solution when it is unstable is depicted in the upper panel of Fig. 3.23. The lower panel of Fig. 3.23 shows the time evolution of the stable FA solution.

3.6 Variational formulations of the FA solutions

Here, we will derive theoretical approximations to the numerical existence and stability results reported above using variational methods. The Lagrangian formalism for the FA solutions will be separated into two cases, i.e. when the coupling constant k is close to the critical coupling k_{ce} at which the FA solutions are close to coupled dark solitons and when it is close to the uncoupled limit $k \approx 0$. The two cases determine the ansatz that will be taken to approximate the solutions.

3.6.1 The case $k \sim k_{ce}$ and $V \neq 0$

When there is a harmonic potential, the dynamics of the solutions will be determined perturbatively. We will particularly follow the method of [72, 122, 123], which was developed for dark solitons, to our case. A similar calculation will be performed to discuss the dynamics and stability of FA solutions in the limit of k close to k_{ce} as in that case the real part, i.e. the dark soliton component, is dominant and C_1, $C_2 \approx 0$.

Due to the presence of the magnetic trap, which is assumed to be slowly varying, i.e. $\Omega^2 \ll 1$, we take the ansatz

$$\Psi_j = \Psi_{TF}\Phi_j, \tag{3.6.1}$$

where Ψ_{TF} is the Thomas-Fermi cloud approximately given by

$$\Psi_{TF} = \sqrt{\max\{(1 - V/(1+k)), 0\}}. \tag{3.6.2}$$

and

$$\Phi_j \;\; = \;\; A\tanh(z) + i\left(C_j \mathrm{sech}(z) + \tilde{v}\right),\; j = 1, 2, \tag{3.6.3}$$

where $z = B(\tilde{x} - x_0)$. The parameters A, B, C, x_0 are in general functions of $\tilde{t}$. Here, $A^2 + \tilde{v}^2 = 1$. When $C_j \equiv 0$, one can recognise that the above function is the usual

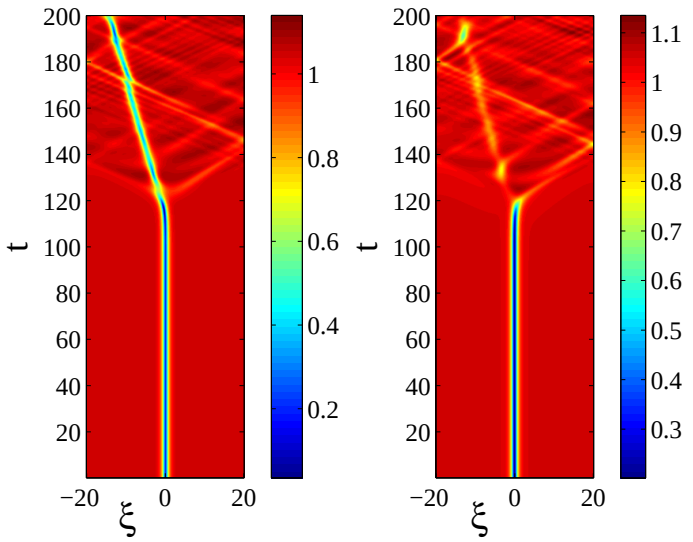

(a)

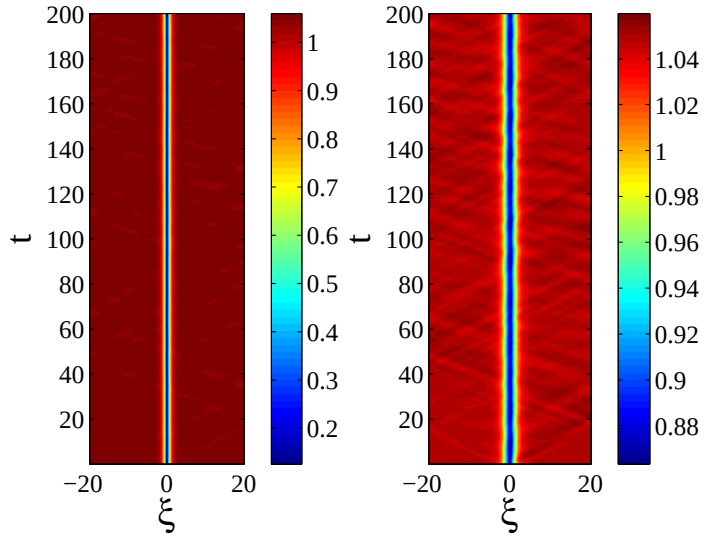

(b)

Figure 3.23: Time dynamics of the travelling coupled dark solitons and the travelling FA for the parameter values $k = 0.1$ and $v = 0.2$. The upper panel shows the instability of the coupled dark solitons and the lower panel depicts the stability of travelling FA solution.

ansatz to describe a dark soliton travelling with the velocity $\tilde{v}$, where in that case the parameters A, B, $\tilde{v}$ and x_0 can be conveniently written as $A = B = \cos\varphi$, $\tilde{v} = \sin\varphi$, and $x_0(\tilde{t}) = \int_0^{\tilde{t}} \sin\varphi(t')\,dt'$ [122].

Note the similarity of Eq. (3.6.1) with the ansatz $\Psi_j = \Psi_{TF}\psi_{ds}$ [122, 123] used to study the dynamics of dark solitons in a harmonic potential. Differentiating the ansatz (3.6.1) with respect to $\tilde{t}$ and $\tilde{x}$, we obtain

$$\begin{aligned}
\Psi_{j\tilde{t}} &= \Psi_{TF}\Phi_{j\tilde{t}}, \\
\Psi_{j\tilde{x}\tilde{x}} &= \frac{-\Phi_j {V_{\tilde{x}}}^2}{4\left(1+k\right)^2\left(1-\frac{V}{1+k}\right)^{3/2}} - \frac{\Phi_{j\tilde{x}}V_{\tilde{x}}}{\left(1+k\right)\sqrt{1-\frac{V}{1+k}}} - \frac{\Phi_j V_{\tilde{x}\tilde{x}}}{2\left(1+k\right)\sqrt{1-\frac{V}{1+k}}} \\
&+ \sqrt{1-\frac{V}{1+k}}\Phi_{j\tilde{x}\tilde{x}}.
\end{aligned}$$

Substituting the ansatz (3.6.1) and its spatial and temporal derivatives into Eq. (3.5.1) and Eq. (3.5.2), we obtain

$$\begin{aligned}
&i\sqrt{1-\frac{V}{1+k}}\Phi_{j\tilde{t}} + \frac{1}{2}\left[\frac{-\Phi_j {V_{\tilde{x}}}^2}{4\left(1+k\right)^2\left(1-\frac{V}{1+k}\right)^{3/2}} - \frac{\Phi_{j\tilde{x}}V_{\tilde{x}}}{\left(1+k\right)\sqrt{1-\frac{V}{1+k}}}\right. \\
&\left. - \frac{\Phi_j V_{\tilde{x}\tilde{x}}}{2\left(1+k\right)\sqrt{1-\frac{V}{1+k}}} + \sqrt{1-\frac{V}{1+k}}\Phi_{j\tilde{x}\tilde{x}}\right] - \left(1-\frac{V}{1+k}\right)^{3/2}|\Phi_j|^2\Phi_j \\
&+ \frac{\sqrt{1-\frac{V}{1+k}}\left(\Phi_j + k\Phi_{3-j}\right)}{1+k} = \frac{V\Phi_j\sqrt{1-\frac{V}{1+k}}}{1+k}.
\end{aligned}$$

Dividing both sides by $\sqrt{1-\frac{V}{1+k}}$, we obtain

$$\begin{aligned}
&i\Phi_{j\tilde{t}} - \frac{\Phi_j {V_{\tilde{x}}}^2}{8\left(1+k\right)^2\left(1-\frac{V}{1+k}\right)^2} - \frac{\Phi_{j\tilde{x}}V_{\tilde{x}}}{2\left(1+k\right)\left(1-\frac{V}{1+k}\right)} - \frac{\Phi_j V_{\tilde{x}\tilde{x}}}{4\left(1+k\right)\left(1-\frac{V}{1+k}\right)} \\
&+ \frac{1}{2}\Phi_{j\tilde{x}\tilde{x}} - \left(1-\frac{V}{1+k}\right)|\Phi_j|^2\Phi_j + \frac{\left(\Phi_j + k\Phi_{3-j}\right)}{1+k} = \frac{V\Phi_j}{1+k}.
\end{aligned}$$

Using the Taylor series expansion of $\frac{1}{1-\frac{V}{1+k}}$ and retaining only terms linear in V, $V_{\tilde{x}}$ and $V_{\tilde{x}\tilde{x}}$ due to smallness of trapping parameter, we obtain

$$i\Phi_{j\tilde{t}} + \frac{1}{2}\Phi_{j\tilde{x}\tilde{x}} - |\Phi_j|^2\Phi_j + \frac{\Phi_j + k\Phi_{3-j}}{1+k} \approx R(\Phi_j), \tag{3.6.4}$$

where

$$R(\Phi_j) = \frac{1}{(1+k)}\left[\left(1-|\Phi_j|^2\right)V\Phi_j + \frac{1}{2}V_{\tilde{x}}\Phi_{j_{\tilde{x}}} + \frac{1}{4}\Phi_j V_{\tilde{x}\tilde{x}}\right].$$

When there is no magnetic trap, (3.6.4) with $V \equiv 0$ can be derived from the Lagrangian

$$\begin{aligned}
\mathcal{L} &= \int_{-\infty}^{\infty}\frac{1}{2}\sum_{j=1}^{2} i\left(\Phi_j^*\Phi_{j_{\tilde{t}}} - \Phi_j\Phi_{j\,\tilde{t}}^*\right)\left(1-\frac{1}{|\Phi_j|^2}\right) - |\Phi_{j_{\tilde{x}}}|^2 - \left(|\Phi_j|^4 - 1\right) \\
&+2\frac{|\Phi_j|^2 + k\Phi_j\Phi_{3-j}^* - (1+k)}{1+k}\,d\tilde{x}.
\end{aligned} \tag{3.6.5}$$

It is not clear how to evaluate the first term of the integral (3.6.5) due to the presence of nonzero C_j in the denominator of $\left(1-1/|\Phi_j|^2\right)$. Because of that, in the following we assume C_j to be small, i.e. we consider the case of $k \sim k_{ce}$, and take the series expansion with respect to C_j about $C_j = 0$ upto $\mathcal{O}(C_j^5)$. The integral of the first term of the Lagrangian density is

$$\int_{-\infty}^{\infty} \frac{1}{2} \sum_{j=1}^{2} i \left(\Phi_j^* \Phi_{j\tilde{t}} - \Phi_j \Phi_{j\tilde{t}}^*\right) \left(1 - \frac{1}{|\Phi_j|^2}\right) d\tilde{x} = x_{0\tilde{t}} \left[4 \arctan\left(\frac{A}{\tilde{v}}\right) - 4A\tilde{v} - \pi A C_3\right]. \tag{3.6.6}$$

The integral of the second term yields

$$\int_{-\infty}^{\infty} \frac{1}{2} \sum_{j=1}^{2} |\Phi_{j\tilde{x}}|^2 \, d\tilde{x} = \frac{B}{3}\left[4A^2 + C_4\right]. \tag{3.6.7}$$

The integral of the third term leads to

$$\begin{aligned} \int_{-\infty}^{\infty} \frac{1}{2} \sum_{j=1}^{2} \left(|\Phi_j|^4 - 1\right) d\tilde{x} &= \frac{1}{3B}\Big[4A^4 - 12A^2 + 3\pi\tilde{v}C_3(2 - A^2) + 2C_4(9 - 8A^2) \\ &+ 3\pi\tilde{v}C_5 + 2C_6\Big]. \end{aligned} \tag{3.6.8}$$

The integral of the last term yields

$$\begin{aligned} \int_{-\infty}^{\infty} \sum_{j=1}^{2} \frac{|\Phi_j|^2 + k\Phi_j\Phi_{3-j}^* - (1+k)}{1+k} d\tilde{x} &= -\frac{2}{B(1+k)}\Big[2A^2(2k+1) - 2kC_1C_2 \\ &- \pi\tilde{v}C_3(1+k)\Big]. \end{aligned} \tag{3.6.9}$$

After, performing all the integrations, the following effective Lagrangian is obtained

$$\begin{aligned} \mathcal{L}_{eff} &= x_{0\tilde{t}}\left[-4A\tilde{v} + 4\tan^{-1}\left(\frac{A}{\tilde{v}}\right) - \pi A C_3\right] - \frac{4}{3B}A^2\left(A^2 + B^2\right) \\ &+ \frac{\pi\tilde{v}}{B}(A^2C_3 - C_5) - \frac{1}{3B}\left[\left(B^2 - 16A^2\right)C_4 + 2C_6\right] \\ &- \frac{2}{B(1+k)}\left[(3k+2)C_4 - 2kC_1C_2\right] + \mathcal{O}(C_j^5), \end{aligned} \tag{3.6.10}$$

where $C_{2+r} = (C_1)^r + (C_2)^r$, $r = 1, \ldots, 4$. One can check that when the soliton is not moving, i.e. $x_{0\tilde{t}} = \tilde{v} = 0$ and $A = 1$, the Euler-Lagrange equations for the remaining parameters B, C_1, and C_2 are

$$2C_j\left(B^2 + 4{C_j}^2\right)(1+k) + 4C_j(k-2) - 12kC_{3-j} = 0, \tag{3.6.11}$$

$$(1+k)\left[2(C_6+2) - B^2(C_4+4)\right] - 4(C_4 + 3kC_1C_2) + 2kC_4 = 0. \tag{3.6.12}$$

The equations can be solved analytically to yield

$$B^{(0)} = \frac{2\sqrt{k}}{\sqrt{1+k}},\ C_1^{(0)} = -C_2^{(0)} = \pm\frac{\sqrt{1-3k}}{\sqrt{1+k}}, \tag{3.6.13}$$

which is nothing else, but the FA solution or $B^{(0)} = 1$, $C_j^{(0)} = 0$, which is the dark soliton. It is important to note here that despite the series expansion with respect to C_j that we took prior to integrating Eq. (3.6.5), our result (3.6.13) corresponds to an exact solution for any value of $0 < k \leq k_{ce}$. It is not yet clear to us why this is the case.

To determine the influence of the magnetic trap, i.e. $V \neq 0$, to the FA solutions, we will follow [72], where the perturbation-induced dynamics of dark solitons using a variational approach was discussed. The Euler-Lagrange equations of motion were derived for a perturbed nonlinear Schrödinger equation similar to Eq. (3.6.4). In our case, we treat the right hand side of Eq. (3.6.4) as perturbations. Due to the presence of the perturbations the Euler-Lagrange equation for the variable α_j, with $\alpha_j = \varphi$, B, and C_j, becomes [72]

$$\frac{\partial \mathcal{L}_{eff}}{\partial \alpha_j} - \partial_{\tilde{t}}\frac{\partial \mathcal{L}_{eff}}{\partial \alpha_{j\tilde{t}}} = 2\,\mathrm{Re}\left(\int_{-\infty}^{\infty}\sum_{j=1}^{2} R(\Phi_j)^*\frac{\partial \Phi_j}{\partial \alpha_j}\,d\tilde{x}\right).$$

Following [117, 122], we need two active variables only. Because of that, we will assume that adiabatically B and C_j are independent of time and are given by Eq. (3.6.13). Hence, we obtain the following set of equations

$$\frac{dA}{d\tilde{t}} = \frac{\Omega^2 x_0 \tilde{v}}{12\sqrt{k}(k+1)^{\frac{5}{2}}}\left[A^2(k+1) + 11k - 1\right], \tag{3.6.14}$$

$$\begin{aligned}\frac{dx_0}{d\tilde{t}} = {} & \frac{\tilde{v}}{576Ak^{\frac{3}{2}}(k+1)^{\frac{5}{2}}}\Big[192k^4(A^2+14) + 576k^3(A^2+8) + 576k^2(A^2+2) \\ & + \Omega^2k^2\Big\{(48{x_0}^2+\pi^2)(A^2+3) + 12(A^2+9)\Big\} \\ & + 2k\Omega^2\Big\{24{x_0}^2(A^2-1) + 12(A^2+4) + \pi^2(A^2+1)\Big\} \\ & + \Omega^2(A^2-1)(\pi^2+12) + 192k(A^2-4)\Big].\end{aligned} \tag{3.6.15}$$

From the two equations above, we obtain

$$\begin{aligned}\frac{d^2x_0}{d\tilde{t}^2} = {} & \frac{-x_0\Omega^2}{144(k+1)^5}\Big[\Omega^2(\pi^2+30)(k+1) + 36(20k^3+36k^2+12k-4) \\ & +48\Omega^2{x_0}^2k\Big],\end{aligned} \tag{3.6.16}$$

Ignoring the terms containing Ω^4 since $\Omega^2 \ll 1$, we are left with

$$\frac{d^2x_0}{dt^2} = \frac{(1-5k)\Omega^2}{1+k}x_0, \tag{3.6.17}$$

where we have assumed that $A \approx 1$ and $x_0 \approx 0$. Note that the derivative in Eq. (3.6.17) is with respect to the original time variable. This shows that the solution is stable for values of $k > \frac{1}{5}$. When $k = 1/3$, we recover the oscillation frequency of dark solitons in a harmonic trap [125] (see also [97, 117, 122]). We checked the validity of our approximation by comparing it with numerical results in Fig. 3.16 where qualitatively a good approximation is obtained.

3.6.2 The case $k \sim 0$ and $V \neq 0$

When k is close to zero, the imaginary part of the FA solution is dominant over the real part. Due to the presence of a magnetic trap, the imaginary part will become the Thomas-Fermi ground state in the limit $k \to 0$. Motivated by, e.g., [126] where a Gaussian ansatz, which is the ground state solution of the linear Schrödinger equations (3.1.1) and (3.1.2) with $k = 0$, was shown to be able to approximate the ground state of the nonlinear equation, in the following we will take a similar ansatz for our problem. For the present case, we will consider the governing equation (3.1.1) to be derived from the Lagrangian

$$\begin{aligned}\mathcal{L} &= \int_{-\infty}^{\infty} \frac{1}{2}\sum_{j=1}^{2} i\left(\Psi_j^*\Psi_{j_t} - \Psi_j\Psi_{j\,t}^*\right) - |\Psi_{j_x}|^2 - \mu|\Psi_j|^4 \\ &\quad +2\left(\rho_0 - V\right)|\Psi_j|^2 + 2k\Psi_j\Psi_{3-j}^*\, dx. \end{aligned} \tag{3.6.18}$$

Note that the main difference between Eq. (3.6.18) and Eq. (3.6.5) is the factor $\left(1 - \frac{1}{|\Psi_j|^2}\right)$ in the first term of the integrand. As for the ansatz, we take

$$\Psi_j = \left(A_j x + iC_j\right) e^{-Bx^2}. \tag{3.6.19}$$

The advantage of such a Gaussian ansatz is that the Lagrangian can be evaluated rather straightforwardly.

We substitute the ansatz into the Lagrangian (3.6.18) and evaluate the integral term by term. The integral of the first term is zero. The integral of the second term is

$$\int_{-\infty}^{\infty} \frac{1}{2}\sum_{j=1}^{2} |\Psi_{jx}|^2 = \frac{1}{16}\sqrt{\frac{2\pi}{B}}\left[3A_3 + 4BC_4\right]. \tag{3.6.20}$$

The integral of the third term yields

$$\int_{-\infty}^{\infty} \frac{1}{2}\sum_{j=1}^{2} \mu|\Psi_j|^4 = \frac{\mu\sqrt{\pi}}{256B^{5/2}}\left[64B^2C_6 + 16BA_6 + 3A_4\right]. \tag{3.6.21}$$

The integral of the fourth term leads to

$$\int_{-\infty}^{\infty} \sum_{j=1}^{2} (\rho_0 - V)|\Psi_j|^2 = \frac{\sqrt{2\pi}}{32B^{5/2}}\left[A_3(8\rho_0 B - 3\Omega^2) + 4BC_4(8\rho_0 B - \Omega^2)\right]. \tag{3.6.22}$$

The integral of the last term is

$$\int_{-\infty}^{\infty} \sum_{j=1}^{2} \Psi_j \Psi_{3-j}^* = \frac{\sqrt{2\pi}k}{4B^{3/2}} \left[A_1 A_2 + 4BC_1C_2)\right]. \tag{3.6.23}$$

Hence, the following effective Lagrangian is obtained

$$\begin{aligned} \mathcal{L}_{eff} &= -\frac{\sqrt{\pi}}{256B^{\frac{5}{2}}}\Big[4\sqrt{2}A_3(12B^2+3\Omega^2-8\rho_0 B)+16\sqrt{2}BC_4(4B^2+\Omega^2-8\rho_0 B) \\ &+ 64\mu B^2 C_6 + 16B(\mu A_6 - 4\sqrt{2}kA_7) + 3\mu A_4\Big], \end{aligned} \tag{3.6.24}$$

from which we obtain the Euler-Lagrange equations

$$A_j\left[3\mu A_j^2 + 6\sqrt{2}\Omega^2 + 8\sqrt{2}B\left(3B - 2\rho_0 + \frac{\mu {C_j}^2}{\sqrt{2}}\right)\right] - 16\sqrt{2}kBA_{3-j} = 0, \tag{3.6.25}$$

$$C_j\left[\mu {A_j}^2 + \sqrt{2}\Omega^2 + 4\sqrt{2}B\left(B - 2\rho_0 + \sqrt{2}\mu {C_j}^2\right)\right] + 8\sqrt{2}BkC_{3-j} = 0, \tag{3.6.26}$$

$$\begin{aligned} &15\mu A_4 + 16\mu B\left(3A_6 + 4BC_6\right) + 16\sqrt{2}BC_4\left(3\Omega^2 - 4B^2 - 8B\rho_0\right) \\ &+12\sqrt{2}A_3\left(5\Omega^2 + 4B^2 - 8B\rho_0\right) - 64\sqrt{2}kB\left(4BC_1C_2 + 3A_1A_2\right) = 0, \end{aligned} \tag{3.6.27}$$

where $A_3 = A_1^2 + A_2^2$, $A_4 = A_1^4 + A_2^4$, $A_5 = A_1C_1 + A_2C_2$, $A_6 = A_1^2C_1^2 + A_2^2C_2^2$, $A_7 = A_1A_2 + 4BC_1C_2$. Solving the system of algebraic equations above yields an approximation to the FA solutions. The validity of the ansatz is checked by comparing the results presented here with numerical results. The comparison is presented in Fig. 3.13. The relatively good agreement deviates rapidly as k increases towards the critical coupling. As for the stability, using a Gaussian ansatz, one will need to include, e.g., chirp variables, which we leave for future investigation.

3.7 Conclusion

We have studied the existence and the stability of FA solutions and coupled dark solitons in linearly coupled Bose-Einstein condensates, both in the absence and presence of a harmonic potential. First, we considered the case when there was no trap, i.e. $V = 0$ and obtained numerically the coupled dark soliton solutions. It is found that the dark soliton is unstable and emits radiation for the values of coupling constant below a critical value k_{cs}. For $k \geq k_{cs}$, the solution becomes stable. In the instability region of coupled dark soliton, we obtained an FA solution. The FA solution exists only below a critical value k_{ce}. At $k = k_{ce}$, it transforms into a coupled dark soliton. The transition between FA solutions and dark solitons can be viewed as a pitchfork bifurcation. The FA solution is found to be stable in its entire domain of existence. We then obtained

a travelling FA and determined the range of values of the coupling constant k where they exist. An explicit relation between the velocity v of the FA and its corresponding critical value of existence k_{ce} is obtained analytically. The relation is compared with the numerical results showing excellent agreement.

In the presence of a magnetic trap, i.e. $V \neq 0$, the value of k_{ce} at which FA changes into a coupled dark solitons is almost independent of the trapping strength Ω. However, the presence of the magnetic trap makes the FA unstable. It has been demonstrated that the stablization of FA solutions is possible by controlling the effective linear coupling k between the condensates. In the region of k where an FA is unstable, it has been shown that the FA still exists, but oscillates about the minimum of the trap non-sinusoidally. We also found that the presence of magnetic trap does not affect the existence and stability of coupled dark solitons. Finally , theoretical approximations based on variational formulations in the two cases when $k \sim k_{ce}$ and $k \sim 0$ have been derived and used to explain the numerical results.

CHAPTER 4

Multiple fluxon analogues and dark solitons in linearly coupled Bose-Einstein condensates

In Chapter 3, we studied the existence and stability of coupled dark solitons and the FA solutions in two effectively one-dimensional parallel linearly coupled BECs in the absence and presence of a magnetic trap. In this chapter, We will study the interactions of FA solutions and dark solitary waves in the same settings. We will also discuss the existence and stability of multiple FA solutions and dark solitary waves in the presence of the trap.

4.1 Introduction

Dark solitons emerge as fundamental macroscopic nonlinear excitations in the study of BECs with repulsive interatomic interaction [70]. Different works on these nonlinear excitations have been carried out in the last few years [119–121, 127, 128] due to their potential application as bit carriers in telecommunication systems [27, 33, 129]. In those experiments, several striking characteristics were highlighted and stimulated the motivation for more investigations. One of the area of investigations is the study of multiple matter wave dark solitons and their interactions in a BECs [119–121].

It has been shown in [69] that the nonlinear interaction of atoms of BECs can be characterized by the NLS (GP) equation

$$i\Psi_t = -\frac{1}{2}\Psi_{xx} + \mu|\Psi|^2\Psi - \rho_0\Psi + V\Psi. \tag{4.1.1}$$

Multiple dark soliton solutions of GP Eq. (4.1.1) in the absence of a magnetic trap are

available. The wavefunction for the simplest case of two dark solitons moving with velocities $v_1 = -v_2 = v$ can be expressed as [130]

$$\Psi(x,t) = \frac{(2\rho_0 - 4\rho_{min})\cosh(qt) - 2\sqrt{\rho_0\rho_{min}}\cosh(px) - 2iq\sinh(qt)}{2\sqrt{\rho_0}\cosh(qt) + 2\sqrt{\rho_{min}}\cosh(px)}, \tag{4.1.2}$$

where $q = 2\sqrt{\rho_{min}(\rho_0 - \rho_{min})}$, $p = 2\sqrt{\rho_0 - \rho_{min}}$ and ρ_{min} is given by Eq. (2.6.16).

Multiple dark solitons were first realized experimental in a BEC of sodium [131], while the interaction and collision between two dark solitons was first studied in [132] in a BEC of rubidium. However, the outcome of the collision in the condensate of rubidium was not clear enough because of the dissipation induced due to collision. Later on, a pair of dark solitons was created in the condensate of rubidium [97, 120] using a different approach employed in [132]. The dynamics of the interaction of dark solitons studied in [97, 120] was found to agree with the theoretical predictions based on the particle-like nature of the dark solitons.

Stability and dynamics of multiple matter wave dark solitons in a cigar-shaped BEC were analyzed in [97]. Extending the work in [97], we investigate the existence, stability and dynamics of multiple dark solitons and FA solutions in two coupled cigar-shaped condensates in the presence of a magnetic trap along the elongated direction. Here, we will also consider the interaction of multiple FA solutions as well as dark solitons in Eq. (3.1.1) in the absence and presence of a magnetic trap. Depending on the symmetry of the imaginary parts of the solutions, multiple FA solutions can be categorized into $(+-)$-configuration and $(++)$-configuration for the case of two FA solutions and $(+-+)$-configuration and $(+++)$-configuration for the case of three FA solutions. Note that for dark solitons, we have a single configuration for both $(+-)$ and $(++)$-configurations as the imaginary part is zero. Similarly we have a single configuration for $(+-+)$ and $(+++)$-configurations. In the context of parametrically driven nonlinear Schrödinger (NLS) equation, the bound states of FA solutions correspond to Bloch-Bloch states and were discussed in [133, 134].

4.2 Overview of the chapter

The structure of the chapter is as follows. In Section 4.3, we will first consider the interaction between dark solitons in Eq. (3.1.1) in the uncoupled case when there is no magnetic trap and derive a mathematical expression for the effective interaction potential between two dark solitons. We will then derive variational formulations for the oscillation frequencies of the $(+-)$ and $(+-+)$-configurations of FA solutions solutions. In Section 4.4, we will numerically analyze the interactions of FA solutions and

coupled dark solitons in Eq. (3.1.1) in the absence and presence of a trap. Here, we will examine the effects of the trapping strength over the existence and the stability of multiple FA solutions and present a comparison between the numerical and the analytical results. We will conclude the work in Section 4.5.

4.3 Variational approximations

In this section, we will first derive the interaction potential of two dark solitons obeying Eq. (4.1.1) in the absence of the magnetic trap, which was discussed rather briefly in [72, 97]. We will then generalize the concept for the interaction of n solitons. The interaction potential will then be used to approximate the oscillation frequency of multiple FA solutions in the presence of the trap.

4.3.1 Determining the interaction potential

When $k = 0$, the system (3.1.1) is decoupled and we are left with the one-dimensional NLS equation (4.1.1). We consider the interaction of two dark solitons in Eq. (4.1.1) where one of the solitons is located at $x = x_0$ while the other is at $x = -x_0$. Both solitons are moving with velocities equal in magnitude but opposite in signs, i.e. $v_1 = -v_2 = v$. Then in the weak interacting limit and in the absence of external potential, one can find the equation of the trajectory of the dip of the soliton x_0 as a function of time t. To do this, we identify the soliton dip x_0 as the point of minimum density (cf. Eq. (2.6.14)). In this case, $|\Psi|^2$ can be obtained from Eq. (4.1.2) and is given by

$$|\Psi|^2 = \frac{[(2\rho_0 - 4\rho_{min})\cosh(qt) - 2\sqrt{\rho_0\rho_{min}}\cosh(px)]^2 + 4q^2\sinh^2(qt)}{[2\sqrt{\rho_0}\cosh(qt) + 2\sqrt{\rho_{min}}\cosh(px)]^2}. \tag{4.3.1}$$

Differentiating $|\Psi|^2$ partially with respect to x and equating the resulting equation to zero yields

$$\begin{aligned}(8\rho_0^2 - 8\rho_0^2v^2 + 16\rho_0^2v^4 - 16\rho_0^2v^2)\cosh^2(qt) + 4q^2\sinh^2(qt)& \\ +(8\rho_0^2v^3 - 8\rho_0^2v)\cosh(px)\cosh(qt) &= 0.\end{aligned}$$

Using $A^2 = 1 - v^2$, the above equation can be written as

$$(8\rho_0^2A^2 - 16\rho_0^2v^2A^2)\cosh^2(qt) + 4q^2\sinh^2(qt) - 8\rho_0^2vA^2\cosh(px)\cosh(qt) = 0.$$

Since $q = 2\sqrt{\rho_{min}(\rho_0 - \rho_{min})}$ or $q^2 = 4\rho_0^2v^2A^2$, substituting the value of q^2 in the above equation and using the identity $\cosh^2(qt) - \sinh^2(qt) = 1$, we obtain

$$8\rho_0^2A^2\cosh^2(qt) - 16\rho_0^2v^2A^2 - 8\rho_0^2vA^2\cosh(px)\cosh(qt) = 0.$$

Dividing throughout by $8\rho_0^2 v A^2 \cosh(qt)$, the equation simplifies to

$$x = \frac{1}{p}\cosh^{-1}\left(\frac{\cosh(qt)}{v} - \frac{2v}{\cosh(qt)}\right). \tag{4.3.2}$$

Then the minimum distance $2x_0^*$ between the two dark solitons corresponding to $t = 0$ can be obtained from the last equation as

$$2x_0^* = \frac{2}{p}\cosh^{-1}\left(\frac{1}{v} - 2v\right). \tag{4.3.3}$$

When the solitons are moving slowly, they remain well separated for every value of time. This suggests that the distance $2x_0^*$ should be large. This can be justified if the second term on the right hand side of Eq. (4.3.2) is much smaller than the first term and hence can be neglected. Then, the resulting equation at $x = x_0$ can be written as

$$x_0 = \frac{1}{p}\cosh^{-1}\left(\frac{\cosh(qt)}{v}\right). \tag{4.3.4}$$

Note that differentiating Eq. (4.3.4) twice with respect to time yields

$$\frac{d^2x_0}{dt^2} = \frac{A^2q^2v^{-3}\cosh(qt)}{p[v^{-2}\cosh^2(qt) - 1]^{3/2}}.$$

From Eq. (4.3.4), we have $v^{-1}\cosh(qt) = \cosh(px_0)$. Substituting this value and using the identity $\cosh^2(px_0) - 1 = \sinh^2(px_0)$ in the second derivative above yields

$$\frac{d^2x_0}{dt^2} = \frac{A^2q^2\cosh(px_0)}{pv^2\sinh^3(px_0)} = -\frac{\partial}{\partial x_0}\left(\frac{A^2q^2}{2p^2v^2\sinh^2(px_0)}\right). \tag{4.3.5}$$

Equation (4.3.5) is the equation of motion of the dip of soliton from which we acquire the repulsive potential W to be

$$W = \frac{A^2q^2}{2p^2v^2\sinh^2(px_0)}.$$

Substituting the values of p and q, we obtain

$$W = \frac{\rho_0 A^2}{2\sinh^2(2\sqrt{\rho_0}Ax_0)}. \tag{4.3.6}$$

It is clear that this potential is velocity dependent as $A^2 = 1 - v^2$. The effective repulsive potential (4.3.6) can be used to construct an approximate potential for the interaction of n solitons. In this case the position of the dip of the i-th soliton (where $i = 1, 2, ..., n$) is at x_i and is moving with velocity v_i and having depth $A_i = \sqrt{1 - v_i^2}$. Even though the potential W is relevant to the symmetric interactions, however it can be applied to the asymmetric interactions as well, provided that the average depth of

the two solitons is used. We may define respectively the average depth and the relative position of the dip for the i-th and j-th solitons as $A_{ij} = (1/2)(A_i + A_j)$ and $x_{ij} = (1/2)(x_i - x_j)$. Then the repulsive potential W_i can be expressed as

$$W_i = \sum_{i \neq j}^{n} \frac{\rho_0 A_{ij}^2}{2 \sinh^2[\sqrt{\rho_0} A_{ij}(x_i - x_j)]}. \tag{4.3.7}$$

The kinetic energy E and the potential energy V of a structure of n interacting solitons are given by $E = \sum_{i=1}^{n} (1/2)\dot{x}_i^2$ and $V = \sum_{i=1}^{n} W_i$. Here dot represents the derivative with respect to time t. The Lagrangian $\mathcal{L}$, which is the difference of kinetic and potential energies, is $\mathcal{L} = E - V$. To find the equations of motion we use the Euler-Lagrange equations

$$\frac{\partial}{\partial t}\left(\frac{\partial \mathcal{L}}{\partial \dot{x}_i}\right) - \frac{\partial \mathcal{L}}{\partial x_i} = 0, i = 1, 2, ..., n. \tag{4.3.8}$$

Hence the following n coupled dynamical equations for the trajectories $x_i(t)$ of n interacting solitons are obtained as

$$\ddot{x}_i - \sum_{k=1}^{n}\left(\frac{\partial^2 V}{\partial x_k \partial \dot{x}_i}\dot{x}_k + \frac{\partial^2 V}{\partial \dot{x}_k \partial \dot{x}_i}\ddot{x}_k\right) + \frac{\partial V}{\partial x_i} = 0. \tag{4.3.9}$$

4.3.2 Variational approximation for multiple FA solutions

We can now use a variational approach to find the oscillation frequency Ω of multiple FA solutions, in the presence of a magnetic trap. In particular, we consider the cases for two and three FA solutions.

4.3.2.1 Lagrangian approach for finding the oscillation frequency of two FA solutions

We start by considering the simplest case of two FA solutions and use a Lagrangian approach to find their common oscillation frequency. Here, we assume that the FA solutions are well separated and performing small oscillations about their equilibrium positions such that $A_1 = A_2 \approx 1$. Then in the limiting case when k is close to the critical coupling for a pitchfork bifurcation, the Lagrangian can be written as

$$\mathcal{L} = \frac{1}{2}\left(\dot{x}_1^2 + \dot{x}_2^2\right) + \left(\frac{1 - 5k}{1 + k}\right)\Omega^2\left(x_1^2 + x_2^2\right) - \frac{\rho_0}{\sinh^2[\sqrt{\rho_0}(x_2 - x_1)]}. \tag{4.3.10}$$

Note that we have used Eq. (3.6.17) to describe the potential due to a magnetic trap to an FA. Since we assume that the FA solutions are well separated, i.e. $|x_2 - x_1| \gg 0$, this

implies that $e^{-\sqrt{\rho_0}(x_2-x_1)}$ approaches zero. Hence, Eq. (4.3.10) can be approximated by

$$\mathcal{L} = \frac{1}{2}\left(\dot{x}_1^2 + \dot{x}_2^2\right) + \left(\frac{1-5k}{1+k}\right)\Omega^2\left(x_1^2 + x_2^2\right) - 4\rho_0 e^{-2\sqrt{\rho_0}(x_2-x_1)}.$$

Using Eq. (4.3.8), we then have the following system of governing equations

$$\ddot{x}_1 = -8\rho_0^{\frac{3}{2}} e^{-2\sqrt{\rho_0}(x_2-x_1)} + 2\left(\frac{1-5k}{1+k}\right)\Omega^2 x_1, \tag{4.3.11}$$

$$\ddot{x}_2 = 8\rho_0^{\frac{3}{2}} e^{-2\sqrt{\rho_0}(x_2-x_1)} + 2\left(\frac{1-5k}{1+k}\right)\Omega^2 x_2. \tag{4.3.12}$$

In order to find the fixed points of this system, we set $\ddot{x}_1 = 0 = \ddot{x}_2$. On adding the resulting equations one can easily see that both fixed points x_1 and x_2 are additive inverse of each other i.e. $x_1 = -x_2 = \tilde{x}$ (say), from which we obtain a single nonlinear algebraic equation which is

$$8\rho_0^{\frac{3}{2}} e^{4\sqrt{\rho_0}\tilde{x}} - 2\left(\frac{1-5k}{1+k}\right)\Omega^2\tilde{x} = 0. \tag{4.3.13}$$

This equation could to be solved numerically to find the values of $\tilde{x}$ corresponding to different values of k.

Now let δ_1 and δ_2 be small perturbations in x_1 and x_2 and $X_1 = \tilde{x} + \delta_1(x_1, t)$, $X_2 = -\tilde{x} + \delta_2(x_2, t)$ be the solutions of Eq. (4.3.11) and Eq. (4.3.12), respectively. Substituting these solutions into Eq. (4.3.11), we obtain

$$\ddot{\delta}_1 = -8\rho_0^{\frac{3}{2}} e^{4\sqrt{\rho_0}\tilde{x}} e^{-2\sqrt{\rho_0}(\delta_2-\delta_1)} + 2\left(\frac{1-5k}{1+k}\right)\Omega^2(\tilde{x} + \delta_1).$$

Using Taylor series expansion of $e^{-2\sqrt{\rho_0}(\delta_2-\delta_1)}$ in the first term on the right hand side yields

$$\ddot{\delta}_1 = -8\rho_0^{\frac{3}{2}} e^{4\sqrt{\rho_0}\tilde{x}}[1 - 2\sqrt{\rho_0}(\delta_2 - \delta_1)] + 2\left(\frac{1-5k}{1+k}\right)\Omega^2(\tilde{x} + \delta_1).$$

Using Eq. (4.3.13), the above equation reduces to

$$\ddot{\delta}_1 = 16\rho_0^2 e^{4\sqrt{\rho_0}\tilde{x}}(\delta_2 - \delta_1) + 2\left(\frac{1-5k}{1+k}\right)\Omega^2\delta_1. \tag{4.3.14}$$

Similarly from Eq. (4.3.12) we obtain

$$\ddot{\delta}_2 = -16\rho_0^2 e^{4\sqrt{\rho_0}\tilde{x}}(\delta_2 - \delta_1) + 2\left(\frac{1-5k}{1+k}\right)\Omega^2\delta_2. \tag{4.3.15}$$

Now let ω be the common oscillation frequency of FA solutions, then we can write $\delta_1 = \gamma_1 e^{i\omega t}$ and $\delta_2 = \gamma_2 e^{i\omega t}$. Substituting these values into Eq. (4.3.14) and Eq. (4.3.15), we obtain

$$-\omega^2\gamma_1 = 16\rho_0^2 e^{4\sqrt{\rho_0}\tilde{x}}(\gamma_2 - \gamma_1) + 2\left(\frac{1-5k}{1+k}\right)\Omega^2\gamma_1, \tag{4.3.16}$$

$$-\omega^2\gamma_2 = -16\rho_0^2 e^{4\sqrt{\rho_0}\tilde{x}}(\gamma_2 - \gamma_1) + 2\left(\frac{1-5k}{1+k}\right)\Omega^2\gamma_2. \tag{4.3.17}$$

This system of equations represents an eigenvalue problem and can be written in matrix form as $AY = \lambda Y$, where

$$A = \begin{bmatrix} 2\left(\frac{1-5k}{1+k}\right)\Omega^2 - 16\rho_0^2 e^{4\sqrt{\rho_0}\tilde{x}} & 16\rho_0^2 e^{4\sqrt{\rho_0}\tilde{x}} \\ 16\rho_0^2 e^{4\sqrt{\rho_0}\tilde{x}} & 2\left(\frac{1-5k}{1+k}\right)\Omega^2 - 16\rho_0^2 e^{4\sqrt{\rho_0}\tilde{x}} \end{bmatrix},$$

$Y = [\gamma_1, \gamma_2]^T$ (T represents the transpose) and $\lambda = -\omega^2$. The characteristic frequency which corresponds to in-phase oscillations (i.e. $\delta_1 = \delta_2$) of FA solutions is

$$\omega = \sqrt{2\left(\frac{5k-1}{k+1}\right)}\Omega, \tag{4.3.18}$$

while the frequency corresponding to out-of-phase oscillations (i.e. $\delta_1 = -\delta_2$) is

$$\omega = \sqrt{2\left(\frac{5k-1}{k+1}\right)\Omega^2 + 32\rho_0^2 e^{4\sqrt{\rho_0}\tilde{x}}}. \tag{4.3.19}$$

It is important to note that in the above calculations we did not distinguish between $(+-)$ and $(++)$-configurations of FA solutions. It is because the imaginary part of the solution is treated as a passive component. Later through comparisons with numerical results we will see that the theoretical results above are only valid for the $(+-)$-configuration.

4.3.2.2 Lagrangian approach for finding the oscillation frequency of three FA solutions

In this section, we follow the same procedure as above and find the oscillation frequency of three FA solutions in the presence of a magnetic trap. We assume that any two neighboring FA solutions are well separated and $A_1 = A_2 = A_3 \approx 1$. Then in this case when k is close to critical coupling, the Lagrangian takes the form

$$\begin{aligned} \mathcal{L} &= \frac{1}{2}\left(\dot{x}_1^2 + \dot{x}_2^2 + \dot{x}_3^2\right) + \left(\frac{1-5k}{1+k}\right)\Omega^2\left(x_1^2 + x_2^2 + x_3^2\right) - \rho_0\left[\frac{1}{\sinh^2[\sqrt{\rho_0}(x_1 - x_2)]}\right. \\ &+ \left.\frac{1}{\sinh^2[\sqrt{\rho_0}(x_2 - x_3)]} + \frac{1}{\sinh^2[\sqrt{\rho_0}(x_1 - x_3)]}\right]. \end{aligned} \tag{4.3.20}$$

Here, we consider $x_1 > x_2 > x_3$, then for well separated FA solutions, we have $|x_i - x_j| \gg 0$, with $i \neq j$, where $i, j = 1, 2, 3$, and the above expression can be written as

$$\begin{aligned} \mathcal{L} &= \frac{1}{2}\left(\dot{x}_1^2 + \dot{x}_2^2 + \dot{x}_3^2\right) + \left(\frac{1-5k}{1+k}\right)\Omega^2\left(x_1^2 + x_2^2 + x_3^2\right) - 4\rho_0\left[e^{-2\sqrt{\rho_0}(x_1 - x_2)}\right. \\ &+ \left. e^{-2\sqrt{\rho_0}(x_2 - x_3)} + e^{-2\sqrt{\rho_0}(x_1 - x_3)}\right]. \end{aligned}$$

The Euler-Lagrange equations corresponding to the above Lagrangian are

$$\ddot{x}_1 = 2\left(\frac{1-5k}{1+k}\right)\Omega^2 x_1 + 8\rho_0^{\frac{3}{2}}\left[e^{-2\sqrt{\rho_0}(x_1-x_2)} - e^{-2\sqrt{\rho_0}(x_1-x_3)}\right], \tag{4.3.21}$$

$$\ddot{x}_2 = 2\left(\frac{1-5k}{1+k}\right)\Omega^2 x_2 - 8\rho_0^{\frac{3}{2}}\left[e^{-2\sqrt{\rho_0}(x_1-x_2)} - e^{-2\sqrt{\rho_0}(x_2-x_3)}\right], \tag{4.3.22}$$

$$\ddot{x}_3 = 2\left(\frac{1-5k}{1+k}\right)\Omega^2 x_3 - 8\rho_0^{\frac{3}{2}}\left[e^{-2\sqrt{\rho_0}(x_2-x_3)} - e^{-2\sqrt{\rho_0}(x_1-x_3)}\right]. \tag{4.3.23}$$

It is easy to see that the system of Eq. (4.3.21), Eq. (4.3.22), Eq. (4.3.23) has a fixed point solution given by $x_1 = -x_3 = \bar{x}$ and $x_2 = 0$. Consequently, we obtain

$$2\left(\frac{1-5k}{1+k}\right)\Omega^2\bar{x} + 8\rho_0^{\frac{3}{2}}\left[e^{-2\sqrt{\rho_0}\bar{x}} - e^{-4\sqrt{\rho_0}\bar{x}}\right] = 0, \tag{4.3.24}$$

This equation can be solved numerically to obtain the values of $\bar{x}$ for different values of k.

Next, suppose that the small perturbations in the equilibrium positions x_1, x_2 and x_3 are δ_1, δ_2 and δ_3 respectively, then from Eq. (4.3.21), Eq. (4.3.22) and Eq. (4.3.23), we derive the following perturbation equations

$$\ddot{\delta}_1 = 2\left(\frac{1-5k}{1+k}\right)\Omega^2\delta_1 - 16\rho_0^2 e^{-2\sqrt{\rho_0}\bar{x}}(\delta_1-\delta_2) + 16\rho_0^2 e^{-4\sqrt{\rho_0}\bar{x}}(\delta_1-\delta_3), \tag{4.3.25}$$

$$\ddot{\delta}_2 = 2\left(\frac{1-5k}{1+k}\right)\Omega^2\delta_2 + 16\rho_0^2 e^{-2\sqrt{\rho_0}\bar{x}}\left(\delta_1 - 2\delta_2 + \delta_3\right), \tag{4.3.26}$$

$$\ddot{\delta}_3 = 2\left(\frac{1-5k}{1+k}\right)\Omega^2\delta_3 + 16\rho_0^2 e^{-2\sqrt{\rho_0}\bar{x}}(\delta_2-\delta_3) - 16\rho_0^2 e^{-4\sqrt{\rho_0}\bar{x}}(\delta_1-\delta_3). \tag{4.3.27}$$

Equations (4.3.25)-(4.3.27) are linear in δ_1, δ_2 and δ_3, we consider solutions of the form $\delta_1 = \gamma_1 e^{i\omega t}$ and $\delta_2 = \gamma_2 e^{i\omega t}$ and $\delta_3 = \gamma_3 e^{i\omega t}$, where as before, ω is the common oscillation frequency of three FA solutions. Inserting these values into Eqs. (4.3.25)-(4.3.27), we obtain the following equations of motion

$$\begin{aligned} -\omega^2\gamma_1 &= 2\left(\frac{1-5k}{1+k}\right)\Omega^2\gamma_1 - 16\rho_0^2 e^{-2\sqrt{\rho_0}\bar{x}}(\gamma_1-\gamma_2) \\ &+ 16\rho_0^2 e^{-4\sqrt{\rho_0}\bar{x}}(\gamma_1-\gamma_3), \end{aligned} \tag{4.3.28}$$

$$-\omega^2\gamma_2 = 2\left(\frac{1-5k}{1+k}\right)\Omega^2\gamma_2 + 16\rho_0^2 e^{-2\sqrt{\rho_0}\bar{x}}\left(\gamma_1 - 2\gamma_2 + \gamma_3\right), \tag{4.3.29}$$

$$\begin{aligned} -\omega^2\gamma_3 &= 2\left(\frac{1-5k}{1+k}\right)\Omega^2\gamma_3 + 16\rho_0^2 e^{-2\sqrt{\rho_0}\bar{x}}(\gamma_2-\gamma_3) \\ &- 16\rho_0^2 e^{-4\sqrt{\rho_0}\bar{x}}(\gamma_1-\gamma_3). \end{aligned} \tag{4.3.30}$$

These equations of motion correspond to an eigenvalue problem $AY = \lambda Y$, where

$$A = \begin{bmatrix} a_{11} & a_{12} & a_{13} \\ a_{21} & a_{22} & a_{23} \\ a_{31} & a_{32} & a_{33} \end{bmatrix},$$

$a_{11} = a_{33} = 2\left(\frac{1-5k}{1+k}\right)\Omega^2 - 16\rho_0^2 e^{-2\sqrt{\rho_0}\bar{x}} + 16\rho_0^2 e^{-4\sqrt{\rho_0}\bar{x}}$, $a_{22} = 2\left(\frac{1-5k}{1+k}\right)\Omega^2 - 32\rho_0^2 e^{-2\sqrt{\rho_0}\bar{x}}$, $a_{12} = a_{21} = a_{23} = a_{32} = 16\rho_0^2 e^{-2\sqrt{\rho_0}\bar{x}}$, $a_{13} = a_{31} = -16\rho_0^2 e^{-4\sqrt{\rho_0}\bar{x}}$, $Y = [\gamma_1, \gamma_2, \gamma_3]^T$. The characteristic frequencies of FA solutions are thus obtained as

$$\omega_1 = \sqrt{2\left(\frac{5k-1}{k+1}\right)}\Omega, \tag{4.3.31}$$

$$\omega_2 = \sqrt{2\left(\frac{5k-1}{k+1}\right)\Omega^2 + 16\rho_0^2 e^{-2\sqrt{\rho_0}\bar{x}} - 32\rho_0^2 e^{-4\sqrt{\rho_0}\bar{x}}}, \tag{4.3.32}$$

$$\omega_3 = \sqrt{2\left(\frac{5k-1}{k+1}\right)\Omega^2 + 48\rho_0^2 e^{-2\sqrt{\rho_0}\bar{x}}}. \tag{4.3.33}$$

4.4 Numerical simulations and computations

4.4.1 Interactions of uncoupled dark solitons without trap

Let us reconsider the interaction of two dark solitons in Eq. (4.1.1), i.e. Eq. (3.1.1) with $k = 0$, which are located at $x = \pm x_0$ and are moving with velocities $v_1 = -v_2 = v$. This problem has been considered in details in [97]. Since the domain of inverse hyperbolic cosine is $[1, \infty[$, Eq. (4.3.3) holds for $1/v - 2v > 1$ or $v^2 < 1/4$, otherwise it gives a complex value for x_0. This means that there exists a critical value of velocity $v_{cr} = 1/2$ which separates two scenarios.

In the first scenario, two dark solitons having velocities $v_1 = -v_2 = v < v_{cr}$ start coming close to each other and at the point of their closest proximity, they repel and continuously go away from each other. In this case, before and after the interaction, both dark solitons can be described by two individual density minima. This shows that dark solitons moving with velocity $v < v_{cr}$ are well separated and can be regarded as low speed soliton. Physically this means that well-separated low speed solitons are repelled by each other and their low kinetic energy could not overcome the interparticle repulsion. A direct numerical integration of Eq. (4.1.1) is performed and shown in Fig. 4.1. Numerical simulations have also been done to check the validity of Eq. (4.3.9). The trajectories obtained through Eq. (4.3.9) are then plotted in Fig. 4.1 and indicated by white solid curves. The approximation shows excellent agreement qualitatively as well as quantitatively with the results obtained through direct numerical integration of Eq. (4.1.1).

In the second scenario, dark solitons approaching each other with velocity greater than the critical velocity will collide and after collision transmit through each other. Unlike low speed solitons, at the collision point they overlap entirely and are indistinguish-

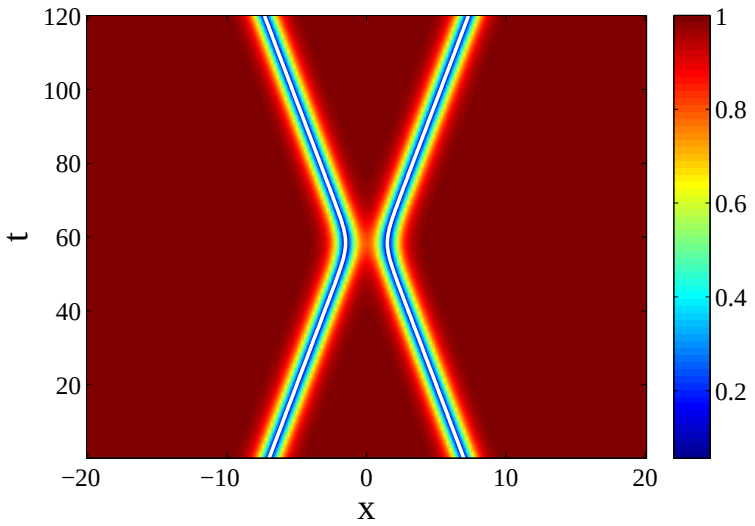

Figure 4.1: Numerical evolutions of interaction of two dark solitons. The solitons are moving with velocities $v_1 = -v_2 = 0.1$. The interparticle repulsion is dominant over the kinetic energies of solitons and solitons are going away from each other after interaction. The white solid curves are simulations of trajectories of solutions obtained through Eq. (4.3.9). Note that an exact analytic solution is given by (4.1.2).

able. Physically this means that due to the high velocity, their kinetic energy defeats the interparticle repulsion. This situation is shown in Fig. 4.2. Even though this case is beyond the particle-like approximation, we show in Fig. 4.2 that Eq. (4.3.9) can still provide an approximate trajectory of the soliton collision.

In the above discussion, we only considered the symmetric case where solitons collide with the same absolute velocity. Let us now consider the asymmetric case. In this case, a dark soliton moving with velocity v will interact with a static dark soliton. At the interaction point, the static soliton is repelled by the travelling soliton. The energy possessed by the moving soliton is used to push the static soliton away from the original position. The travelling soliton transfers all its kinetic energy to the static soliton and becomes stationary after collision as shown in Fig. 4.3. The white solid lines in this figure depict the trajectories obtained through the numerical integration of Eq. (4.3.9).

4.4.2 Interaction of dark solitons in coupled NLS equations without trap

Next, we consider the case $k \neq 0$. Let us first consider the symmetric case in which a pair of coupled dark solitons interact with each other. The interaction scenarios for coupled dark solitons are almost similar to the scenarios for the uncoupled dark solitons in the previous section. The scenario for slow moving solitons is presented in Fig.

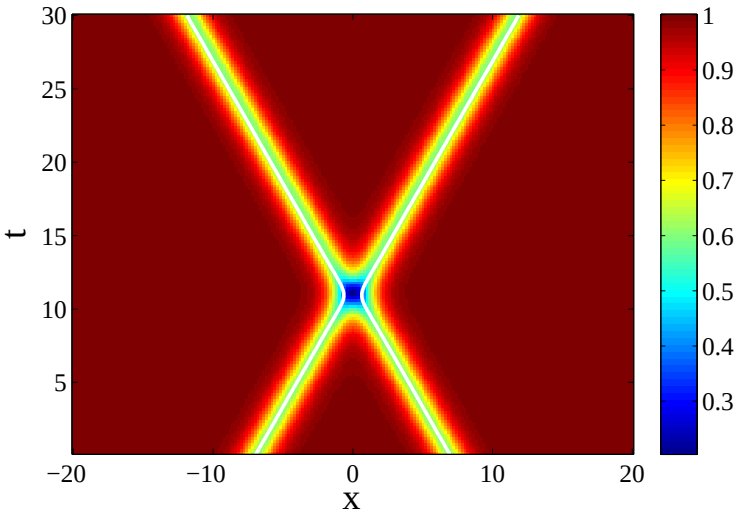

Figure 4.2: Numerical evolutions of interaction of two dark solitons. The solitons are moving with velocities $v_1 = -v_2 = 0.6$. The interparticle repulsion is suppressed by the kinetic energies of the solitons and they transmit through each other at the interacting point. The white solid curves are simulations of trajectories of solutions obtained through Eq. (4.3.9). The exact analytic solution is given by (4.1.2).

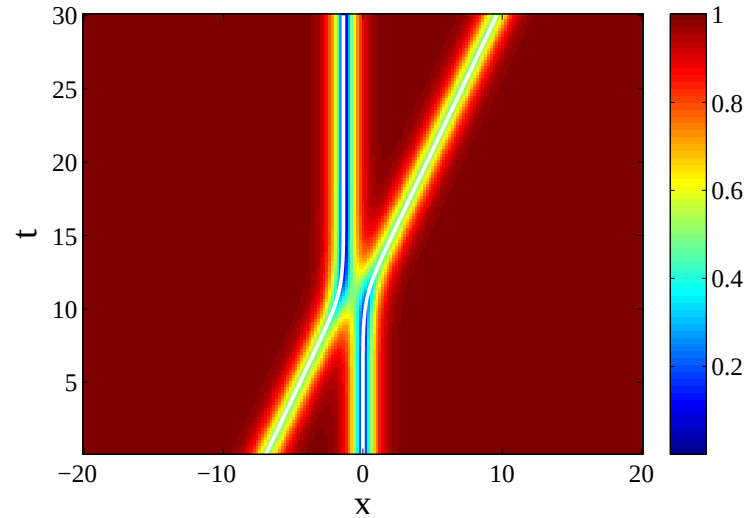

Figure 4.3: Numerical evolutions of interaction of two dark solitons. One of the solitons is static and the other is moving with velocity $v = 0.5$. After interaction, the travelling soliton becomes stationary and the static soliton starts moving with the velocity of the other soliton. The white solid curves are simulations of trajectories of solutions obtained through Eq. (4.3.9).

4.4, where we can see that both coupled solitons are repelling each other and remain well separated for all time t. The only difference from the uncoupled case is that there is radiation emerging after interaction which was not seen in the uncoupled case. The reason for the emergence of this radiation is because the system is non-integrable. Also after a particular time the coupled dark solitons break up because they are unstable for the parameter values used for the interaction. Since a travelling uncoupled dark soliton is stable for all values of velocity, no radiation or break up could be seen. In the interaction scenario of the fast moving coupled solitons, they transmit through each other. Like in the uncoupled case, their high kinetic energy overcomes the interparticle repulsion as shown in Fig. 4.5. In an asymmetric interaction when one of the coupled dark solitons is static while the other is moving with some non-zero velocity v, the interaction scenario is similar to that of the uncoupled case and is shown in Fig. 4.6. The trajectories of dips obtained by doing numerical simulations of Eq. (4.3.9) are compared with the trajectories found through direct numerical integration of Eq. (3.1.1). The white solid curves in Figs. 4.4-4.6 are the approximations obtained through Eq. (4.3.9) showing excellent agreement.

We also consider the interaction of three coupled dark solitons when one of the solitons is static and the other two are moving with opposite velocities. The scenarios resemble to that of the interaction scenarios of two solitons as above. The interaction of slow moving solitons is shown in Fig. 4.7. The travelling solitons are repelling each other without affecting the static soliton in the middle. However, the break up could be seen due to the instability of the travelling dark solitons. The interaction of the fast moving solitons is presented in Fig. 4.8, where the moving solitons transmit through each other leaving the stationary dark soliton at rest.

4.4.3 Interaction of FA solutions in the absence of a magnetic trap

In this section, we will consider symmetric as well as asymmetric interactions of two FA solutions. An FA solution moving with velocity v corresponding to a particular value of k is shown in Fig. 3.21. We use a numerically obtained FA solution to construct a collision of two FA solutions. Since FA are coupled solutions which consist of Ψ_1 and Ψ_2, there are two possibilities to connect two FA solutions. In the first possibility, Ψ_1 and Ψ_2 of the first FA are connected respectively to Ψ_1 and Ψ_2 of the second FA solution. In the second possibility, Ψ_1 and Ψ_2 of the first FA are connected respectively to Ψ_2 and Ψ_1 of the second FA solution. The combined pictures for both possibilities are shown in Fig. 4.9. From the symmetry of the imaginary parts, we refer to the first possibility as an odd symmetric interaction or $(+-)$-configuration and the second possibility as

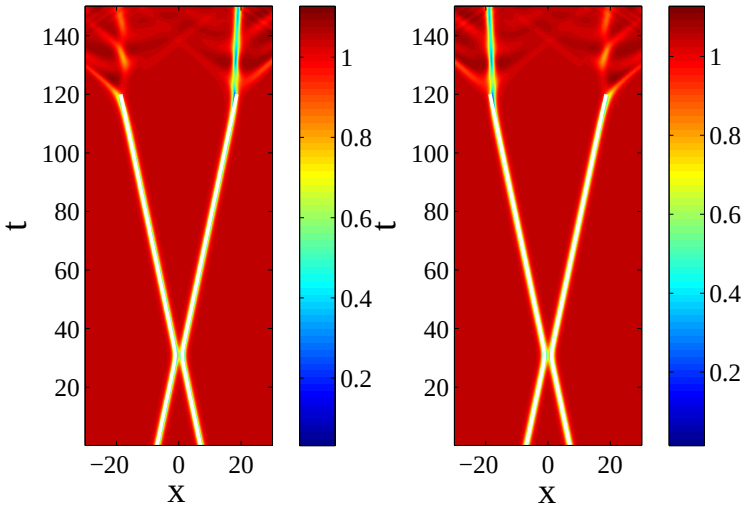

Figure 4.4: Numerical evolutions of interaction of two coupled dark solitons for $k = 0.1$. The solitons are moving with velocities $v_1 = -v_2 = 0.2$. The interparticle repulsion is dominant over the kinetic energies and the solitons are going away from each other after interaction. Due to an instability, they break down at approximately $t = 120$. The white solid curves are simulations of trajectories of solutions obtained through Eq. (4.3.9).

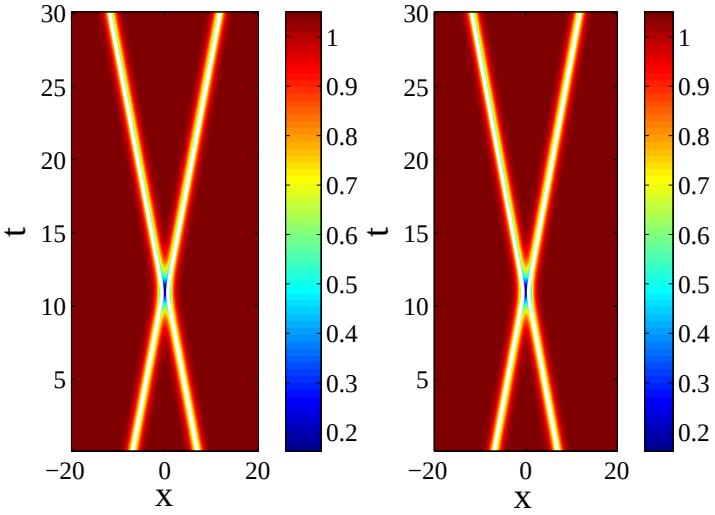

Figure 4.5: Numerical evolutions of interaction of two coupled dark solitons for $k = 0.1$. The solitons are moving with velocities $v_1 = -v_2 = 0.6$. The interparticle repulsion is suppressed by the kinetic energies of the solitons and they transmit through each other at the interacting point. The white solid curves are simulations of trajectories of solutions obtained through Eq. (4.3.9).

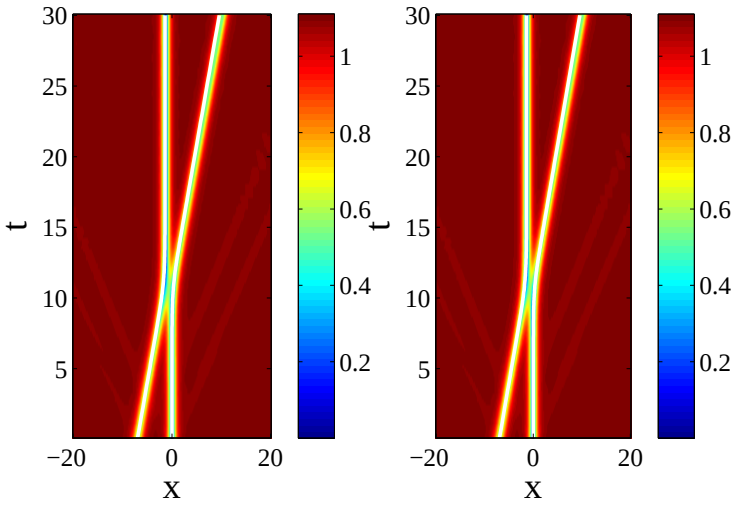

Figure 4.6: Numerical evolutions of interaction of two coupled dark solitons for $k = 0.1$. One of the coupled solitons is static and the other is moving with velocity $v = 0.5$. The white solid curves are simulations of trajectories of solutions obtained through Eq. (4.3.9).

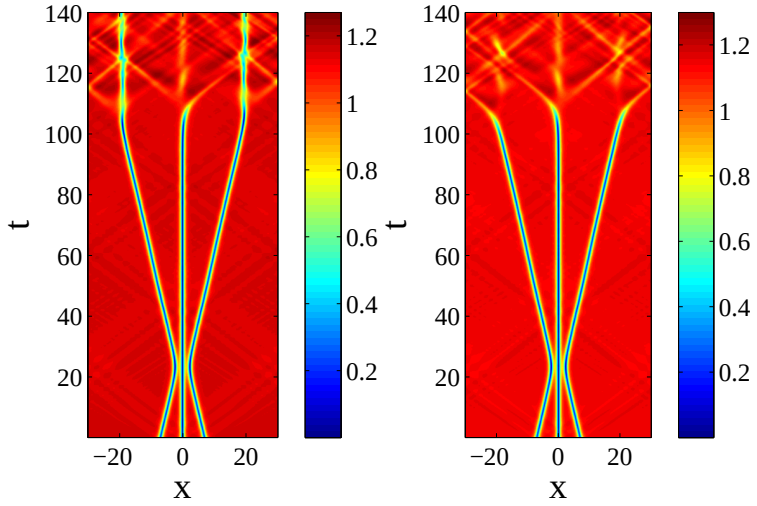

Figure 4.7: Numerical evolutions of collision of three coupled dark solitons for $k = 0.1$. Two solitons are moving with velocities $v_1 = -v_3 = 0.2$ and the soliton between these moving solitons is at rest, i.e. $v_2 = 0$. The interparticle repulsion is dominant over the kinetic energies and the solitons are going away from each other after interaction. The break up is due to the instability of the travelling dark solitons.

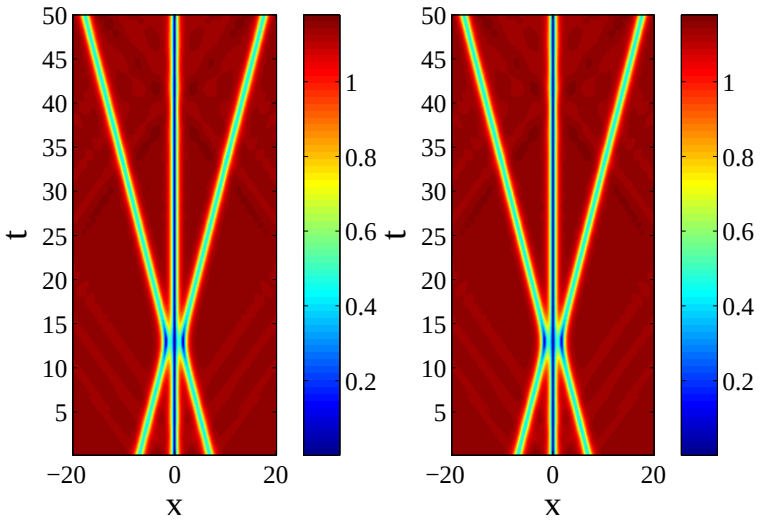

Figure 4.8: Numerical evolutions of collision of three coupled dark solitons for $k = 0.1$. The solitons are moving with velocities $v_1 = -v_2 = 0.6$ and $v_2 = 0$. The interparticle repulsion is suppressed by the kinetic energies of the solitons and the moving solitons transmit through each other at the interacting point leaving the static soliton undisturbed.

an even symmetric interaction or $(++)$-configuration.

First, we discuss the odd symmetric interaction. In this case, two FA solutions initially localized at $x = \pm x_0$ move with opposite velocities. Shown in Fig. 4.10 is the interaction of relatively slow moving FA solutions. Both FA solutions can be characterized by an individual density minimum before and after collision while at the interacting point they exhibit a single nonzero density minima. Both FA solutions show attraction towards each other at the interacting point which results in the deflection of positions of dips of both solutions. Radiation emerges and phase shift is induced due to collision. Fig. 4.11 depicts an interaction of relatively high speed FA solutions. Neither of the FA solutions show any resistance during collision. Due to their high kinetic energies, both FA solutions pass through each other without shifting the phase and without showing any deflection in the trajectories of their dips.

Next, we consider the even symmetric interaction. An interaction of extremely slow moving FA solutions is displayed in Fig. 4.12. The FA solutions come close to each other, but at the point of their closest proximity, they repel each other. Both the solutions can be identified by two individual density minima before and after the interaction as well as at the point of interaction. Another output from the interaction of two FA solutions moving with relatively slow velocities is shown in Fig. 4.13. In this scenario, the solitons merge and form a breather similar to that reported in [133] in a

parametrically driven Schrödinger equation. Radiation emerging after the collision is clear. Shown in Fig. 4.14 is the collision of FA solution moving with relatively high velocities. The FA solutions collide with each other and become indistinguishable at the interacting point.

Finally, we consider asymmetric interactions of two FA solutions. We show in Fig. 4.15 an odd interaction of a relatively slow moving FA with a static FA. The travelling FA pushes the static FA away from the interacting point. This means that the travelling FA transfers all its kinetic energy to the static FA. Due to collision, radiation appears. In Fig. 4.16 we show an interaction of a relatively fast moving FA solution with a static FA solution, where we obtain a similar behavior as before. Even interactions of a slow and a fast moving FA with a static FA are shown in Fig. 4.17 and Fig. 4.18, respectively. From Figs. 4.15-4.18, one can conclude that the collisions of a moving and a static FA are strongly inelastic. The radiation after the collision is so pronounced that it can be difficult to identify the outputs of the collisions.

The interactions of three FA solutions when one of them is at rest and the other two are moving is considered as well. In Fig. 4.19, we present the interaction of relatively slow moving FA solutions, where one of the travelling FA solutions transmits through the other FA solutions with a small shift in its trajectory. The other two FA solutions are indistinguishable after the collision. The interaction of the fast moving FA solutions is depicted in Fig. 4.20. Here, the fast moving FA solutions collide with each other and are indistinguishable.

4.4.4 Stationary multiple FA solutions and dark solitons in the presence of magnetic trap

In this section, we will consider the existence, stability and time-dynamics of multiple FA solutions and dark solitons in the coupled NLS Eq. (3.1.1) in the presence of a magnetic trap. In particular, we consider stationary solutions of the governing equations.

To seek static solutions in the time-independent framework of Eq. (3.1.1), we use a Newton-Raphson continuation method. The spatial second order derivative is approximated using central finite differences with three-point or five-point stencils. At the computational boundaries, we use Neumann boundary conditions. In all the calculations, the grid spacing $\Delta x = 0.2$ or smaller. Numerical linear stability analysis of a solution $\Psi_j^{(0)}(x)$ is then performed by looking for perturbed solutions of the form

$$\Psi_j = \Psi_j^{(0)}(x) + \epsilon[a_j(x)\, e^{i\lambda t} + b_j^*(x)\, e^{-i\lambda^* t}],\ j = 1, 2.$$

Substituting the ansatz into the governing Eq. (3.1.1) and keeping the linear terms in

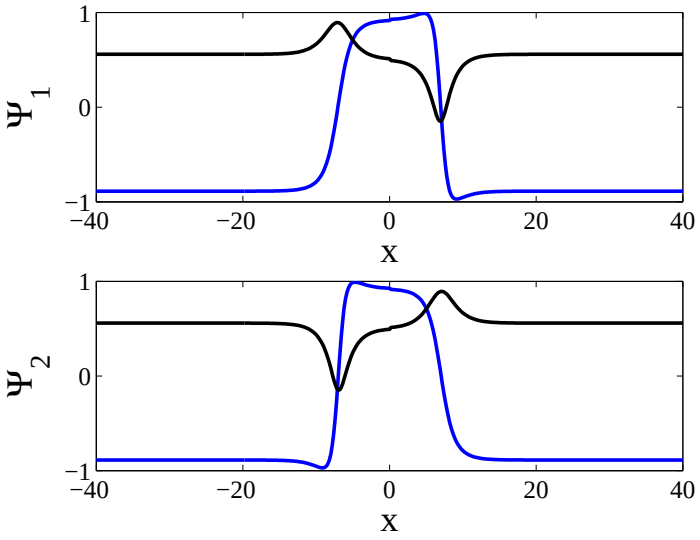

(a)

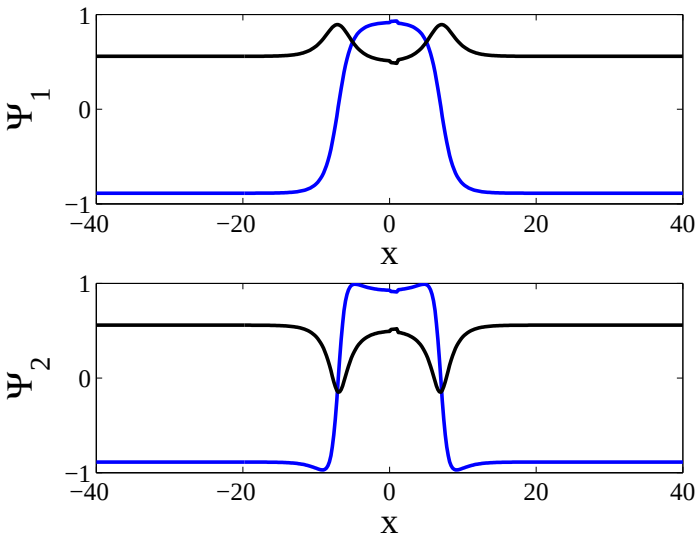

(b)

Figure 4.9: Profiles of an initial condition representing two coupled FA solutions travelling with velocities $v_1 = -v_2 = 0.2$ corresponding to $k = 0.1$. The figure in the upper panel represents the odd interaction referred to as $(+-)$-configuration, while figure in the lower panel is the even interaction and referred to as $(++)$-configuration of FA solution.

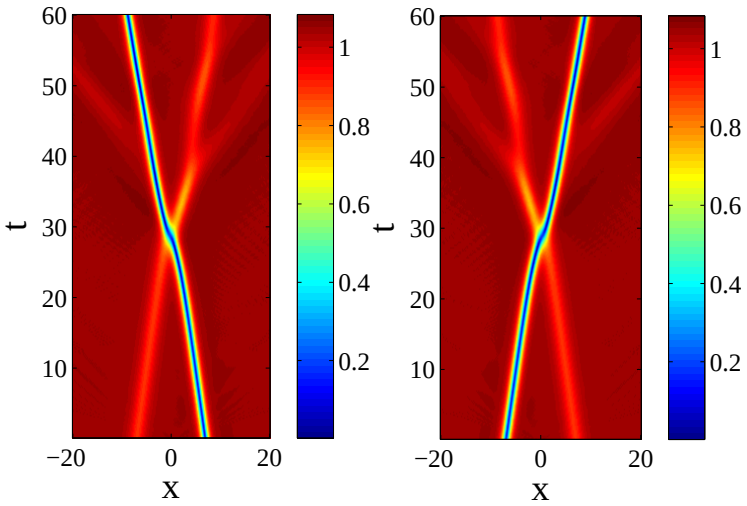

Figure 4.10: As Fig. 4.1, but for the odd symmetric collision of FA solutions for $v = 0.2$ and $k = 0.1$.

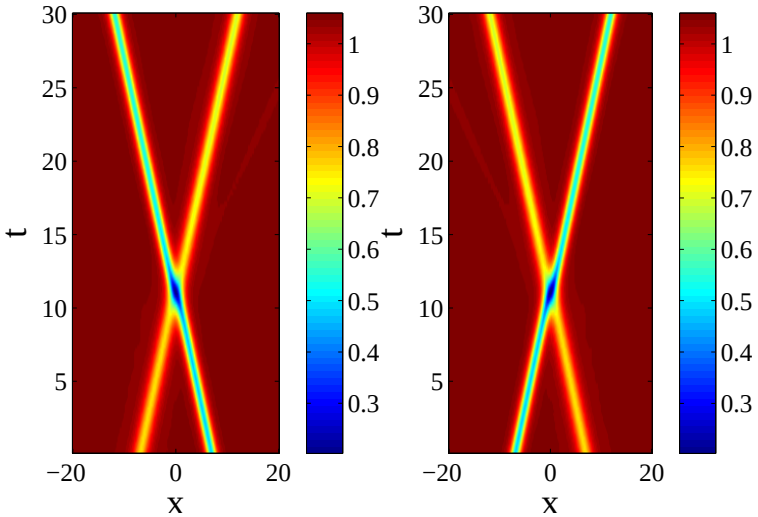

Figure 4.11: As Fig. 4.1, but for the odd symmetric collision of FA solutions for $v = 0.6$ and $k = 0.1$.

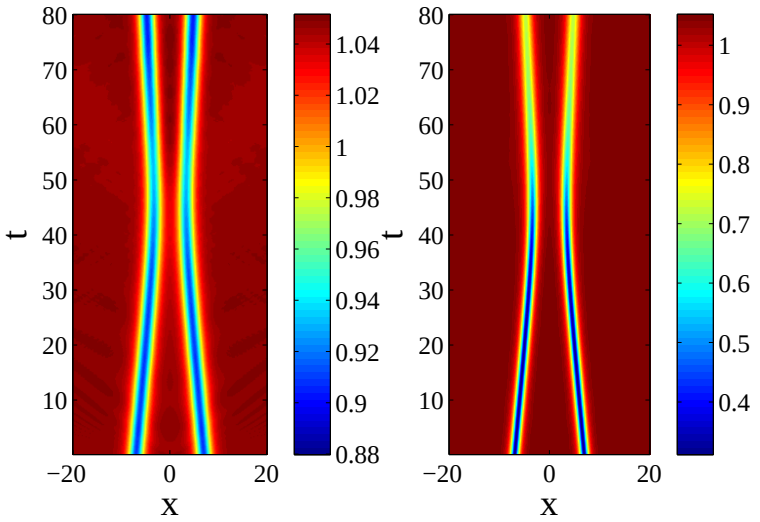

Figure 4.12: As Fig. 4.1, but the even symmetric collision of FA solutions for $v = 0.1$ and $k = 0.1$.

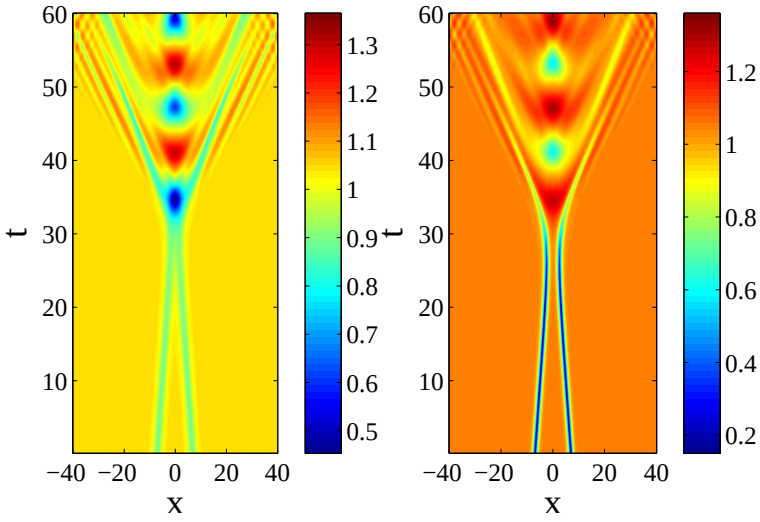

Figure 4.13: As Fig. 4.1, but the even symmetric collision of FA solutions for $v = 0.2$ and $k = 0.1$.

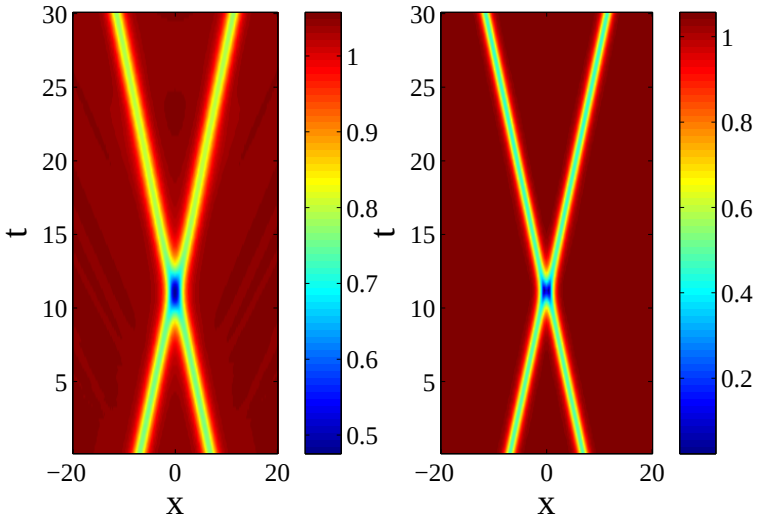

Figure 4.14: As Fig. 4.1, but the even symmetric collision of FA solutions for $v = 0.6$ and $k = 0.1$.

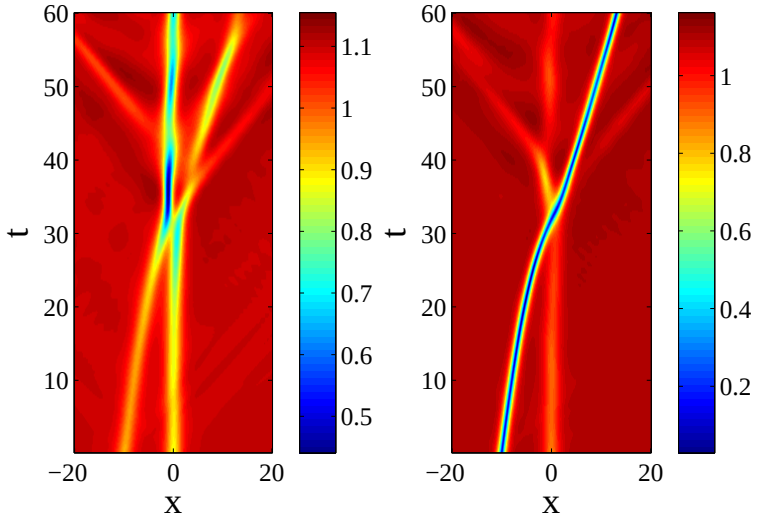

Figure 4.15: Numerical evolutions of the odd symmetric collisions of two FA solutions when one of them is static while the other is moving with velocity $v = 0.2$ and $k = 0.1$.

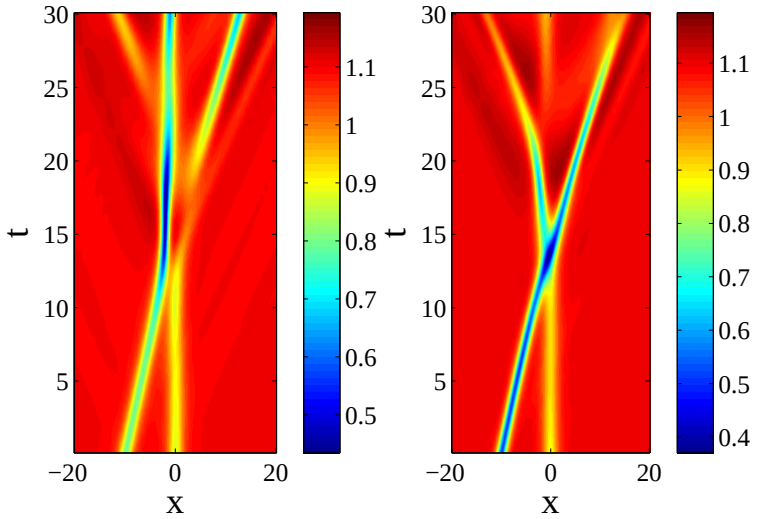

Figure 4.16: Numerical evolutions of the odd symmetric collisions of two FA solutions when one of them is static while the other is moving with velocity $v = 0.6$ and $k = 0.1$.

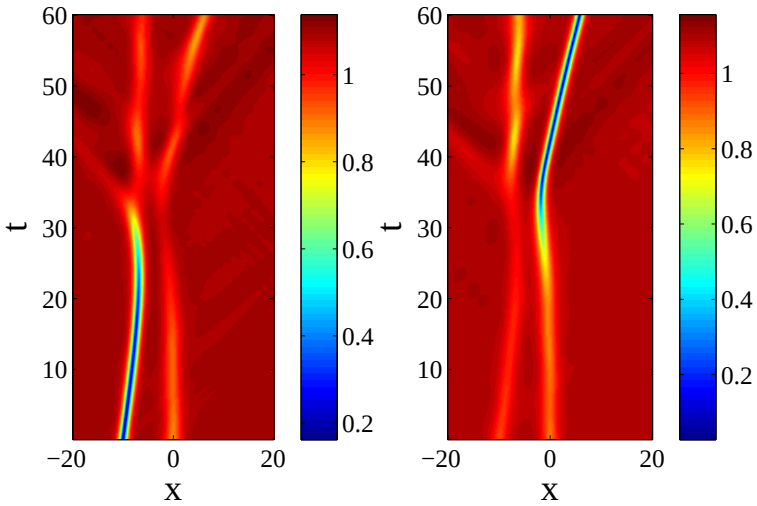

Figure 4.17: As Fig. 4.15, but the even symmetric collision of FA solutions for $v = 0.2$ and $k = 0.1$.

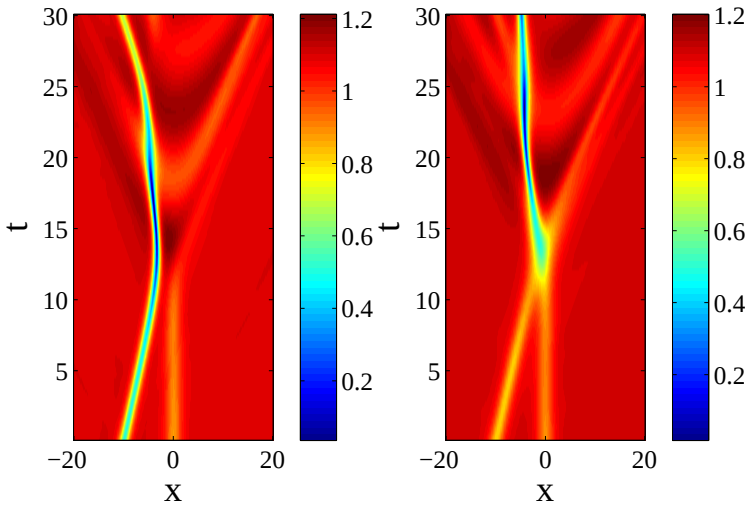

Figure 4.18: As Fig. 4.15, but the even symmetric collision of FA solutions for $v = 0.6$ and $k = 0.1$.

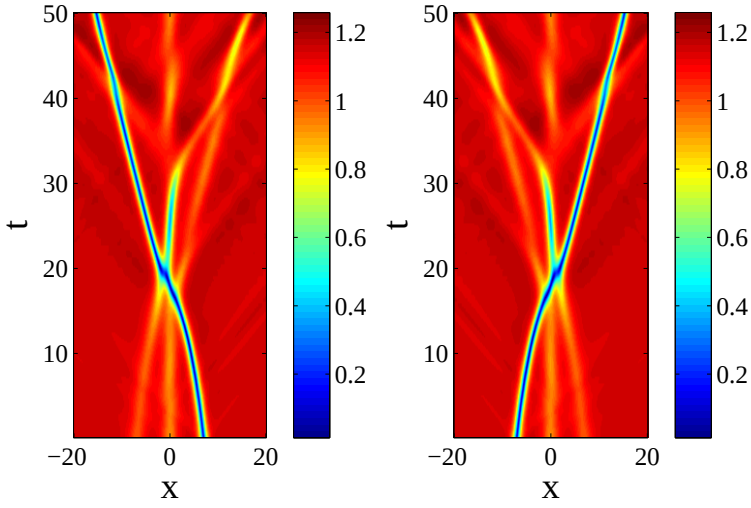

Figure 4.19: Numerical evolutions of collision of three FA solutions for $k = 0.1$. Two FA solutions are moving with velocities $v_1 = -v_3 = 0.2$ and the FA solution in the middle is at rest.

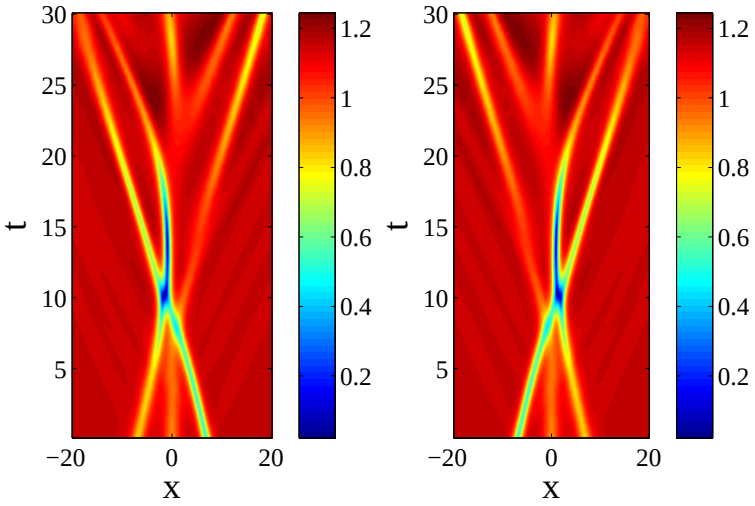

Figure 4.20: Numerical evolutions of collision of three FA solutions for $k = 0.1$. Two FA solutions are moving with velocities $v_1 = -v_3 = 0.6$ and the other one is at rest. The FA solutions are indistinguishable after the interaction.

ϵ, one will obtain a linear eigenvalue problem for the stability of $\Psi_j^{(0)}$. The ensuing eigenvalue problem is then discretized using a similar finite difference scheme as above and solved numerically for the eigenfrequency λ and corresponding eigenfunctions a_j and b_j. It is then clear that $\Psi_j^{(0)}(x)$ is a stable solution if the imaginary parts of all the eigenvalues vanish, i.e. $\mathrm{Im}(\lambda) = 0$.

4.4.4.1 (+−)-configuration of FA

First, we consider the (+−)-configuration of FA solutions of Eq. (3.1.1), which is shown in Fig. 4.21. The amplitude of the imaginary parts of the solution reduces with k and ultimately become zero at a critical value k_{ce}, when we obtain coupled dark solitons. The imaginary parts remain zero for all values of k greater than or equal to k_{ce}.

We have calculated the existence and stability of FA solutions for different non-zero values of trapping parameter Ω. The critical value k_{ce} for which this FA solution changes into dark soliton decreases with the increment of Ω and is depicted in Fig. 4.22. The conversion of FA into coupled dark solitons for $\Omega = 0.1$ is shown in Fig. 4.23. The variation in the value of Ω also affects the stability of the solution. The critical coupling k_{cs} where the solution becomes stable increases with Ω as shown in Fig. 4.24. In this case, the value of k_{cs} always remains greater than its corresponding value of k_{ce}. This shows that the (+−)-configuration of FA solution is completely unstable for all values of k where it exists. We note that the value of k_{cs} corresponding to a specific value of Ω

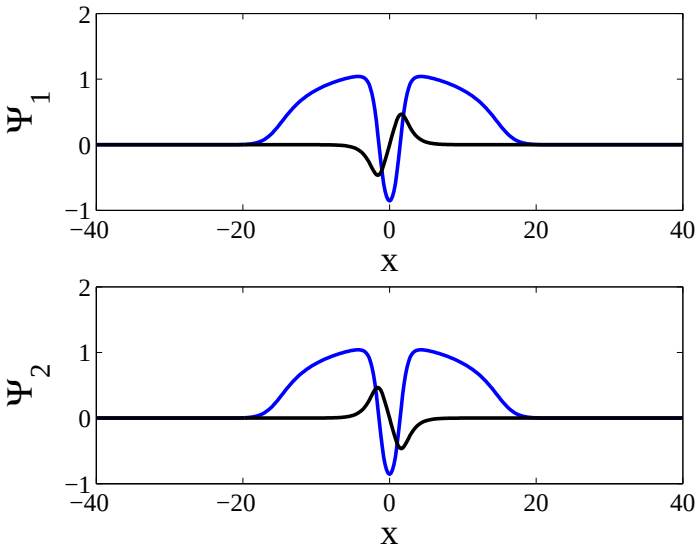

Figure 4.21: Numerically obtained multiple FA with a $(+-)$-configuration for $\Omega = 0.1$, $\rho_0 = 1$, $k = 0.2$.

is actually the critical value for dark soliton at which it attains stability. The eigenvalue structure of FA for a specific value of Ω is displayed in Fig. 4.25 showing that most of the eigenvalues are real as they are lying on the horizontal axis, while few of them are complex. The most unstable eigenvalues are purely imaginary. The magnitude of the most unstable pair of eigenvalues increases for all $k \leq k_{ce}$ and then decreases with k and ultimately becomes zero at $k = k_{cs}$. The stable eigenvalue structure for $\Omega = 0.1$ is shown in Fig. 4.26 where all eigenvalues are lying on the horizontal axis showing the stability of the solution. The stability curve is shown in Fig. 4.27 by a solid curve. In the figure, we also present the stability curve of coupled dark solitons in dashed line. At $k = k_{ce}$ the solid and dashed curves meet. This corresponds to the situation when FA turn into dark solitons, i.e. $k = k_{ce}$ is a pitchfork bifurcation point. The dark soliton becomes stable for $k \geq k_{cs}$. The dashed dotted curve shows the approximation (4.3.19) obtained through a variational approach for $\Omega = 0.1$, where one can see that a qualitatively good agreement is obtained.

In order to verify our results, we solve the time-dependent system (3.1.1) numerically for the configuration of FA solutions above. For $\Omega = 0.1$ and $k = 0.2$, the numerical evolution of the unstable FA solutions represented by Ψ_1 and Ψ_2 is shown in Fig. 4.28. Different from the collisions of two moving FA solutions with $(+-)$-configuration that are attractive (see Figs. 4.10 and 4.11), the dynamics of unstable stationary FA solutions in here is rather repulsive. This can be seen in Fig. 4.28 where at $t \approx 100$, the FA solutions are moving away from each other.

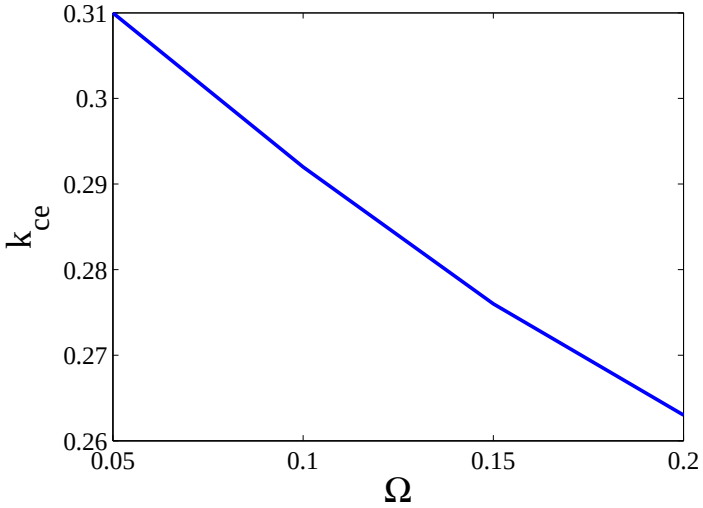

Figure 4.22: Graph of Ω and k_{ce} for the $(+-)$-configuration of FA solution. The curve shows the dependence of k_{ce} on the trapping strength Ω.

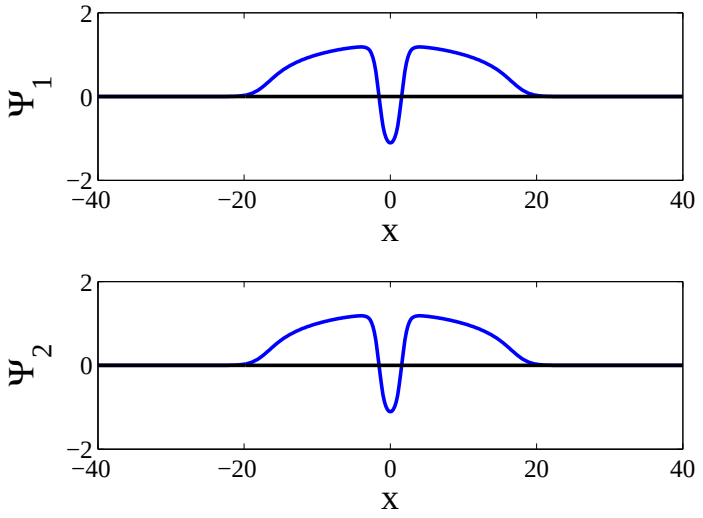

Figure 4.23: Coupled dark soliton solutions for $\Omega = 0.1$, $\rho_0 = 1$, $k = 0.5$.

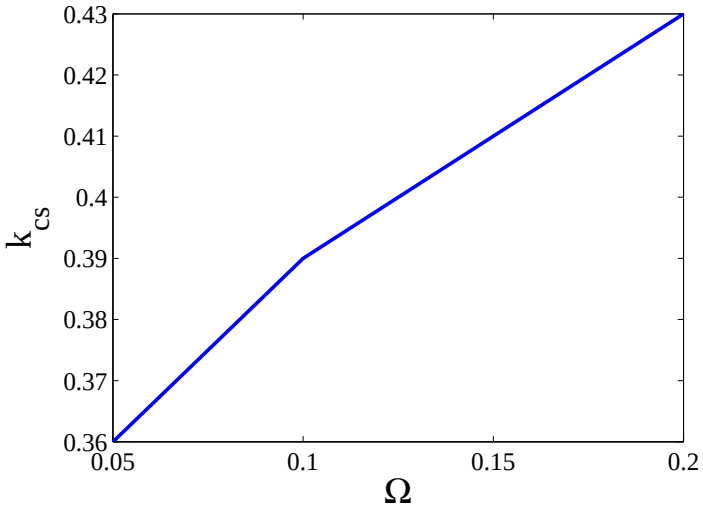

Figure 4.24: Graph of Ω and k_{cs} for the $(+-)$-configuration of FA solution. The curve shows the dependence of k_{cs} on the trapping strength Ω.

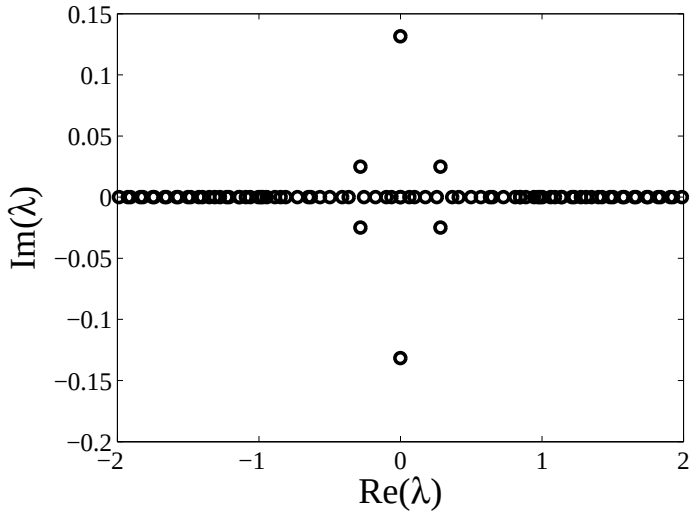

Figure 4.25: The eigenvalue structure of the soliton in Fig. 4.21 in the complex plane.

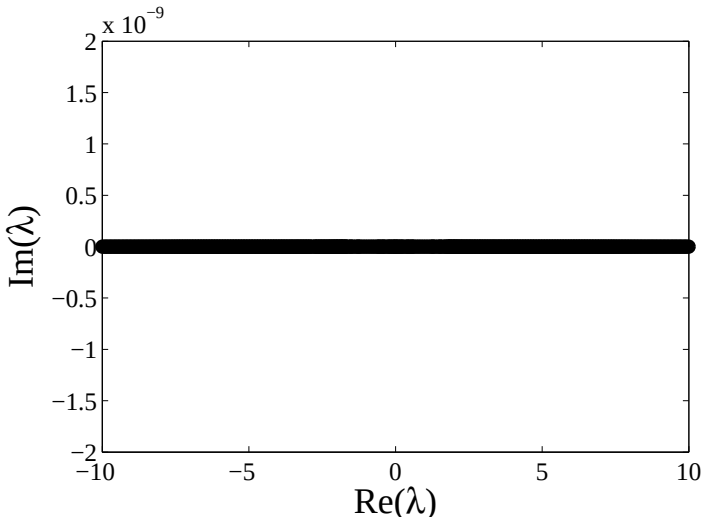

Figure 4.26: The spectrum of eigenvalues in the middle for $\Omega = 0.1$ and $k = 0.5$ showing the stability of the solution shown in Fig. 4.23.

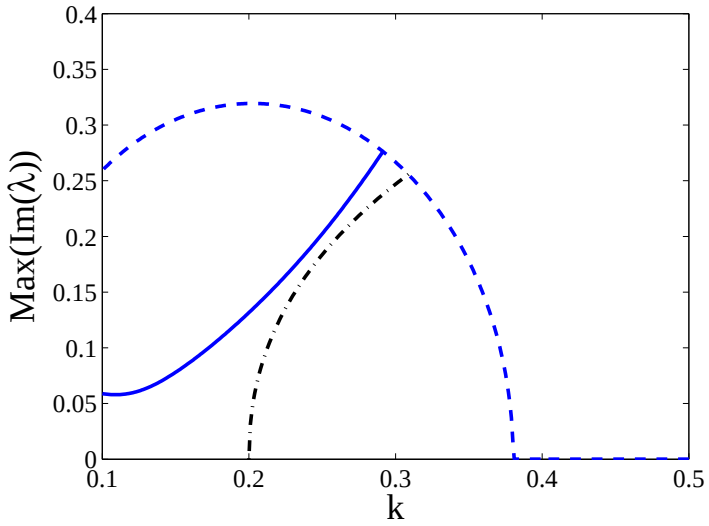

Figure 4.27: The graph of k and the maximum imaginary parts of eigenvalues for $\Omega = 0.1$. The solid and dashed curves represent the trajectories of the most unstable eigenvalue for FA and dark soliton as a function of k respectively. The dash-dotted curve represents the approximation (4.3.19) for the oscillation frequency of the $(+-)$-configuration of FA.

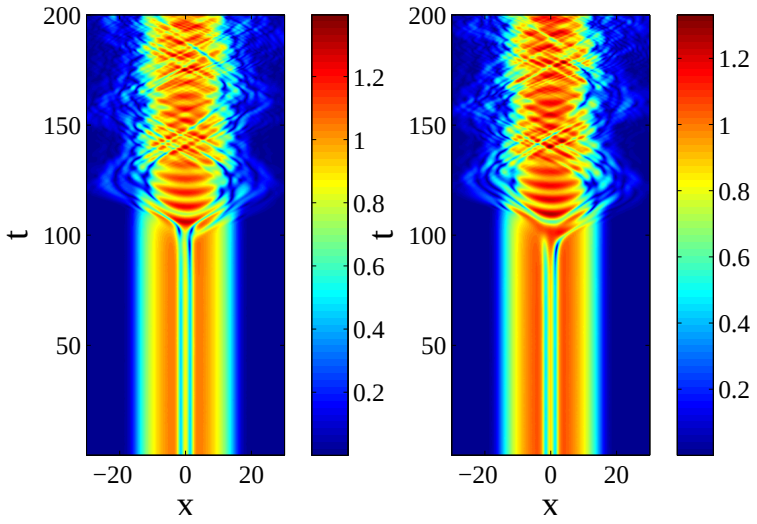

Figure 4.28: Numerical evolution of the solution shown in Fig. 4.21 for $\Omega = 0.1$ and $k = 0.2$.

4.4.4.2 (++)-configuration of FA

Next, we consider FA solutions of Eq. (3.1.1) with (++)-configuration as shown in Fig. 4.29. Similarly to the (+−)-configuration, the imaginary parts of the solution reduce to zero with k and at the critical value $k = k_{ce}$ coupled dark solitons are obtained. The critical value k_{ce} increases with Ω. The change in the value of Ω also changes the critical value k_{cs} for the stability of this solution. The stability curves for different values of Ω are plotted in Fig. 4.31. We elaborate here, for example, for $\Omega = 0.1$, the (++)-configuration of FA solution is unstable for $k < 0.16$ due to two pairs of purely imaginary eigenvalues. The solution remains stable up to $k = 0.21$, at which two pairs of unstable eigenvalues emerge from the spectrum. The imaginary part of the unstable eigenvalues becomes zero at $k = 0.38$ showing that the solution is stable for $k \geq 0.38$. The eigenvalues structure for $\Omega = 0.1$ and $k = 0.25$ is shown in Fig. 4.30. Since this solution changes into a dark soliton at $k = 0.38$, so the dark soliton is unstable for $k < 0.38$ but becomes stable for $k \geq 0.38$. The stability curve for $\Omega = 0.1$ is shown in Fig. 4.31(b) by a solid line. The real part of the most unstable eigenvalue as a function of k is displayed in the same figure by a dashed line. At $k = k_{ce}$, the (++)-configuration in FA solutions merges with dark solitons, similarly to the case of (+−)-configuration in a pitchfork bifurcation. Note that our analytical result (4.3.19) cannot be used to approximate the instability of the (++)-configuration. It is because (4.3.19) only yields purely imaginary eigenvalues while the instability of the solution here is oscillatory.

The results obtained for the (++)-configuration of FA solutions above are also verified

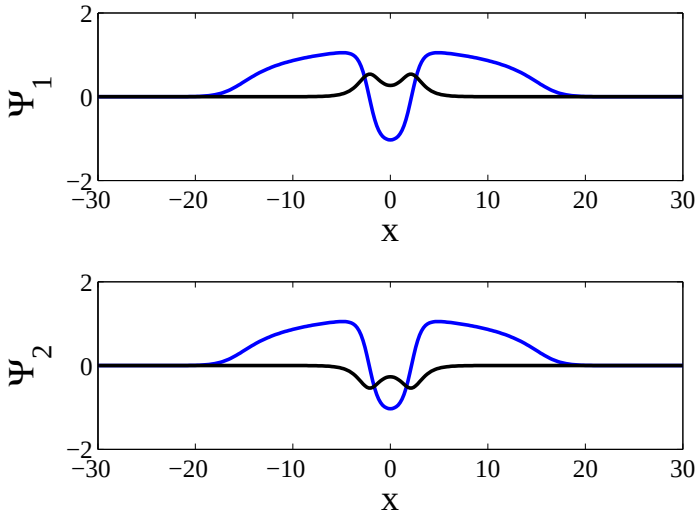

Figure 4.29: Numerically obtained FA for a $(++)$-configuration with $\Omega = 0.1$, $\rho_0 = 1$, $k = 0.25$.

by direct numerical integration of the time-dependent system (3.1.1). A typical evolution of unstable FA solutions is shown in Fig. 4.32 for $\Omega = 0.1$ and $k = 0.25$. In a similar fashion as the $(+-)$-configuration (see Fig. 4.28), the FA solutions repel each other. One difference between Fig. 4.28 and Fig. 4.32 is that in the latter case the break up is preceded by oscillations of the soliton pair. This is caused by the fact that the stability is oscillatory.

4.4.4.3 $(+-+)$-configuration of FA

Now we analyze the $(+-+)$-configuration of FA solutions of Eq. (3.1.1) which is displayed in Fig. 4.33. The amplitude and width of the real parts of the solution increases while the amplitude of the imaginary parts decreases with k and become zero at $k = k_{ce}$, i.e. we obtain dark solitons as depicted in Fig. 4.34. The values of k_{ce} and k_{cs} for different values of Ω are found. Similarly to the $(+-)$-configuration of FA solutions, k_{ce} decreases and k_{cs} increases with Ω. We also noticed that the critical value k_{ce} always remains smaller than k_{cs} corresponding to a particular value of Ω. This means that the $(+-+)$-configuration of FA solution is unstable for all values of k in its domain of existence. The eigenvalues structure for a particular value of Ω is shown in Fig. 4.35. The critical eigenvalue as a function of k is depicted in Fig. 4.36 by a solid curve. The dotted curve in the same figure is the critical eigenvalue for dark solitons. The dotted curve indicates the existence of dark solitons in the domain of existence of $(+-+)$-configuration of FA solutions. At $k = k_{ce}$, the FA bifurcates into a dark solitons as a

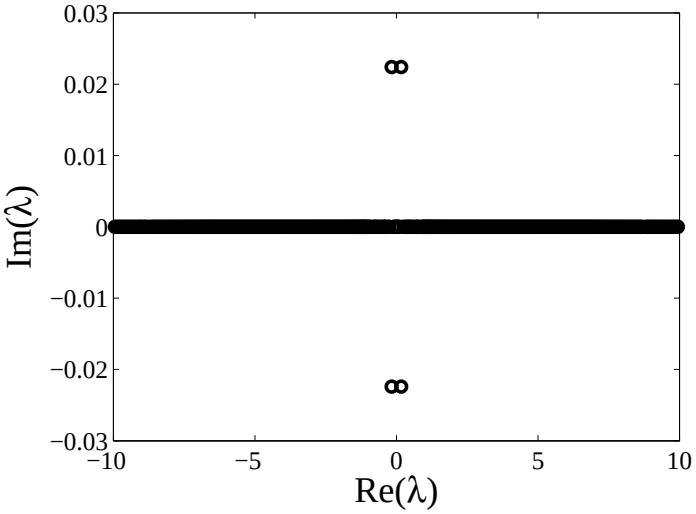

Figure 4.30: The eigenvalue structure of the soliton in Fig. 4.29. All eigenvalues are real except two pairs of eigenvalues, which are complex, indicating the instability of the solution.

pitchfork bifurcation.

We then solve the time-dependent Eq. (3.1.1) numerically for the $(+-+)$-configuration of FA solutions. The spatiotemporal contour plot for $\Omega = 0.1$ and $k = 0.1$ is shown in Fig. 4.37. One can see that the repulsion between the right and the middle solitons is dominant over the repulsion between the middle and the left solitons. As a result, the middle and the right solitons appear to oscillate and the whole structure break up.

4.4.4.4 $(+++)$-configuration of FA

Finally, we examine the $(+++)$-configuration of FA solution of Eq. (3.1.1) as shown in Fig. 4.38. The variation in the profile of the solution is similar to the $(+-+)$-configuration of FA solution, i.e. at a critical value $k = k_{ce}$, we obtain a dark soliton with a pitchfork bifurcation. Like the $(++)$-configuration of FA, both k_{ce} and k_{cs} increases with Ω. The unstable eigenvalues structure for $\Omega = 0.1$ is presented in Fig. 4.39. The stability curves for different values of Ω are shown in Fig. 4.40. The contour plot obtained on solving the time-dependent Eq. (3.1.1) is depicted in Fig. 4.41. Like the $(+-+)$-configuration, the FA solutions herein repel each other which results in the breakage of the structure.

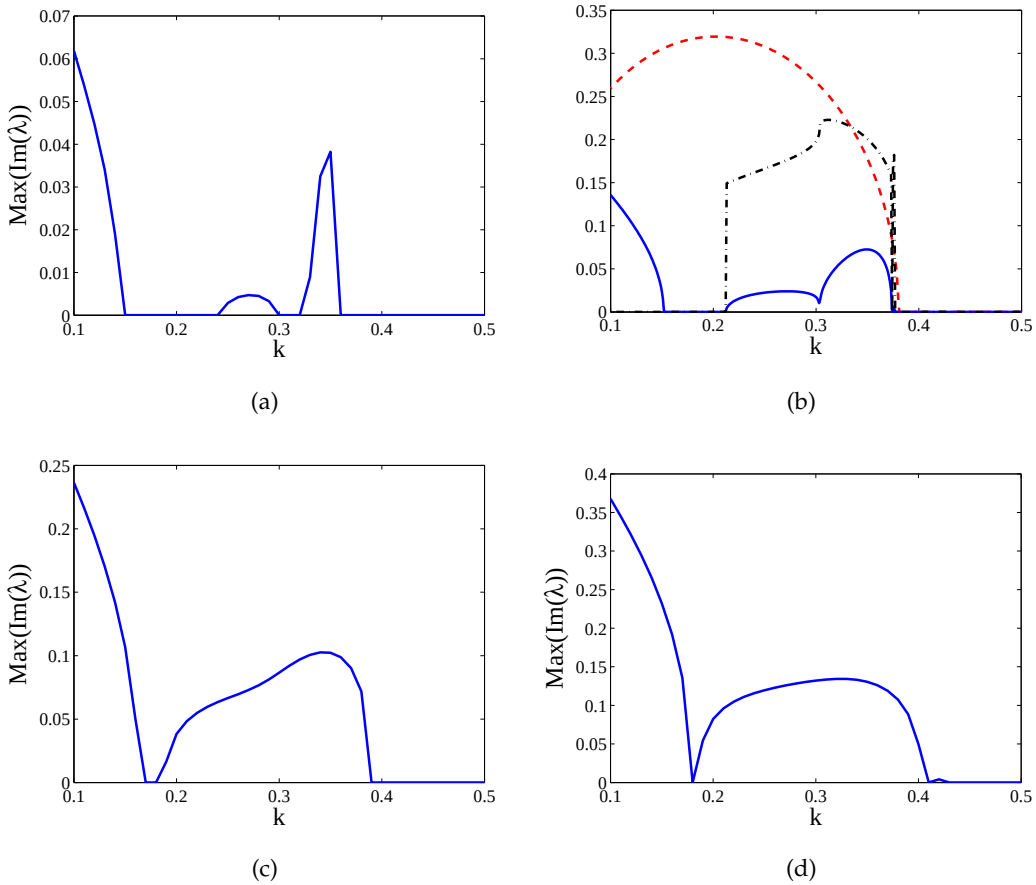

Figure 4.31: The trajectories of the most unstable eigenvalue λ_{max} corresponding to $\Omega = 0.05, 0.1, 0.15, 0.2$ for FA solution with the $(++)$-configuration. In (b), the imaginary part of λ_{max} is represented by the solid curve. The dashed line is the eigenvalue of coupled dark solitons (see Fig. 4.27). The dash-dotted curve shows the real part of λ_{max} indicating an oscillatory instability when it is nonzero.

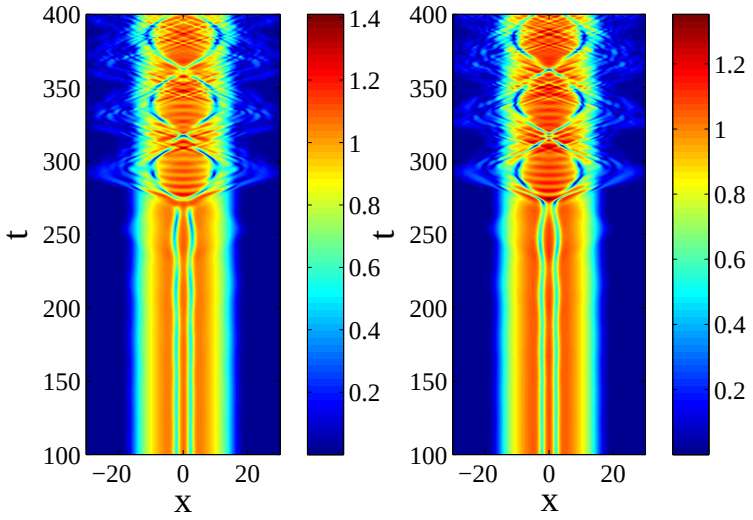

Figure 4.32: Numerical evolution of the solution shown in Fig. 4.29.

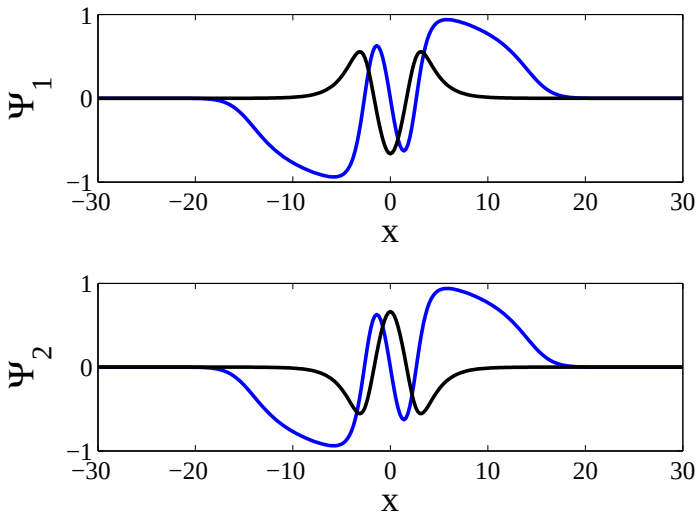

Figure 4.33: Numerically obtained multiple FA with a $(+-+)$-configuration for $\Omega = 0.1$, $\rho_0 = 1$, $k = 0.1$. The blue curves represent the real parts and the black curves represent the imaginary parts of Ψ_1 and Ψ_2.

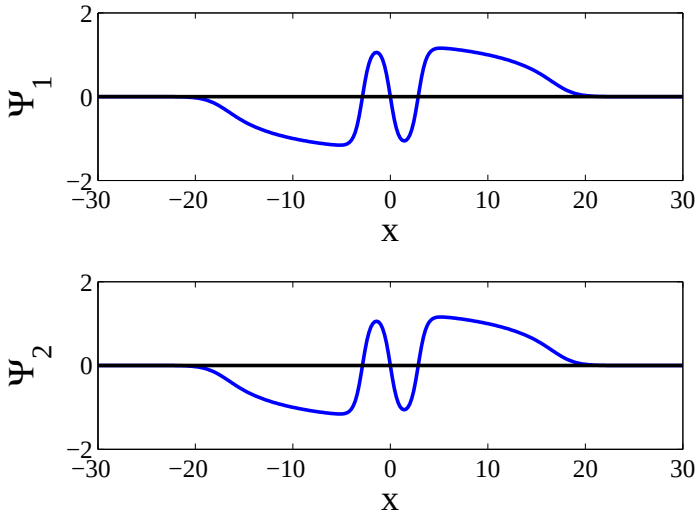

Figure 4.34: Coupled dark soliton solutions for $\Omega = 0.1$, $\rho_0 = 1$, $k = 0.5$.

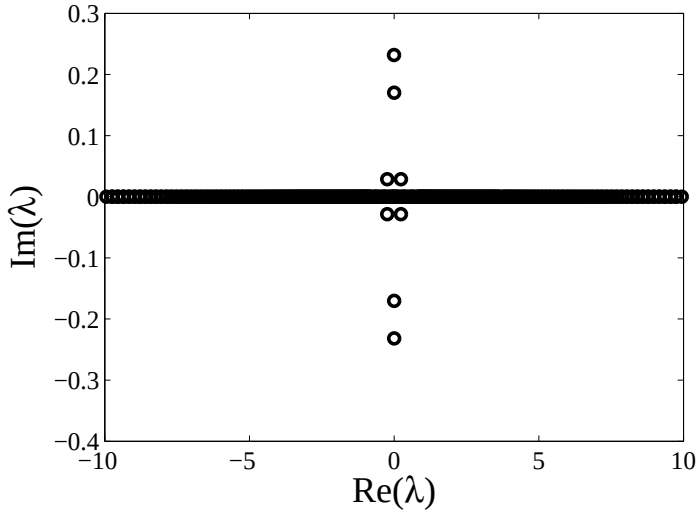

Figure 4.35: The eigenvalue structure of the $(+-+)$-configuration of FA in the complex plane for $\Omega = 0.1$, $\rho_0 = 1$, $k = 0.2$.

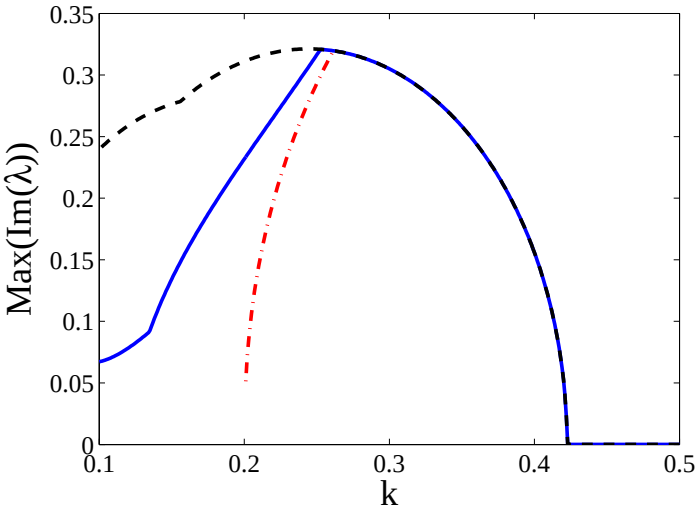

Figure 4.36: The graph of k and the maximum imaginary parts of eigenvalues for $\Omega = 0.1$. The solid and dashed curves represent the trajectories of the most unstable eigenvalue for FA and dark soliton as a function of k respectively. The dash-dotted curve represents the approximation (4.3.33) for the oscillation frequency of the $(+-+)$-configuration of FA.

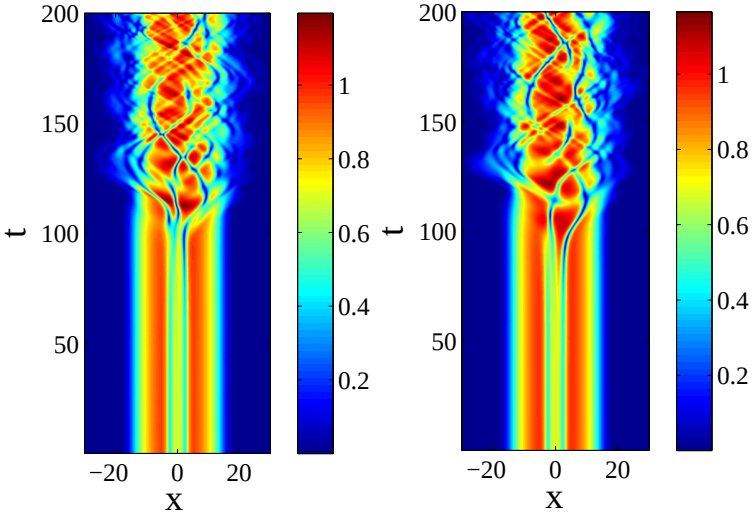

Figure 4.37: Numerical evolution of the solution shown in Fig. 4.33 for $\Omega = 0.1$, $\rho_0 = 1$, $k = 0.1$.

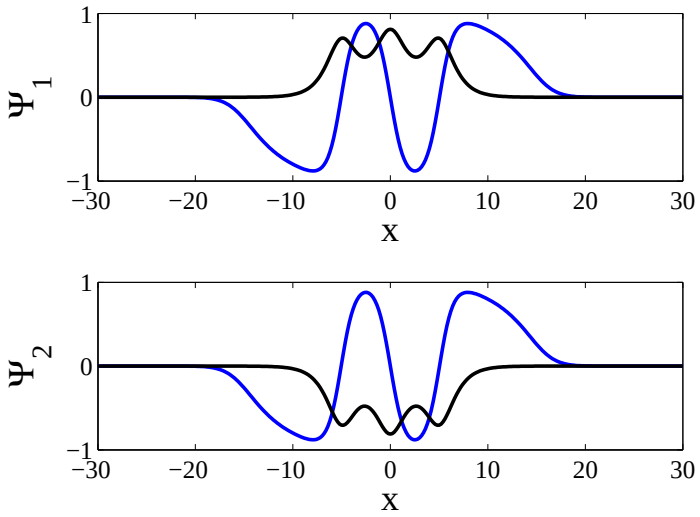

Figure 4.38: Numerically obtained multiple FA with a $(+++)$-configuration for $\Omega = 0.1$, $\rho_0 = 1$, $k = 0.15$. The blue curves represent the real parts and the black curves represent the imaginary parts of Ψ_1 and Ψ_2.

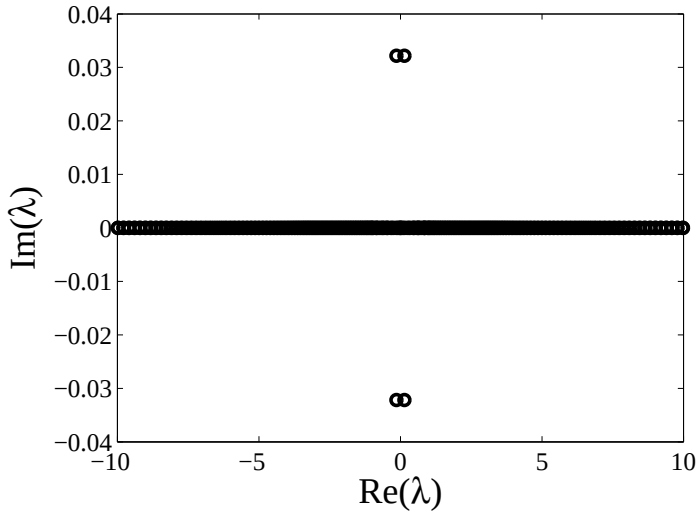

Figure 4.39: The eigenvalue structure of the $(+++)$-configuration of FA in the complex plane for $\Omega = 0.1, \rho_0 = 1, k = 0.2$. All the eigenvalues are real except two pairs of eigenvalues which are complex and showing the instability of the solution.

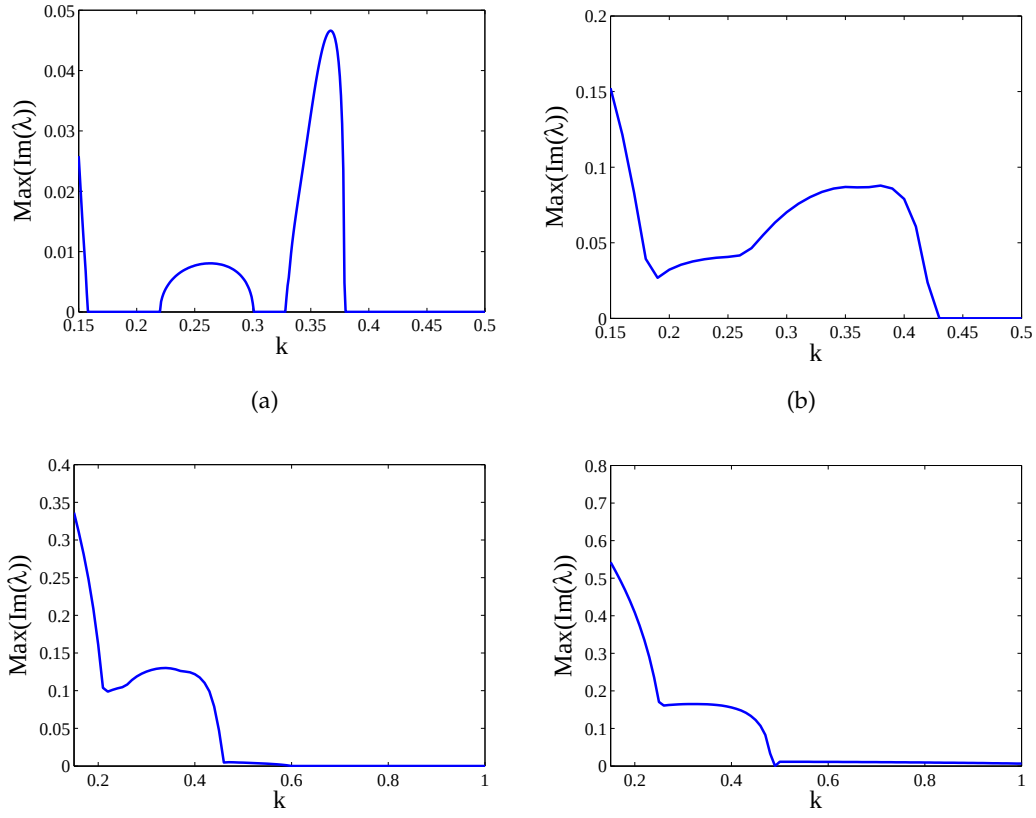

Figure 4.40: The most unstable eigenvalue corresponding to $\Omega = 0.05, 0.1, 0.15, 0.2$ for FA solution for the $(+++)$-configuration as a function of k.

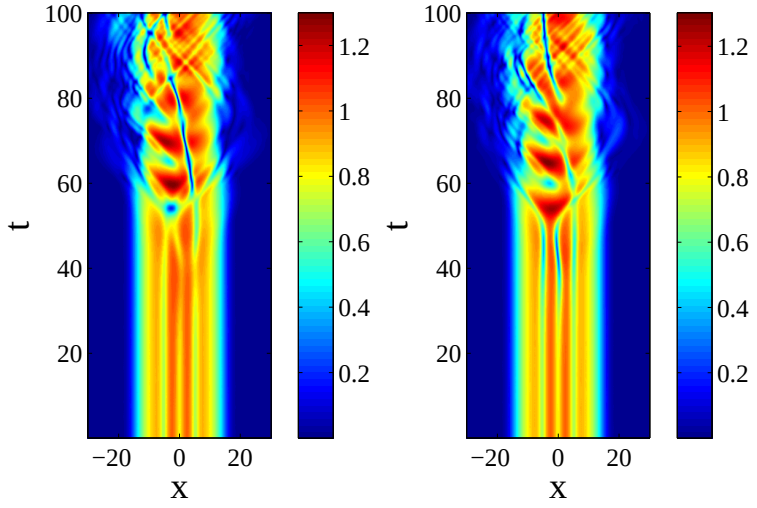

Figure 4.41: Numerical evolution of the solution shown in Fig. 4.38 for $\Omega = 0.1$, $\rho_0 = 1$, $k = 0.15$.

4.5 Conclusion

We have studied the existence and stability of multiple FA solutions and coupled dark solitons in linearly coupled BECs. In the absence of a harmonic trap, we have shown numerically that the interactions of the solitary waves are strongly inelastic, especially in the case of slow incoming velocities. Symmetric and asymmetric interactions of coupled dark solitons as well as FA solutions for different values of velocity were discussed. Interesting outcomes, such as breathers that do not exist in the uncoupled case, due to the inelastic collisions of FA solutions were observed. In the presence of a magnetic trap, bound states of solitons were shown to exist. The effects of variation of the trapping strength on the existence and stability of the multiple solitary waves were investigated numerically. It was found that for FA solutions with the $(+-)$ and $(+-+)$-configurations, the critical coupling for existence k_{ce} decreases while the critical value for stability k_{cs} increases with the magnetic strength Ω. However, both configurations are found to be unstable in their domains of existence. For the $(++)$ and $(+++)$-configurations, k_{ce} and k_{cs} increase with Ω. Stabilization for both configurations can be possible by a suitable choice of trapping strength and a control over the linear coupling between the condensates. Analytical approximations were derived based on variational formulations to calculate the oscillation frequencies of FA solutions with the $(+-)$ and $(+-+)$-configurations, where a qualitatively good agreement was obtained.

CHAPTER 5

Radially symmetric nonlinear states of coupled harmonically trapped Bose-Einstein condensates

In Chapter 4, we studied the existence, stability and dynamics of multiple FA solutions and dark solitons in one-dimensional linearly coupled BECs in the absence and presence of a magnetic trap. We also studied the interactions of FA solutions and coupled dark solitons. In this chapter, we consider the higher excited states i.e. vortices in two effectively two-dimensional parallel coupled BECs in the presence of a harmonic trap. The system is modelled by two GP equations that are coupled by linear and nonlinear terms. The existence, stability and time evolution of nontopologically and topologically charged ground and higher excited states are investigated.

5.1 Introduction

BECs have been one of the most active areas of condensed matter physics since their experimental birth in 1995. Due to the complex nature of experiments, it is natural to think about the observation of BECs in reduced dimensions. The study of lower dimensional systems is important due to the dependence of collective excitations of the systems on the spatial degrees of freedom [53]. The phenomenon of BEC does not occur in a one and a two-dimensional homogeneous systems. However, the observation of quantum degeneracy in a two-dimensional atomic gas of hydrogen [135] and the realization of dilute atomic gases in low-dimensional traps [53, 136–138] have provoked curiosity in the possibilities of BEC in reduced dimensions. The alterations of the density of states due to the trapping potential in a two-dimensional system permits the

existence of a real condensate even at a finite temperature [136].

To study the nonlinear excitations and the interatomic interactions at the mean field level, the GP equation is a well known model for BECs. For the theoretical examination of the excited states of BEC, one can use the methods based on the corresponding linear problem such as the perturbation theory used in [139]. The eigenstates of the fundamental linear system in the presence of a harmonic trap are well known. Starting from the linear equation, the nonlinear states representing the interparticle interaction can be obtained numerically which can persist, bifurcate or vanish. The existence of these states in one-dimensional system has been considered in [126, 140] while their stability analysis is done in [140]. The existence of radially symmetric nonlinear solutions in higher dimensions was studied in [141]. The dynamical evolution of vortices, vortex lattices [142] and ring solitons [139] has been done in quasi-two-dimensional settings. The analysis of the existence, linear stability and evolution dynamics of these states in a two-dimensional system of GP equation in the presence of a harmonic trap was shown in [98].

The systems of coupled GP equations describe binary mixtures of BEC in cigar-shaped traps [116]. In this chapter, we present a systematic study of the existence, linear stability and time dynamics of the radially symmetric nonlinear states which exist in a two-components BEC confined in a double well potential. These states can be obtained by solving the corresponding coupled system of GP equations. The significant three principal branches, i.e. the ground state having a single hump with $n_r = 0$, (where n_r describes the number of zeros in the radial direction) and the first and second excited states having two and three humps with $n_r = 1$ and $n_r = 2$ respectively, are investigated as a function of nonlinear coupling which is referred to as the cross-phase modulation. It is found that the ground as well as all higher excited states are linearly unstable in both cases of focusing and defocusing nonlinearity and scatter as we explain below in the absence and presence of a topological charge. Nevertheless, the ground state in the case of defocusing nonlinearity with or without a topological charge can be made stable by controlling the effective cross-phase modulation.

5.2 Overview of the chapter

The chapter is organized as follows. In the following section the model is formulated and numerical techniques are presented. The numerical simulations are presented and discussed in Section 5.4. First, we consider a nonlinearly coupled system of GP equations and examine the existence, stability and time dynamics of the ground and the

excited states in the absence and presence of a topological charge. Then we discuss the existence and stability of the solutions when the system of GP equations is linearly coupled. We also consider the case when the system is coupled with linear and nonlinear terms. Finally, we study the dynamics of the solutions when the two components of BECs have unequal values of the topological charges. The chapter is summarized and concluded in Section 5.5.

5.3 Theoretical setup and numerical methods

We consider two effectively two-dimensional parallel BECs in the presence of a double well potential. The condensates in each well have almost ring or pancake shapes and are coupled by the linear and nonlinear cross-phase modulation terms. The corresponding coupled system of GP equations takes the form [116]

$$i\Psi_{jt} = -\tfrac{1}{2}\nabla^2\Psi_j + \mu_{jj}|\Psi_j|^2\Psi_j + \mu_{j,3-j}|\Psi_{3-j}|^2\Psi_j - \rho_0\Psi_j + V(x,y)\Psi_j - k\Psi_{3-j}, \tag{5.3.1}$$

where $\nabla^2 = \partial_{xx} + \partial_{yy}$, $\Psi_j(x,y,t)$, $j = 1,2$, is the two dimensional wave function such that $|\Psi_j|^2$ represents the local condensate density in each well and $-\infty < x,y < \infty$. The variables t, x and y are the time and space coordinates respectively. $V(x,y)$ is the external magnetic trap having trapping frequency Ω that describes the strength of the trap, i.e.

$$V(x,y) = \frac{1}{2}\Omega^2\left(x^2+y^2\right). \tag{5.3.2}$$

For the planar condensates considered here, we assume $\Omega \ll 1$; in particular, we used $\Omega = 0.1$ for the numerical computations. ρ_0 is the chemical potential which is considered to be same in both wells. The coefficients μ_{jj} and $\mu_{j,3-j}$ in Eq. (5.3.1) account for the self-phase modulation (intra-species interaction) and cross-phase modulation (interspecies interactions) respectively. The values of μ_{jj} and $\mu_{j,3-j}$ can be either positive or negative. Their positive values correspond to the repulsion while negative values correspond to the attraction between the atoms. In this chapter, we will consider $\mu_{11} = \mu_{22}$ and $\mu_{12} = \mu_{21}$. The linear coupling coefficient stands for the interconversion between the two spin states of the condensates.

First we study the defocusing case with $k = 0$. The two condensates satisfying the inequality $\mu_{j,3-j}^2 > |\mu_{jj}\mu_{3-j,3-j}|$ are considered to be immiscible [143]. The physical meaning of the inequality is that the atoms of the two species do not mix together if the inter-species interaction is stronger than the intra-species interaction.We begin with the immiscible case and examine the existence and stability of a large set of nonlinear solu-

tion of Eq. (5.3.1). We then discuss the existence and stability of these nonlinear states when the condensates of the two components become miscible. The system (5.3.1) in polar coordinates can be written as

$$i\Psi_{jt} = -\tfrac{1}{2}\nabla^2\Psi_j + \mu_{jj}|\Psi_j|^2\Psi_j + \mu_{j,3-j}|\Psi_{3-j}|^2\Psi_j - \rho_0\Psi_j + V(r)\Psi_j, \tag{5.3.3}$$

where $\nabla^2 = \partial_{rr} + \frac{1}{r}\partial_r + \frac{1}{r^2}\partial_{\theta\theta}$, $V(r) = \frac{1}{2}\Omega^2 r^2$ and $0 \le r < \infty$, $0 \le \theta \le 2\pi$. The densities of the solutions in both wells are assumed to be radially symmetric. The total number of atoms in the two channels N is conserved, with

$$\begin{aligned} N &= \int_{-\infty}^{\infty}\int_{-\infty}^{\infty}\sum_{j=1,2}|\Psi_j|^2 dxdy \\ &= \int_0^{\infty}\int_0^{2\pi}\sum_{j=1,2}|\Psi_j|^2 rdrd\theta \\ &= \int_0^{\infty} 2\pi\sum_{j=1,2}|\Psi_j|^2 rdr. \end{aligned}$$

The time-independent radially symmetric nonlinear solutions of Eq. (5.3.3) can be obtained numerically by using the ansatz $\Psi_j = u_j(r)\exp(-im_j\theta)$, where r and θ are the polar coordinates in the (x, y)-plane and $m_{1,2}$ are the topological charges (vorticities) of condensates in the two wells. The substitution of these ansatz into Eq. (5.3.3) yield the steady state equations for radial wave functions $u_j(r)$:

$$\frac{1}{2}\left(u_{jrr} + \frac{1}{r}u_{jr} - \frac{m_j^2}{r^2}u_j\right) - \mu_{jj}|u_j|^2u_j - \mu_{j,3-j}|u_{3-j}|^2u_j + \rho_0 u_j - V(r)u_j = 0. \tag{5.3.4}$$

The system (5.3.4) possesses infinitely many nonlinear solutions. Each solution can originate from the corresponding mode of the linear problem. To solve this system numerically, we discretize the above system and approximate the first and second order derivatives using central finite differences with three points, i.e.

$$\begin{aligned} &\frac{1}{2}\left[\frac{u_{j,i+1} - 2u_{j,i} + u_{j,i-1}}{\Delta r^2} + \frac{1}{r_i}\frac{u_{j,i+1} - u_{j,i-1}}{2\Delta r} - \frac{m_j^2}{r_i^2}u_{j,i}\right] - \mu_{jj}|u_{j,i}|^2u_{j,i} \\ &-\mu_{j,3-j}|u_{3-j,i}|^2u_{j,i} + \rho_0 u_{j,i} - V(r_i)u_{j,i} = 0. \end{aligned} \tag{5.3.5}$$

The above system (5.3.5) can be solved using Newton-Raphson continuation method. It is important to mention that the boundary condition at the origin is not known. We can avoid the boundary condition at the origin by manipulating the grid points. This can be done by selecting the grid points which are half-integrated in the radial direction [144], i.e. $r_i = \left(i - \frac{1}{2}\right)\Delta r$, $i = 1, 2, ..., N+1$. One can see that, when i=1, the $u_{j,0}$ appears in the above system which cancels out by substituting $r_1 = \Delta r/2$. At the other computational boundary, we use the Neumann boundary conditions.

The numerical linear stability analysis of the solutions $u_j^{(0)}(r)$ is then performed by looking for the perturbed solutions of the form

$$\psi_j = u_j^{(0)}(r)e^{im_j\theta} + \epsilon\left[a_j(r)e^{i\left[(q+m_j)\theta+\lambda t\right]} + b_j^*(r)e^{-i\left[(q-m_j)\theta+\lambda^* t\right]}\right], \tag{5.3.6}$$

where q is the perturbation wave number. Substituting the ansatz (5.3.6) into Eq. (5.3.3) and retaining only the linear terms in ϵ, one obtains a linear eigenvalue problem for the stability of $u_j^{(0)}$ which is

$$\frac{1}{2}\left[a_{jrr} + \frac{1}{r}a_{jr} - \frac{1}{r^2}(q+m_j)^2 a_j\right] - 2\mu_{jj}|u_j^{(0)}|^2 a_j - \mu_{j,3-j}|u_{3-j}^{(0)}|^2 a_j - \mu_{jj}\left(u_j^{(0)}\right)^2 b_j$$
$$-\mu_{j,3-j}u_j^{(0)}u_{3-j}^{(0)}b_{3-j} - \mu_{j,3-j}u_j^{(0)}u_{3-j}^{(0)*}a_{3-j} + \rho_0 a_j - \frac{1}{2}\Omega^2 r^2 a_j = \lambda a_j, \tag{5.3.7}$$

$$-\frac{1}{2}\left[b_{jrr} + \frac{1}{r}b_{jr} - \frac{1}{r^2}(q-m_j)^2 b_j\right] + 2\mu_{jj}|u_j^{(0)}|^2 b_j + \mu_{j,3-j}|u_{3-j}^{(0)}|^2 b_j + \mu_{jj}\left(u_j^{(0)*}\right)^2 a_j$$
$$+\mu_{j,3-j}u_j^{(0)*}u_{3-j}^{(0)*}a_{3-j} + \mu_{j,3-j}u_j^{(0)*}u_{3-j}^{(0)}b_{3-j} - \rho_0 b_j + \frac{1}{2}\Omega^2 r^2 b_j = \lambda b_j \tag{5.3.8}$$

The ensuing eigenvalue problem is then discretized using a similar finite difference scheme as above and solved numerically for the eigenvalues $\lambda = \lambda_q$ and the corresponding eigenmodes $\{a_j(r), b_j(r)\} = \{a_{jq}(r), b_{jq}(r)\}$. The solutions $u_j^{(0)}(r)$ will be generically stable if the imaginary parts of all the eigenvalues vanish for all q, i.e. $\mathrm{Im}(\lambda) = 0$.

In order to establish the validity of solutions found as stable or unstable and to investigate their time dynamics, we begin with the one-dimensional radially symmetric steady state solutions of Eq. (5.3.3) as an initial condition and solve the corresponding time-dependent governing equations using a Runga-Kutta method of order four. The outcomes of existence, linear stability and time evolution are presented below.

5.4 Numerical results

We present a comprehensive analysis of the stability and dynamical evolution of the radially symmetric steady state nonlinear solutions of the coupled system (5.3.1) in the cases of defocusing nonlinearity, i.e. $\mu_{jj} > 0$ and focusing nonlinearity, i.e. $\mu_{jj} < 0$. In particular, for defocusing nonlinearity, we take $\mu_{jj} = 1$ while in case of focusing nonlinearity, $\mu_{jj} = -1$. First we consider the case of $m_1 = m_2 = m$. We found that when the interatomic interaction is repulsive, the ground state as well as the higher excited states are unstable for both repulsive and attractive intra-atomic interactions. This is true for all topological charges considered (i.e. $m \geq 0$). The instability growth rate is directly found to be small in all cases of repulsive intra-atomic interaction. On the other

hand, for the attractive intra-atomic interaction, the instability growth rate seemed to be very high. However, in the repulsive case, the ground state with topological charge $m = 0, 1, 2$ can be made stable by controlling the nonlinear coupling.

5.4.1 Stability analysis of the nonlinearly coupled system

We depict the radial profiles of the coupled solutions and the eigenvalues spectra for the ground state and the first two excited states for repulsive and attractive interactions in Figs. 5.1-5.9. The maximum imaginary parts of the primary $(q = 0, 1, 2, 3, 4)$ eigenvalues for $m = 0, 1$ and 2, respectively, are presented in Figs. 5.10-5.12. Corresponding to each value of m, the stability curves for the ground state $(n_r = 0)$ and first two excited states $(n_r = 1, 2)$ are shown respectively in left panels for the repulsive case and in the right panels for the attractive case. The existence of at least one complex eigenvalue manifests the instability of the solution. The time evolution of the solutions shown in Figs. 5.1-5.9 are depicted in Figs. 5.13-5.30.

Table 5.1: Table representing different symbols corresponding to each value of q. A black dot has been used for eigenvalues with $q \geq 12$ or $|\mathrm{Im}(\lambda)| < 10^{-12}$.

Values of q	0	1	2	3	4	5	6	7	8	9	10	11	$12 - 50$
Symbols	◯	×	+	∗	□	◇	▽	△	◁	▷	⬠	⬡	•

Let us analyze the stability curves of each solution in detail. Shown in the upper and lower left panels of Figs. 5.1-5.9 are the radial profiles of the coupled solutions for the ground state and the first two excited states for the defocusing and focusing cases respectivley. We are interested herein with the dynamics of the solution with the variation in the nonlinear coupling. The amplitude of radial profiles increases with decreasing $\mu_{12} = \mu_{21}$. The stability spectra in the complex plane for a specific value of μ_{12} are shown in the right panels of each figure. The unstable eigenvalues are given different symbols corresponding to different values of q. The different symbols are shown in Table 5.1. The eigenvalues with $|\mathrm{Im}(\lambda)| < 10^{-12}$ or $q > 11$ are plotted with small dark dots. There is a long range of values of nonlinear coupling in the defocusing case where the ground state is stable as displayed in Fig. 5.10(a). This is true even for the case when nonlinear coupling changes its sign. However, the ground state becomes unstable when nonlinear coupling exceeds a certain critical value. The first and second excited states remain unstable for all values of nonlinear coupling (cf. the middle and bottom left panels of Fig. 5.10. However, in the focusing case, the ground and the higher excited states are unstable for all values of nonlinear coupling as can be seen in the right panels of Fig. 5.10).

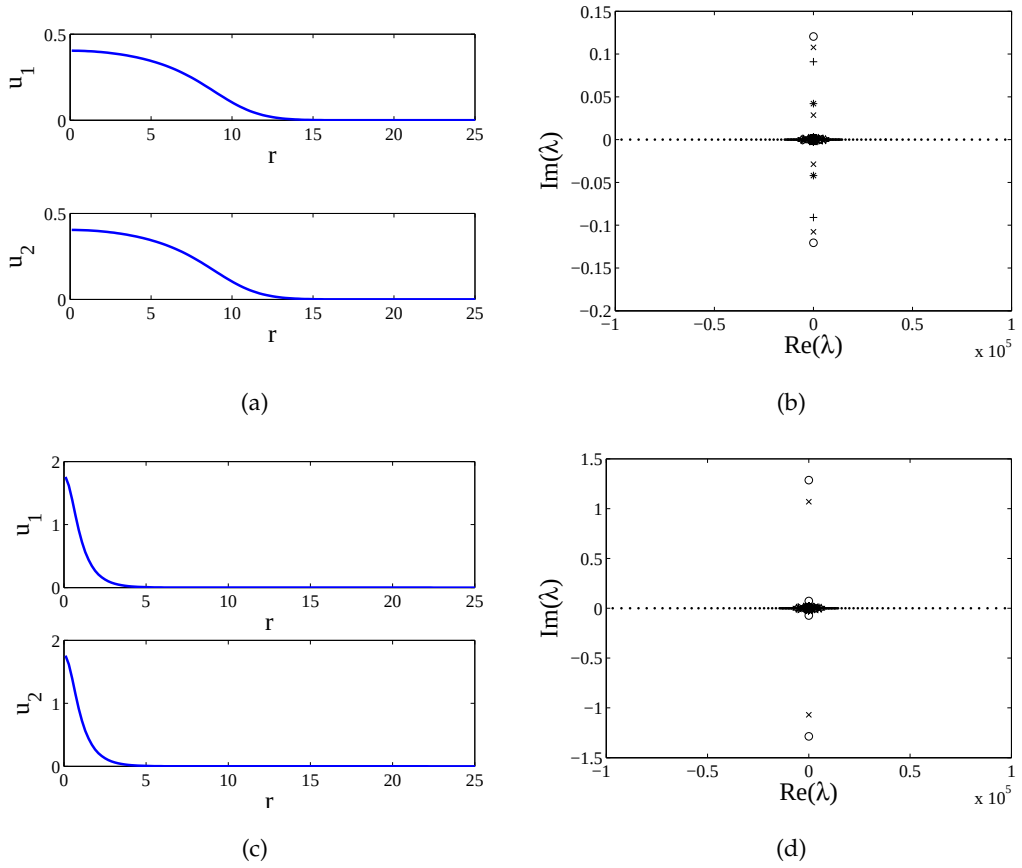

Figure 5.1: Figures for the chargeless ground state $(m = 0, n_r = 0)$. The top left panel depicts the profile of the solution in the repulsive case for $\rho_0 = 0.5$ and $\mu_{12} = \mu_{21} = 2$. The solution in the attractive case for $\rho_0 = -0.5$ and $\mu_{12} = \mu_{21} = 0.2$ is presented in bottom left panel. The eigenvalues spectra on the complex plane corresponding to $q = 0, 1, ..., 50$ is shown in the top right panel for the repulsive and bottom right panel for the attractive cases. The symbols used to represent the eigenvalues for different values of q are shown in the Table 5.1.

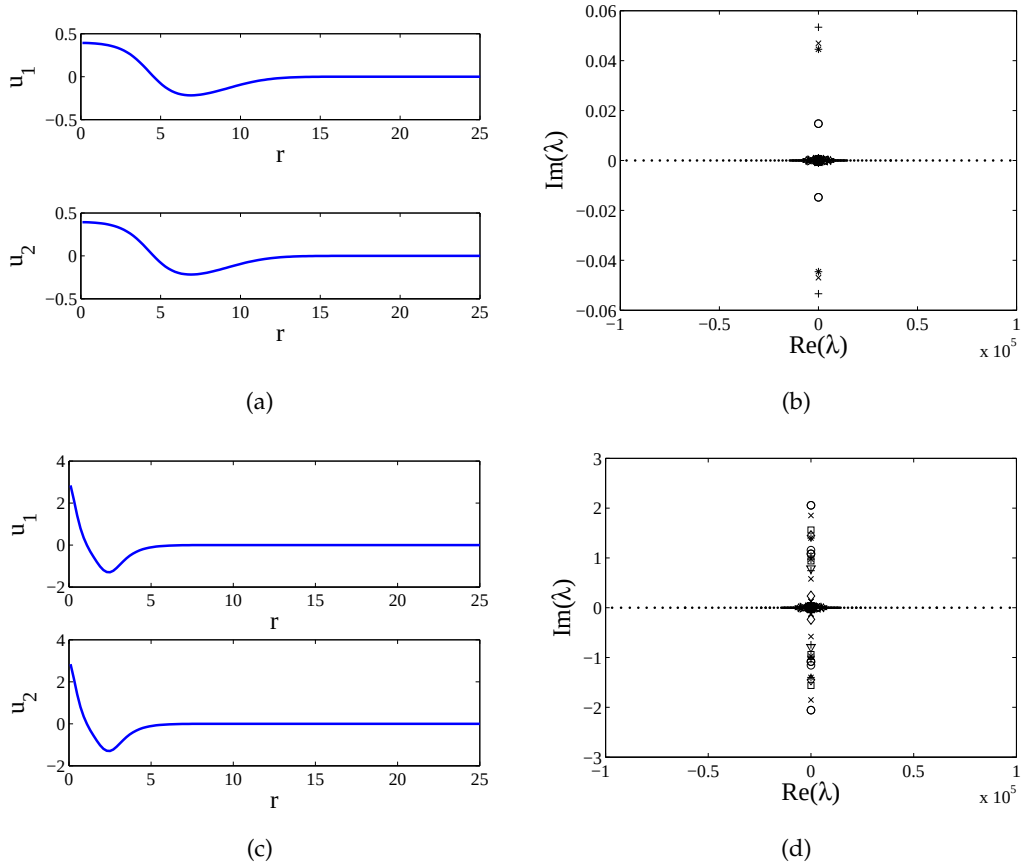

Figure 5.2: Same as Fig. 5.1 but for chargeless first excited state ($m = 0$ and $n_r = 1$).

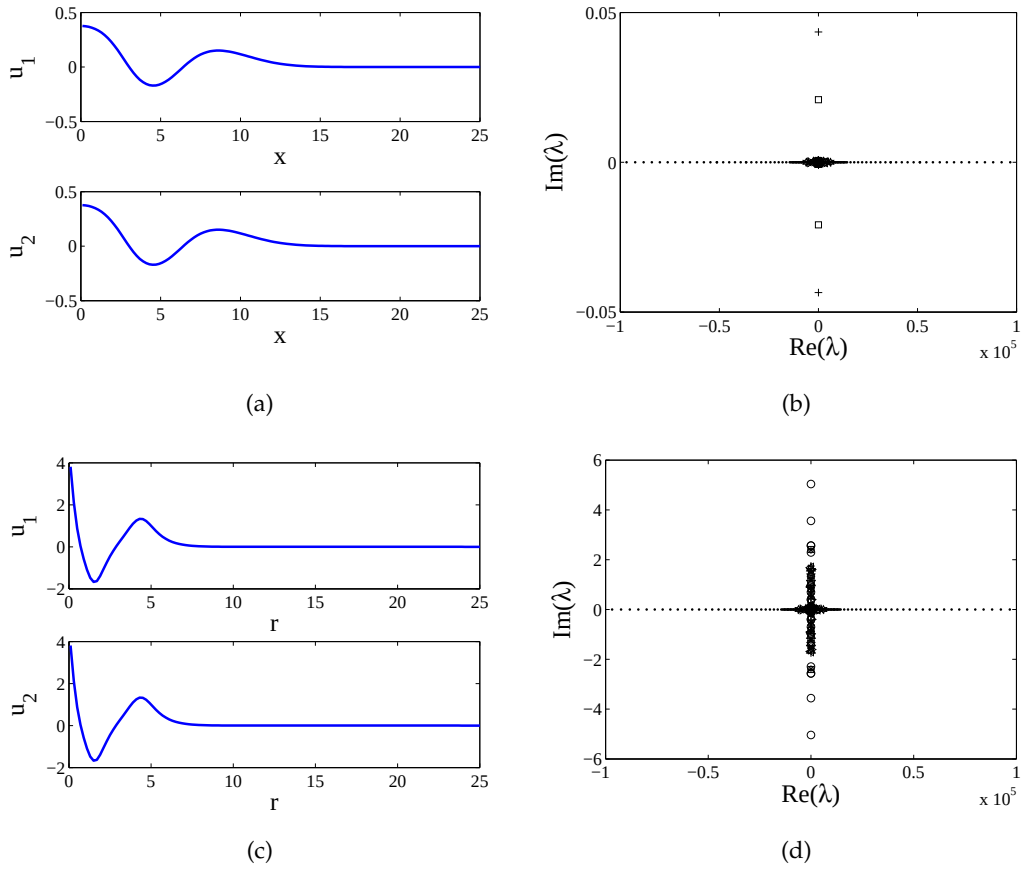

Figure 5.3: Same as Fig. 5.1 but for chargeless second excited state ($m = 0$ and $n_r = 2$) with $\rho_0 = 0.6$ for the repulsive case.

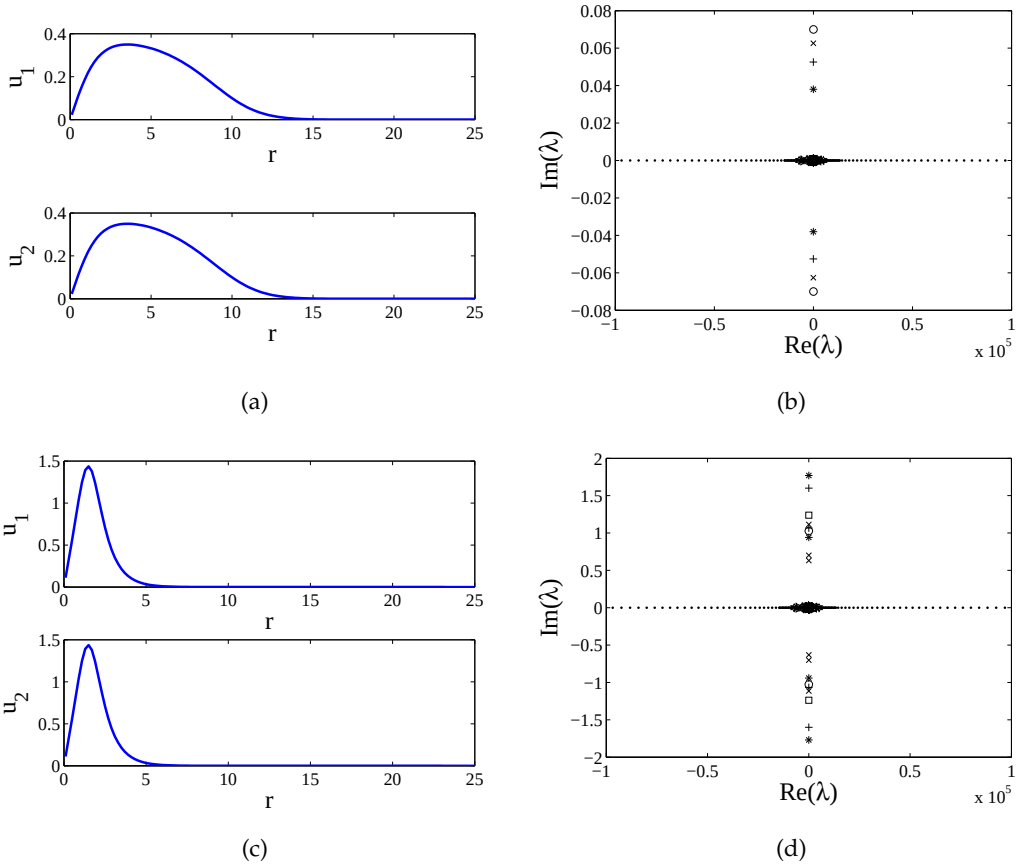

Figure 5.4: Same as Fig. 5.1 but with topological charge $m = 1$ and $n_r = 0$.

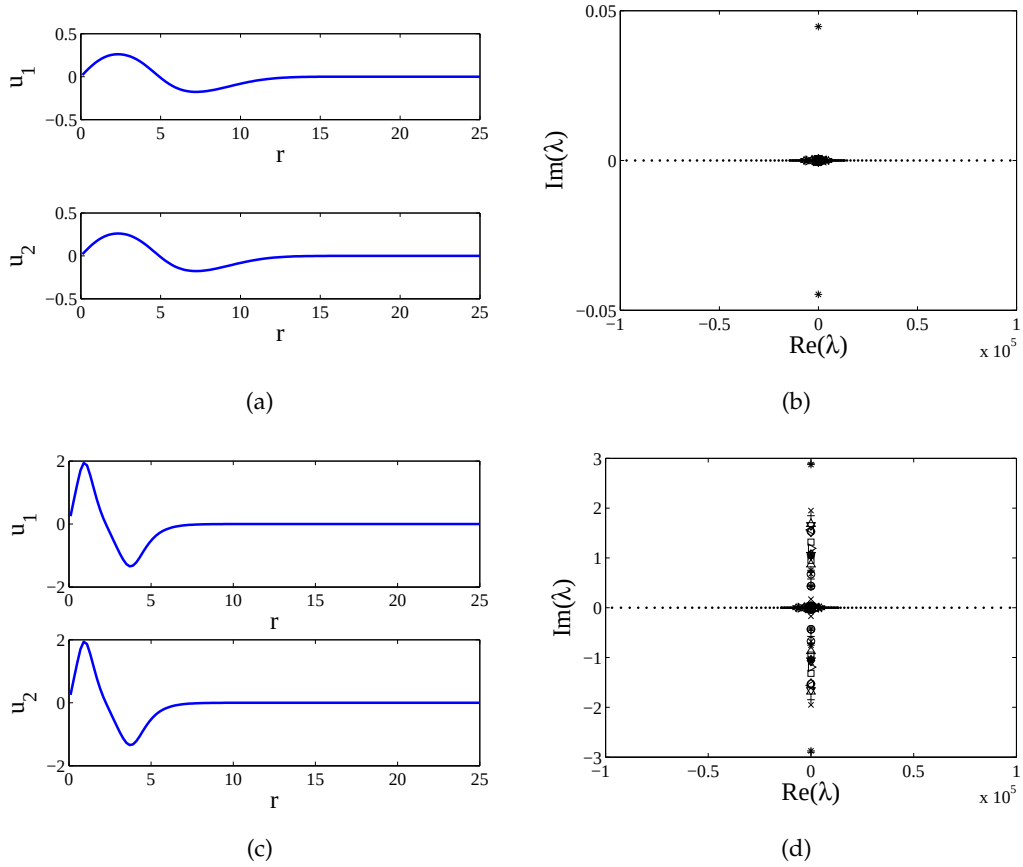

Figure 5.5: Same as Fig. 5.1 but with topological charge $m = 1$ and $n_r = 1$.

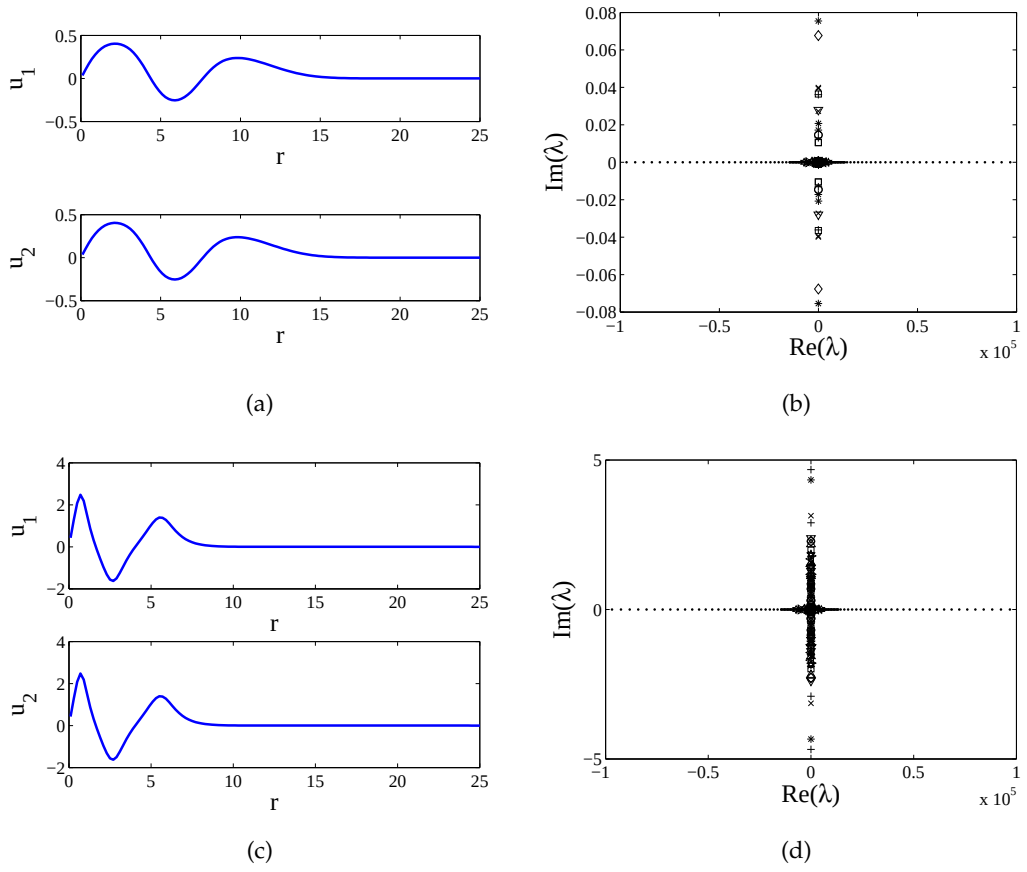

Figure 5.6: Same as Fig. 5.1 but with topological charge $m = 1$, $n_r = 2$ and $\rho_0 = 0.8$ for the repulsive case.

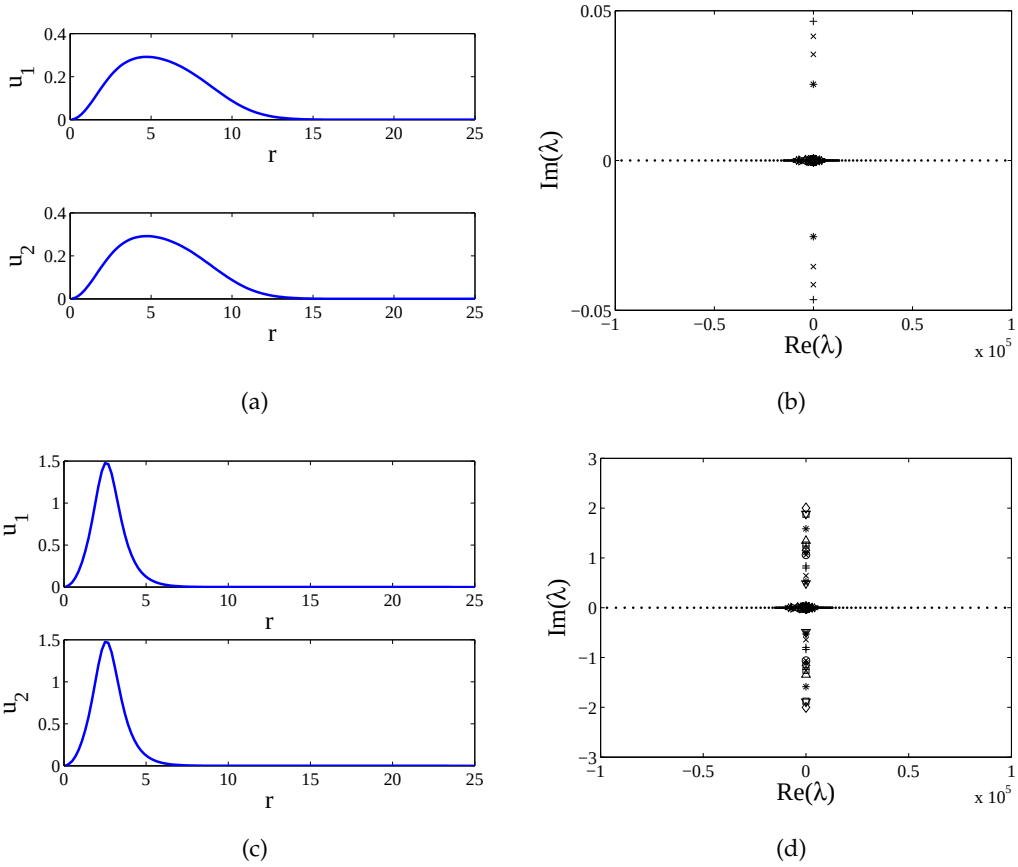

Figure 5.7: Same as Fig. 5.1 but with topological charge $m = 2$ and $n_r = 0$.

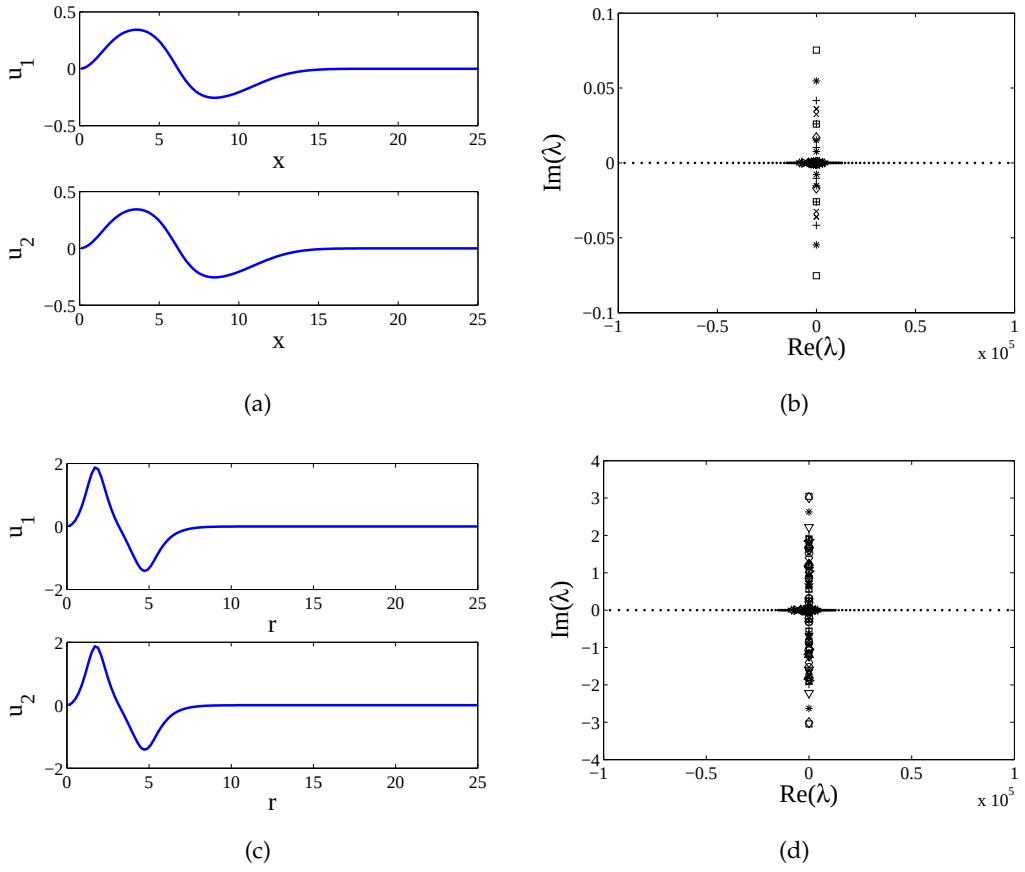

Figure 5.8: Same as Fig. 5.1 but with topological charge $m = 2$, $n_r = 1$ and $\rho_0 = 0.7$ for the repulsive case.

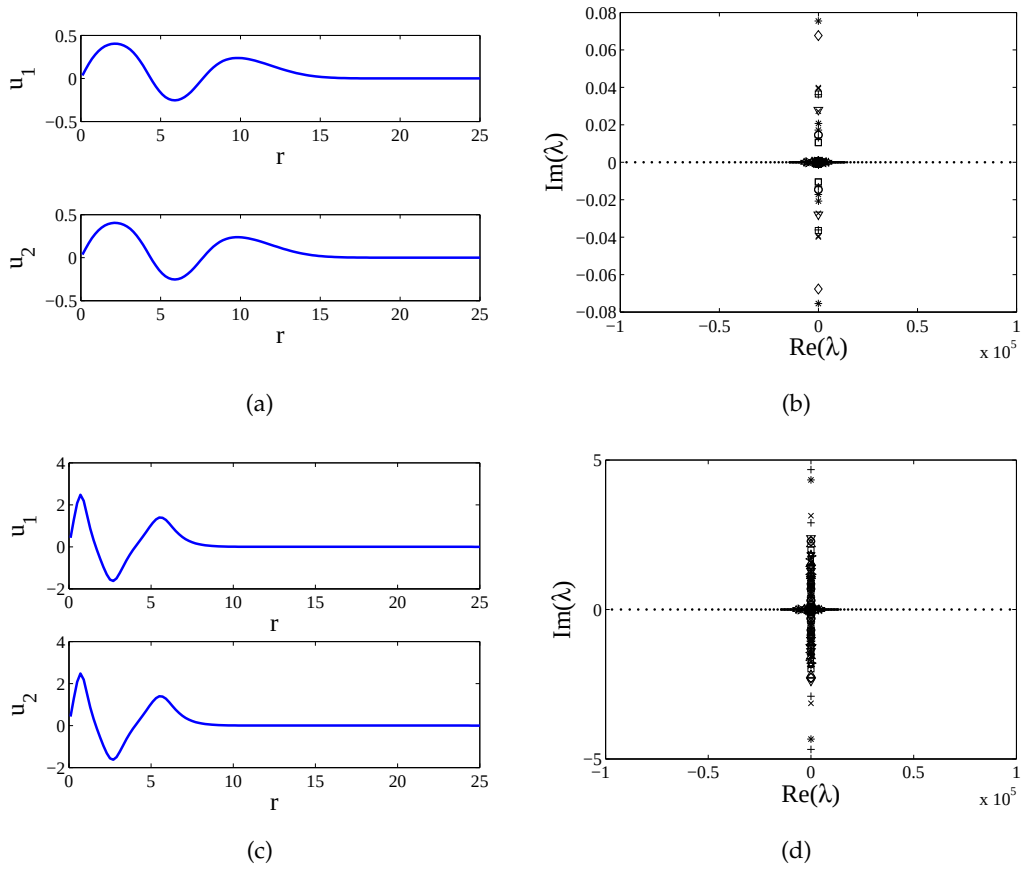

Figure 5.9: Same as Fig. 5.1 but with topological charge $m = 2$, $n_r = 2$ and $\rho_0 = 0.8$ for the repulsive case.

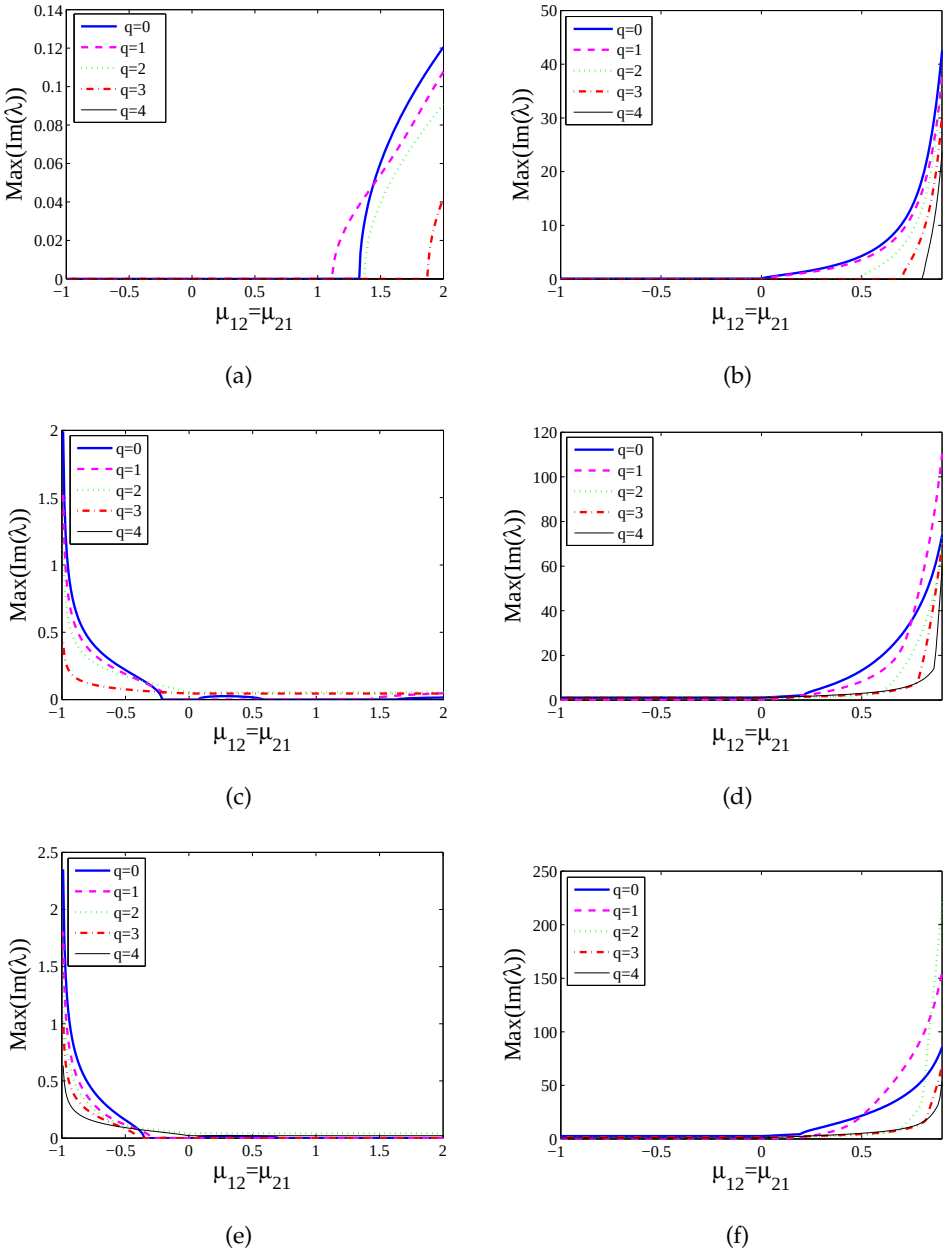

Figure 5.10: Linear stability curves for non topological charge $(m = 0)$ solutions. The left and right panels correspond to the repulsive and attractive intra-atomic interactions, respectively. The upper two panels show the graphs of maximum imaginary parts as functions of nonlinear coupling $\mu_{12} = \mu_{21}$ of primary eigenvalues for $q = 0, 1, 2, 3, 4$ for the ground state $(n_r = 0)$. The middle and the lower panels depict respectively the first and second excited states. The small magnitude of the unstable eigenvalues in the left panels indicate the slow dynamical development of the instability. This also reveals that such steady state solutions when perturbed slightly, will show deformation or destruction of initial structure after a relatively long time. On the other hand, the magnitude of the unstable eigenvalues in the right panels is very high and indicates the shattering of the structure after a small time.

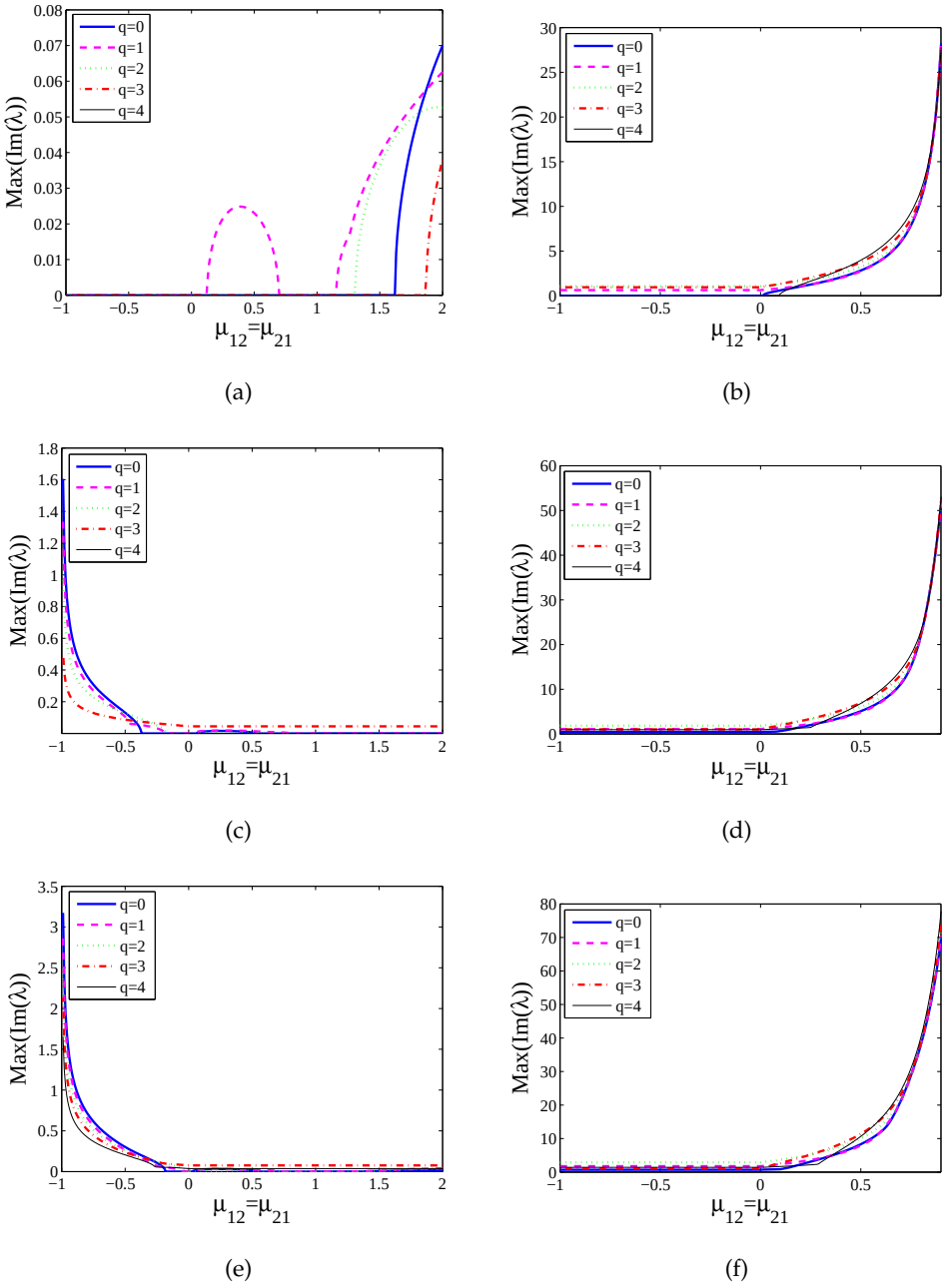

Figure 5.11: Same as Fig. 5.10 but for unit topological charge $(m = 1)$ solutions. In the top left panel, their exist stability regions of nonlinear coupling where the ground state can be stable for the case of repulsive intra-atomic interaction. The top right panel shows that the ground state for the case of attractive intra-atomic interaction remains unstable. The remaining panels show that the first and second excited states are unstable in both cases.

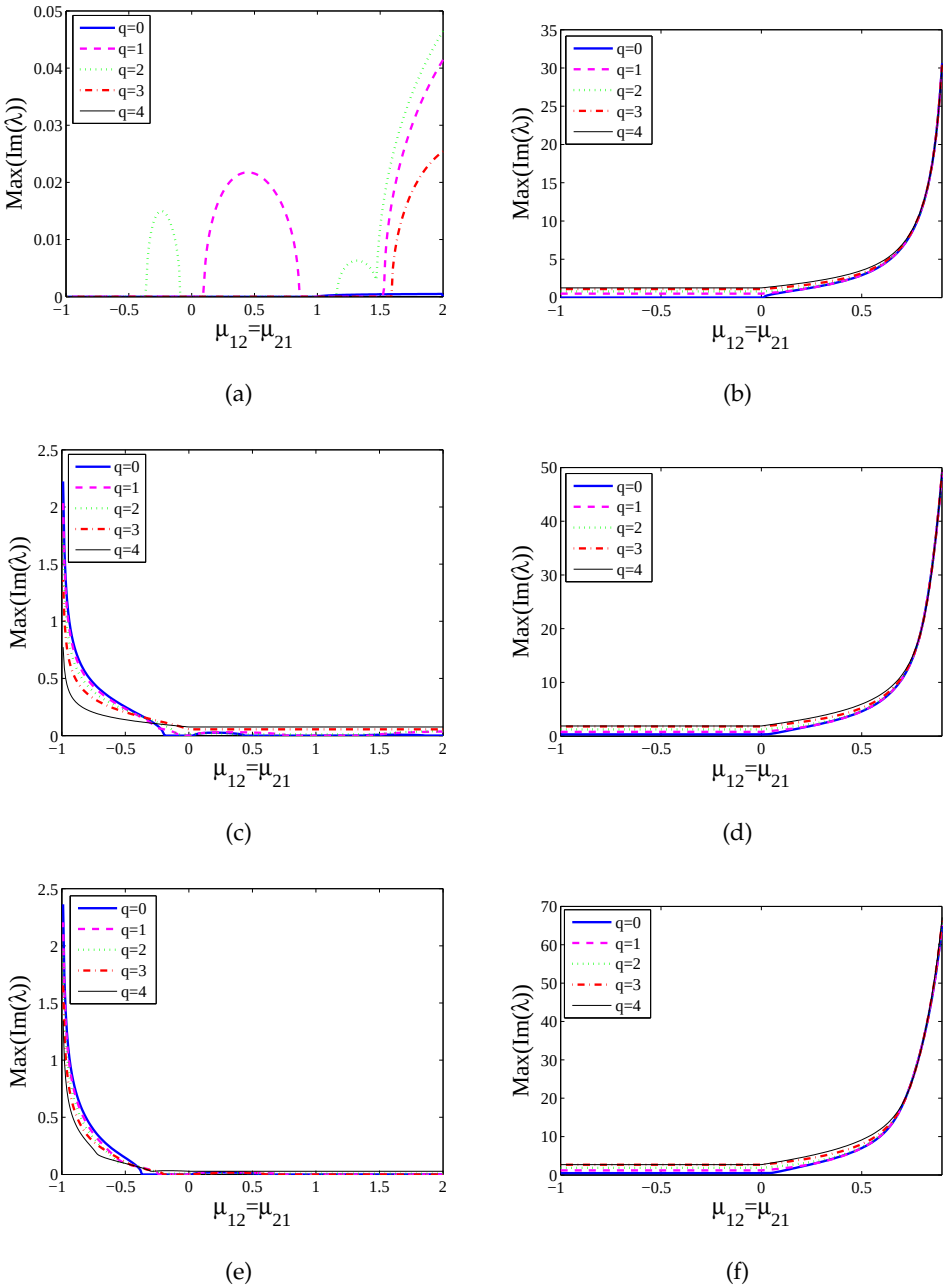

Figure 5.12: Same as Fig. 5.10 but for doubly charged $(m = 2)$ solutions.

Next, we examine the cases of unit ($m = 1$) and doubly ($m = 2$) charged solutions. The top left panels of Fig. 5.11 and Fig. 5.12 show the instability of the ground state in the defocusing case. However, there exist regions for the values of nonlinear coupling where stability of these ground states can be possible. In the focusing case, the ground states are unstable for all values of nonlinear coupling as can be seen in the top right panels of Fig. 5.11 and Fig. 5.12. Similarly, the first and second excited states are also unstable in both attractive and repulsive cases (cf. the middle and bottom panels of Fig. 5.11 and Fig. 5.12).

Let us now investigate the time evolution of each solution in detail. We discuss the time evolution of each solution when a random perturbation of order 10^{-4} is added to the steady state structure at time $t = 0$. First, we consider the case of $m = 0$. In the defocusing case, the ground state for different values of time is shown in Fig. 5.13. The solution is unstable for the parameter values used due to the $q = 0, 1, 2, 3$ modes. A strong inter-atomic repulsion results in the shift of the respective central atomic densities away from the centres in both components, however, in the opposite directions. The solutions tend to carry all the mass due to the $q = 0$ mode. Moreover, the solution is subject to azimuthal modulational instability due to the $q = 1, 2, 3$ eigenmodes. On the other hand, the time evolution of the ground state in the focusing case is displayed in Fig. 5.14. The solution in this case is unstable due to the $q = 0, 1$ eigenmodes. The solution in one of the components tends to a thin spike carrying all the mass due to the $q = 0$ eigenmode. However, the solution in the other component start rotating due to the $q = 1$ eigenmode and results in the reduction of the central atomic density. Also, the atomic mass is pushed away from the centre due to repulsive interatomic interaction. The central atomic density in this component reduces up to a critical value and then starts increasing and ultimately tends to a thin spike carrying all the mass at the centre.

The results obtained for the first excited state with $m = 0$ in the defocusing case are demonstrated in Fig. 5.15. The solution is unstable due to the same values of q as for the ground state. However, the instability rate is comparatively smaller. The central atomic density peak of the first excited state decays due to the $q = 0$ mode while the two humps at $t = 200$ corroborate the instability due to the $q = 2$ mode. It is also evident that the decay of the central atomic density peaks are simultaneously followed by irregular deposition of atoms on the brim of the basal rings in both components. The central and the other atomic density peaks localized on the outer brim of the basal ring become more intense with time. The broadening of the atomic density peaks formed on the outer rings corresponds to the reduction in the width of central atomic density

peaks. The process results in the deformation of outer rings and ultimately the whole atomic structure breaks up.

On the other hand, for the focusing case in Fig. 5.16, the instability develops as the eigenmodes corresponding to nonzero values of q induce rotation in the outer rings in one of the components. The value of cental atomic density in other component increases due to the most unstable mode $q = 0$ and ultimately results in the appearance of thin spikes in both components.

Next, we explain the second excited state in the absence of topological charge in Fig. 5.17. Unlike the ground and the first excited states, the solution in the defocusing case is stable to the $q = 0$ mode and hence there is no growth or decay seen in the central atomic density peak. However, the instability appears due to the $q = 2$ mode. The instability rate is small like the first excited state. Due to the instability, localized density peaks appear on the peripheries of first and second rings and grow with time which results in the destruction of the structure. In Fig. 5.18, for the focusing case, the decrease in the central atomic density in both components is directly linked with the increase in the atomic density on the peripheries of the outer rings. Nevertheless, the solution in both components tend to thin spikes due to the most unstable mode $q = 0$.

We have discussed the dynamical evolution and stability of non topologically charged solutions. Now, we take into account the solutions with non-zero topological charge at the centre of the external magnetic trap. We present the time evolution of the ground state with unit topological charge $m = 1$ in Fig. 5.19 and Fig. 5.20 for the defocusing and focusing cases respectively. The solutions start rotating due to the nonzero value of m as can be seen at $t = 100$ and $t = 5$ respectively in the defocusing and focusing cases. The vortices urge the atomic mass away from the centre of the trap in both cases. This act of shoving the atomic mass is a general characteristic in topologically charged solution.

In Figs. 5.21-5.24, we display the time dynamics of the first and second excited states in the presence of unit topological charge. In the defocusing case, both states are affected by very small values of the $q = 0, 3$ eigenmodes where instability emerges in the rings of the clouds and results in the deformation of the structures. In the focusing case, several spikes appear that indicate the instability of the solutions. Finally, we present the similar results for the stability of ground and excited states in case of topological charge $m = 2$ in Figs. 5.25-5.30

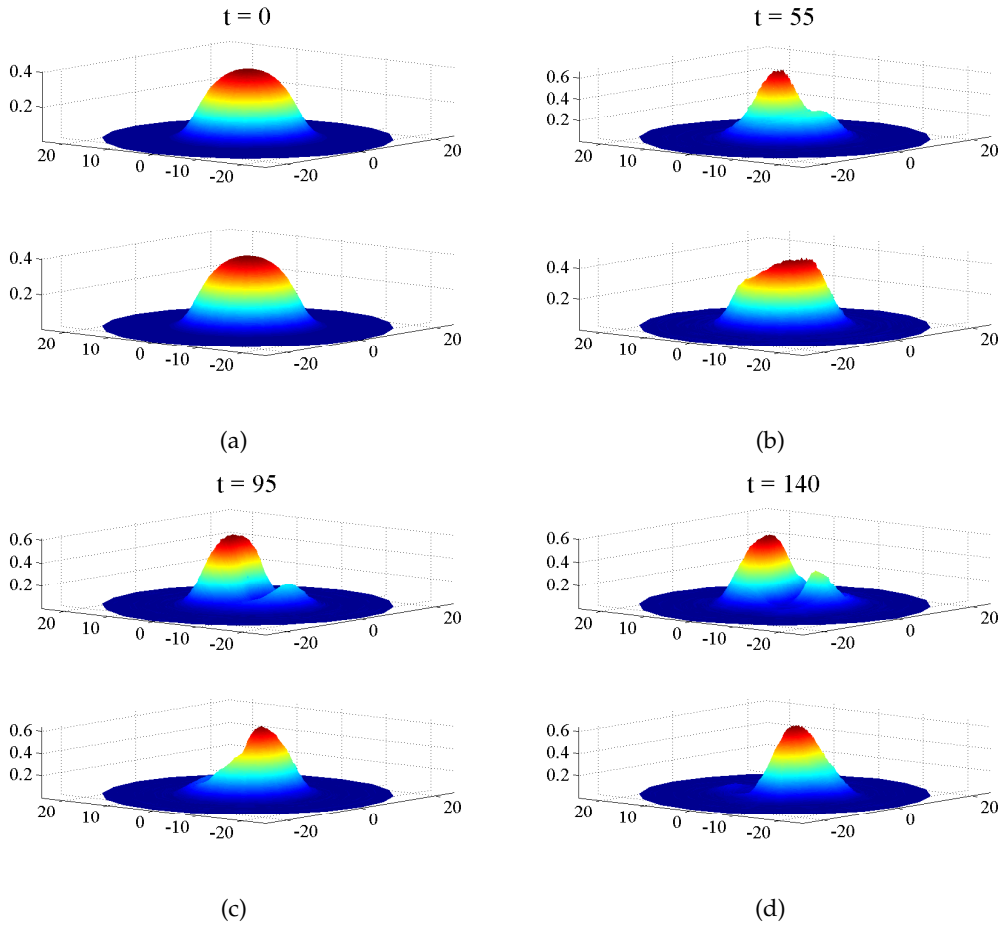

Figure 5.13: Time evolution of the solution shown in the top left panel of Fig. 5.1 in case of defocusing nonlinearity with $m = 0$, $n_r = 0$ and $\mu_{12} = \mu_{21} = 2$.

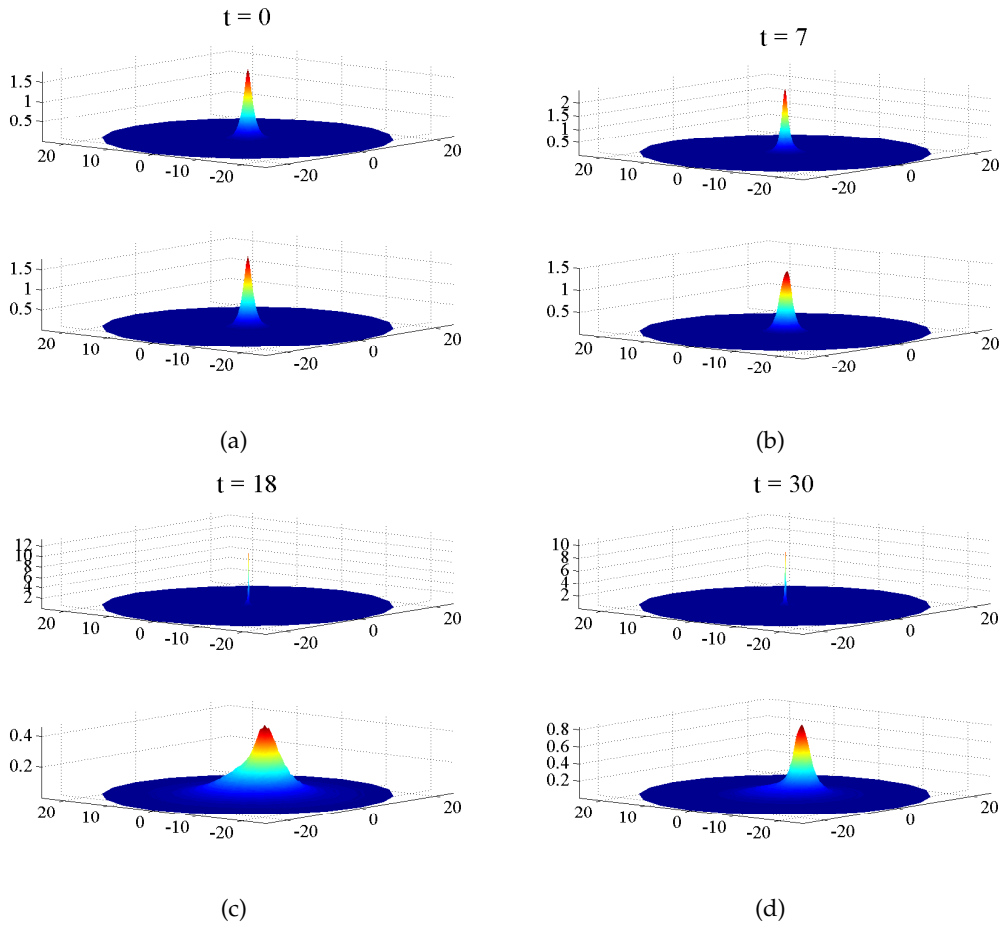

Figure 5.14: Time evolution of the solution shown in bottom left panel of Fig. 5.1 in case of focusing nonlinearity with $m = 0$, $n_r = 0$ and $\mu_{12} = \mu_{21} = 0.2$.

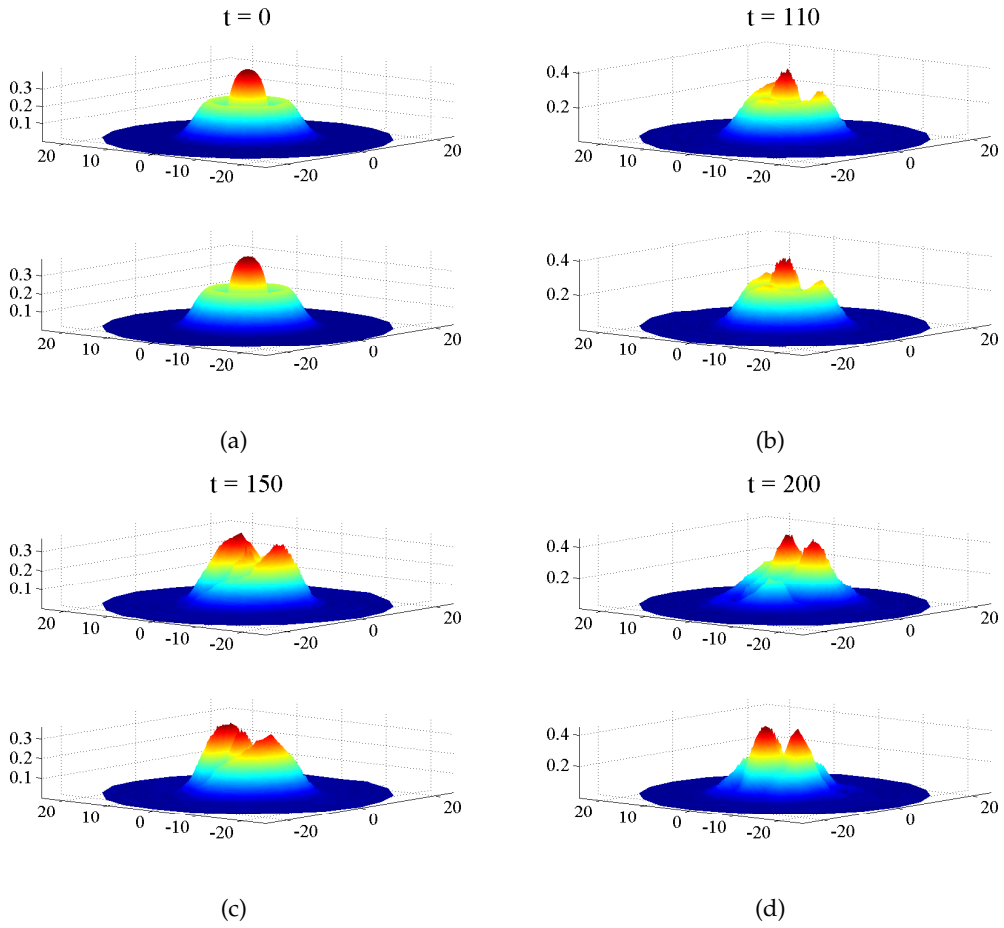

Figure 5.15: Time evolution of the solution shown in the top left panel of Fig. 5.2 in case of defocusing nonlinearity with $m = 0$, $n_r = 1$ and $\mu_{12} = \mu_{21} = 2$.

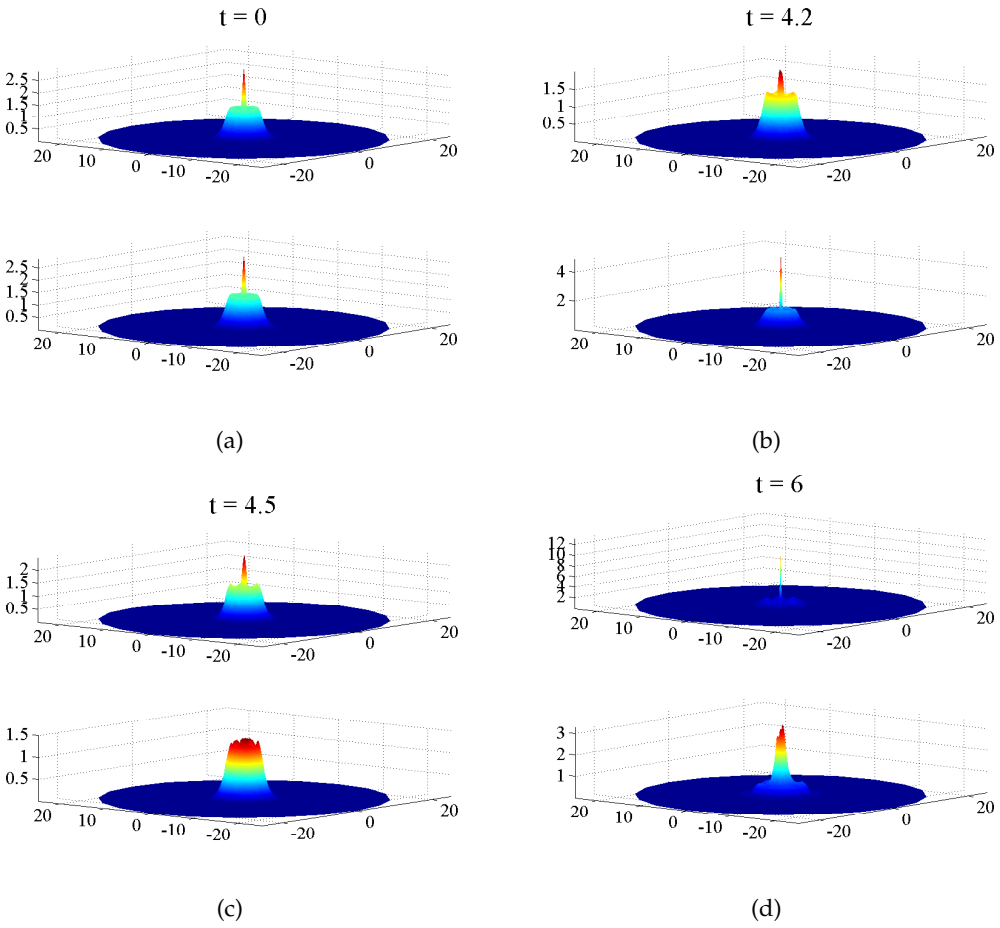

Figure 5.16: Time evolution of the solution shown in bottom left panel of Fig. 5.2 in case of focusing nonlinearity with $m = 0$, $n_r = 1$ and $\mu_{12} = \mu_{21} = 0.2$.

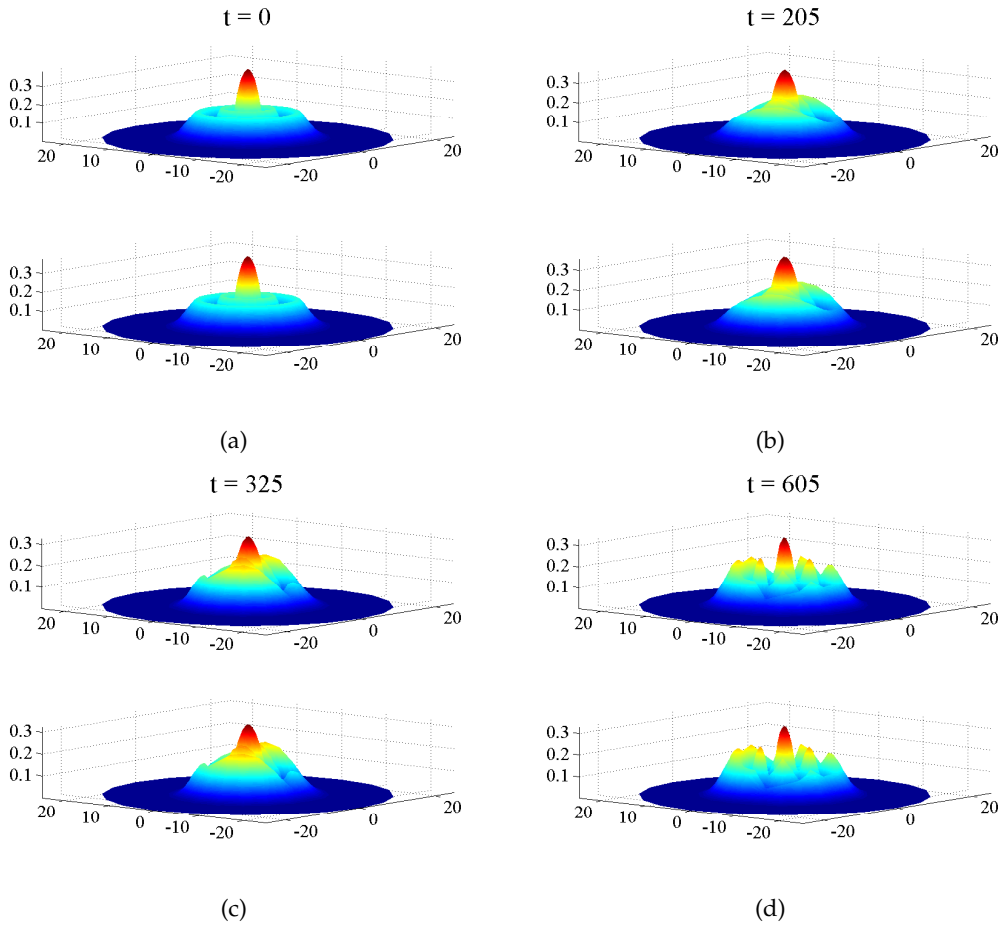

Figure 5.17: Time evolution of the solution shown in the top left panel of Fig. 5.3 in case of defocusing nonlinearity with $m = 0$, $n_r = 2$ and $\mu_{12} = \mu_{21} = 2$.

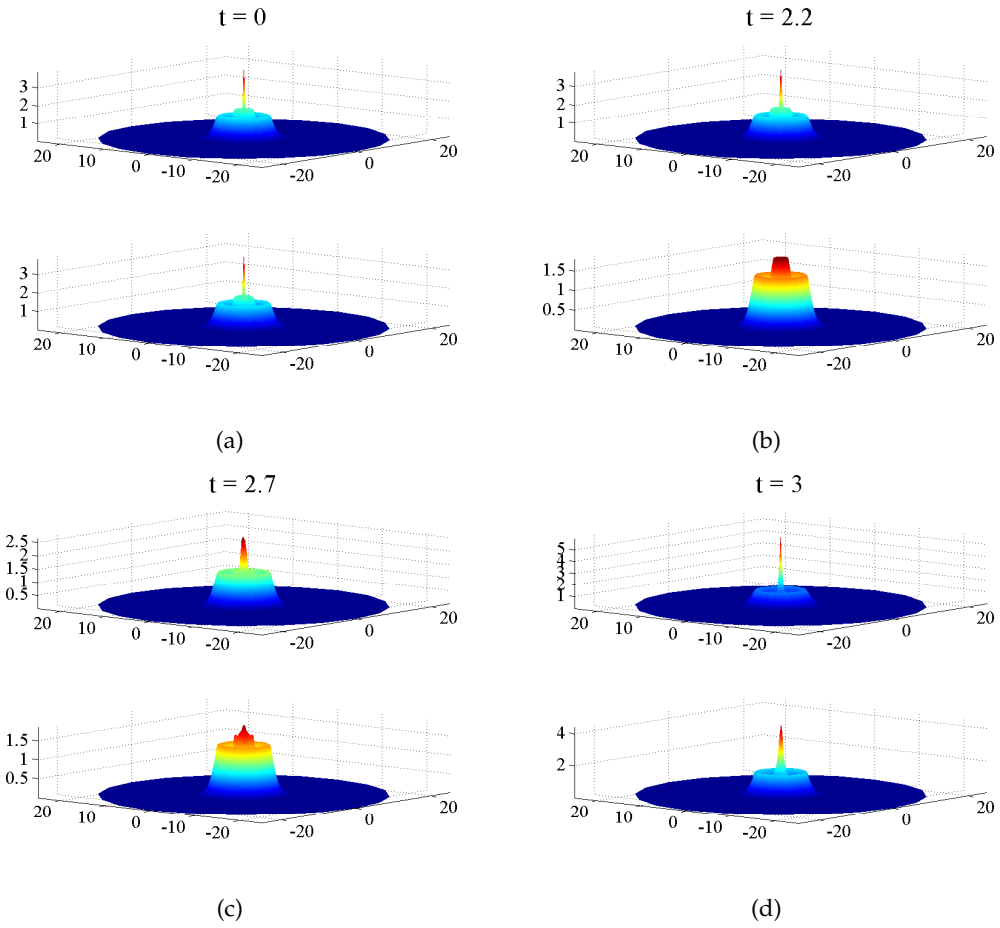

Figure 5.18: Time evolution of the solution shown in bottom left panel of Fig. 5.3 in case of focusing nonlinearity with $m = 0$, $n_r = 2$ and $\mu_{12} = \mu_{21} = 0.2$.

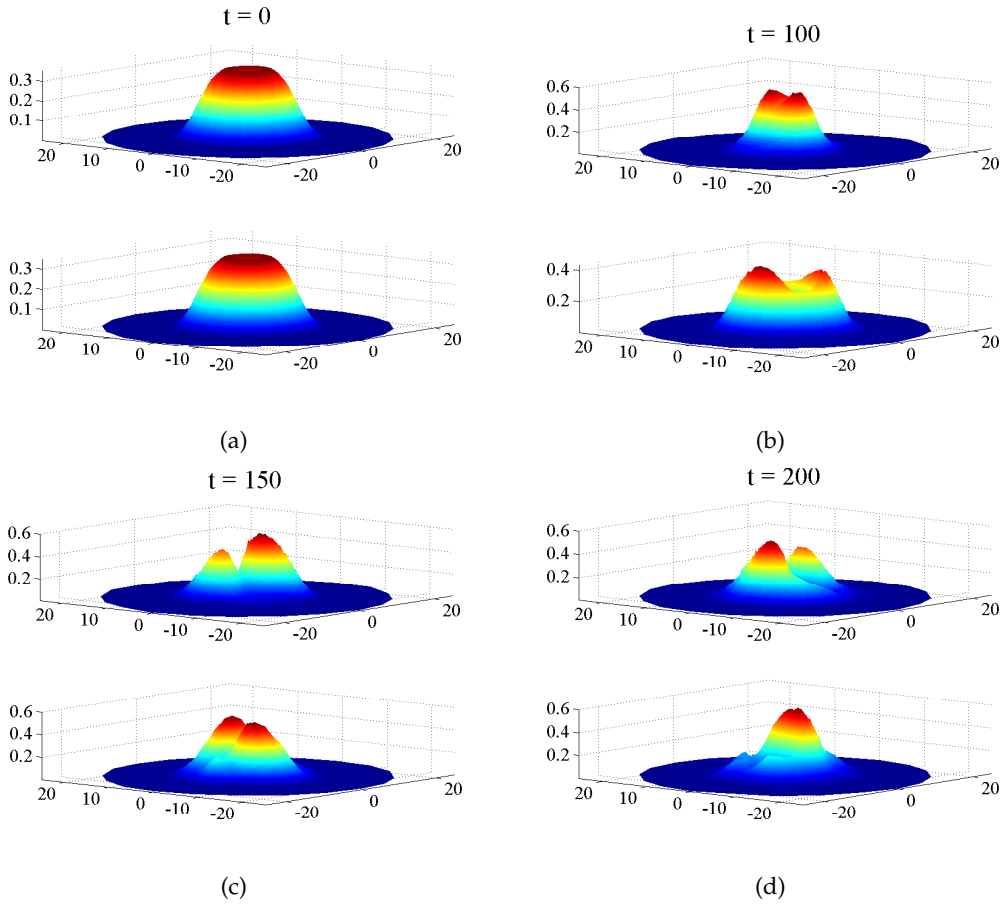

Figure 5.19: Time evolution of the solution shown in the top left panel of Fig. 5.4 in case of defocusing nonlinearity with $m = 1$, $n_r = 0$ and $\mu_{12} = \mu_{21} = 2$.

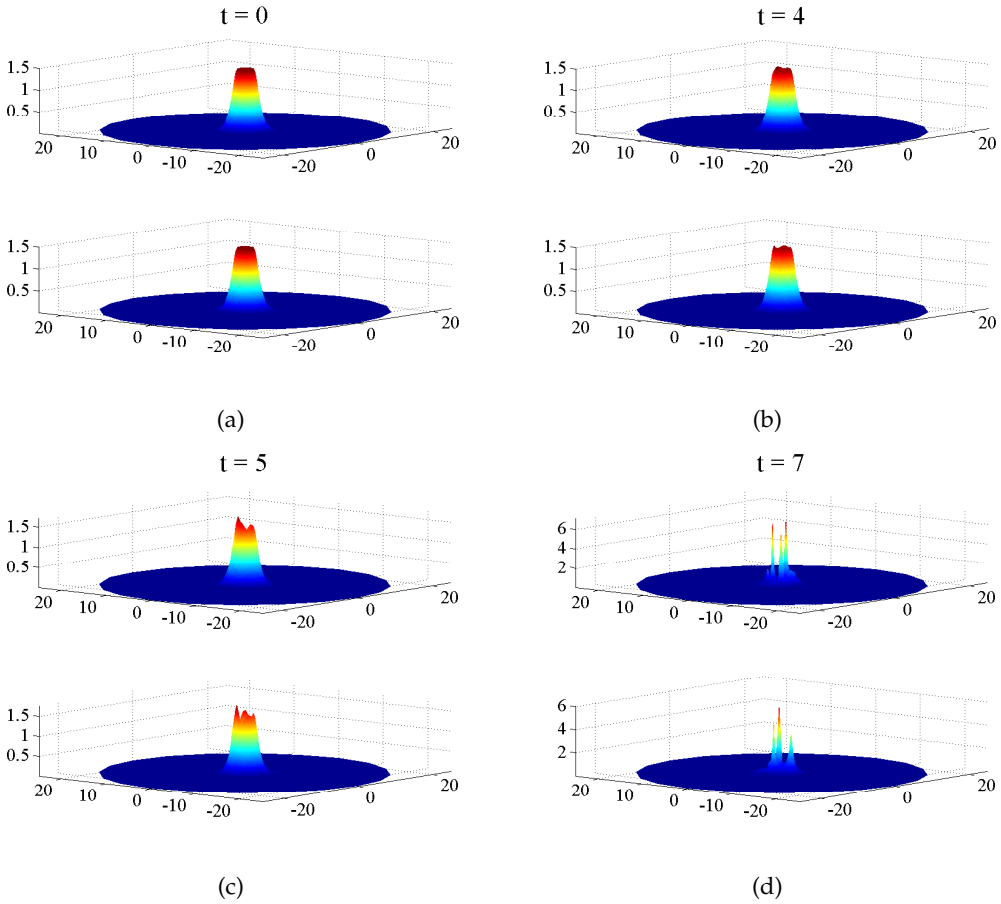

Figure 5.20: Time evolution of the solution shown in bottom left panel of Fig. 5.4 in case of focusing nonlinearity with $m = 1$, $n_r = 0$ and $\mu_{12} = \mu_{21} = 0.2$.

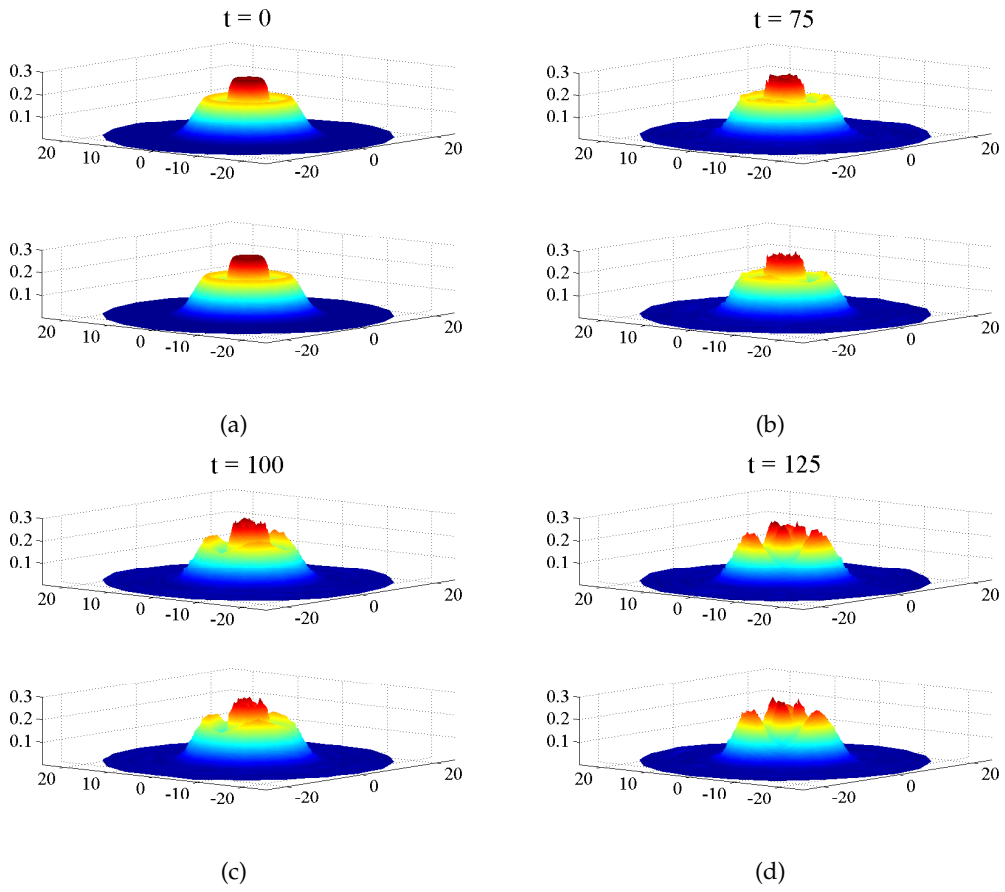

Figure 5.21: Time evolution of the solution shown in the top left panel of Fig. 5.5 in case of defocusing nonlinearity with $m = 1$, $n_r = 1$ and $\mu_{12} = \mu_{21} = 2$.

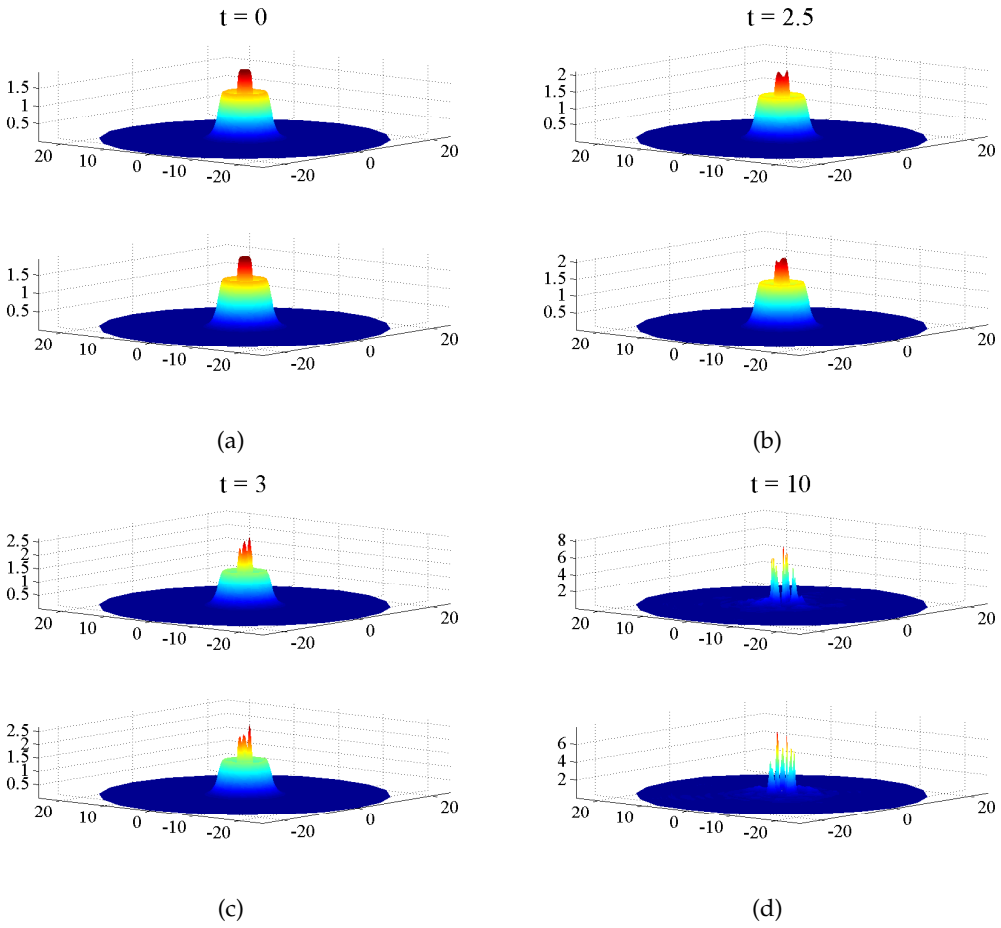

Figure 5.22: Time evolution of the solution shown in bottom left panel of Fig. 5.5 in case of focusing nonlinearity with $m = 1$, $n_r = 1$ and $\mu_{12} = \mu_{21} = 0.2$.

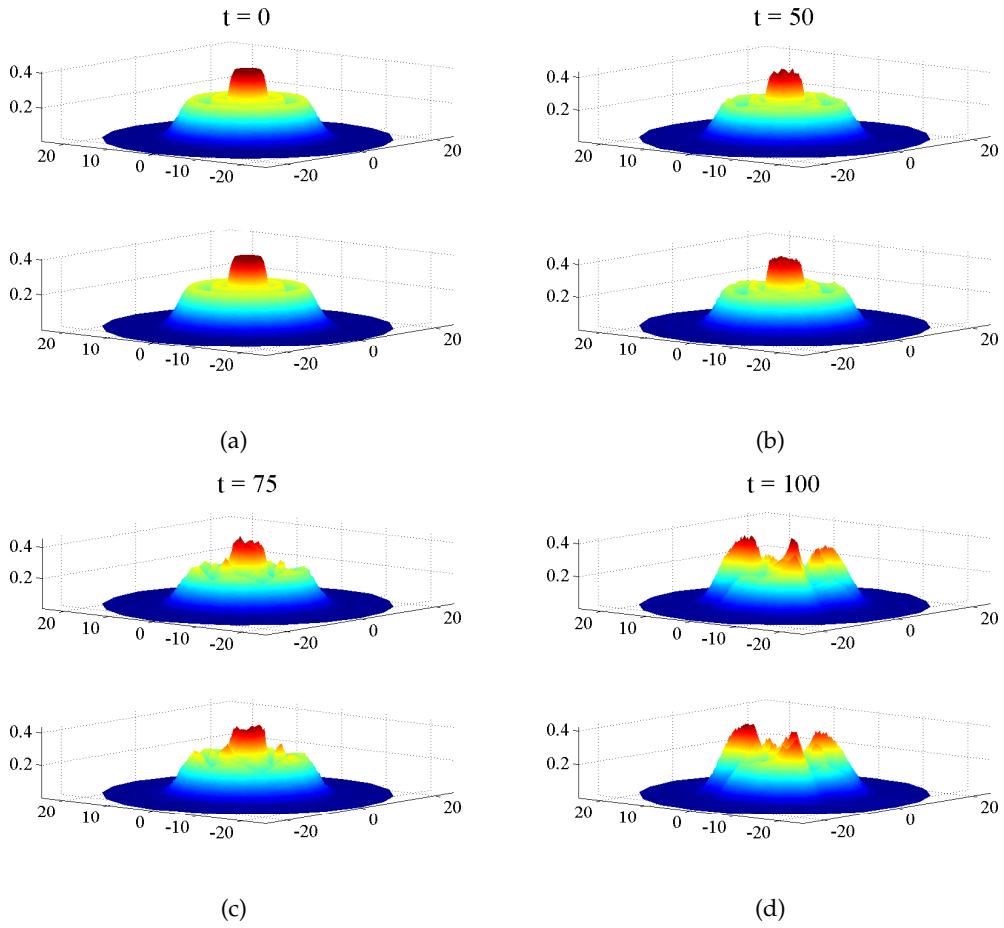

Figure 5.23: Time evolution of the solution shown in the top left panel of Fig. 5.6 in case of defocusing nonlinearity with $m = 1$, $n_r = 2$ and $\mu_{12} = \mu_{21} = 2$.

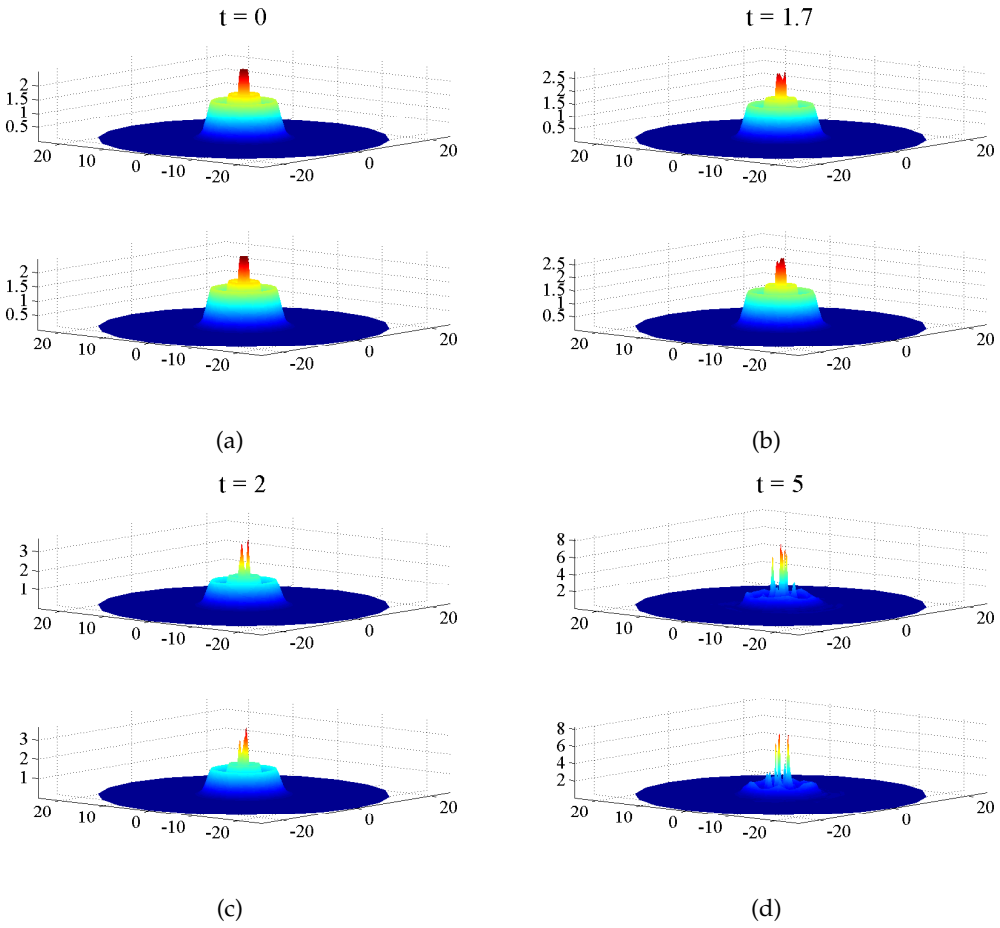

Figure 5.24: Time evolution of the solution shown in bottom left panel of Fig. 5.6 in case of focusing nonlinearity with $m = 1$, $n_r = 2$ and $\mu_{12} = \mu_{21} = 0.2$.

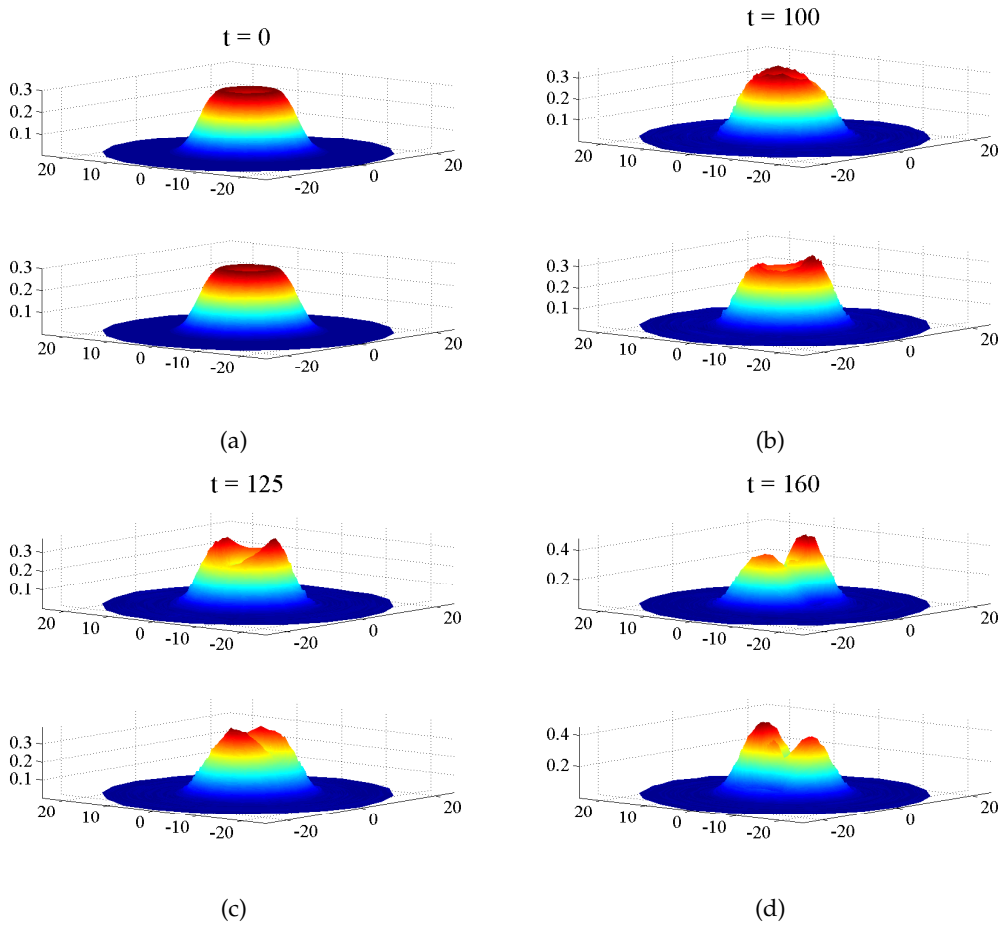

Figure 5.25: Time evolution of the solution shown in the top left panel of Fig. 5.7 in case of defocusing nonlinearity with $m = 2$, $n_r = 0$ and $\mu_{12} = \mu_{21} = 2$.

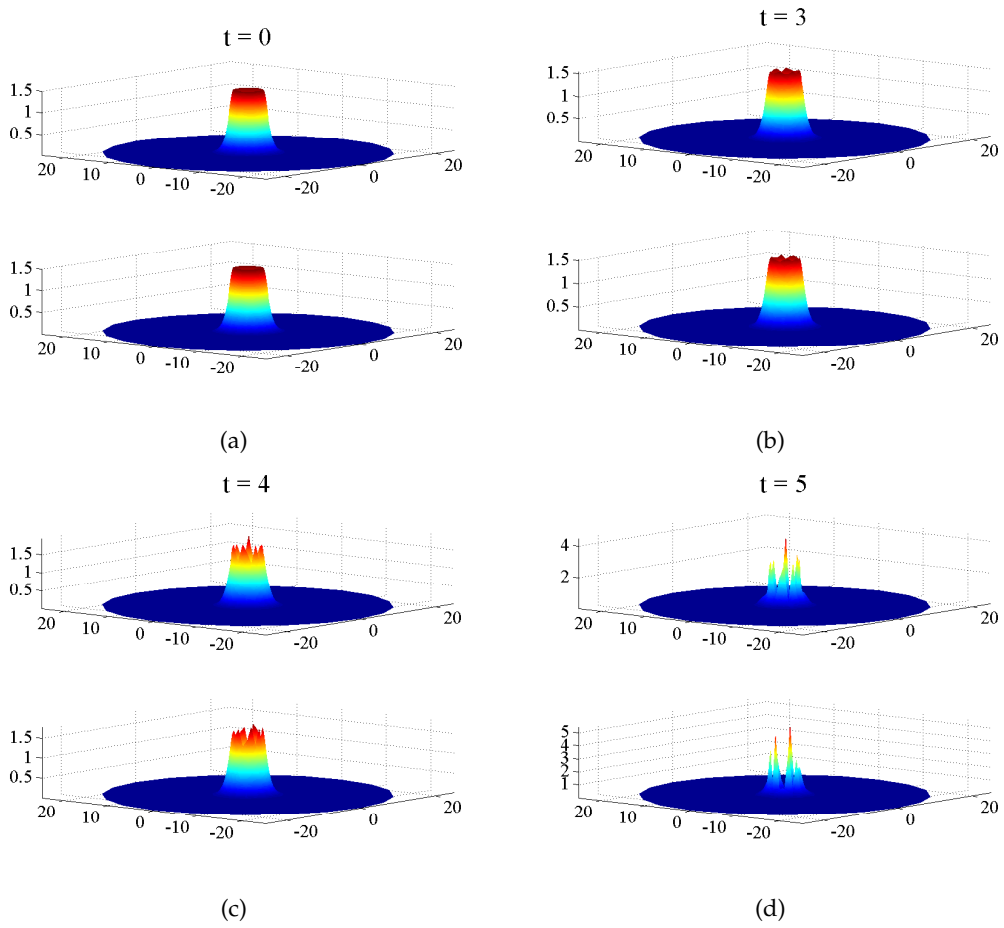

Figure 5.26: Time evolution of the solution shown in bottom left panel of Fig. 5.7 in case of focusing nonlinearity with $m = 2$, $n_r = 0$ and $\mu_{12} = \mu_{21} = 0.2$.

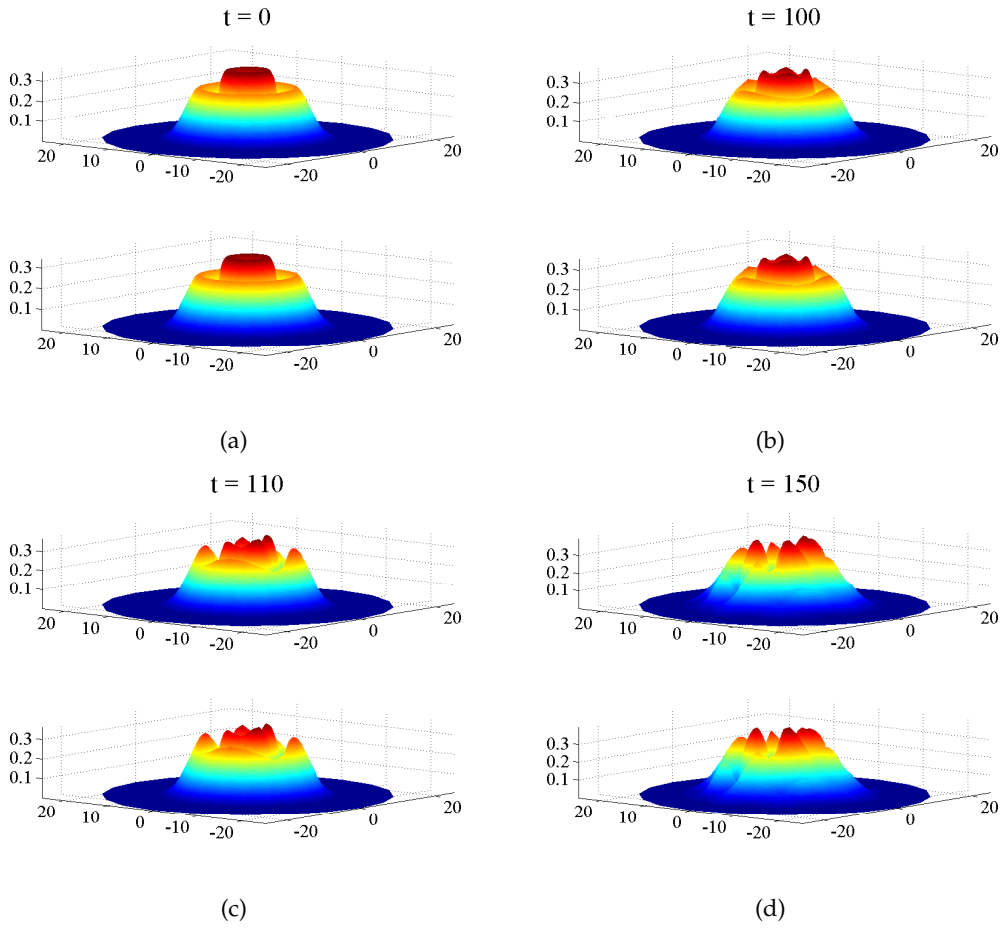

Figure 5.27: Time evolution of the solution shown in the top left panel of Fig. 5.8 in case of defocusing nonlinearity with $m = 2$, $n_r = 1$ and $\mu_{12} = \mu_{21} = 2$.

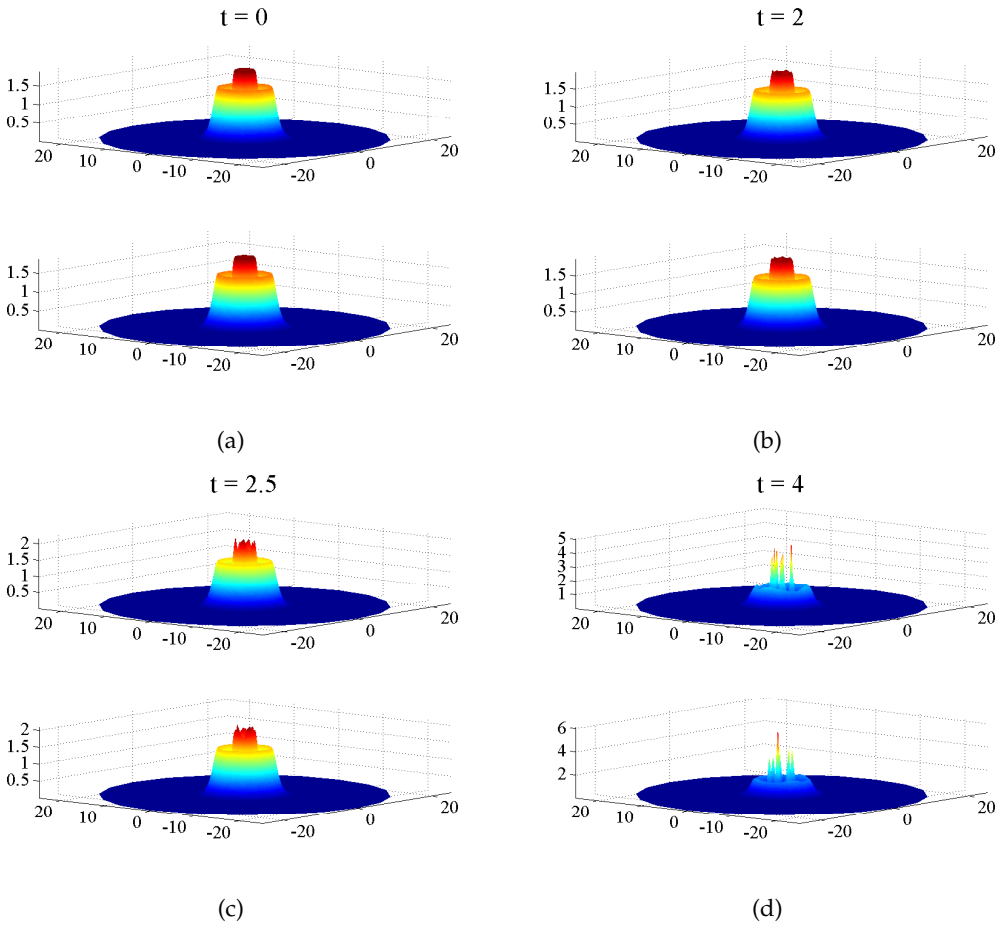

Figure 5.28: Time evolution of the solution shown in bottom left panel of Fig. 5.8 in case of focusing nonlinearity with $m = 2$, $n_r = 1$ and $\mu_{12} = \mu_{21} = 0.2$.

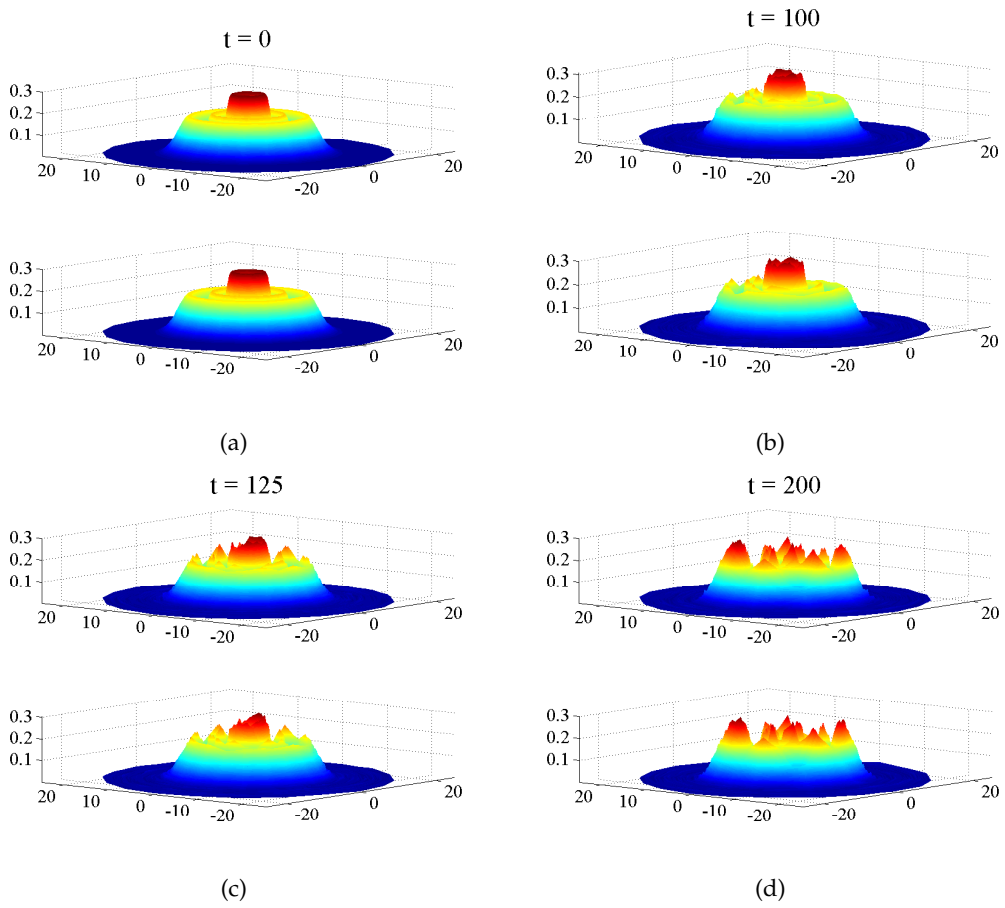

Figure 5.29: Time evolution of the solution shown in the top left panel of Fig. 5.9 in case of defocusing nonlinearity with $m = 2$, $n_r = 2$ and $\mu_{12} = \mu_{21} = 2$.

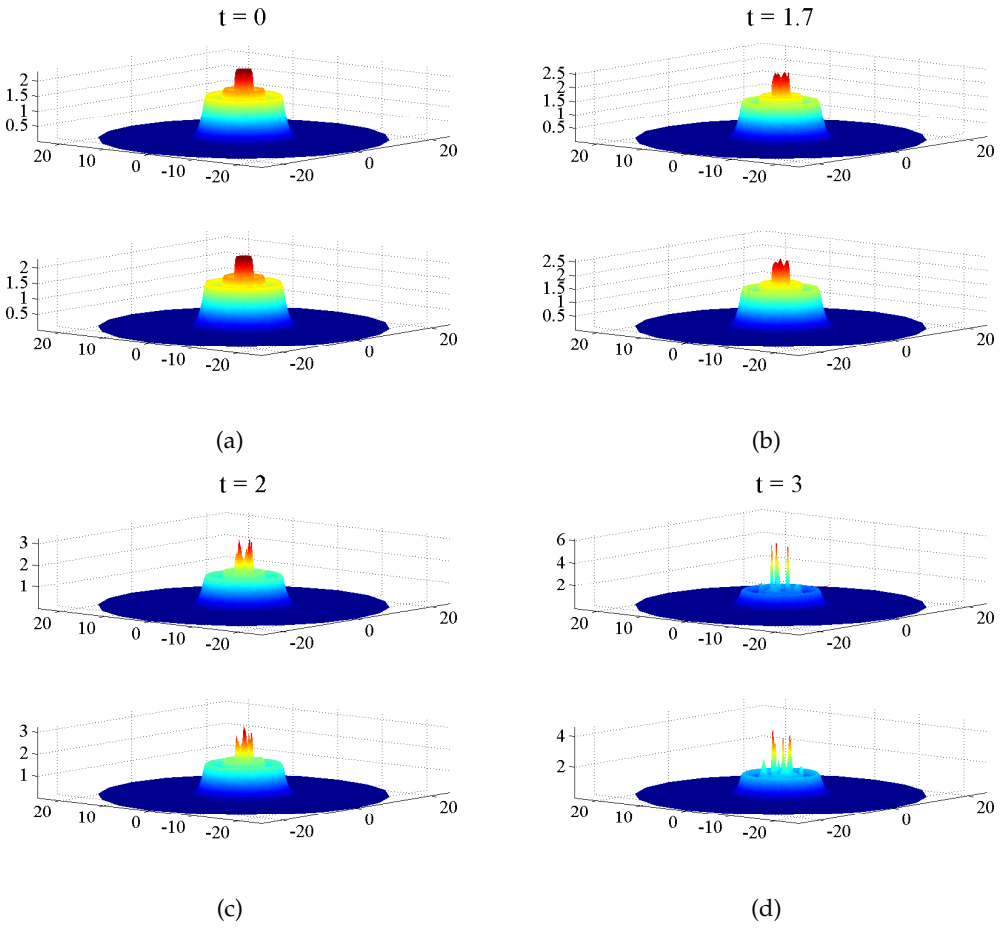

Figure 5.30: Time evolution of the solution shown in bottom left panel of Fig. 5.9 in case of focusing nonlinearity with $m = 2$, $n_r = 2$ and $\mu_{12} = \mu_{21} = 0.2$.

5.4.2 Stability analysis of the linearly coupled system

So far, we considered the case of $k = 0$. Let us analyze the stability of the solutions presented above in the case when system of GP Eq. (5.3.1) is linearly coupled, i.e. $k \neq 0$ with $\mu_{12} = \mu_{21} = 0$. The maximum imaginary parts of the primary $(q = 0, 1, 2, 3, 4)$ eigenvalues for $m = 0, 1$ and 2, respectively, are displayed in Figs. 5.31-5.33. For each value of m, the stability curves for the ground and first two excited states are depicted respectively in left panels for the defocusing case and in the right panels for the focusing case. In Fig. 5.31, the top left and right panels show that the ground states with $m = 0$ are unstable in the defocusing and focusing cases. Nonetheless, these states can be made stable by controlling the value of linear coupling. The stability can be possible only for the positive values of k in both cases. The first and second excited states with $m = 0$ are unstable in focusing and defocusing cases as can be seen in the middle and lower panels of Fig. 5.31.

The top left panels of Fig. 5.32 and Fig. 5.33 depict that the unit and doubly charged ground states in the defocusing case are unstable but can be stabilize by adjusting the value of k. In fact, the ground state with unit topological charge is stable for all positive values of k where it exists whereas for the ground state with $m = 2$, there exists zones of positive values of k where the solution is stable. The other excited states are found to be unstable.

5.4.3 Stability analysis in the presence of linear and nonlinear coupling

Now, we examine the stability of the solutions of the system of GP Eq. (5.3.1) for the case when $k \neq 0$ and $\mu_{12} = \mu_{21} \neq 0$. In this case, we fix the value of nonlinear coupling and investigate the stability of the solutions with the variation in the value of linear coupling. The stability curves are shown in Figs. 5.34-5.36. As before, the left panels show the stability curves for the defocusing case while the right panels depict the focusing case. One can see in the top left panels of Figs. 5.34-5.36 that the ground states in the defocusing case in the absence and presence of topological charge can be made stable by adjusting the values of linear and nonlinear coupling. The top right panels of Figs. 5.34-5.36 show that in the focusing case, the ground states with or without charge are unstable. Similarly, the first and second excited states remain unstable in focusing and defocusing cases as can be seen in the remaining panels of Figs. 5.34-5.36.

5.4.4 Stability analysis in case of unequal vorticity in the two components of BECs

In the above discussion, we considered the cases of equal vorticities in both components of BECs, i.e. $m_1 = m_2$. Now we will discuss the cases of unequal vorticities, i.e. $m_1 \neq m_2$ in the defocusing case with $k = 0$. The stability curves for three different cases of unequal vorticities with $(q = 0, 1, 2, 3, 4)$ eigenvalues is presented in Fig. 5.37. First, we consider the case in which one of the components has no topological charge $m_1 = 0$ while the other component possesses a unit topological charge $m_2 = 1$. The solution and the corresponding eigenvalues spectra is shown in left and right panels of Fig. 5.38. The solution is unstable but can be stabilized by controlling the value of nonlinear coupling as can be seen in the stability curve in Fig. 5.37(a). The time evolution of the solution is depicted in Fig. 5.38. The solution is unstable due to the $q = 0, 1$ eigenmodes. One can see that the instability only affects that component which has a nonzero topological charge. Due to these unstable eigenmodes and the presence of vorticities, there is fluctuation in the central atomic density peak and on the outer ring of the component with topological charge. However, the phenomenon looks periodic and the structure regains itself as can be seen at $t = 795$. Despite, the fact that the miscibility criteria is satisfied, the component with no vorticities remains stable. The case of $m_1 = 0$ and $m_2 = 2$ is almost similar as above and is not presented here.

Lastly, we discuss the case of $m_1 = 1$ and $m_2 = 2$. Like the case of $m_1 = 0$ and $m_2 = 1$, the solution can be made stable by adjusting the value of nonlinear coupling. The solution and the eigenvalues spectra are shown in the upper panels of Fig. 5.39. The remaining panels of Fig. 5.39 depict the time evolution of the solution. The first excited state in one of the components appears to be affected due to the $q = 0, 1$ eigenmodes. Due the presence of double topological charge, the outer ring and the central atomic density peak start rotating and results in the deformation of the structure. The other component carrying unit topological charge also starts rotating. However, the deformation in this component occurs after a relatively longer time as can be seen at time $t = 1500, 2100$.

5.5 Conclusion

In this study, we have considered a collection of radially symmetric nonlinear solutions of a coupled system of GP equations in the presence of a harmonic trap. The numerical linear stability and time dynamics of ground states as well as excited states were investigated both in the absence and presence of a topological charge. In particular, we

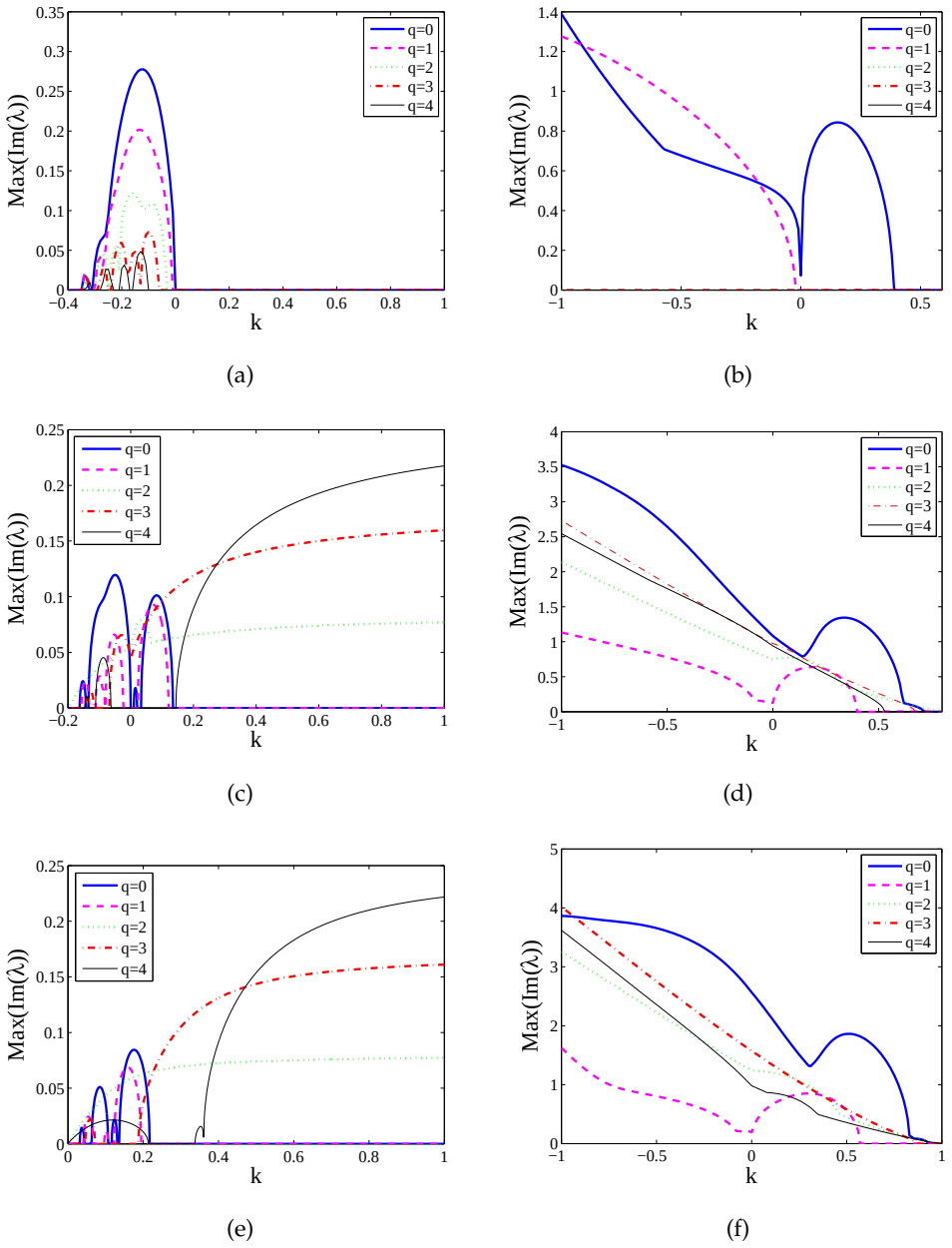

Figure 5.31: Linear stability curves for non topological charge $(m = 0)$ solutions. The left panels correspond to the defocusing case in which $\rho_0 = 0.5$ while the right panels correspond to the focusing case in which $\rho_0 = -0.5$. In all panels $\mu_{12} = \mu_{21} = 0$. The upper two panels show the graphs of maximum imaginary parts as functions of linear coupling of primary eigenvalues for $q = 0, 1, 2, 3, 4$ for the ground state $(n_r = 0)$. The middle and the lower panels depict respectively the first and second excited states. The magnitude of the unstable eigenvalues is small in the left panels and indicates the slow dynamical development of the instability. On the other hand, the magnitude of the unstable eigenvalues in the right panels is very high and indicates a rapid deformation of the structure.

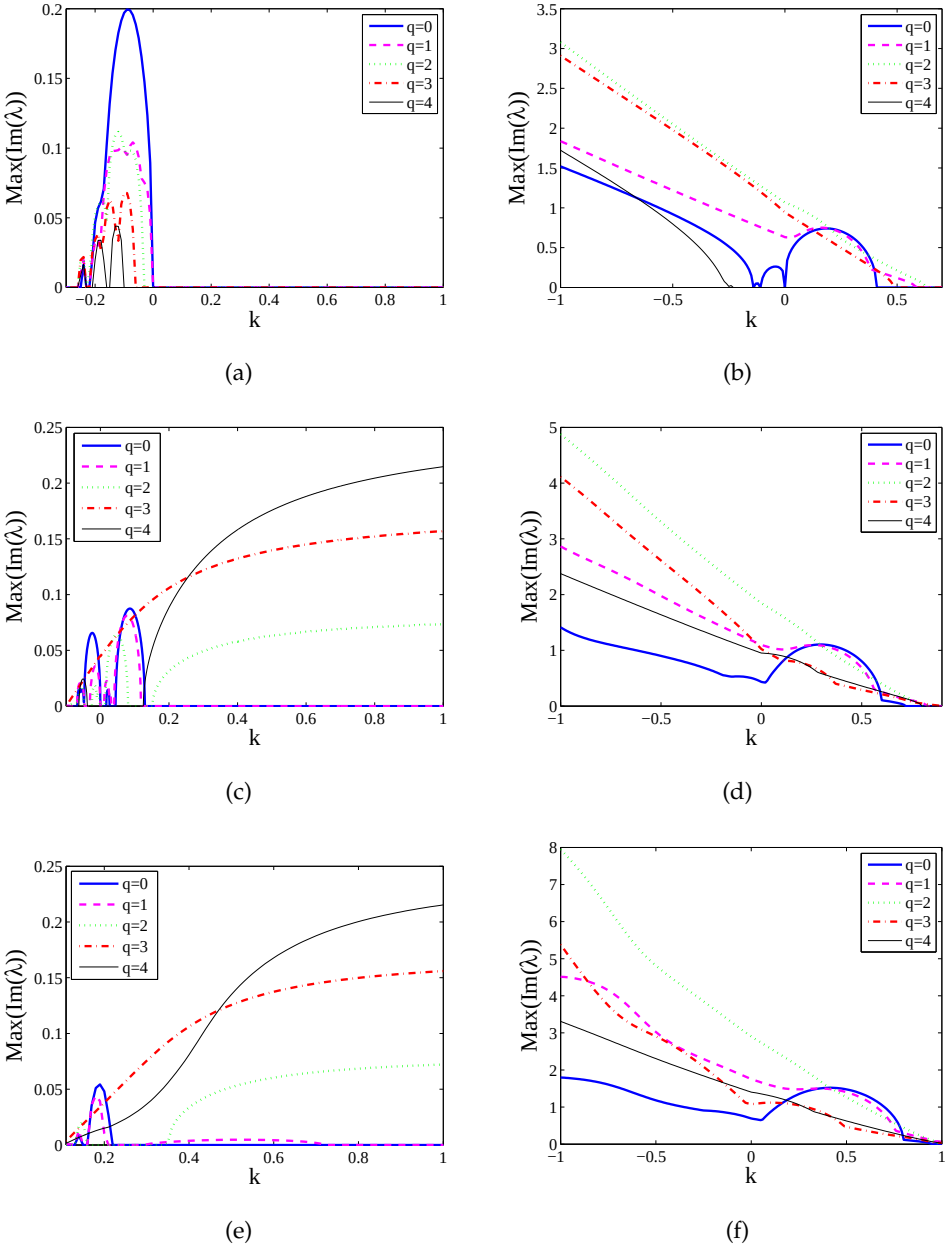

Figure 5.32: Same as Fig. 5.31 but for unit topological charge $(m = 1)$ solutions.

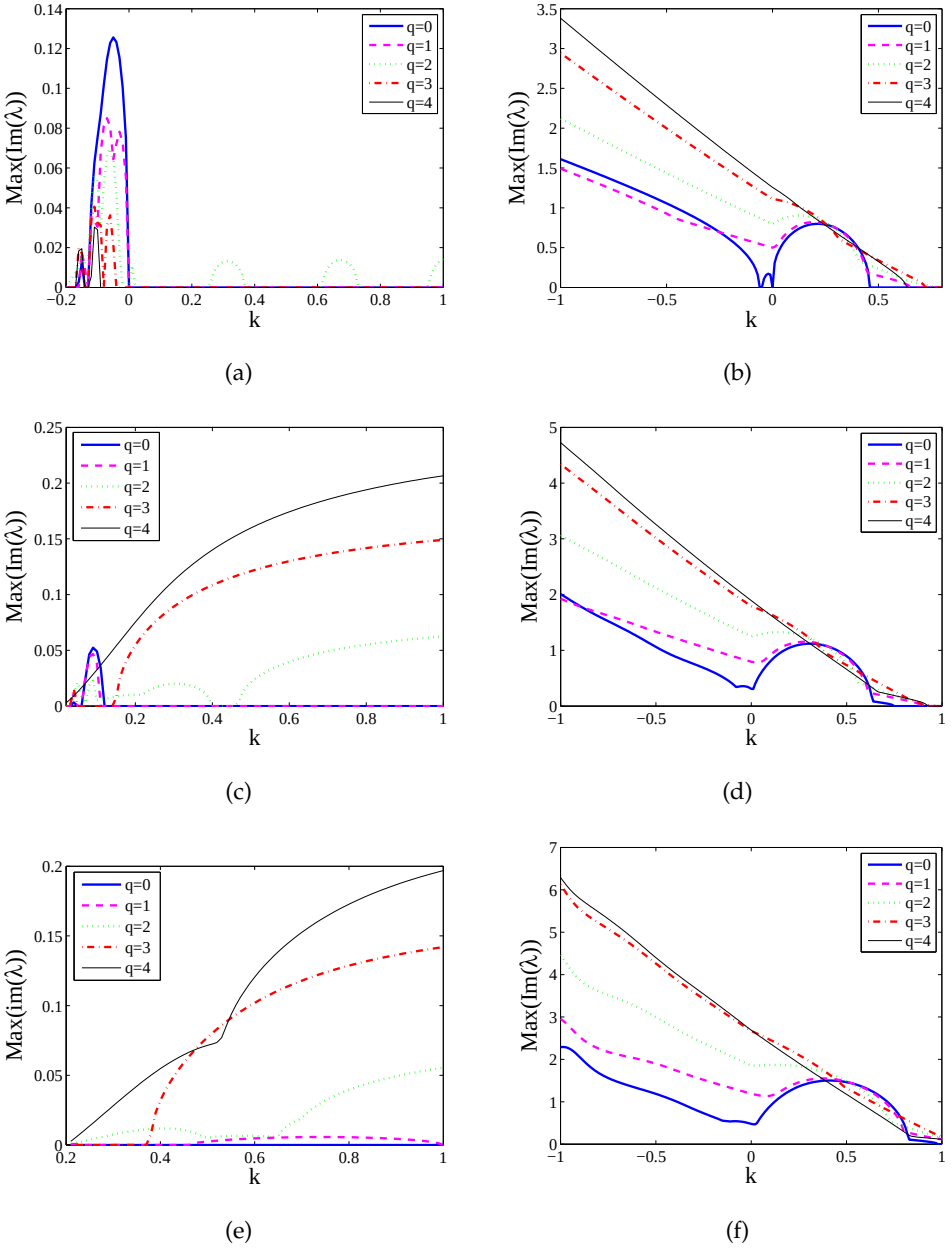

Figure 5.33: Same as Fig. 5.31 but for doubly charged $(m = 2)$ solutions.

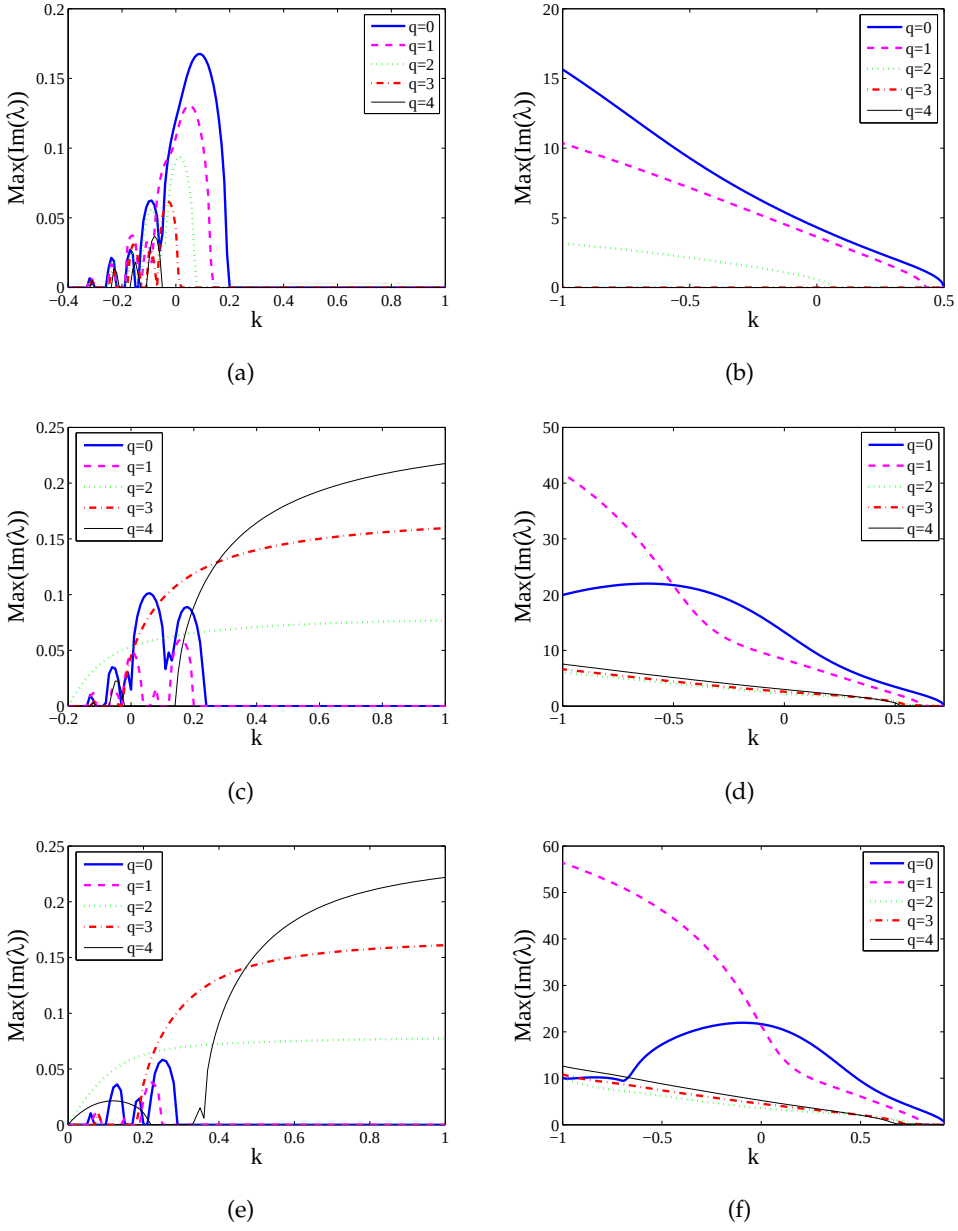

Figure 5.34: Linear stability curves for non topological charge $(m = 0)$ solutions. The left panels correspond to the defocusing case in which $\rho_0 = 0.5$, $\mu_{12} = \mu_{21} = 2$ while the right panels correspond to the focusing case in which $\rho_0 = -0.5$, $\mu_{12} = \mu_{21} = -0.5$. The upper two panels show the graphs of maximum imaginary parts as functions of linear coupling of primary eigenvalues for $q = 0, 1, 2, 3, 4$ for the ground state $(n_r = 0)$. The middle and the lower panels depict respectively the first and second excited states. The magnitude of the unstable eigenvalues is small in the left panels and indicates the slow dynamical development of the instability. On the other hand, the magnitude of the unstable eigenvalues in the right panels is very high and indicates a rapid deformation of the structure.

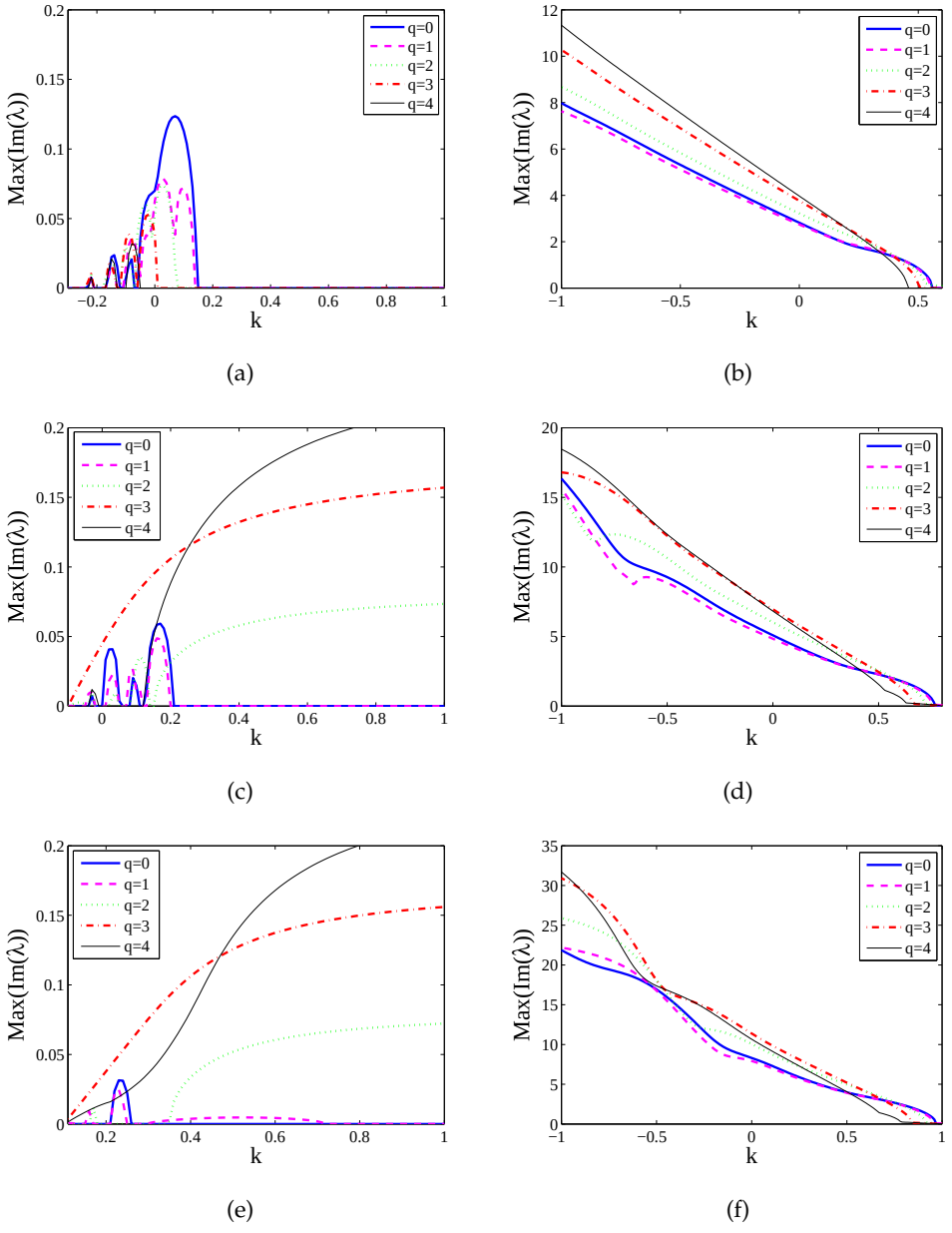

Figure 5.35: Same as Fig. 5.34 but for unit topological charge $(m = 1)$ solutions.

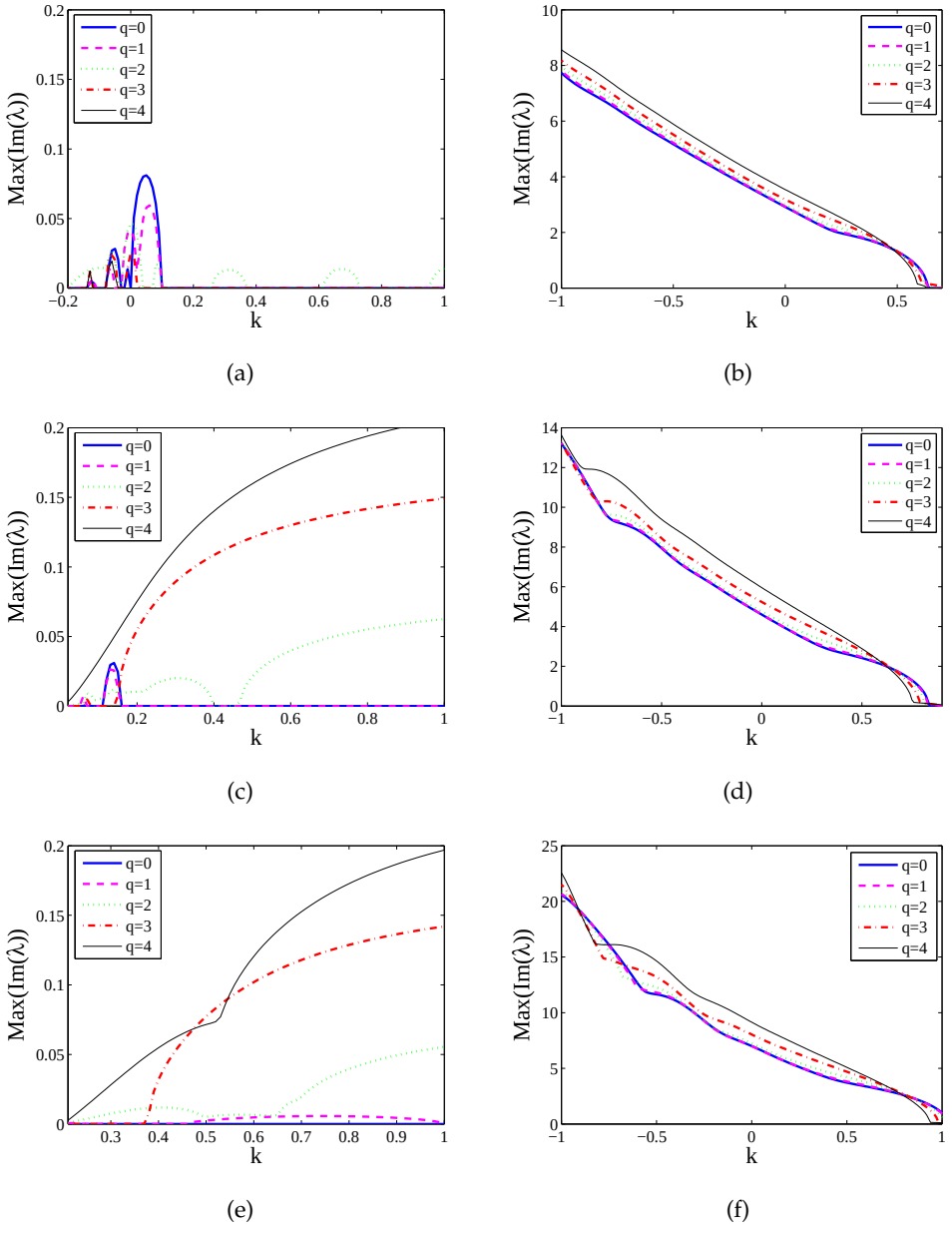

Figure 5.36: Same as Fig. 5.34 but for doubly charged $(m = 2)$ solutions.

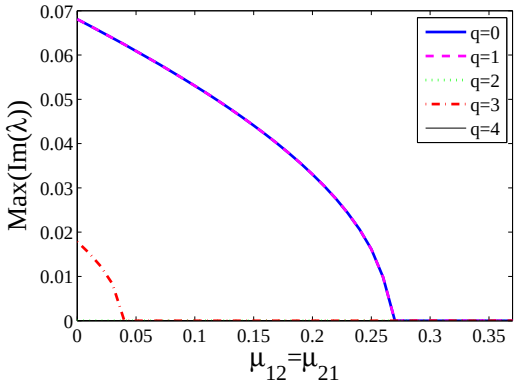

(a)

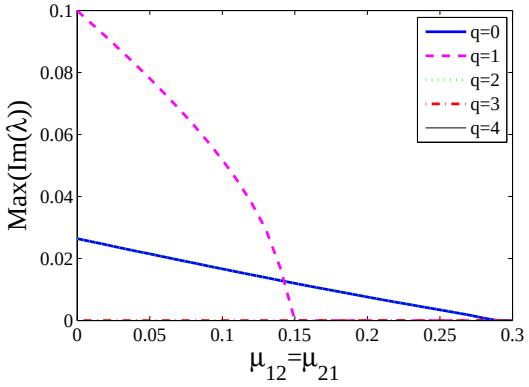

(b)

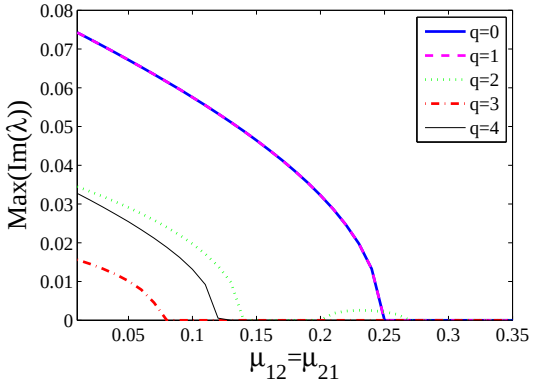

(c)

Figure 5.37: Linear stability curves for the case when (a) one of the components has zero topological charge $m_1 = 0$ and the other component has unit topological charge $m_2 = 1$, (b) $m_1 = 0$ and $m_2 = 2$, (c) $m_1 = 1$ and $m_2 = 2$.

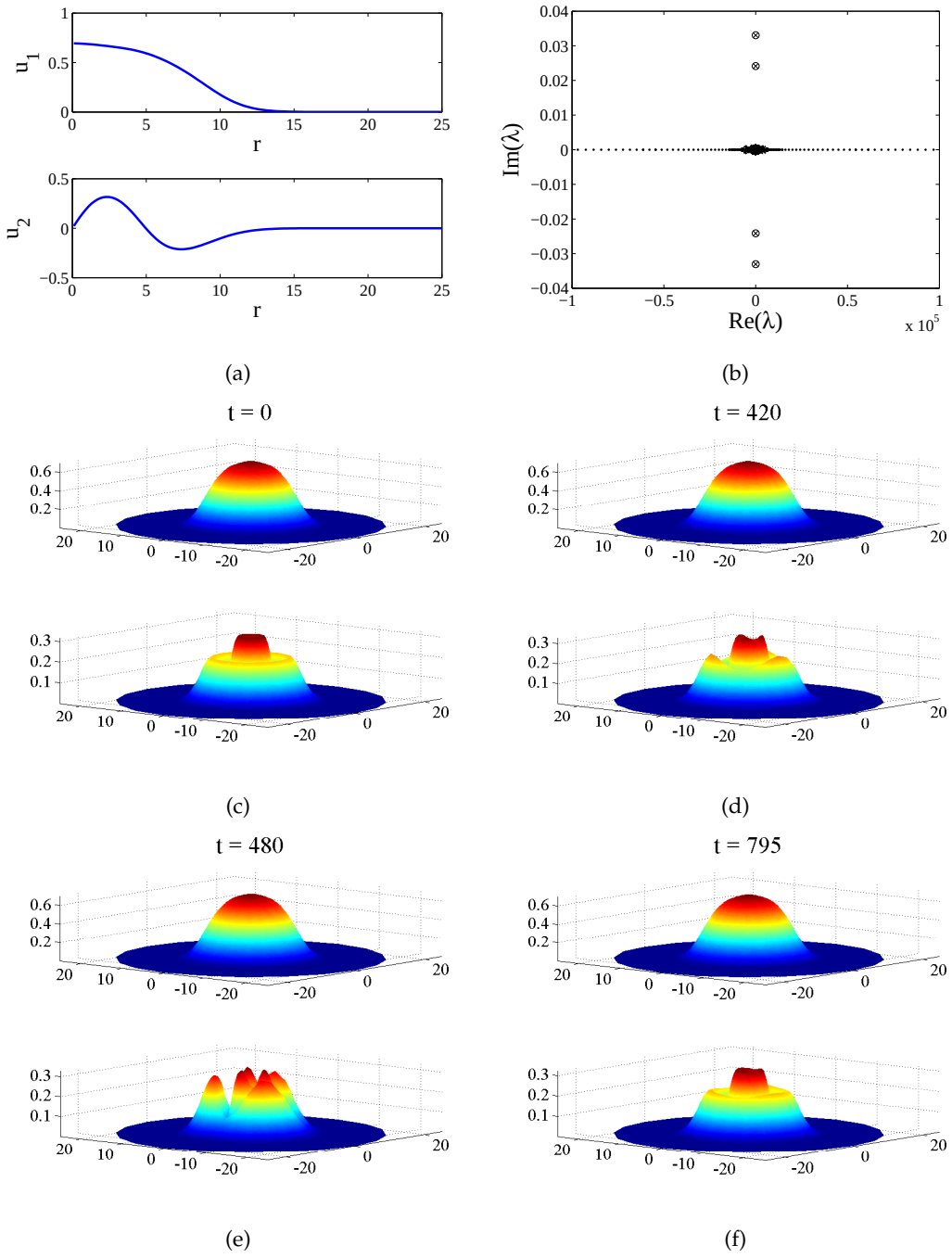

Figure 5.38: Figures with topological charges $m_1 = 0$, $m_2 = 1$. The top left panel depicts the profiles of the solution for $\rho_0 = 0.5$ and $\mu_{12} = \mu_{21} = 0.2$. The eigenvalues spectra on the complex plane corresponding to $q = 0, 1, ..., 50$ is shown in the top right panel. The symbols used to represent the eigenvalues for different values of q are shown in the Table 5.1. The remaining figures show the time evolution of the solution.

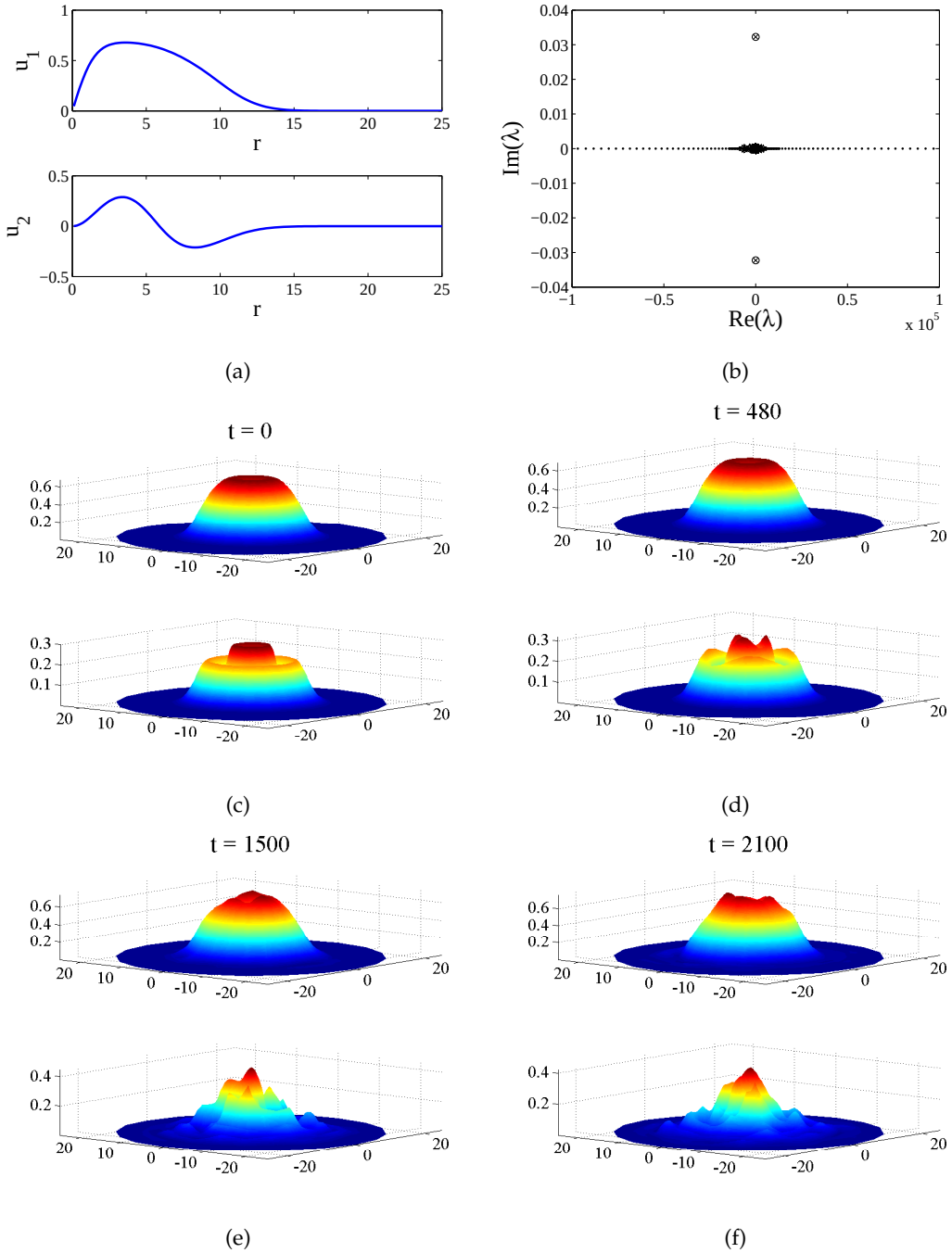

Figure 5.39: Same as Fig. 5.38 but with topological charges $m_1 = 1$, $m_2 = 2$, $\mu_{12} = \mu_{21} = 0.2$ and $\rho_0 = 0.6$.

were interested in the linear stability analysis of these states with the variation of linear or nonlinear coupling. First we considered linear coupling $k = 0$ and observed that the ground states with or without vorticities are unstable in both focusing and defocusing cases. However, it can be possible to stabilize the chargeless and charged ground states by tuning the nonlinear coupling between the condensates in the defocusing case. The charged excited states are found to be unstable in both cases. Moreover, the nonlinear coupling in these cases cannot stabilize the excited states.

Next, we turned the nonlinear coupling off and the linear coupling on, i.e. $\mu_{12} = \mu_{21} = 0$ and $k \neq 0$. All solutions except ground states were found to be unstable. Nevertheless, the chargeless ground state in the focusing case can be made stable by adjusting the value of linear coupling. Also, the chargeless and charged ground states in the defocusing case can be made stable by controlling the value of k. We also considered the case when both linear and nonlinear coupling were nonzero, i.e. $\mu_{12} = \mu_{21} \neq 0$ and $k \neq 0$. Again, all solutions were found to be unstable except the ground states of the defocusing case with or without vorticities which can be stabilize by selecting suitable values of $\mu_{12} = \mu_{21}$ and k. The ground and higher excited states in the focusing case were all found to be unstable in the absence and presence of topological charge.

Finally, we studied the stability of the solutions having different values of topological charge in the defocusing case when linear coupling was off. These solution were found to be unstable too.

In general, the instability growth rate in all cases of defocusing nonlinearity was found to be small and shattering of structures in the time evolution appeared after a relatively long time. On the other hand, in the focusing case, the instability rate was very high that resulted in the rapid destruction of the structures.

CHAPTER 6

Conclusion and Future Work

In this thesis, we have examined the existence and stability of dark solitons and fluxon analogues (FA) solutions in two effectively one dimensional parallel coupled Bose-Einstein condensates (BECs) in the presence of an external potential. The interactions of coupled dark solitons as well as well FA solutions are studied, too. Moreover, the existence, stability and time dynamics of the ground and higher excited states in the absence and presence of a topological charge in two-dimensional harmonically trapped parallel coupled BECs are analyzed. In the following, we summarize our work and the main results obtained and point out several interesting problems that would be investigated in the future.

6.1 Summary

We began our discussion in Chapter 1 by providing background information about solitons and some physical and mathematical aspects of the theory of BECs. These include the formation of BECs by laser cooling technique and some of its potential applications. The types of external potential to confine BECs were also presented.

In Chapter 2, a mean-field description of BECs in which Gross-Pitaevskii (GP) equation that describes their dynamics was derived using a variational approach and the ground state properties of BECs were presented. The basic nonlinear structures such as the plane wave solution, the bright solitons and the dark solitons that are ubiquitous in one-dimensional GP equations were considered and their stability analysis was presented. In the homogeneous case when there was no magnetic trap, the steady state dark soliton was found to be stable. In the nonhomogeneous case, even though the presence of magnetic trap affected the profile of the dark soliton, nonetheless the soliton remained stable.

In Chapter 3, we considered two effectively one-dimensional parallel BECs confined in a double well potential. The condensates were assumed to be linearly coupled by a weak coupling k. Due to tunnelling and extended spatial dimension along the waveguides, a long Bose-Josephson junction was suggested to be formed by Kaurov and Kuklov [95, 96]. It was shown that such a system supports atomic Josephson vortex and can be given by coupled dark-soliton-like solutions. In the thesis, we referred to these solutions as fluxon analogues (FA). These stable objects can be controlled at high speed and are used as a basic bit in information processing systems.

We numerically studied the existence and stability of FA solutions and coupled dark solitons in the absence and presence of a magnetic trap. In carrying out the investigations of the stability of the solitons, the corresponding eigenvalue problems were solved numerically, and the stability regions for the coupling constant were obtained. Moreover, numerical integrations of the coupled system of GP equations were performed to verify the results of the stability of solitons.

We began with the case when there was no trap and obtained the coupled dark solitons numerically. The dark solitons were found to be unstable below a critical coupling k_{cs} but became stable for $k \geq k_{cs}$. It was observed that the dark solitons emit radiation when they become unstable. In the instability region of coupled dark solitons, an FA solution was obtained. The FA solution was found to exist below a critical value k_{ce}. At $k = k_{ce}$, it transformed into a coupled dark soliton. Both FA and coupled dark solitons coincided at $k = k_{ce}$ in a pitchfork bifurcation. FA solution was found to be stable in its domain of existence.

We extended the work in [95, 96] and investigated the existence, stability and time dynamics of FA solutions and coupled dark solitons in the presence of a harmonic trap. It was noted that the external potential did not affect the domain of existence of FA solution. However, the presence of the trap destabilized the FA solution. Due to the instability, FA solution started oscillating about the minimum of the trap non-sinusoidally. It was shown that the FA solution can be stabilized by adjusting the linear coupling between the condensates. The existence and stability of coupled dark solitons could not be influenced by the presence of trap.

Next, a travelling FA solution was obtained numerically and deformation in its profile was seen due to non-zero value of velocity v. We then found the domain of existence for k corresponding to different values of velocity for FA solution. It was noted that the critical value k_{ce} at which solution changes into a coupled dark soliton reduced with v. Nevertheless, the travelling FA solution remained stable in its entire domain of existence like static FA solution. The travelling dark solitons were found to be unstable

for $k < k_{ce}$ and were stable for $k \geq k_{ce}$. We also derived a relationship between the velocity v and critical coupling k_{ce} analytically. The relation was compared with the numerical results showing excellent agreement.

To study the dynamical behavior of FA solutions analytically, a variational approach was employed to approximate the solutions. The Lagrangian formalism was separated into two cases, i.e. when the coupling constant k was close to the critical coupling k_{ce} at which the FA solutions were close to coupled dark solitons and when it was close to the uncoupled limit $k \approx 0$. In the former case, the oscillation frequency of dark solitons in a harmonic trap which was first presented by Busch and Anglin in [125] was recovered. In the latter case, the solution was approximated using an ansatz similar to Gaussian ansatz and a good approximation is obtained. The theoretical approximations were used to explain the results obtained numerically.

In Chapter 4, we attempted to investigate the existence, stability and dynamics of multiple FA solutions and coupled dark solitons in linearly coupled BECs. In particular, we examined the prototypical cases of two and three FA solutions and dark solitons. First, we considered the uncoupled case, i.e. $k = 0$ and analyzed the homogeneous weakly interacting case of a symmetric collision of two dark solitons. A formula for the effective repulsive potential in this case was derived and then generalized it for the cases of asymmetric collisions and an arbitrary number of dark solitons. Next, we considered the coupled nonhomogeneous system of GP equations and determined the in-phase and out-of-phase oscillation frequencies of two and three FA solutions in the limit of $k \approx k_{ce}$. This has been done by incorporating the effective repulsive potential with the external harmonic potential using a variational approach and qualitatively good approximations were obtained.

The interactions of dark solitons in the uncoupled case were first investigated in [97]. We then studied the interactions of multiple coupled dark solitons and FA solutions in the absence and presence of a harmonic trap. First, we took into consideration the homogeneous case. The symmetric and asymmetric collisions of multiple dark solitons were analyzed in Section 4.4.2. In symmetric cases, it was observed that two slow moving dark solitons repelled each other at the point of their closest proximity while fast moving solitons transmitted through each other. In cases of asymmetric collisions, the moving solitons transferred all their energy to static solitons and became static after collision. The interaction scenarios of the coupled dark solitons were found almost similar to interactions in the uncoupled cases. The only difference was the emergence of radiation which was not seen in the uncoupled case.

Next, we studied the interactions of multiple FA solutions. In case of symmetric col-

lisions, two types of possible interactions of FA solutions were introduced. From the symmetry of the imaginary parts, the first possibility was referred to as the odd symmetric interaction or $(+-)$-configuration and the second possibility as even symmetric interaction or $(++)$-configuration. It was noticed that in case of odd symmetric collisions, two slow moving FA solutions showed attraction towards each other at the interaction point and phase shift was induced. The fast moving FA solutions passed through each other due to their high velocities without changing their phase. On the other hand, in case of even symmetric collisions, two slow moving FA solutions formed a breather similar to that reported in [133] in a parametrically driven Schrödinger equation while the fast moving FA solutions collide and become unidentifiable.

We also examined the existence, stability and time dynamics of stationary multiple FA solutions and coupled dark solitons in the presence of a magnetic trap. In particular, we studied that how the domains of existence and stability of these multiple states varies with the trapping strength. Our calculations showed that the $(+-)$ and $(+-+)$-configurations of FA solutions were unstable in their domains of existence. For the $(++)$ and $(+++)$- configurations of FA solutions, there exist regions of stability where these configurations were found to be stable.

In Chapter 5, we considered two effectively two-dimensional parallel coupled BECs confined in a double well potential. The system was modelled by two GP equations coupled by linear and nonlinear terms. We used the polar coordinates and converted the GP equations to polar form. A large set of radially symmetric nonlinear solutions of the coupled system of GP equations in the presence of a harmonic trap was taken into account. The existence, linear stability and time dynamics of nontopological and topologically charged ground and higher excited states were analyzed numerically.

In particular, we were concerned about the stability of radially symmetric states with the variation in linear or nonlinear coupling. First, we considered the case when the condensates were nonlinearly coupled and the linear coupling was off. It was found that the chargeless and charged ground state solutions in the focusing and defocusing cases are unstable. Nevertheless, in the defocusing case, stabilization of the chargeless and charged ground state solutions was possible by manipulating the nonlinear coupling between the condensates. On the contrary, the ground states with or without a charge in the focusing case remained unstable. Unlike the defocusing case, these states could not be stabilized through nonlinear coupling. Similarly, the charged excited states were shown to be unstable in focusing and defocusing cases.

Then we dealt with the situations when the nonlinear coupling was inoperative and the condensates were only linearly coupled. The ground and all higher excited states were

found to be unstable in both focusing and defocusing cases. However, it was possible to stabilize the chargeless ground states in focusing and defocusing cases by controlling the linear coupling. The same was true for the charged ground states in the defocusing case. We also considered the stability of nonlinear states in the presence of linear and nonlinear coupling. It was shown that only the chargeless and charged ground states in the defocusing case can be made stable with an appropriate choice of values of linear and nonlinear couplings. Finally, we examined the stability of the nonlinear states in the defocusing case when the condensates were nonlinearly coupled and had different values of topological charge in the two components. All solutions were found to be unstable.

6.2 Future work

We identify several problems in this section that could be intriguing for future work. Some of these problems originate from the development of the ideas of the present work, while others emanate from the questions raised during this study that call for analysis.

One of the possible problems is to reconsider the work of Chapters 3 and 4 in a finite spatial dimension by incorporating the periodic boundary conditions. The situation corresponds the case of confining BECs in two concentric rings in the presence of external harmonic trap which was considered in [109]. The transverse excitations in each ring were assumed to be squeezed and the condensates were supposed to be linearly coupled in absolutely one dimension and hence can be modelled by the coupled system of GP Eq. (3.1.1). The effects of the trapping strength on the existence and stability of the dark solitons and FA solutions could be investigated. Furthermore, the interactions of coupled dark solitons and FA solutions in the absence and presence of a harmonic potential could be examined.

Another interesting problem that could be pursued in future is to study the dynamics of linearly coupled one-dimensional BECs with repulsive interatomic interaction in the presence of magnetic trap by dragging an obstacle through the condensates. The obstacle can be created by using a blue-detuned laser beam that acts as a potential and can be given by Gaussian function Ae^{-x^2/σ^2}, where A and σ represent respectively the strength and width of the laser obstacle [145]. The analysis of the generation of grey solitons by dragging an obstacle through a quasi one-dimensional trapped BEC was presented in [146]. It was shown that the generation of grey solitons depends on the velocity and shape of the obstacle. In a coupled system of BECs, FA solutions and dark

solitons can be expected to exist in a specific domain for dragging velocity and may show bifurcation.

Next, it could be fascinating to extend the study of Chapter 5 for coupled Gross-Pitaevskii system to the full three dimensional problem, similarly as before by considering the radially symmetric states and investigating the linear stability as well as time dynamics. However, the numerical computations in this case will be rich and comprehensive.

An interesting model that has important applications in nonlinear optics and atomic physics is the discrete nonlinear Schrödinger equation. This equation arises in the description of a BEC confined in deep periodic optical lattices. These lattices split the condensate into an array of droplets. As our study in this thesis was focused on the coupled nonlinear GP equations, parallel to this study, one can consider the one-dimensional linearly coupled system of discrete nonlinear Schrödinger equations given by

$$i\dot{\Psi}_n^j = -C\left(\Psi_{n+1}^j - 2\Psi_n^j + \Psi_{n-1}^j\right) + \mu|\Psi_n^j|^2\Psi_n^j - \rho_0\Psi_n^j - k\Psi_n^{3-j},$$

where $j = 1, 2$ and dot represents the derivative with respect to time t. Here, the spatial variable is discrete and the evolution variable is continuous. The parameter C denotes the coupling between the adjacent optical lattice potentials. μ and ρ_0 are respectively the nonlinearity coefficient and chemical potential. k is the linear coupling between the two condensates. The above coupled system admits different types of configurations. In particular, we could consider discrete coupled dark solitons and FA solutions. Once an exact solution of a specific configuration with $C = 0$ is constructed, it could be numerically continued to obtain the solution for non-zero values of C. Then the existence, stability and dynamics of these discrete structures could be investigated.

References

[1] J. S. Russell. Report on waves. *Fourteenth meeting of the British Association for the Advancement of Science, London*, 1845.

[2] A. Scott. *Nonlinear Science: Emergence and Dynamics of Coherent Structures*. Oxford University Press, New York, USA, 2003.

[3] V. E. Zakharov and A. B. Shabat. Exact theory of two-dimensional self-focusing and one-dimensional self-modulation of waves in nonlinear media. *Sov. Phys. JETP*, 34:62–69, 1972.

[4] J. R. Taylor. *Optical solitons: Theory and Experiment*. Cambridge University Press, New York, USA, 1992.

[5] I. Calder, A. Ovassapian, and N. Calder. John Logie Baird–fibreoptic pioneer. *J. R. Soc. Med.*, 93(8):438–439, 2000.

[6] G. I. A. Stegeman, D. N. Christodoulides, and M. Segev. Optical spatial solitons: Historical perspectives. *IEEE J. Sel. Topics Quantum Electron*, 6(6):1419–1427, 2000.

[7] Y. S. Kivshar and X. Yang. Perturbation-induced dynamics of dark solitons. *Phys. Rev. E*, 49(2):1657, 1994.

[8] C. S. Gardner, J. M. Greene, M. D. Kruskal, and R. M. Miura. Method for solving the Korteweg-deVries equation. *Phys. Rev. Lett.*, 19(19):1095–1097, 1967.

[9] G. P. Agrawal. *Applications of nonlinear fiber optics*. Academic press, USA, 2008.

[10] C. Sulem and P. L. Sulem. *The nonlinear Schrödinger equation: self-focusing and wave collapse*. Springer, New York, USA, 1999.

[11] K. B. Dysthe. Note on a modification to the nonlinear Schrödinger equation for application to deep water waves. *Proc. Roy. Soc. London Ser. A. Math. Phys. Sci.*, 369(1736):105–114, 1979.

[12] D. H. Peregrine. Water waves, nonlinear Schrödinger equations and their solutions. *J. Austral. Math. Soc. Ser. B*, 25(01):16–43, 1983.

[13] K. Trulsen and K. B. Dysthe. A modified nonlinear Schrödinger equation for broader bandwidth gravity waves on deep water. *Wave motion*, 24(3):281–289, 1996.

[14] T. Taniuti and H. Washimi. Self-trapping and instability of hydromagnetic waves along the magnetic field in a cold plasma. *Phys. Rev. Lett.*, 21(4):209–212, 1968.

[15] E. P. Gross. Hydrodynamics of a superfluid condensate. *J. Math. Phys.*, 4:195, 1963.

[16] L. P. Pitaevskii. Vortex lines in an imperfect Bose gas. *Sov. Phys. JETP*, 13(2): 451–454, 1961.

[17] I. S. Aranson and L. Kramer. The world of the complex Ginzburg-Landau equation. *Rev. Mod. Phys.*, 74(1):99–143, 2002.

[18] M. C. Cross and P. C. Hohenberg. Pattern formation outside of equilibrium. *Rev. Mod. Phys.*, 65(3):851–1112, 1993.

[19] A. Hasegawa and F. Tappert. Transmission of stationary nonlinear optical pulses in dispersive dielectric fibers. I. anomalous dispersion. *Appl. Phys. Lett.*, 23(3): 142–144, 1973.

[20] L. F. Mollenauer, R. H. Stolen, and J. P. Gordon. Experimental observation of picosecond pulse narrowing and solitons in optical fibers. *Phys. Rev. Lett.*, 45(13): 1095–1098, 1980.

[21] L. F. Mollenauer, M. J. Neubelt, S. G. Evangelides, J. P. Gordon, J. R. Simpson, and L. G. Cohen. Experimental study of soliton transmission over more than 10,000 km in dispersion-shifted fiber. *Opt. Lett.*, 15(21):1203–1205, 1990.

[22] A. Afroozeh, I. S. Amiri, M. Kouhnavard, M. A. Jalil, J. Ali, and P. P. Yupapin. Optical dark and bright soliton generation and amplification. *AIP Conf. Proc.*, 1341:259–263, 2010.

[23] P. A. Ruprecht, M. J. Holland, K. Burnett, and M. Edwards. Time-dependent solution of the nonlinear Schrödinger equation for Bose-condensed trapped neutral atoms. *Phys. Rev. A*, 51(6):4704–4711, 1995.

[24] K. E. Strecker, G. B. Partridge, A. G. Truscott, and R. G. Hulet. Formation and propagation of matter-wave soliton trains. *Nature*, 417(6885):150–153, 2002.

[25] L. Khaykovich, F. Schreck, G. Ferrari, T. Bourdel, J. Cubizolles, L. D. Carr, Y. Castin, and C. Salomon. Formation of a matter-wave bright soliton. *Science*, 296(5571):1290–1293, 2002.

[26] A. Hasegawa and F. Tappert. Transmission of stationary nonlinear optical pulses in dispersive dielectric fibers. II. normal dispersion. *Appl. Phys. Lett.*, 23(4):171–172, 1973.

[27] A. M. Weiner, J. P. Heritage, R. J. Hawkins, R. N. Thurston, E. M. Kirschner, D. E. Leaird, and W. J. Tomlinson. Experimental observation of the fundamental dark soliton in optical fibers. *Phys. Rev. Lett.*, 61(21):2445–2448, 1988.

[28] D. Krökel, N. J. Halas, G. Giuliani, and D. Grischkowsky. Dark-pulse propagation in optical fibers. *Phys. Rev. Lett.*, 60(1):29–32, 1988.

[29] M. Lisak, D. Anderson, and B. A. Malomed. Dissipative damping of dark solitons in optical fibers. *Opt. Lett.*, 16(24):1936–1937, 1991.

[30] Y. S. Kivshar and V. V. Afanasjev. Dark optical solitons with reverse-sign amplitude. *Phys. Rev. A*, 44(3):R1446–R1449, 1991.

[31] Y. Chen and J. Atai. Absorption and amplification of dark solitons. *Opt. Lett.*, 16 (24):1933–1935, 1991.

[32] B. Luther-Davies and X. Yang. Steerable optical waveguides formed in self-defocusing media by using dark spatial solitons. *Opt. Lett*, 17(24):1755–1757, 1992.

[33] P. Emplit, M. Haelterman, and J. P. Hamaide. Picosecond dark soliton over a 1-km fiber at 850 nm. *Opt. Lett.*, 18(13):1047–1049, 1993.

[34] S. Burger, K. Bongs, S. Dettmer, W. Ertmer, K. Sengstock, A. Sanpera, G. V. Shlyapnikov, and M. Lewenstein. Dark solitons in Bose-Einstein condensates. *Phys. Rev. Lett.*, 83(25):5198–5201, 1999.

[35] Y. S. Kivshar and B. Luther-Davies. Dark optical solitons: physics and applications. *Phys. Rep.*, 298(2):81–197, 1998.

[36] M. Chen, M. A. Tsankov, J. M. Nash, and C. E. Patton. Microwave magnetic-envelope dark solitons in yttrium iron garnet thin films. *Phys. Rev. Lett.*, 70(11): 1707–1710, 1993.

[37] B. Denardo, W. Wright, S. Putterman, and A. Larraza. Observation of a kink soliton on the surface of a liquid. *Phys. Rev. Lett.*, 64(13):1518–1521, 1990.

[38] C. Elphick and E. Meron. Localized structures in surface waves. *Phys. Rev. A*, 40 (6):3226–3229, 1989.

[39] B. Denardo, B. Galvin, A. Greenfield, A. Larraza, S. Putterman, and W. Wright. Observations of localized structures in nonlinear lattices: Domain walls and kinks. *Phys. Rev. Lett.*, 68(11):1730–1733, 1992.

[40] B. A. Malomed. *Soliton management in periodic systems*. Springer New York, 2006.

[41] M. H. Anderson, J. R. Ensher, M. R. Matthews, C. E. Wieman, and E. A. Cornell. Observation of Bose-Einstein condensation in a dilute atomic vapor. *science*, 269 (5221):198–201, 1995.

[42] K. B. Davis, M. O. Mewes, M. R. Andrews, N. J. van Druten, D. S. Durfee, D. M. Kurn, and W. Ketterle. Bose-Einstein condensation in a gas of sodium atoms. *Phys. Rev. Lett.*, 75(22):3969–3973, 1995.

[43] W. Pauli. *Z. Physik*, 31:765, 1925.

[44] Cohen-Tannoudji, N. Claude, and W. D. Phillips. New mechanisms for laser cooling. *Phys. Today*, 43(10):33, 1990.

[45] T. Dauxois and M. Peyrard. *Physics of solitons*. Cambridge University Press, 2006.

[46] C. J. Pethick and H. Smith. *Bose-Einstein condensation in dilute gases*. Cambridge University Press, 2002.

[47] L. V. Hau, S. E. Harris, Z. Dutton, and H. C. Behroozi. Light speed reduction to 17 metres per second in an ultracold atomic gas. *Nature*, 397(6720):594–598, 1999.

[48] S. N. Ginsberg, S. R. Garner, and L. V. Hau. Coherent control of optical information with matter wave dynamics. *Nature*, 445(7128):623–626, 2007.

[49] E. A. Cornell and C. E. Wieman. Nobel lecture: Bose-Einstein condensation in a dilute gas, the first 70 years and some recent experiments. *Rev. Mod. Phys.*, 74(3): 875–893, 2002.

[50] D. S. Petrov, G. V. Shlyapnikov, and J. T. M. Walraven. Regimes of quantum degeneracy in trapped 1D gases. *Phys. Rev. Lett.*, 85(18):3745–3749, 2000.

[51] D. S. Petrov, G. V. Shlyapnikov, and J. T. M. Walraven. Phase-fluctuating 3D Bose-Einstein condensates in elongated traps. *Phys. Rev. Lett.*, 87(5):050404, 2001.

[52] J. O. Andersen, U. Al Khawaja, and H. T. C. Stoof. Phase fluctuations in atomic Bose gases. *Phys. Rev. Lett.*, 88(7):070407, 2002.

[53] A. Görlitz, J. M. Vogels, A. E. Leanhardt, C. Raman, T. L. Gustavson, J. R. Abo-Shaeer, A. P. Chikkatur, S. Gupta, S. Inouye, T. Rosenband, and W. Ketterle. Realization of Bose-Einstein condensates in lower dimensions. *Phys. Rev. Lett.*, 87 (13):130402, 2001.

[54] M. Greiner, I. Bloch, O. Mandel, W. T. Hänsch, and T. Esslinger. Exploring phase coherence in a 2D lattice of Bose-Einstein condensates. *Phys. Rev. Lett.*, 87(16): 160405, 2001.

[55] J. H. Denschlag, J. E. Simsarian, H. Häffner, C. McKenzie, A. Browaeys, D. Cho, K. Helmerson, S. L. Rolston, and W. D. Phillips. A Bose-Einstein condensate in an optical lattice. *J. Phys. B: At., Mol. Opt. Phys.*, 35(14):3095, 2002.

[56] D. M. Stamper-Kurn, M. R. Andrews, A. P. Chikkatur, S. Inouye, H.-J. Miesner, J. Stenger, and W. Ketterle. Optical confinement of a Bose-Einstein condensate. *Phys. Rev. Lett.*, 80(10):2027–2030, 1998.

[57] M. D. Barrett, J. A. Sauer, and M. S. Chapman. All-optical formation of an atomic Bose-Einstein condensate. *Phys. Rev. Lett.*, 87(1):010404, 2001.

[58] M. Albiez, R. Gati, J. Fölling, S. Hunsmann, M. Cristiani, and M. K. Oberthaler. Direct observation of tunnelling and nonlinear self-trapping in a single Bosonic Josephson junction. *Phys. Rev. Lett.*, 95(1):010402, 2005.

[59] B. P. Anderson and M. A. Kasevich. Macroscopic quantum interference from atomic tunnel arrays. *Science*, 282(5394):1686–1689, 1998.

[60] M. R. Andrews, C. G. Townsend, H.-J. Miesner, D. S. Durfee, D. M. Kurn, and W. Ketterle. Observation of interference between two Bose condensates. *Science*, 275(5300):637–641, 1997.

[61] W. Hänsel, P. Hommelhoff, T. W. Hänsch, and J. Reichel. Bose-Einstein condensation on a microelectronic chip. *Nature*, 413(6855):498–501, 2001.

[62] H. Ott, J. Fortagh, G. Schlotterbeck, A. Grossmann, and C. Zimmermann. Bose-Einstein condensation in a surface microtrap. *Phys. Rev. Lett.*, 87(23):230401, 2001.

[63] D. J. Kaup and T. K. Vogel. Quantitative measurement of variational approximations. *Phys. Lett. A*, 362(4):289–297, 2007.

[64] B. A. Malomed. Variational methods in nonlinear fiber optics and related fields. *Prog. Optics*, 43:71–193, 2002.

[65] A. J. Leggett. Bose-Einstein condensation in the alkali gases: Some fundamental concepts. *Rev. Mod. Phys.*, 73(2):307–356, 2001.

[66] G. F. Gribakin and V. V. Flambaum. Calculation of the scattering length in atomic collisions using the semiclassical approximation. *Phys. Rev. A*, 48(1):546–553, 1993.

[67] C. A. Sackett, J. M. Gerton, M. Welling, and R. G. Hulet. Measurements of collective collapse in a Bose-Einstein condensate with attractive interactions. *Phys. Rev. Lett.*, 82(5):876–879, 1999.

[68] E. A. Donley, N. R. Claussen, S. L. Cornish, J. L. Roberts, E. A. Cornell, and C. E. Wieman. Dynamics of collapsing and exploding Bose-Einstein condensates. *nature*, 2001.

[69] F. Dalfovo, S. Giorgini, L. P. Pitaevskii, and S. Stringari. Theory of Bose-Einstein condensation in trapped gases. *Rev. Mod. Phys.*, 71(3):463–512, 1999.

[70] R. Carretero-González, D. J. Frantzeskakis, and P. G. Kevrekidis. Nonlinear waves in Bose-Einstein condensates: physical relevance and mathematical techniques. *Nonlinearity*, 21(7):R139, 2008.

[71] V. E. Zakharov and A. B. Shabat. Interaction between solitons in a stable medium. *Sov. Phys. JETP*, 37:823, 1973.

[72] Y. S. Kivshar and W. Królikowski. Lagrangian approach for dark solitons. *Opt. Commun.*, 114(3):353–362, 1995.

[73] L. D. Menza and C. Gallo. The black solitons of one-dimensional NLS equations. *Nonlinearity*, 20(2):461, 2007.

[74] D. E. Pelinovsky and P. G. Kevrekidis. Dark solitons in external potentials. *Angew. Math. Phys.*, 59(4):559–599, 2008.

[75] C. C. Bradley, C. A. Sackett, and R. G. Hulet. Bose-Einstein condensation of lithium: Observation of limited condensate number. *Phys. Rev. Lett.*, 78(6):985–989, 1997.

[76] C. J. Myatt, E. A. Burt, R. W. Ghrist, E. A. Cornell, and C. E. Wieman. Production of two overlapping Bose-Einstein condensates by sympathetic cooling. *Phys. Rev. Lett.*, 78(4):586–589, 1997.

[77] J. Stenger, S. Inouye, D. M. Stamper-Kurn, H. J. Miesner, A. P. Chikkatur, and W. Ketterle. Spin domains in ground state Bose-Einstein condensates. *nature*, 1998.

[78] G. Roati R. J. Brecha A. Simoni M. Inguscio G. Modugno, G. Ferrari. Bose-Einstein condensation of potassium atoms by sympathetic cooling. *Science*, 294(5545): 1320, 2001.

[79] M. Mudrich, S. Kraft, K. Singer, R. Grimm, A. Mosk, and M. Weidemüller. Sympathetic cooling with two atomic species in an optical trap. *Phys. Rev. Lett.*, 88 (25):253001, 2002.

[80] D. Ananikian and T. Bergeman. Gross-Pitaevskii equation for Bose particles in a double-well potential: Two-mode models and beyond. *Phys. Rev. A*, 73(1):013604, 2006.

[81] F. Dalfovo and S. Stringari. Bosons in anisotropic traps: Ground state and vortices. *Phys. Rev. A*, 53(4):2477–2485, 1996.

[82] K.-P. Marzlin, W. Zhang, and E. M. Wright. Vortex coupler for atomic Bose-Einstein condensates. *Phys. Rev. Lett.*, 79(24):4728–4731, 1997.

[83] B. M. Caradoc-Davies, R. J. Ballagh, and K. Burnett. Coherent dynamics of vortex formation in trapped Bose-Einstein condensates. *Phys. Rev. Lett.*, 83(5):895–898, 1999.

[84] H. Susanto, P. G. Kevrekidis, R. Carretero-González, B. A. Malomed, D. J. Frantzeskakis, and A. R. Bishop. Čerenkov-like radiation in a binary superfluid flow past an obstacle. *Phys. Rev. A*, 75(5):055601, 2007.

[85] M. R. Matthews, B. P. Anderson, P. C. Haljan, D. S. Hall, C. E. Wieman, and E. A. Cornell. Vortices in a Bose-Einstein condensate. *Phys. Rev. Lett.*, 83(13):2498–2501, 1999.

[86] F. Chevy, K. W. Madison, and J. Dalibard. Measurement of the angular momentum of a rotating Bose-Einstein condensate. *Phys. Rev. Lett.*, 85(11):2223–2227, 2000.

[87] K. W. Madison, F. Chevy, W. Wohlleben, and J. Dalibard. Vortex formation in a stirred Bose-Einstein condensate. *Phys. Rev. Lett.*, 84(5):806–809, 2000.

[88] E. Hodby, G. Hechenblaikner, S. A. Hopkins, O. M. Maragò, and C. J. Foot. Vortex nucleation in Bose-Einstein condensates in an oblate, purely magnetic potential. *Phys. Rev. Lett.*, 88(1):010405, 2001.

[89] B. Jackson, J. F. McCann, and C. S. Adams. Vortex formation in dilute inhomogeneous Bose-Einstein condensates. *Phys. Rev. Lett.*, 80(18):3903–3906, 1998.

[90] T. Winiecki, J. F. McCann, and C. S. Adams. Pressure drag in linear and nonlinear quantum fluids. *Phys. Rev. Lett.*, 82(26):5186–5189, 1999.

[91] D. R. Scherer, C. N. Weiler, T. W. Neely, and B. P. Anderson. Vortex formation by merging of multiple trapped Bose-Einstein condensates. *Phys. Rev. Lett.*, 98(11): 110402, 2007.

[92] R. Carretero-González, B. P. Anderson, P. G. Kevrekidis, D. J. Frantzeskakis, and C. N. Weiler. Dynamics of vortex formation in merging Bose-Einstein condensate fragments. *Phys. Rev. A*, 77(3):033625, 2008.

[93] K. W. Madison, F. Chevy, V. Bretin, and J. Dalibard. Stationary states of a rotating Bose-Einstein condensate: Routes to vortex nucleation. *Phys. Rev. Lett.*, 86(20): 4443–4446, 2001.

[94] B. Deconinck, P. G. Kevrekidis, H. E. Nistazakis, and D. J. Frantzeskakis. Linearly coupled Bose-Einstein condensates: From Rabi oscillations and quasiperiodic solutions to oscillating domain walls and spiral waves. *Phys. Rev. A*, 70(6):063605, 2004.

[95] V. M. Kaurov and A. B. Kuklov. Josephson vortex between two atomic Bose-Einstein condensates. *Phys. Rev. A*, 71(1):011601, 2005.

[96] V. M. Kaurov and A. B. Kuklov. Atomic Josephson vortices. *Phys. Rev. A*, 73(1): 013627, 2006.

[97] G. Theocharis, A. Weller, J. P. Ronzheimer, C. Gross, M. K. Oberthaler, P. G. Kevrekidis, and D. J. Frantzeskakis. Multiple atomic dark solitons in cigar-shaped Bose-Einstein condensates. *Phys. Rev. A*, 81(6):063604, 2010.

[98] G. Herring, L. D. Carr, R. Carretero-González, P. G. Kevrekidis, and D. J. Frantzeskakis. Radially symmetric nonlinear states of harmonically trapped Bose-Einstein condensates. *Phys. Rev. A*, 77(2):023625, 2008.

[99] B. D. Josephson. Possible new effects in superconductive tunnelling. *Phys. Lett.*, 1:251–253, 1962.

[100] A. Smerzi, S. Fantoni, S. Giovanazzi, and S. R. Shenoy. Quantum coherent atomic tunnelling between two trapped Bose-Einstein condensates. *Phys. Rev. Lett.*, 79 (25):4950–4953, 1997.

[101] S. Raghavan, A. Smerzi, S. Fantoni, and S. R. Shenoy. Coherent oscillations between two weakly coupled Bose-Einstein condensates: Josephson effects, π oscillations, and macroscopic quantum self-trapping. *Phys. Rev. A*, 59(1):620–633, 1999.

[102] S. Giovanazzi, A. Smerzi, and S. Fantoni. Josephson effects in dilute Bose-Einstein condensates. *Phys. Rev. Lett.*, 84(20):4521–4524, 2000.

[103] S. Levy, E. Lahoud, I. Shomroni, and J. Steinhauer. The a.c. and d.c. Josephson effects in a Bose-Einstein condensate. *Nature*, 449(7162):579–583, 2007.

[104] F. S. Cataliotti, S. Burger, C. Fort, P. Maddaloni, F. Minardi, A. Trombettoni, A. Smerzi, and M. Inguscio. Josephson junction arrays with Bose-Einstein condensates. *Science*, 293(5531):843–846, 2001.

[105] E. A. Ostrovskaya, Y. S. Kivshar, M. Lisak, B. Hall, F. Cattani, and D. Anderson. Coupled-mode theory for Bose-Einstein condensates. *Phys. Rev. A*, 61(3):031601, 2000.

[106] X. Y. Jia, W. D. Li, and J. Q. Liang. Nonlinear correction to the Boson Josephson-junction model. *Phys. Rev. A*, 78(7):023613, 2008.

[107] A. Barone and G. Paterno. *Physics and Applications of the Josephson Effect*. John Wiley & sons Inc., New York, USA, 1982.

[108] A. V. Ustinov. Solitons in Josephson junctions. *Physica D: Nonlinear Phenomena*, 123(1):315–329, 1998.

[109] J. Brand, T. J. Haigh, and U. Zülicke. Rotational fluxons of Bose-Einstein condensates in coplanar double-ring traps. *Phys. Rev. A*, 80(1):011602, 2009.

[110] I. Lesanovsky and W. V. Klitzing. Spontaneous emergence of angular momentum Josephson oscillations in coupled annular Bose-Einstein condensates. *Phys. Rev. Lett.*, 98(5):050401, 2007.

[111] J. Brand, T. J. Haigh, and U. Zülicke. Sign of coupling in barrier-separated Bose-Einstein condensates and stability of double-ring systems. *Phys. Rev. A*, 81(2): 025602, 2010.

[112] A. Gubeskys and B. A. Malomed. Symmetric and asymmetric solitons in linearly coupled Bose-Einstein condensates trapped in optical lattices. *Phys. Rev. A*, 75(6): 063602, 2007.

[113] B. A. Malomed. Optical domain walls. *Phys. Rev. E*, 50(2):1565–1571, 1994.

[114] B. A. Malomed and A. A. Nepomnyashchy. Stability limits for arrays of kinks in two-component nonlinear systems. *Europhys. Lett.*, 27(9):649, 1994.

[115] N. Dror, B. A. Malomed, and J. Zeng. Domain walls and vortices in linearly coupled systems. *Phys. Rev. E*, 84(4):046602, 2011.

[116] P. G. Kevrekidis, D. J. Frantzeskakis, and R. Carretero-González. *Emergent Nonlinear Phenomena in Bose-Einstein Condensates: Theory and Experiment*. Springer, Berlin, 2008.

[117] D. J. Frantzeskakis. Dark solitons in atomic Bose-Einstein condensates: from theory to experiments. *J. Phys. A*, 43(21):213001, 2010.

[118] D. E. Pelinovsky, D. J. Frantzeskakis, and P. G. Kevrekidis. Oscillations of dark solitons in trapped Bose-Einstein condensates. *Phys. Rev. E*, 72(1):016615, 2005.

[119] C. Becker, S. Stellmer, P. Soltan-Panahi, S. Dörscher, M. Baumert, E. M. Richter, J. Kronjäger, K. Bongs, and K. Sengstock. Oscillations and interactions of dark and dark-bright solitons in Bose-Einstein condensates. *Nature Phys.*, 4(6):496–501, 2008.

[120] A. Weller, J. P. Ronzheimer, C. Gross, J. Esteve, M. K. Oberthaler, D. J. Frantzeskakis, G. Theocharis, and P. G. Kevrekidis. Experimental observation of oscillating and interacting matter wave dark solitons. *Phys. Rev. Lett.*, 101(13): 130401, 2008.

[121] S. Stellmer, C. Becker, P. Soltan-Panahi, E.-M. Richter, S. Dörscher, M. Baumert, J. Kronjäger, K. Bongs, and K. Sengstock. Collisions of dark solitons in elongated Bose-Einstein condensates. *Phys. Rev. Lett.*, 101(12):120406, 2008.

[122] D. J. Frantzeskakis, G. Theocharis, F. K. Diakonos, P. Schmelcher, and Y. S. Kivshar. Interaction of dark solitons with localized impurities in Bose-Einstein condensates. *Phys. Rev. A*, 66(5):053608, 2002.

[123] L. Hong and W. Dong-Ning. Effects of localized impurity on a dark soliton in a Bose-Einstein condensate with an external magnetic trap. *Chinese Phys. B*, 18(7): 2659, 2009.

[124] D. R. Gulevich, S. Savelev, V. A. Yampolskii, F. V. Kusmartsev, and F. Nori. Josephson vortices as flexible waveguides for terahertz waves. *J. Appl. Phys.*, 104(6): 064507, 2008.

[125] T. Busch and J. R. Anglin. Motion of dark solitons in trapped Bose-Einstein condensates. *Phys. Rev. Lett.*, 84(11):2298–2301, 2000.

[126] Y. S. Kivshar, T. J. Alexander, and S. K. Turitsyn. Nonlinear modes of a macroscopic quantum oscillator. *Phys. Lett. A*, 278(4):225–230, 2001.

[127] P. Engels and C. Atherton. Stationary and nonstationary fluid flow of a Bose-Einstein condensate through a penetrable barrier. *Phys. Rev. Lett.*, 99(4):160405, 2007.

[128] I. Shomroni, E. Lahoud, S. Levy, and J. Steinhauer. Evidence for an oscillating soliton/vortex ring by density engineering of a Bose-Einstein condensate. *Nature Phys.*, 5(3):193–197, 2009.

[129] W. Zhao and E. Bourkoff. Generation, propagation, and amplification of dark solitons. *J. Opt. Soc. Am. B*, 9(7):1134–1144, 1992.

[130] N. Akhmediev and A. Ankiewicz. First-order exact solutions of the nonlinear Schrödinger equation in the normal-dispersion regime. *Phys. Rev. A*, 47(4):3213–3221, 1993.

[131] J. Denschlag, J. E. Simsarian, D. L. Feder, C. W. Clark, L. A. Collins, J. Cubizolles, L. Deng, E. W. Hagley, K. Helmerson, and W. P. Reinhardt. Generating solitons by phase engineering of a Bose-Einstein condensate. *Science*, 287(5450):97–101, 2000.

[132] K. Bongs, S. Burger, S. Dettmer, D. Hellweg, J. Arlt, W. Ertmer, and K. Sengstock. Coherent manipulation and guiding of Bose-Einstein condensates by optical dipole potentials. *C. R. Acad. Sci. Paris*, 2(4):671–680, 2001.

[133] I. V. Barashenkov, S. R. Woodford, and E. V. Zemlyanaya. Parametrically driven dark solitons. *Phys. Rev. Lett.*, 90(5):054103, 2003.

[134] I. V. Barashenkov, S. R. Woodford, and E. V. Zemlyanaya. Interactions of parametrically driven dark solitons. I. Néel-Néel and Bloch-Bloch interactions. *Phys. Rev. E*, 75(2):026604, 2007.

[135] A. I. Safonov, S. A. Vasilyev, I. S. Yasnikov, I. I. Lukashevich, and S. Jaakkola. Observation of quasicondensate in two-dimensional atomic hydrogen. *Phys. Rev. Lett.*, 81(21):4545–4548, 1998.

[136] V. Bagnato and D. Kleppner. Bose-Einstein condensation in low-dimensional traps. *Phys. Rev. A*, 44(11):7439–7441, 1991.

[137] H. Gauck, M. Hartl, D. Schneble, H. Schnitzler, T. Pfau, and J. Mlynek. Quasi-2D gas of laser cooled atoms in a planar matter waveguide. *Phys. Rev. Lett.*, 81(24): 5298–5301, 1998.

[138] O. Zobay and B. M. Garraway. Two-dimensional atom trapping in field-induced adiabatic potentials. *Phys. Rev. Lett.*, 86(7):1195–1198, 2001.

[139] G. Theocharis, D. J. Frantzeskakis, P. G. Kevrekidis, B. A. Malomed, and Y. S. Kivshar. Ring dark solitons and vortex necklaces in Bose-Einstein condensates. *Phys. Rev. Lett.*, 90(12):120403, 2003.

[140] P. G. Kevrekidis, V. V. Konotop, A. Rodrigues, and D. J. Frantzeskakis. Dynamic generation of matter solitons from linear states via time-dependent scattering lengths. *J. Phys. B: At., Mol. Opt. Phys.*, 38(8):1173, 2005.

[141] Y. S. Kivshar and T. J. Alexander. Trapped Bose-Einstein condensates: Role of dimensionality. *arXiv preprint cond-mat/9905048*, 1999.

[142] A. L. Fetter and A. A. Svidzinsky. Vortices in a trapped dilute Bose-Einstein condensate. *J. Phys.: Condens. Matter*, 13(12):R135, 2001.

[143] V. P. Mineev. The theory of the solution of two near-ideal Bose gases. *Sov. Phys. JETP*, 40:132, 1974.

[144] M. C. Lai. A note on finite difference discretizations for Poisson equation on a disk. *Numer. Methods Partial Differential Equations*, 17(3):199–203, 2001.

[145] H. Susanto, P. G. Kevrekidis, R. Carretero-González, B. A. Malomed, D. J. Frantzeskakis, and A. R. Bishop. Cerenkov-like radiation in a binary superfluid flow past an obstacle. *Phys. Rev. A*, 75(5):055601, 2007.

[146] A. Radouani. Soliton and phonon production by an oscillating obstacle in a quasi-one-dimensional trapped repulsive Bose-Einstein condensate. *Phys. Rev. A*, 70(1):013602, 2004.